DEVELOPMENT OF MULTI-COMPONENT IRON-BASED AMORPHOUS ALLOY

by

PETER JAMES SQUIRE

A thesis submitted to
The University of Birmingham
for the degree of
DOCTOR OF PHILOSOPHY

Department of Metallurgy and Materials
The University of Birmingham
April 2009

SYNOPSIS

This present study is concerned with developing a new alloy system which is capable of forming a metallic glass on rapid solidification of the melt, rather than modifying a known glass forming composition, and assessing its glass forming ability. Iron (Fe) was chosen as the solvent element because it is significantly cheaper than the base elements found in some other metallic glasses and does not require the addition of large quantities of expensive alloying elements to enable vitrification. A ternary system using carbon (C) and boron (B) was studied initially as these metalloids are known to aid glass formation in other systems. Manganese and molybdenum were selected as secondary alloying additions in order to determine if they would have an effect on the Fe-C-B alloy with the best glass forming ability.

A combination of optical microscopy, scanning electron microscopy, transmission electron microscopy, X-ray diffractometry and secondary ion mass spectroscopy was used to investigate the microstructure of as-cast and rapidly solidified alloys. Differential scanning calorimetry (DSC) was used to investigate the thermal behaviour of the alloys.

The ability of the iron-based alloys to form a glass on rapid solidification from the melt could not be predicted by observation of the as-cast microstructure or through computational methods. It was found that vitrification of the ternary system was only possible for compositions which were close to a eutectic point and that stabilisation of the supercooled liquid was caused by competition for nucleation between austenite and

metastable phases, rather than between primary equilibrium solidification products. Of the ternary compositions where an amorphous phase was produced it was concluded that $Fe_{80.9}C_5B_{14.1}$ had the best glass forming ability (GFA).

It was determined that the addition of manganese and/or molybdenum to the base composition generally had the effect of improving the GFA through the increased complexity of the system making it more difficult for recrystallisation to occur. Of the multi-component alloys it was concluded that $Fe_{60.9}Mn_{10}Mo_{10}C_5B_{14.1}$ had the best GFA as it had the highest values for each of the parameters used to describe GFA. It is believed that this is due to competition between the austenite and alpha stabilisers (manganese and molybdenum respectively) causing enhanced stability of the supercooled liquid.

PREFACE

The work described in this thesis was carried out by the author in the Department of Metallurgy and Materials, at The University of Birmingham, from October 2004 to October 2008, under the supervision of Dr. I.T.H. Chang.

The material presented here is original and no part of this work has been submitted for a degree at this or any other university. Where the work of others has been drawn upon, it is acknowledged in the text.

This thesis follows on from preliminary work from which has been presented at the Twelfth International Conference on Rapidly Quenched Metastable Materials (RQ12), Jeju, South Korea, 2005 and published as:

[1] Squire, P.J., Chang, I.T.H., *Development of Rapidly Solidified Al–Y–Ni-based Alloys*. Materials Science and Engineering A 449-451 (2007) 1009-1012.

Papers based on Chapters 4 and 5 are in preparation.

I dedicate this work to my nieces

Angel and Blossom

both of whom were born during the course of this PhD

ACKNOWLEDGEMENTS

I am extremely grateful to Dr. I. T. H. Chang for his patience, guidance and helpful insights during the course of this work.

I would like to thank the following technical staff for their invaluable assistance: Mr. Jeff Sutton; Miss Chris Hardy; Mr. Frank Biddlestone; Miss Avril Rogers; Mr. Jaswinder Singh; Mr. John Lane; and Mr. Derek Boole. I would also like to acknowledge all the other technical and support staff who have helped make this work possible.

I am grateful to Dr. Artemis Stamboulis for arranging the secondary ion mass spectroscopy (SIMS) that was performed outside the university; and to Mr. Richard Chater of Imperial College London for carrying out the work.

I am indebted to Dr. Heiko Widmann for help in translating parts of a paper written in German, and for keeping me smiling – especially when he performed the schuhplattler (traditional German slap dance) in his group's office!

Finally, I would like to offer sincere thanks to my family, friends, Professor Peter Brown and Dr. Claire Davis, who have all offered me support and encouragement throughout my time as an undergraduate and postgraduate at The University of Birmingham.

TABLE OF CONTENTS

CHAPTER 1 INTRODUCTION 1

1.1 Metallic Glass 1

1.2 Metallic Glass Applications 2

1.3 Alloy System Selection 4

1.4 Aims and Objectives of Thesis 6

CHAPTER 2 LITERATURE REVIEW 8

2.1 Metallic Glass Structure 8

2.1.1 Geometrical Description 8

2.1.2 Dense Random Packing of Hard Spheres 9

2.1.3 Network Models 12

2.2 Metallic Glass Types 14

2.3 Metallic Glass Production Methods 19

2.3.1 Non-melt Processing Techniques 22

2.3.1.1 Deposition Techniques 22

2.3.1.2 Spark Erosion 23

2.3.1.3 Irradiation Techniques 24

2.3.1.4 Pressure Induced Transformation (PIT) 25

2.3.1.5 Solid State Diffusion (SSD) 25

2.3.1.6 Hydrogen Induced Amorphization (HIA) 26

2.3.1.7 High Energy Ball Milling 26

2.3.2 Melt Processing Techniques 27

2.3.2.1 Atomisation Techniques 29

2.3.2.2 Chill Techniques 31
2.4 Characteristics of Metallic Glasses 35
2.4.1 Structural Properties 35
2.4.1.1 X-Ray Diffractometry (XRD) 35
2.4.1.2 Transmission Electron Microscopy (TEM) 36
2.4.2 Glass Transition and Thermal Behaviour 39
2.4.2.1 Vitrification 39
2.4.2.2 Devitrification 39
2.4.3 Glass Forming Ability 43
2.5 Alloy Design 48
2.5.1 Early Design 48
2.5.2 Modern Design 49
2.5.2.1 Empirical Guidelines for Alloy Design 52
2.5.2.1.1 Guideline Refinements 55
2.5.2.2 Composition Optimization 57
2.5.2.3 The Alpha Parameter 57
2.5.2.4 Primary Compositions for Research Project 59
CHAPTER 3 EXPERIMENTAL TECHNIQUES 66
3.1 Materials Processing 66
3.1.1 Starting Elements 66
3.1.2 Alloy Compositions 68
3.1.2.1 Ternary Alloys 68
3.1.2.2 Multi-component Alloys 68
3.1.3 Alloy Production 68

3.1.4 Melt Spinning 69

3.2 Materials Characterisation 70

3.2.1 Optical Microscopy 70

3.2.2 X-Ray Diffraction (XRD) 70

3.2.3 Differential Scanning Calorimetry (DSC) 72

3.2.4 Scanning Electron Microscopy (SEM) 72

3.2.5 Transmission Electron Microscopy (TEM) 73

3.2.6 Secondary Ion Mass Spectroscopy (SIMS) 73

3.2.7 Micro-Hardness Testing 74

3.2.8 Computer Modelling 74

CHAPTER 4 DEVELOPMENT OF TERNARY IRON-CARBON-BORON ALLOYS 75

4.1 Introduction 75

4.2 As-Cast Alloys 76

4.2.1 Optical Microscopy 76

4.2.1.1 Alloys with B/Fe Ratio ≥0.19 and Carbon Content >7 Atomic% 76

4.2.1.2 Alloys with B/Fe Ratio ≥0.19 and Carbon Content <7 Atomic% 78

4.2.1.3 Alloys with B/Fe Ratio 0.16 to 0.17 83

4.2.1.4 Alloys with B/Fe Ratio 0.09 to 0.1 83

4.2.1.5 Alloy with B/Fe Ratio 0.07 87

4.2.2 Scanning Electron Microscopy (SEM) 87

4.2.2.1 Alloys with B/Fe Ratio ≥0.19 87

4.2.2.2 Alloys with B/Fe Ratio ≥0.16 91

4.2.2.3 Alloys with B/Fe Ratio 0.09 to 0.1 93

4.2.2.4 Alloys with Additional Features 93

4.2.3 Secondary Ion Mass Spectroscopy (SIMS) 97

4.2.4 X-Ray Diffraction (XRD) 97

4.2.5 Transmission Electron Microscopy (TEM) 100

4.2.6 Differential Scanning Calorimetry (DSC) 104

4.2.6.1 Alloys with B/Fe Ratio ≥0.19 and Carbon Content >7 Atomic% 104

4.2.6.2 Alloys B/Fe Ratio ≥0.19 and Carbon Content <7 Atomic% 104

4.2.6.3 Alloys B/Fe Ratio <0.19 106

4.3 Melt-Spinning 107

4.3.1 X-Ray Analysis 109

4.3.2 Differential Scanning Calorimetry (DSC) 111

4.3.2.1 Devitrification 111

4.3.2.2 Melting 113

4.3.2.2.1 Alloys with B/Fe Ratio ≥0.19 and Carbon Content >7 Atomic% 113

4.3.2.2.2 Alloys with B/Fe Ratio ≥0.19 and Carbon Content <7 Atomic% 113

4.3.2.2.3 Alloys B/Fe Ratio <0.19 115

4.4 Discussion 116

4.4.1 Solidification Sequences 117

4.4.1.1 Transformation During Slow Cooling of the Melt 117

4.4.1.2 Transformation During Rapid Cooling of the Melt 123

4.4.2 Predicting GFA 126

4.4.2.1 Observation of As-Cast Microstructure 126

4.4.2.2 The Alpha (α) Parameter 127

4.4.3 Glass Formation in the Fe-C-B System 130

CHAPTER 5 DEVELOPMENT OF MULTI-COMPONENT IRON-BASED AMORPHOUS ALLOY 133

5.1 Introduction 133

5.2 As-Cast Alloys 136

5.2.1 Optical Microscopy 136

5.2.1.1 Alloys with Manganese Additions 136

5.2.1.2 Alloys with Molybdenum Additions 136

5.2.1.3 Alloys with Manganese and Molybdenum Additions 146

5.2.2 Scanning Electron Microscopy (SEM) 150

5.3 Melt-Spinning 158

5.3.1 X-Ray Diffraction (XRD) 158

5.3.2 Differential Scanning Calorimetry (DSC) 163

5.3.2.1 Devitrification of the Amorphous Phase 163

5.3.2.2 Melting 167

5.3.3 Hardness Testing 170

5.4 Discussion 172

5.4.1 Observation of As-Cast Microstructure 172

5.4.2 Glass Forming Ability of
Multi-Component Fe-Based Systems 172
5.4.2.1 The Alpha Parameter 174
5.4.2.2 The Effect of Manganese
Addition to $Fe_{80.9}C_5B_{14.1}$ 175
5.4.2.3 The Effect of Molybdenum
Addition to $Fe_{80.9}C_5B_{14.1}$ 175
5.4.2.4 The Effect of Manganese and
Molybdenum Addition to $Fe_{80.9}C_5B_{14.1}$ 176
5.4.2.5 Glass Forming Ability of
Multi-Component Alloys 177
CHAPTER 6 CONCLUSIONS AND FUTURE WORK 180
6.1 Conclusions 180
6.2 Future Work 183
REFERENCES 185

CHAPTER 1

INTRODUCTION

1.1 Metallic Glass

What is metallic glass? To the person in the street these words are not concomitant. Glass is the transparent stuff you put in windows and metallic means an opaque material made of metal. When people think of a metal, although they might not know it, they are usually envisaging an alloy with a crystalline microstructure.

In a crystal, atoms are arranged in a periodic (regular and repeatable) array over long atomic distances, hence a crystal can be considered as a solid with long-range order in three dimensions. A simplified description of an alloy is that it is a polycrystalline material which contains a large quantity of small crystals (commonly called grains) that are randomly orientated. However, depending on composition selection and processing methods, alloys can also exist as single crystals, quasicrystals, or even in an amorphous form.

In a quasicrystal the atoms have long-range orientational order but, unlike a crystal, there is no three-dimensional periodicity [1,2]. Instead of translational symmetry a quasicrystal has five-, eight-, ten-, or twelve-fold rotational symmetry [2,3].

In an alloy where there is neither long-range order nor periodicity the overall structure is random or amorphous, much like that of a liquid, or a ceramic glass. For this reason metallic glass is the term used to refer to an alloy with an amorphous structure.

1.2 Metallic Glass Applications

Metallic glasses are of interest because they can have different or unique physical and chemical properties compared to crystalline alloys of the same composition. This is due to the fact that they lack features associated with polycrystalline materials, e.g., long-range ordering, grain boundaries, stacking faults, and dislocations [4].

Many metallic glasses have a higher resistance to corrosion compared to their crystalline counterparts. This is due to their chemical homogeneity. For example, they do not have grain boundaries where intergranular corrosion could occur [4,5,6].

Some metallic glasses are magnetically soft [5,6,7,8]. A principal use is as transformer cores with reduced power losses and increased current compared to cores made of silicon steel [6,9].

An electrical characteristic of metallic glasses is that their resistivity at room temperature is significantly larger than that of the alloys in a crystalline state – $\rho_{am}(300K)/\rho_{crys}(300K) \approx 1.78$ [5,10]. Resistivity is inversely proportional to conductivity, which is governed by the ease of movement of an electron through a lattice. Hence, the amorphous structure of a metallic glass reduces the mobility (μ_e) of an electron.

Mechanically, metallic glasses can have properties such as high compressive strength (and in some cases high tensile strength), high fracture toughness and improved wear resistance [6,11]. For example, age-hardened conventional Al-based crystalline alloys have a fracture toughness (σ_f) around 550 MPa and a Vickers hardness of 180 while for an amorphous system like $Al_{88}Y_2Ni_{10}$ the values are 920 MPa and 340, respectively [12]. It has also been reported that in some zirconium-based alloys the elastic limit is as high as 2%, more than double that for conventional cast stainless steel, aluminium and titanium alloys [6]. The lack of 'defects' within fully amorphous metallic glasses means they have low resistance to shear band formation and propagation, making them susceptible to cyclic fatigue. Where reliability is critical this limits their applications as catastrophic failure (formation of a crack and its subsequent rapid growth until fracture) can occur with little plastic deformation being exhibited beforehand [5]. One way to control shear band propagation and therefore improve the mechanical properties of a metallic glass is to introduce a second phase into the microstructure. This can be either extrinsic (metal or ceramic particles) or intrinsic (formation of crystals from the melt or on controlled devitrification) [5,6,11].

Currently there are two main companies (Liquidmetal Technologies and Metglas) which commercially produce metallic glasses, with applications in industrial coatings; electronic casings; sporting goods; space projects; fine jewellery; [13]; electrical distribution transformers, high-frequency switching power supplies, sensors, anti-theft tags, and brazing alloys – where the initial state of the material is important, i.e, contaminant free (no organic binders) ductile foil with low melting point [14].

1.3 Alloy System Selection

A problem with many of the metallic glass systems developed to date is that they use expensive metals (some of which are listed in table 1.1) as the solvent material, thus limiting their use to non-commercial purposes. This has prompted many researchers to look for amorphous systems based on cheaper elements.

From table 1.1 it can clearly be seen that magnesium, copper, iron and aluminium are attractive candidates for developing amorphous systems as their values are orders of magnitude lower than the most expensive metals. For this research programme aluminium, copper and magnesium were rejected as base elements. Aluminium: because Al-based systems can currently only be produced in thin or powdered forms. Copper: because known glass forming systems require a large percentage of high cost elements such as zirconium or hafnium [16,17]. Magnesium: partly because it is almost twice the cost of copper or iron; but also because it has a boiling point much lower than the melting points of the common alloying elements copper and gadolinium [18,19], which can cause difficulty in achieving desired compositions [20]. This left iron as the best choice for the solvent metal. The semi-metals carbon, boron and phosphorus are known to aid the glass

Table 1.1 Comparison of a selection of metals used as the solvent element for metallic glasses. These values are for the cheapest form and minimum purity and assume no discount for bulk orders [15].

Element	Cost (£/kg)	Form	% Purity by metal basis	
Palladium	37,240	Ø6.35mm rod	99.95	
Neodymium	5,257	Ø12.7mm rod	99.9	excluding Tantalum
Lanthanum	2,180	Pieces	99.9	excluding Tantalum
Zirconium	990	Ø6.2mm rod	99	excluding Hafnium
Titanium	176	sponge	99.7	
Magnesium	107	Ø33mm rod	99.8	
Copper	49	shot	99.9	
Iron	47	pieces	99.97	
Aluminium	25	shot	99.9	

forming ability of several systems, and in particular, it has been shown that the commercial cast iron FC20 can be vitrified by the addition of extra boron [21]. Therefore carbon and boron were selected as the elements to make up a simple system. Phosphorus was not chosen because it is a hazardous material in its elemental form, and if used in a pre-alloyed form such as iron phosphide would limit the compositions which could be studied due to the processing techniques available.

The CALPHAD method (*Cal*culation of *Pha*se *D*iagrams) is a technique which can model the thermodynamic functions of various phases in a system. For example, it can be used to determine the liquidus point of a particular composition, or calculate the free energy curves of phases within a system. Regarding the latter example, if thermodynamic data from amorphous compositions can be obtained, then the CALPHAD method can even be used to determine the compositional range over which a system could be vitrified. ThermoCalc is a computer software package that uses this technique, and in conjunction with the steels TCFE2 database (both of which were developed by the Division of Computational Thermodynamics at the Royal Institute of Technology in Stockholm), might therefore be used to aid in the development and understanding of a new iron-based amorphous alloy.

1.4 Aims & Objective of Thesis

The aim of this research programme is to develop a new iron-based amorphous system - rather than optimising the composition of a known system or introducing additional element(s) in order to improve it - and to assess its glass forming ability.

Early research into metallic glasses noted that glass-forming tendency in systems generally increases around the eutectic point(s) of an alloy [22]. This project investigates ternary compositions taken from the invariant points in the iron-carbon-boron system and compositions based on combining values from binary iron-carbon and iron-boron systems. The project is also concerned with the effect of the alloying additions of manganese (an austenite stabiliser) and molybdenum (a ferrite former) on the ternary alloy with the best glass forming ability.

Chapter 2 is a literature review of amorphous alloys and covers development of glass forming ability, processing methods and characterisation techniques.

Chapter 3 describes experimental techniques used in this programme. Processing of the alloys is achieved through arc-melting and melt-spinning. Characterisation of the resultant material is achieved by optical microscopy, scanning electron microscopy (SEM), transmission electron microscopy (TEM), X-ray diffraction (XRD), differential scanning spectroscopy (DSC) and hardness testing.

Chapter 4 presents experimental results and discussion of GFA in the ternary Fe-C-B system.

Chapter 5 presents experimental results and discussion of the GFA of $Fe_{80.9}C_5B_{14.1}$ with the addition of manganese and/or molybdenum.

Chapter 6 summarizes the project and gives suggestions for further work.

CHAPTER 2

LITERATURE REVIEW

2.1 Metallic Glass Structure

Metallic glasses are alloys which have an amorphous structure – meaning there is no long-range order or periodicity in the arrangement of atoms. Over the years that they have been studied, there have been several attempts to describe the actual configuration of atoms in a metallic glass. They are all based on the notion that an amorphous structure is analogous to that of the liquid state, so the methods used to describe a liquid can also be used to describe metallic glass.

2.1.1 Geometrical Description

It was Bernal [23] who thought that liquid structure could be modelled through a geometrical approach. In his theory simple liquids can be thought of in terms of the packing of irregular polyhedra – such as in a foam. The polyhedron is the space surrounding a single molecule of the liquid, such that each point within the polyhedron is

closer to the molecule than any other molecule in the system. This is similar to the description of a Voronoi cell, where the partitioning of space is about a single point rather than a molecule. Figure 2.1 shows Bernal's two-dimensional representation of the packing of irregular polyhedra while for comparison figure 2.2 shows a Voronoi diagram of a set of random points in a plane.

2.1.2 Dense Random Packing of Hard Spheres

Scott [25] later used the random packing of hard spheres, rather than irregular polyhedra, as the model for a simple liquid. This is probably because solid materials are usually modelled using hard spheres to represent the positions of individual atoms (rather than molecules) in a crystalline lattice. The reason hard spheres are used is that the Bohr model of an atom can be represented by a sphere. It consists of a series of nested shells with a small core at the centre. The core is a nucleus (consisting of protons and neutrons) around which electrons revolve in discrete orbitals, or shells, each of which contains electrons of the same energy level. Quantum mechanics now tells us that an atom is better described by a wave-mechanical model. Here an electron does not orbit the nucleus in a discrete orbital, rather its position about the nucleus can be anywhere and is given by a probability function, where the area of the greatest chance for finding the electron is equivalent to the discrete orbital of the Bohr model. In either case an atom can be represented by a hard sphere.

In his modelling of a liquid, Scott [25] found that there is a well-defined range for random packing. The limiting values are 0.63 for dense random packing (DRP) and 0.59 for loose random packing (LRP). It should be noted that these values are for spheres of equal size

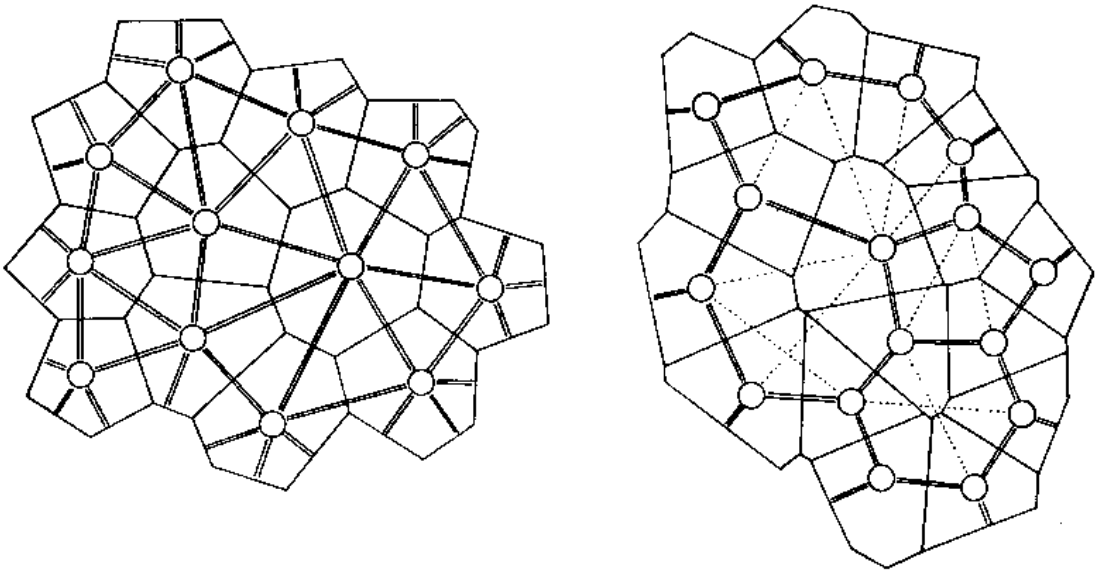

(a) (b)

Figure 2.1 Bernal polyhedra for a two-dimensional array [23]. The circle represents a molecule. Each polyhedron is defined such that any point surrounding a molecule is closer to that molecule than any other molecule. (a) high co-ordination, where all molecules have physical neighbours. (b) low co-ordination, where some molecules have geometric neighbours – shown by dotted line.

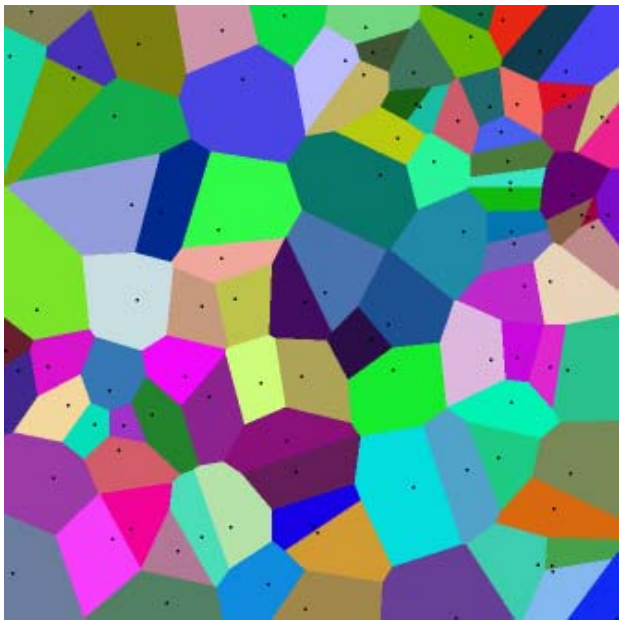

Figure 2.2 Two-dimensional Voronoi diagram showing the equal partitioning of space between a set of randomly distributed points [24].

and metallic glass systems are amorphous *alloys.* They must be modelled with spheres of different sizes as the atomic radii of the different elements used are never exactly the same. Clarke and Wiley [26] have performed simulations of the dense random packing of hard spheres (DRPHS) for binary mixtures of spheres of all compositions with a radius ratio of large spheres to small spheres up to 2:1. They found that packing fraction ranged from 0.64 to 0.68. From these values they calculated that metallic glasses should be 8-13.5% less dense than that for crystalline alloys of the same composition. This led them to the conclusion that there was a problem with DRPHS as they stated that most metallic glasses are actually much closer in density to their crystalline counterparts, typically being only 0.5-2% less dense. To accommodate the small difference in densities they found Clarke and Wiley [26] thought the DRPHS model could be modified. They suggested that if the spheres are not hard, and are in fact 'spongy', that would enable them to be distorted and compressed thereby allowing a higher density.

It should be noted though, that for this comparison Clarke and Wiley used a packing fraction of 0.74 for the crystalline system. This is the value for the greatest packing density of single sized spheres and is found in face-centred-cubic (FCC) and hexagonal-close-packed (HCP) crystal systems. If other monatomic systems such as body-centred-cubic (BCC) had been used the calculated difference in density between crystalline and amorphous alloys would have been much closer, possibly even to the point where a metallic glass could be more dense than its crystalline counterpart. However, it has been shown that even for binary alloys with only a small difference in atomic radii that packing density can increase. This would lead to a greater difference between the calculated and measured values. To complicate things even further, it is worth mentioning that the

comparison also assumed a single phase system, whereas binary or larger systems often contain more than one phase. For example, the iron-carbon system has a BCC phase (ferrite) and an orthorhombic phase (cementite). Rather than amending the DRPHS model to fit experimental data it could be concluded that DRHPS is just not the correct depiction of the structure in a metallic glass, at least for monatomic and binary systems.

2.1.3 Network Models

It has been suggested the atomic arrangement in metallic glasses is not entirely random and that there is a degree of chemically induced short range order. Two new models for the structure of metallic glasses have been proposed, with both still using hard spheres to represent atoms.

The first is that of a structure-reinforced network [27], similar in fashion to a cross-linked polymer. In this theory it is thought that where there is particularly strong bonding between certain pairs of atoms of the appropriate concentrations then these atoms may form a percolating network or reinforcing ‘backbone’ in the amorphous structure (as shown in figure 2.3). Although not stated, it is assumed that the remaining atoms are packed in a dense random manner.

The second theory of metallic glass structure, which comes from a study of Al-based alloys [28], is based on the now widely accepted Zachariasen model for metal/metalloid oxide glasses [29] where there is a continuous random network of oxide tetrahedra. Instead of tetrahedra there are atomic clusters with a co-ordination number up to 16, or even higher if a small amount of strain is allowed. In the case of some metal/metalloid systems the

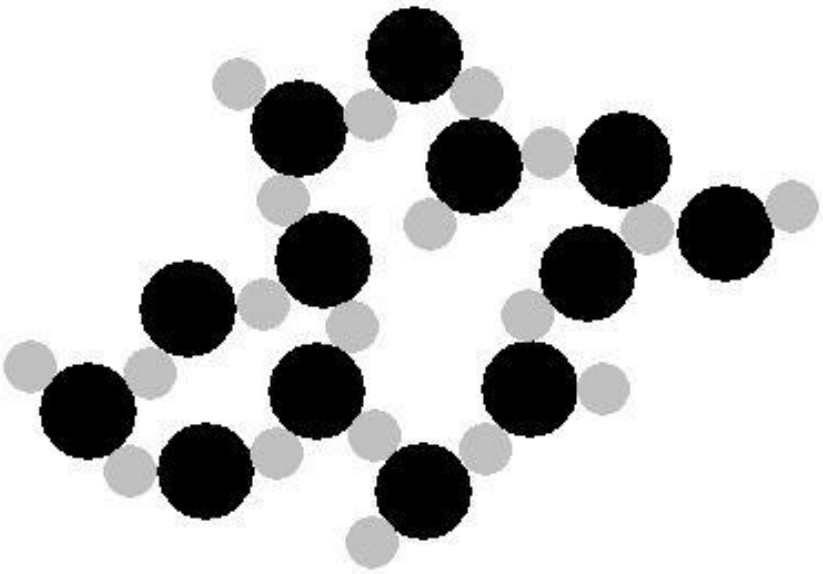

Figure 2.3 A percolating network of atoms with strong bonding - a reinforcing ‘backbone’ - in an amorphous structure. After Poon *et al* [27].

clusters are in the form of trigonal prisms with the metalloid at the centre. The prisms are distorted in ternary or larger systems, as one or more apexes will be occupied by a metal atom that is not the same size as the solvent atom [30]. Figures 2.4 to 2.8 show examples of possible clusters. For the overall structure to retain efficient packing each cluster must share faces. Although in the case of the trigonal prisms, it is the edges and vertices which must be shared.

2.2 Metallic Glass Types

There are two types of metallic glasses and in general terms are classified by their critical cooling rates. Alloys which require a critical cooling rate (R_c , see section 2.3.2) greater than 10^5 Ks^{-1} can only be fabricated as thin-layered forms or small particles, as a high cooling rate cannot be maintained uniformly throughout bulkier samples, and are referred to as ordinary metallic glasses / amorphous alloys (OMGs), or marginal glass forming alloys [33,34]. Alloys with a R_c of less than 10^3 Ks^{-1} can be produced with dimensions in the millimetre range and are known as bulk metallic glasses (BMGs) [35]. Currently, some of the maximum diameters achieved for fully amorphous alloys are 16, 40 and 72mm, for $Fe_{41}Co_7Cr_{15}Mo_{14}C_{15}B_6Y_2$, $Zr_{41.2}Ti_{13.8}Cu_{12.5}Ni_{10}Be_{22.5}$ and $Pd_{40}Ni_{10}Cu_{30}P_{20}$ respectively [36,37,38].

Senkov and Miracle have shown that one can differentiate between BMGs and OMGs using topology – the characteristic configurations of atoms in the structures. [28,34]. For any system the atomic percentage of each element in that system can be plotted against its atomic radius. A trend line can be drawn through the data points to produce a curve known as an atomic size distribution plot (ASDP) for that particular system. There are common

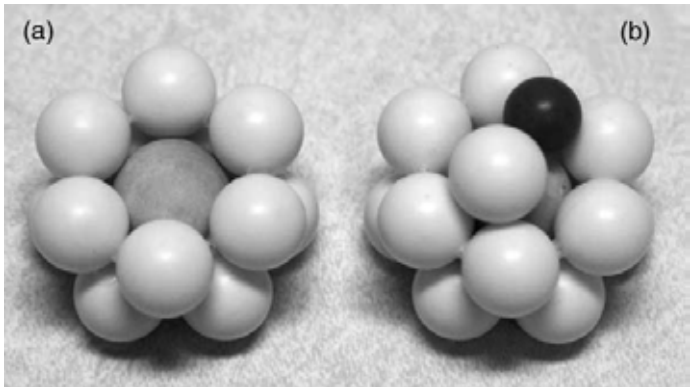

Figure 2.4 High co-ordination clusters based on two parallel sixfold rings rotated 30° with respect to one another about a central Y atom [28]. Cluster (a) shows the resulting hexagonal antiprism structure, and (b) illustrates the same cluster with a termination of one Al atom and one Ni atom.

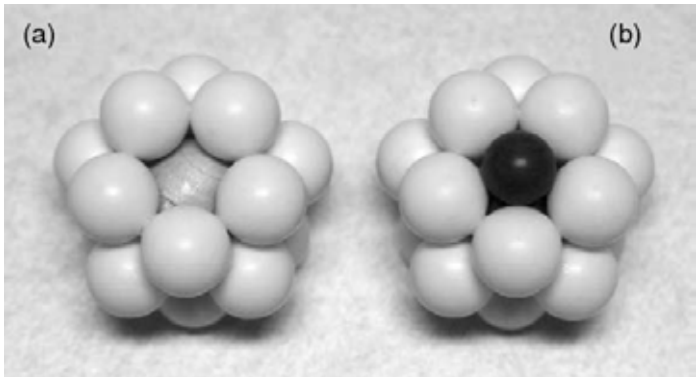

Figure 2.5 Tri-pentagonal clusters composed of three parallel fivefold rings of Al atoms coordinated around a central Y atom [28]. (a) has a total co-ordination of 15 while (b) which has a co-ordination of 17, with the addition of nickel atoms at the base and top.

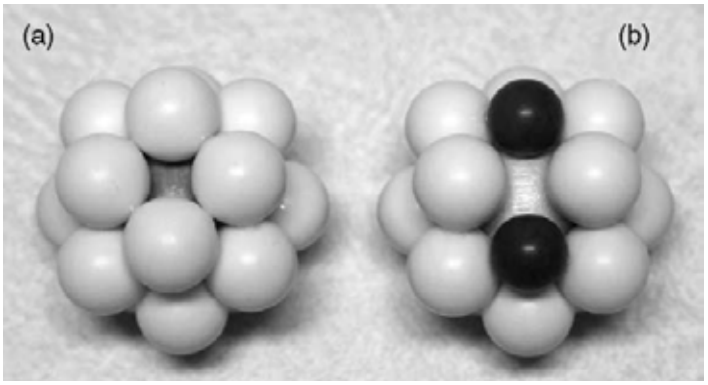

Figure 2.6 A cluster based on four parallel fourfold rings of Al atoms coordinated around a central Y atom [28]. (a) is slightly unstable in an Al–Y system but is stabilized by the substitution of two Al atoms with Ni atoms in (b).

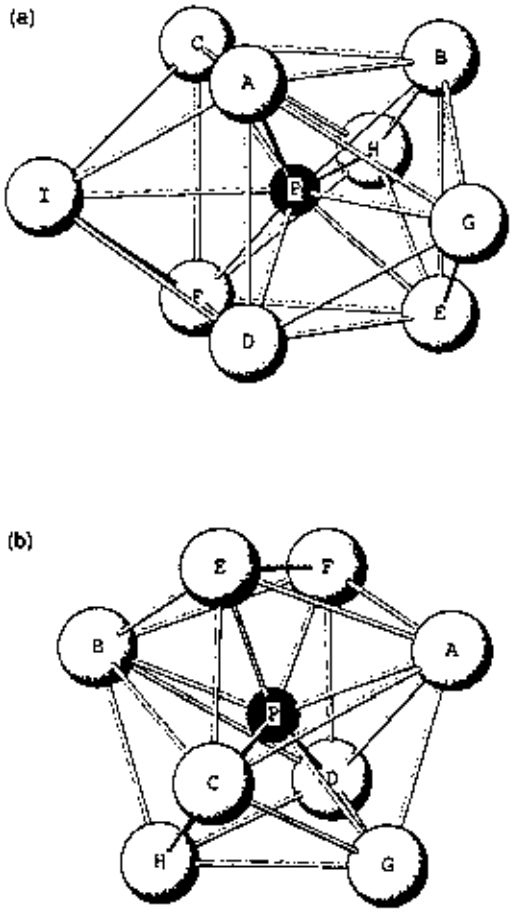

Figure 2.7 Clusters with phosphorus as a central atom surrounded by a majority of palladium atoms with additional copper and/or nickel atoms. (a) trigonal prism capped with three half-octahedra. (b) tetragonal dodecahedron. [31]

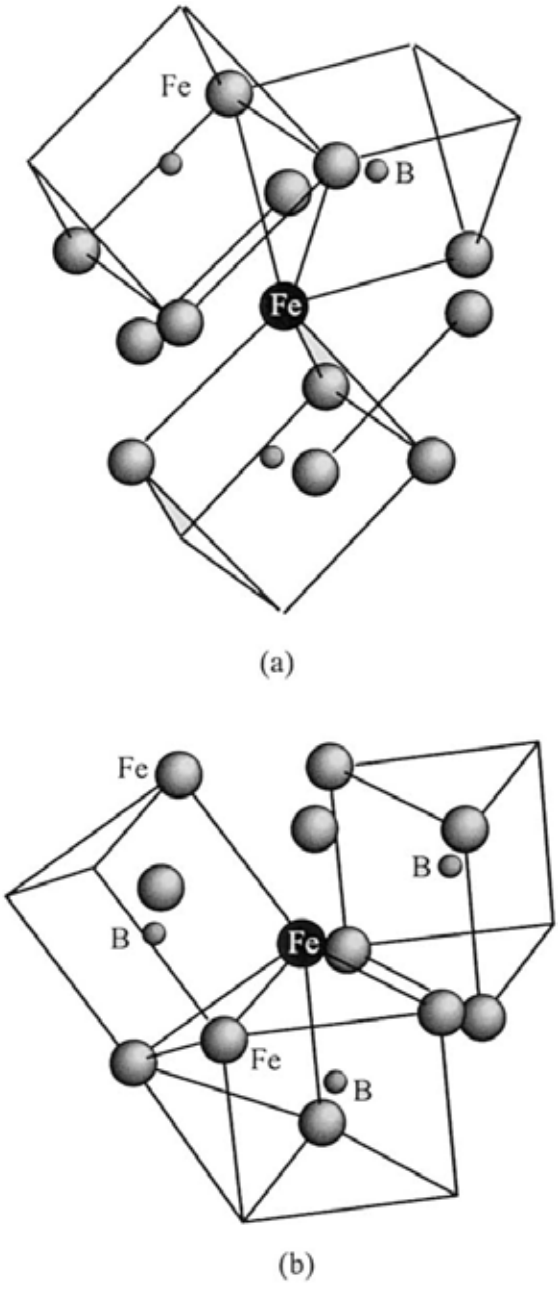

Figure 2.8 Atomic arrangements for (a) vertex sharing and (b) edge sharing trigonal prisms. Only the near neighbour atoms surround the central iron atom are shown [32]. In ternary or larger systems a prism will be distorted when an apex is occupied by a metal atom with a different size to the solvent atom [30].

trends in these plots and they result in three distinct types of curve each of which corresponds to one of the metallic glass types, examples of which are shown in figure 2.9. When viewed from the base of the plot, a concave 'parabola' (cone shape) is characteristic of OMGs when the apex (which equates to the solvent content) is over 70 atomic percent, and to some BMGs when the apex is below 70 atomic percent. A convex 'parabola' (cup shape) is uniquely representative of most BMGs.

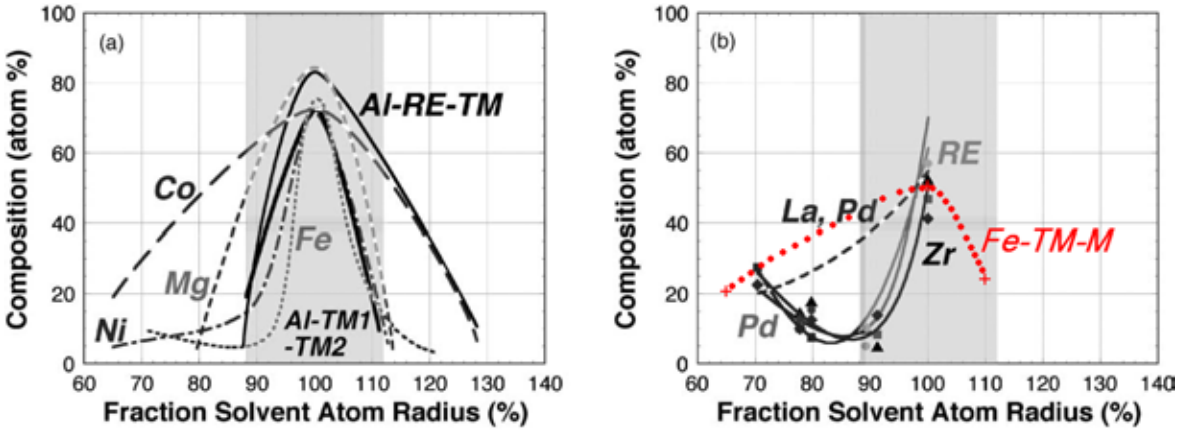

Figure 2.9 Atomic size distribution plots (after Miracle) [34]. (RE = Rare Earth, TM = Transition Metal, and M = Metalloid). The grey band represents a limit of where solid solubility may occur in crystalline alloys. (a) Ordinary metallic glass. (b) Bulk metallic glass.

Work by Poon et al is in agreement with these findings. In this case BMGs are again classified by atomic size distribution and are split into two basic groups: LS/SL and MSL (where L = large, S = small, and M = medium sized atoms respectively) [27]. These groups are listed in table 2.1. OMGs also fall into the MSL class but it is stated that they generally contain a significantly higher proportion of large atoms compared to those in BMGs of this class. For the two BMG classes, the alloys have been found to fall within a compositional range (in atomic percent) for each type. In MSL systems the ranges are M = 60-70, S = 30-20 and L is approximately 10. In LS/SL systems the ranges are L = 40-75 and S = 60-25.

It should be noted that in this class S includes some medium sized atoms. If an ASDP is drawn for these classes a cone shape is produce for the MSL type, and a cup shape or downward sloping curve with respect to the majority atom, is produced for the LS/SL type.

Table 2.1 Bulk metallic glasses grouped into two structural classes according to their atomic size-composition relationships [27]. The large atom groups are in parenthesis and the majority atom groups are underlined. For each class the alloying content of the elemental group increases from left to right.

MSL class BMG	LS/SL class BMG
Mg-Cu-(Y)	(La)-Al-Ni-Cu
Fe-P-B-C-Si-(Ga,Al)	(Pd)-Ni-Cu-P
Fe-B-(Zr,Nb,Mo)	(Zr,Ti)-Ni-Cu-Be
Fe-Co-B-(Ln)	(Zr,Nb)-Ni-Cu-Al
Fe-Cr-C-B-P-(Mo)	Ni-Si-(Zr,Ti)
Ti-Zr-Ni-Cu-(Sn)	Cu-Ni-(Ti,Zr)
	(Ti)-Cu-Ni-Si-B

2.3 Metallic Glass Production Methods

Amorphous forms of elemental iron, nickel, platinum, zinc, tin, cadmium and antimony were reported in 1934 [39]. It is possible, though, that nickel phosphide could have been produced in an amorphous form as far back as 1845, but was not recognised as being amorphous because the X-ray technology needed to identify it as non-crystalline was not available at that time [40]. Since their discovery, metallic glasses have been fabricated by many different production methods. They can be classified into two basic categories: melt processing and non-melt processing. The latter methods include various deposition techniques and solid state processing, while the former include atomisation and non-atomisation procedures. Examples of metallic glasses and the method by which they were produced are listed in tables 2.2 and 2.3.

Table 2.2 Non-melt production techniques with examples of the amorphous alloys that can be produced. Where given, compositions are in atomic percent or fraction.

Production Technique	**Alloy**	**Form**	**Diameter/Thickness**
Physical Vapour Deposition [41]	$Ti_{49.4}Al_{46.5}Nb_2Cr_{1.6}W_{0.5}$	sheet	150μm
Chemical Vapour Deposition [42]	$Ru_{80.4}P_{19.6}$	film, unknown carbon impurity	33nm
Electrodeposition [43]	$Ni_{80}P_{20}$	disk	1mm
Electrolessdeposition [44]	Ni-Co-B	compacted particles	20nm diameter
Spark Erosion [45]	$Fe_{75}Si_{15}B_{10}$	powder	10nm (condensed vapour) <30μm (quenched particles)
Electron Irradiation [46]	$Nd_2Fe_{14}B$	amorphous phase within foil	foil prepared for electron beam microscopy
Ion Beam Mixing [47]	$Cu_{70}Nb_{30}$	foil	42nm
Thermobaric Treatment [48]	$Zn_{43}Sb_{57}$	n/a	n/a
Shock Compression [49]	$Au_{81.4}Si_{18.6}$	amorphous phase within foil	foil prepared for electron beam microscopy
Solid State Diffusion [50]	Au-Ln	thin film	<1μm
Hydrogen Induced Amorphization [51]	$YFe_2.H$	powder	<100mesh (150μm)
Mechanical Milling [52]	Nb_3Sn	powder	n/a
Mechanical Alloying [53]	Fe-Ni-Zr-B	powder	25-125μm

Table 2.3 Rapid solidification processing techniques with examples of the amorphous alloys that can be produced. Where given compositions are in atomic percent or fraction.

Production Technique	**Alloy**	**Form**	**Diameter/Thickness**
Gas Atomization [54]	$Al_{85}Ni_5Y_6Co_2Fe_2$	powder	<25μm
Water Atomization [55]	$Fe_{74}Si_{11}B_{14}Ni_1$	powder	<40μm
Gas-Water Atomization [56]	$Cu_{60}Zr_{40}$	powder	<44μm
Centrifugal Atomization [57]	$Co_{70.5}Fe_{4.5}Si_{10}B_{15}$	flaky powder	25-150μm
Electrohydrodynamic Atomization [58]	$Al_{70}Ge_{30}$	powder	<100nm
Duwez Gun [59]	$Au_{75}Si_{25}$	splat	10μm
Hammer and Anvil [60]	$Ga_{23.7}Te_{76.3}$	splat	30μm
Twin Piston [61]	$Fe_{82}B_{12}Si_6$	foil	40μm
Melt Spinning [62,63]	$Al_{88}Ni_1Pd_1Y_{10}$	ribbon	<100μm
Planar Flow Casting [64]	$Pd_{80}Si_{12}Ge_8$	wide ribbon	<100μm
Twin Roller [65]	$(Co_{1-a}Ni_a)_{75}Si_{10}B_{15}$	ribbon	30μm
In-Rotating-Water [66]	$Pd_{77.5}Cu_6Si_{16.5}$	wire	0.3mm
Melt Drag [67]	Fe-Cr-Si-B	wide ribbon	<760μm
Melt Extraction [68]	$Fe_{75}Si_{10}B_{15}$	wire	<80μm
Taylor Wire Process [69]	$Co_{80}Si_{10}B_{10}$	wire	<20μm
Die Casting [70]	$(Cu_{61.8}Zr_{38.2})_{1-x}Al_x$	rod	3mm
Quenching [37,71]	$Zr_{41.2}Ti_{13.8}Cu_{12.5}Ni_{10}Be_{22.5}$	rod	40mm
Self-Quench [72]	$Fe_{83}B_{17}$	surface layer	<500nm

2.3.1 Non-melt Processing Techniques

2.3.1.1 Deposition Techniques

Physical Vapour Deposition (PVD)

In PVD the surface of a target block of material is vaporised and the evaporated atoms condense onto a substrate. There are several PVD techniques and they differ mainly by the manner in which the starting material is vaporized. They include: evaporative deposition, where vaporization occurs through electrically resistive heating; electron beam evaporation, where vaporization occurs by electron bombardment; sputter deposition, where a glow plasma discharge causes sputtering of the material (this particular PVD technique is often just called sputtering); cathodic arc deposition, where a high power arc causes vaporization; and pulsed laser deposition, where a high energy laser causes vaporization.

Chemical Vapour Deposition (CVD)

CVD relies on the chemical reaction of gaseous precursor species above the surface of a substrate. The reaction products then form a layer on that surface. There are many methods by which CVD can be modified. These involve changing reaction rates by a change in pressure or temperature, or modification of precursor chemicals and their introduction to the substrate.

Electrodeposition

Electrodeposition is the shortened term for electrochemical deposition which is also known as electroplating. In electrodeposition, a cathode (the substrate) and an anode are immersed in a molten electrolyte or electrolytic solution. When a current is applied cations (metallic ions with a positive charge) are attracted to the cathode where they are reduced to a metal.

Electrolessdeposition

Electrolessdeposition is a chemical deposition technique where an electric current is not required. The substrate is placed in an aqueous solution of metal ions. The substrate itself is a catalyst which causes the reduction of metal ions. With continued deposition the surface of the deposit becomes the catalyst, so the reaction becomes autocatalytic. For this reason electrolessdeposition is also known as autocatalytic plating.

2.3.1.2 Spark Erosion

Spark Erosion is a process which involves maintaining a spark discharge between two electrodes immersed in a dielectric fluid. The electrodes are made from the material of interest. The spark discharge causes localised heating of the electrodes and the temperature can be raised well above the melting point of the material. The superheated region boils violently throwing out droplets and vapour. The droplets are quenched by the dielectric fluid as are the particles which condense from the vapour [45].

2.3.1.3 Irradiation Techniques

In irradiation methods, charged particles are accelerated to high velocities and directed at crystalline samples. The particles cause atomic displacement directly by giving an individual atom enough kinetic energy to effect permanent long range relocation, or by causing a cascade of multiple short range atomic displacements. It has also been proposed that at high energies (MeV range) atomic displacement occurs indirectly, where the movement of the charged particle through the system causes ionisation of the atoms surrounding its path, leading to their subsequent mutual repulsion and relocation [73].

Electron Irradiation

In this technique high energy electrons are used. The irradiation causes a gradual build-up of defects (e.g. voids) within a crystal. When the defects reach a critical level, the crystal becomes unstable and changes to an amorphous phase.

Ion Beam Mixing

In this technique the particle beam consists of ions (typically from an inert gas such as Xenon), and the starting material is composed of thin layers of alternating elements or compounds. The irradiation causes mixing of the layers, creating a disordered mixture with much higher energy than its corresponding equilibrium state, thus allowing transformation to metastable structure such as the amorphous phase.

2.3.1.4 Pressure Induced Transformation (PIT)

Thermobaric Treatment

In this technique a melt is quenched while under high pressure. This may produce a crystalline phase not present in the equilibrium phase diagram of an alloy produced at standard pressure. On subsequent heating the non-standard phase may transform to an amorphous phase [48].

Shock Compression

In shock compression, a projectile is fired at $70ms^{-1}$ [49] at a crystalline sample causing high-speed plastic deformation.

2.3.1.5 Solid State Diffusion (SSD)

In any system there is a tendency for something to move from an area of high concentration to an area of low concentration. In SSD diffusion-couples occur when thin bi-layers/multi-layers of dissimilar metals are created. As interdiffusion proceeds each metal becomes supersaturated until the point where a new phase is nucleated. Usually this would be an intermetallic compound. However, it has been noted [50,74,75] that in glass forming systems there is often asymmetric diffusion – that is, one element diffuses more quickly through the other, than when the situation is reversed. It is thought that the fast diffusing component allows mixing of the elements, while the slow diffusing component hinders the structural changes necessary to maintain the equilibrium structure for that composition, thereby allowing formation of a metastable phase. Alternatively it is thought that interdiffusion proceeds until the original crystal structures become destabilised and catastrophic vitrification occurs [74].

2.3.1.6 Hydrogen Induced Amorphization (HIA)

Hydrogenation of an alloy is effected by heating in a pressurised hydrogen atmosphere. The amount of hydrogen absorbed is dependent on the processing conditions and lowers the bulk-modulus of a crystal's lattice and sublattices. This normally leads to simple volume expansion. However, in some systems hydrogenation is thought to affect the bulk modulus of one sublattice more than another, thereby allowing greater expansion of that sublattice [76]. This causes an elastic strain which produces an internal elastic stress on the material. When the elastic limit is exceeded the crystal lattice collapses, thereby lowering the free energy of the system, resulting in an amorphous structure [77].

2.3.1.7 High Energy Ball Milling

In this technique, metal powders are placed in a milling pot along with appropriately sized milling balls. The pot is then rotated at a high rate causing the balls to acquire high kinetic energy. When the powder particles become trapped between two balls or between the wall of the mill and a ball some of the kinetic energy is transferred to the powder.

Mechanical Milling (MM)

In MM, the powder is of a homogenous composition. The milling creates defects within the crystals, which continue to build up until the crystalline structure becomes destabilised. In other words, the free energy stored within the system becomes greater than the free energy of the amorphous phase, meaning transformation to a glass is possible.

Mechanical Alloying (MA)

In MA the starting material is a powder blend consisting of elemental metals and/or metallic compounds. The milling process causes repeated deformation, fracturing and cold welding of the constituent powders, leading to the creation of diffusion couples. Eventually either a homogenous powder (supersaturated solid solution) or intermetallic phase is formed. In the former case the amorphous state may have a lower free energy than that of the solution, so transformation to a glass is possible. In the latter case vitrification would occur in the same manner as in MM.

2.3.2 Melt Processing Techniques

Glass, in the traditional sense of the term, is used to refer to a material which, on continuous cooling from its molten state, becomes increasingly viscous until it is deemed to be mechanically solid in behaviour and yet still have a liquid-like structure. The point at which this happens is known as the glass transition temperature (T_g). So, a glass can be thought of as just an extremely viscous supercooled liquid. It is normally considered to be solid when η (its shear viscosity) exceeds a certain arbitrary value: one author states it as 10^{14} N s m^{-2} (10^{14} Pa-s) [78], another gives it as 10^{14} Poise (10^{13} Pa-s) [79], while others give it as 10^{13} Poise (10^{12} Pa-s) [80, 81]. It is this description of glass that has prompted some researchers to make a distinction between non-crystalline metals based on their method of production: *metallic glass*, like traditional glass, is formed from the melt, while an *amorphous alloy* is produced through a non-melt processing technique [79]. For the remainder of this review, unless specifically stated, the term metallic glass will refer to a non-crystalline alloy produced from the melt.

In order for a glass to form it is necessary to avoid the nucleation of crystals in the melt [82], or at least to avoid detectable crystallization [83]. Solidification from the melt is a time and temperature dependent process. Why vitrification rather than crystallization can occur on continuous cooling is illustrated by the time-temperature-transformation (TTT) diagram shown in figure 2.10. If the rate of cooling is sufficiently high then the cooling curve will miss the nose of the first c-curve (the point which represents the minimum time needed to form stable nuclei) in the TTT diagram and a fully amorphous structure forms. At the critical cooling rate (R_c) the cooling curve just intersects the first c-curve and nucleation is initiated, but there is no time for growth, and the remaining liquid solidifies with an amorphous structure thereby forming a composite of crystallites embedded in a glassy matrix. If the cooling curve just penetrates the first c-curve then there is time for growth so detectable crystals will be present. Provided the cooling rate is sufficiently slow then complete crystallization of the melt will occur.

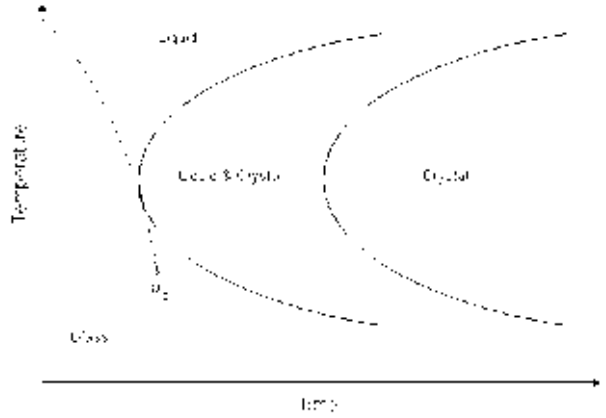

Figure 2.10 Crystal formation as a function of time and temperature.

If a glass is formed, by regarding the TTT diagram, it can be inferred that it will eventually transform to a crystalline material. However, the timescale for this to take place is so great that a glass is considered to be a stable solid, or more precisely, a metastable material.

The mainly covalent nature of the bonding in oxide/fluoride melts causes the rate of atomic or molecular rearrangements needed to maintain thermodynamic equilibrium during cooling to be severely hindered. R_c is in the order of 10^{-2} Ks^{-1}[80]. For metallic melts where atomic movement is more rapid the degree of cooling is much higher. Typically R_c is required to be around 10^5 Ks^{-1} or greater [80]. For this reason the production of metallic glass from a melt is often referred to as rapid solidification processing (RSP). It should be noted though that in recent years some amorphous alloys with R_c as low as 1 Ks^{-1}, and even 0.1 Ks^{-1}, have been reported [38,84].

In RSP the melt is delivered in the form of droplets, cylindrical stream or ribbon stream, and the rapid removal of heat is achieved by conduction through a solid, or convection in a liquid or gas, and produces solids in powder/flake, ribbons and foil form respectively.

2.3.2.1 Atomisation Techniques

These methods involve disintegration of a melt stream into fine droplets which solidify via convective cooling during flight. The powder generally has a broad range of particle sizes with only the finest grades (e.g. less than 45μm) being fully amorphous and having a smooth spherical morphology. Larger, or agglomerated, particles have a lower surface area to volume ratio, with a corresponding reduction in cooling rate, so can be partially or fully crystalline.

Gas Atomisation

On exit from a guide tube into an atomization chamber the melt stream is blasted by a jet of inert gas, such as nitrogen, with a typical pressure around 3MPa [54]. The fine droplets begin to solidify during flight through the inert gas atmosphere of the chamber, and continue to cool to ambient temperature at the base of the chamber.

Water Atomisation

In this method a jet of water, with a typical pressure around 20MPa [55], is used to fragment the melt stream and simultaneously quench the resulting droplets. Powders can display minor porosity and high levels of oxygen content.

Gas-Water Atomisation

The melt stream is gas-atomised and the resulting droplets are quenched by jets of water with a pressure around 0.5 MPa [56].

The main advantage of the techniques which use water to quench the fine droplets is that the cooling rate is improved so there is a broader range of fully amorphous powder. However, using water as the cooling medium has the disadvantage of needing to dry the resultant powders so the production rate is lower than that for gas atomization.

Centrifugal Atomisation

This is a two stage quenching technique. In the first stage a melt stream is gas atomised. The resulting droplets are directed on to a spinning rotator (cone-shape) where, if they have not already solidified, they are deformed and/or broken up before being thrown off by centrifugal action. This results in the mean particle size being smaller compared to the distribution in other atomization techniques [85].

Electrohydrodynamic Atomization (EDHA)

In this process the melt surface is exposed to an intense electric field and charged droplets are ejected from the melt. EDHA is carried under vacuum conditions so particles cool by radiation during flight.

2.3.2.2 Chill Techniques

These methods involve removal of heat energy from molten metal primarily by conduction through a substrate with good thermal conductivity. Table 2.4 lists the thermal conductivity of various materials. It can be seen that diamond would make the best substrate but in practical terms copper is most often used.

The Duwez Gun.

In this method a droplet of molten material is accelerated to high speed and directed at a substrate which is inclined at an angle that ensures good thermal contact. This technique produces solids in the form of small thin foils commonly called ‘splats’. This was the first technique able to produce a metallic glass directly from the melt [59].

Hammer and Anvil

Splats are produced by forging molten droplets between a stationary substrate and a moving piston in an inert atmosphere.

Twin Piston

A small amounted of material is levitated inside a coil and heated up under vacuum. It is then allowed to drop and is forged between two pistons, forming a splat.

Table 2.4 Thermal conductivity (at room temperature) of selected materials [86]. The higher the value the better the material is able to transfer heat, and is therefore more suitable for rapidly removing the heat from a melt.

Material	**W/m-K**
Red oak wood (12% moisture) (perpendicular to the grain)	0.18
High density polyethylene	0.48
Borosilicate glass (Pyrex)	1.4
Invar ($Fe_{64}Ni_{36}$)	10
Alumina	39
Iron	80
Brass ($Cu_{70}Zn_{30}$)	120
Aluminium	247
Gold	315
Copper	398
Silver	428
Diamond	1440-4650
Synthetic diamond	3150

Melt Spinning

A small ingot of an alloy is melted inside a crucible by induction heating. The molten alloy is then ejected through a small circular orifice by application of overpressure of inert gas. The melt stream is directed onto the surface of a vertically mounted rotating wheel where it forms a temporary reservoir from which melt is drawn and quenched. Alternative methods include directing the jet onto the inside surface of a wheel or drum, or near to the rim of a horizontally mounted wheel. Melt spinning typically produces long narrow ribbons of material.

Planar Flow Casting

The same technique as in melt spinning except the crucible nozzle is in the form of a slit and is situated close to the surface of the wheel so a wider ribbon, or foil, can be produced.

Twin Roller

Similar to melt spinning except the melt stream is directed through a small gap between two rolls rotating in opposite directions, so the melt is quenched from both sides.

In-Rotating-Water

This method is a variation of melt spinning where the melt stream is directed onto the inside surface of a rotating drum. What is different is that there is water on the inside of the drum, so heat removal is by conduction through the substrate and convection in the water. The material produced is in the form of a wire with near circular cross-section.

Melt Drag

In the melt drag (also known as melt draw) technique the melt is dragged from a slotted nozzle of a tundish which is placed close to the surface of a rotating wheel or drum. The material produced is in the form of a wide ribbon.

Melt Extraction

A stationary melt pool is grazed by the edge of a rotating wheel. Some of the melt wets the periphery of the wheel and is extracted from the pool. The quenched material is thrown off in the form of a fine wire.

Taylor Wire Process

In this process an alloy is melted inside a glass tube. The glass is softened by contact with the melt and can be drawn, thus acting as a continuous mould which is cooled by water jets or in air. The resulting composite is a fine amorphous wire in a glass sheath, which can be removed by using aqueous HF solutions if necessary.

Die Casting

This technique is similar to traditional casting in that the melt fills a mould. However, the mould is usually water cooled and limited to simple geometries like rods, cones, or plates. The melt is fed into the mould by an injection or vacuum-suction technique rather than simply pouring it into a feeder system.

Quenching

This technique simply involves the induction heating and melting of an alloy inside a silica tube which is subsequently plunged into water.

Self-quenching

This is a surface processing technique which produces a thin amorphous layer. A laser or electron beam, either of which has a high energy density [87], is used to rapidly melt a thin layer at the surface of an alloy enabling the bulk of the alloy to act as its own heatsink.

2.4 Characteristics of Metallic Glasses

2.4.1 Structural Properties

The amorphous nature of metallic glasses can be revealed by x-ray diffractometry (XRD) or transmission electron microscopy (TEM). Each analytical technique can clearly distinguish between amorphous and crystalline states.

2.4.1.1 X-Ray Diffractometry (XRD)

In XRD a monochromatic X-ray beam is projected onto the surface of an alloy. The beam penetrates the metal and interacts with the atoms. Part of the beam is transmitted, part is absorbed by the sample, part is refracted and scattered, and part is diffracted. Diffraction occurs when Bragg's Law is satisfied:

$$n\lambda=2d\sin\theta \qquad (2.1)$$

where n is an integer, λ is the wavelength of the x-ray beam, d is the spacing between adjacent planes of atoms, and θ is the angle of incidence of the x-ray beam. The angle at

which constructively interfered diffraction takes place, and the intensity at which this occurs, causes sharp peaks on an XRD trace. Each peak represents a plane of a different Miller Indices. For an amorphous structure where there are no planes of atoms, diffraction still occurs as there will still be a small amount of constructive interference. However, the intensity of the diffracted beams is much weaker than for a crystalline material and they will be produced over a large range of angles, so only a broad peak appears on and XRD trace. Examples of XRD traces are shown in figure 2.11. The position of an XRD broad peak can be used to determine the nearest neighbour distance (NND) of atoms within the amorphous structure [89].

2.4.1.2 Transmission Electron Microscopy (TEM)

In TEM a coherent beam of high energy electrons is directed at a thin sample. Provided that sample is extremely thin (less than 100nm) then most of the electrons are transmitted through it. If the beam is focused on a single crystal then each plane of atoms causes diffraction of the beam by a different amount. When the incident beam is normal to a plane in the crystal this gives rise to a well defined pattern of spots, commonly called a selected area diffraction pattern (SADP), where each spot corresponds to diffraction from planes with different Miller Indices. Examples of SADPs are shown in figure 2.12. The actual distance (R) between spots, corresponds to the interplanar spacing (d) after correction for specific magnification and is represented by the following simple relationship:

$$d=LR \qquad (2.2)$$

where L is a camera constant and R is the measured distance between spots on the TEM negative.

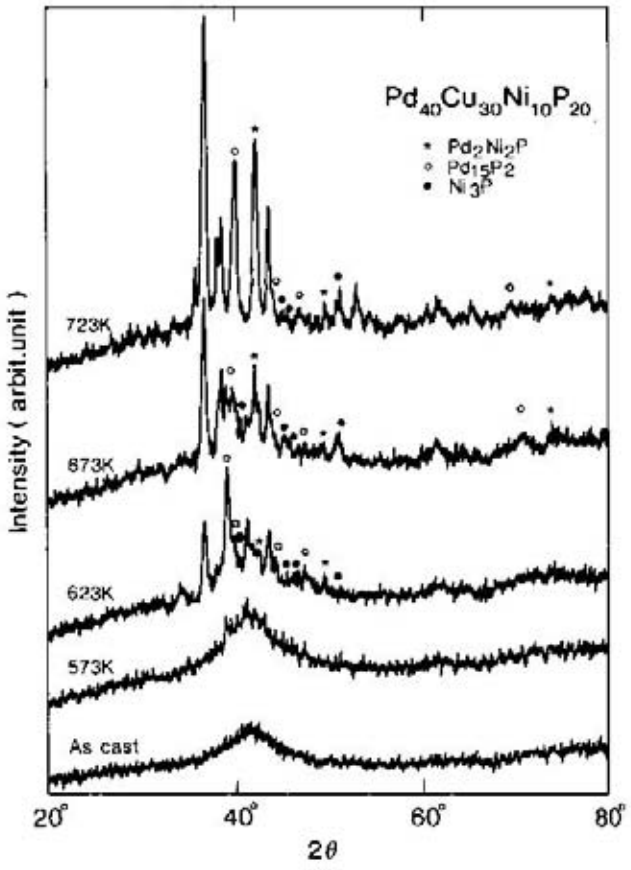

Figure 2.11 X-ray diffraction traces showing the devitrification of a glass forming palladium-based alloy [88], ranging from a single broad peak in the as-cast state (characteristic of a fully amorphous structure) to multiple sharp peaks with high intensity (characteristic of a crystalline structure) at 723 K.

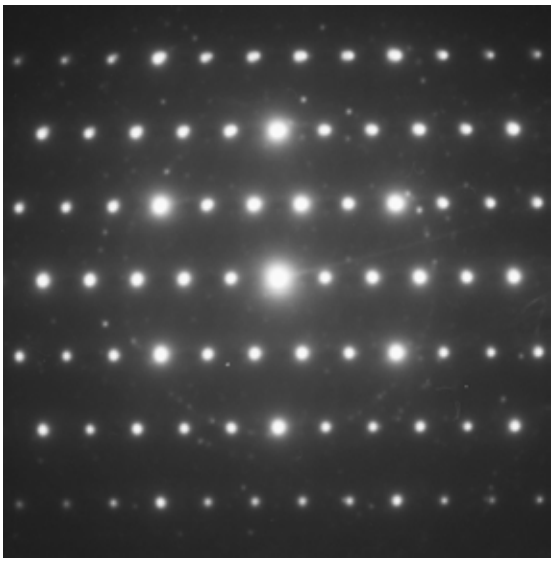

(a)

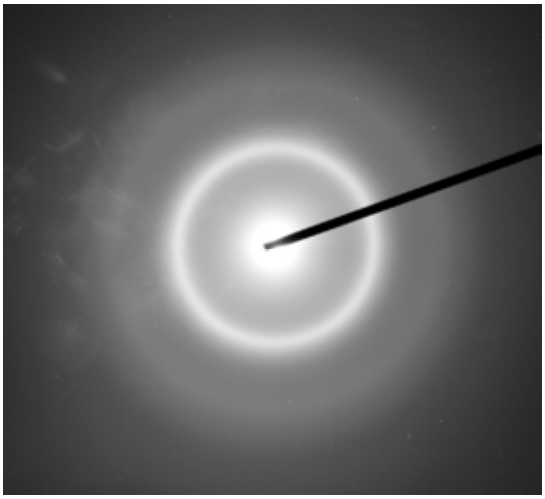

(b)

Figure 2.12 Selected Area Diffraction Patterns (SADPs) for $Al_{88}Ni_1Pd_1Y_{10}$ [90] (a) **[**101**]** zone axis in $Al_{23}(Ni,Pd)_6Y_4$ crystal. (b) Diffuse halo from melt spun alloy indicative of amorphous structure.

As with XRD, the lack of atomic planes in an amorphous structure causes the beam to be diffracted over a wide range of angles with the resulting SADP in the form of a diffuse halo ring. The radius of the halo ring therefore corresponds to the NND of atoms ion the amorphous structure [89].

2.4.2 Glass Transition and Thermal Behaviour

2.4.2.1 Vitrification

Normally when a molten alloy is cooled there is a continuous change in volume (V), entropy (S) and enthalpy (H) and viscosity (η) until, at the melting point (T_m) of the material, crystallization occurs and there is an abrupt change in these values. If the cooling rate is sufficient for amorphization, then once T_m is passed the melt becomes 'supercooled' and continues to act like a liquid until T_g is reached and a glass is formed. During the transition from supercooled liquid to glass there is a gradual change in the extensive variables (V, S, H and η) over a narrow temperature range whereas the intensive (or differential) thermodynamic variables, such as the coefficient of thermal expansion (α_T), compressibility (κ_T) and heat capacity (C_p), undergo a discontinuous change at T_g [81]. Figures 2.13 and 2.14 illustrate these changes using V and C_p as examples. The other variables would exhibit similar trends.

2.4.2.2 Devitrification

On continuous heating, a metallic glass gains energy and is able to undergo various transformations. These can be determined by a technique known as differential scanning calorimetry (DSC). Figure 2.15 shows an idealised DSC trace of heat flow against temperature for a metallic glass where each change in the rate of heat flow indicates a transformation in the alloy.

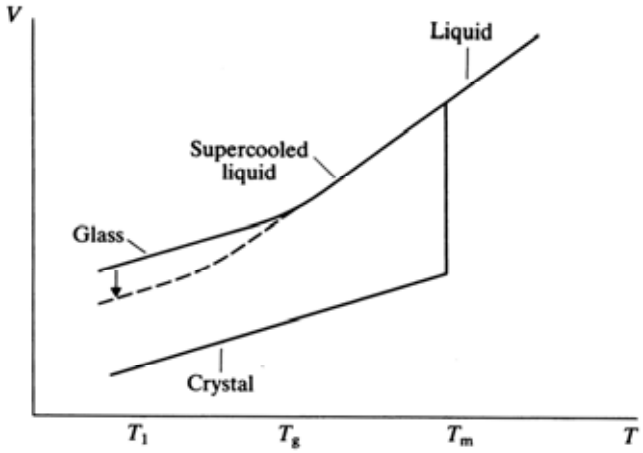

Figure 2.13 The change in volume with temperature. With slow cooling a melt will undergo a discontinuous change in volume at T_m. If the rate of cooling is high enough to suppress nucleation the melt will continue to act as a liquid until T_g, where the viscosity of the melt increases gradually over a narrow range until melt is deemed mechanically solid. The vertical arrow represents volume change on structural relaxation of the glass if held at temperature T_1. Other extrinsic variables such as entropy and enthalpy will show a similar trend [81].

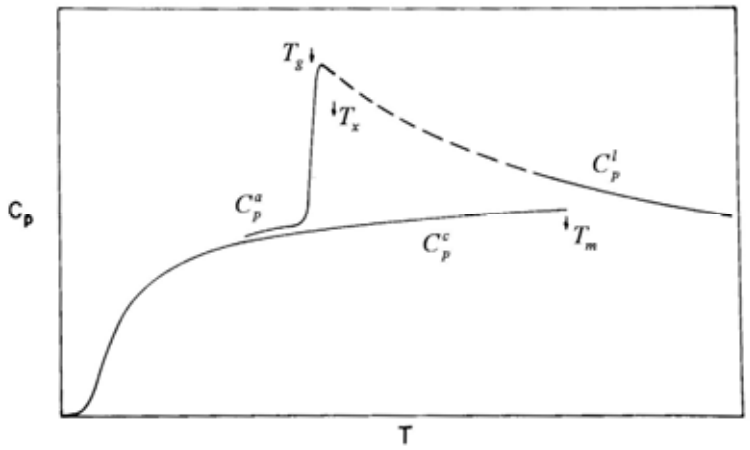

Figure 2.14 Representation of the relationship between the specific heat of the crystal C_p^c; that of the solid amorphous phase C_p^a; and that of the liquid C_p^l. T_m is the crystalline melting point; T_g is the glass transition temperature; and T_x is the temperature at which rapid crystallization occurs on heating at a selected rate. Other intrinsic variable such as compressibility and the coefficient of thermal expansion will show a similar trend. After Polk and Giessen [91].

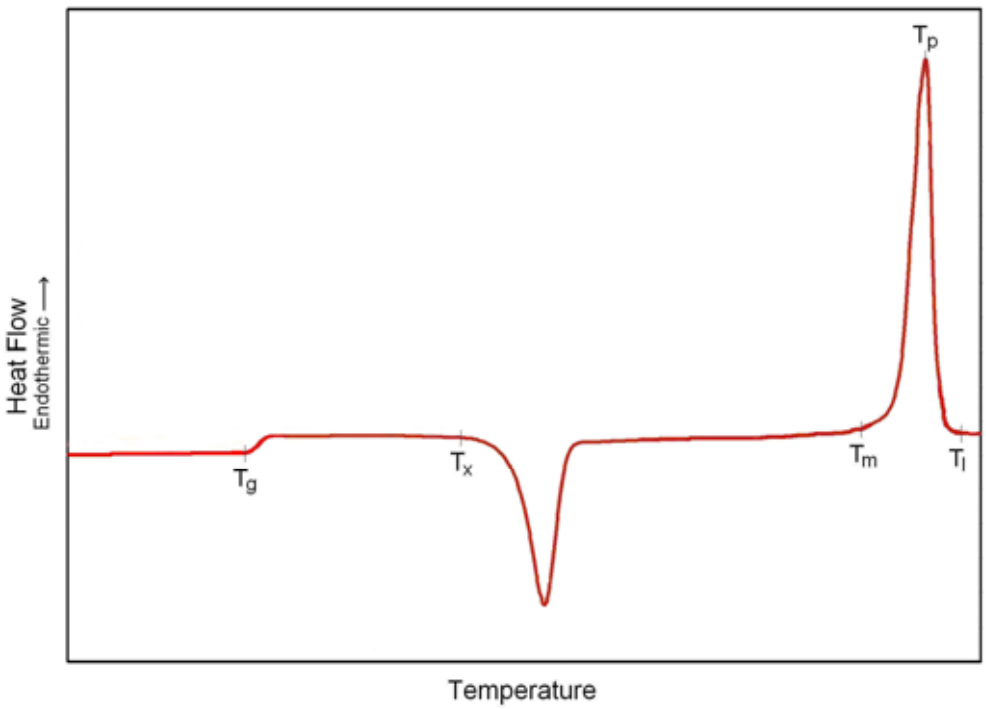

Figure 2.15 Idealised DSC trace for a metallic glass, showing glass transition temperature (T_g), crystallization temperature (T_x), melting temperature (T_m), peak melting temperature (T_p), and liquidus temperature (T_l).

The first transformation is from solid to supercooled liquid and is known as the glass transition. The glass transition temperature (T_g) is usually regarded as the onset of this change in the plot, although sometimes the inflexion point is used.

On further heating, the alloy gains enough energy to allow for rapid long-range reordering of atoms enabling nucleation and growth of crystalline phases from the supercooled liquid. The transformation from amorphous to crystalline involves nucleation of either a primary phase or eutectic phase. This point at which this begins is called the (onset of) crystallization temperature (T_x). Depending on the alloy system there may be multiple crystallization events or transformations of crystalline phases upon continued heating.

Eventually the alloy reaches a temperature where it begins to melt (T_m), followed by a peak melting temperature (T_p), before coming to the liquidus temperature (T_l) – the point where the alloy is completely liquid with no solid particles remaining.

It should be noted that the area under the peaks corresponds to the enthalpy of transformation, so at T_x this is the heat of crystallisation and at T_m it is the latent heat of fusion. It is also worth noting that the activation energy for crystallisation can be determined by a technique known as the Kissenger Analysis, which involves measuring the area of the primary crystallisation peak formed at different heating rates.

2.4.3 Glass Forming Ability

What constitutes a good metallic glass? The answer to this is quite subjective. For example, one could look at various electrical, magnetic or mechanical properties. Perhaps the simplest way of characterizing the glass forming ability (GFA) of an alloy is through its critical casting thickness (Z_c). This is defined as the maximum thickness or diameter into which an alloy can be cast and retain a fully amorphous structure. However, this does not take into account the thermal properties of the metallic glass. These are important in the production of an alloy, any post-production processing of that alloy and in its intended application. In thermodynamic terms, GFA is normally described as a function of two or more of the transformation temperatures T_g, T_x, T_m or T_l.

The reduced glass transition temperature (T_{rg}) is the ratio between T_g and T_m and was one of the earliest parameters used to describe GFA. T_{rg} represents the relative breadth of the supercooled liquid range on *quenching* and therefore is an indicator of the ease of forming a glassy metal. A high T_g coupled with a low T_m gives a large T_{rg} meaning there is a narrow temperature range to cool the melt through in order to achieve vitrification. Therefore a lower, and more easily achievable, R_c can be used, so a large T_{rg} shows good GFA.

ΔT_x is the difference between T_g and T_x and represents the temperature range of the supercooled liquid during *heating*. In this region the liquid is stable and able to suppress crystallization. Therefore a large ΔT_x indicates good GFA. This is also an important parameter for secondary processing of a metallic glass. When ΔT_x is large enough an appropriate temperature can be maintained and a metallic glass can be forged safely (i.e.

without crystallization occurring) into complex parts that cannot be formed directly through casting [92]. This is because within the supercooled liquid range the alloy acts with Newtonian behaviour and can flow, thereby allowing plastic deformation. It has even been shown that metallic glass can be blown like an ordinary glass [93]. Examples of forged and blown metallic glasses are shown in figures 2.16 and 2.17 respectively.

It has been pointed out that many alloy systems show contrasting trends when using both T_{rg} and ΔT_x to indicate GFA [94]. This should not be surprising as T_{rg} is a consideration of GFA from an amorphization perspective while ΔT_x is from a devitrification perspective. Lu and Liu have proposed a new parameter (γ, where $\gamma = T_x/(T_g+T_l)$) which combines the two ideas, with a high value indicating good GFA. They have shown that it has good correlation with both R_c and Z_c. Recently Shen et al have proposed a similar parameter (δ, where $\delta=T_x/(T_l-T_g)$) claiming an even closer correlation with Z_c than either T_{rg} or γ [95].

A comparison of GFA parameters and their correlation to Z_c for various bulk metallic glasses is shown in table 2.5.

The GFA of some metallic glasses can only be classified by Z_c as the critical thermal parameter T_g is not revealed by DSC. It is thought that these alloys contain high quantities of quenched-in nuclei which are undetectable by XRD and TEM analysis. During heating of these alloys the nuclei grow into nano-sized crystals as the temperature approaches T_g, but the growth rate is so slow that the heat evolved is too low to be measured by conventional means. At T_g crystallisation occurs rapidly as the growth rate increases, so T_x and T_g effectively coincide [114].

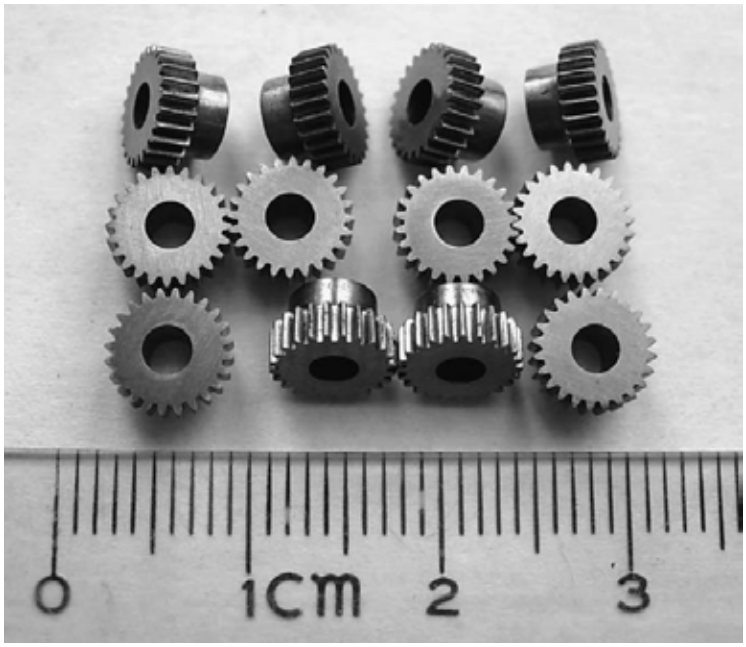

Figure 2.16 $Zr_{41.25}Ti_{13.75}Ni_{10}Cu_{12.5}Be_{22.5}$ BMG spur gears obtained through two-stage super-plastic forming process [92].

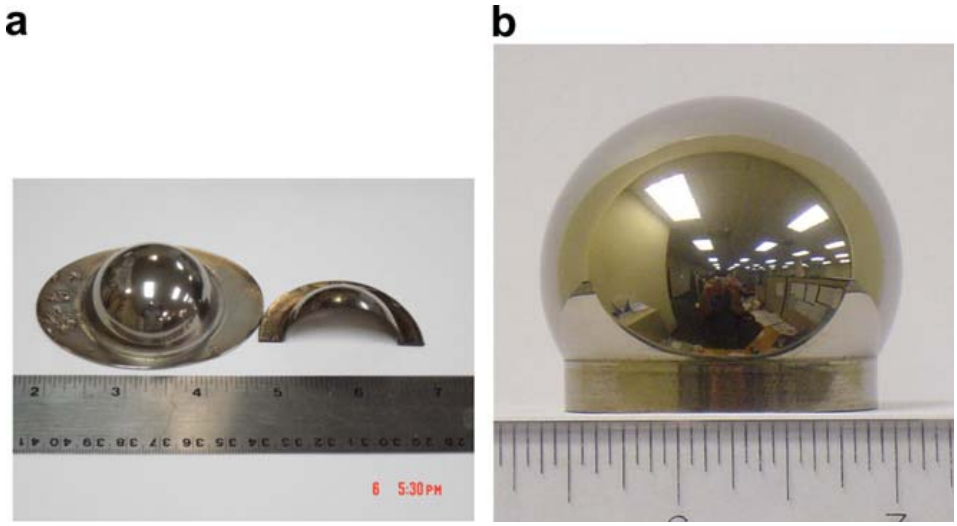

Figure 2.17 Free expansion of $Zr_{44}Ti_{11}Cu_{10}Ni_{10}Be_{25}$ using blow molding at 460°C. (a) Pressure 10^4 Pa - approximately the pressure exerted by human lung. (b) Pressure difference of $2x10^5$ Pa [93].

Table 2.5 Thermodynamic properties of bulk metallic glasses and associated glass-forming ability parameters. Thermal quantities determined by differential scanning calorimetry using a heating rate of 20 Ks^{-1} unless otherwise noted. T_g = Glass transition temperature. T_x = Onset of crystallization. T_m = Onset of melting. T_l = Liquidus temperature. $\Delta T_x = T_x - T_g$. Z_c = Critical casting dimension. $T_{rg}^m = T_g/T_m$. $T_{rg}^l = T_g/T_l$. $\gamma = T_x/(T_g+T_l)$. $\delta = T_x/(T_l-T_g)$.

a DSC at 10 Ks^{-1}, b DSC at 40 Ks^{-1}, c DTA at 20 Ks^{-1}, d DTA 40Ks^{-1}. * derived from reference

Alloy	T_g (K)	T_x (K)	T_m (K)	T_l (K)	ΔT_x	Z_c (mm)	T_{rg}^m	T_{rg}^l	γ	δ	Ref.s
$Cu_{46}Zr_{54}$	696	746	-	1201	50	2	-	0.580	0.393	1.477	96
$Cu_{46}Zr_{47}Al_7$	705	781	1135 *	1163	76	3	0.621	0.606	0.418	1.705	96
$Cu_{46}Zr_{37}Al_7Y_{10}$	665	743	1055 *	1118	78	4	0.630	0.595	0.417	1.640	96
$Cu_{46}Zr_{45}Al_7Y_2$	693	770	1005 *	1143	77	8	0.689	0.606	0.419	1.711	96
$Cu_{46}Zr_{37}Al_7Y_5$	672	772	1060 *	1113	100	10	0.634	0.604	0.432	1.751	96
$Y_{56}Al_{24}Co_{20}$	636	690	1035	1080 *	54	1.5	0.614	0.589	0.402	1.554	97
$Y_{36}Sc_{20}Al_{24}Co_{20}$	645	760	976	1035 *	115	25	0.661	0.623	0.452	1.949	97
$Y_{36}Sc_{20}Al_{24}Co_{10}Ni_{10}$	645	731	937	1015 *	86	25	0.688	0.635	0.440	1.976	97
$Mg_{70}Ni_{15}Nd_{15}$ [b]	472	484	728	794 [d]	12	1	0.648	0.594	0.382	1.503	98
$Mg_{75}Ni_{15}Nd_{10}$ [b]	455	473	719	780 [d]	18	2.8	0.633	0.583	0.383	1.455	98
$Mg_{65}Ni_{20}Nd_{15}$ [b]	467	503	738	794 [d]	36	3.5	0.633	0.588	0.399	1.538	98
$Mg_{55}Cu_{25}Er_{10}$ [b]	422	480	741	766	58	3	0.570	0.551	0.404	1.395	99
MgCuGd	422	483	690	737	61	12	0.612	0.573	0.417	1.533	19
$Mg_{65}Cu_{15}Ag_{10}Er_{10}$ [b]	427	465	706	733	38	6	0.605	0.583	0.401	1.520	99
$Mg_{65}Cu_{7.5}Ni_{7.5}Zn_5Ag_5Y_{10}$	426	464	693	717	38	9	0.615	0.594	0.406	1.595	100
$Zr_{65}Al_{7.5}Ni_{10}Cu_{17.5}$ [b]	625	750	1100 *	1170 *	125	16	0.568	0.534	0.418	1.376	101
$Zr_{35}Ti_{30}Be_{35}$	592	712	1122	1135	120	6	0.528	0.522	0.412	1.319	102
$Zr_{57.5}Cu_{17.5}Be_{25}$	609	715	-	1109	106	8	-	0.549	0.416	1.430	103
$Zr_{35}Ti_{30}Be_{27.5}Cu_{7.5}$	575	740	948	1071	165	15	0.607	0.537	0.450	1.492	102
$Zr_{57}Ti_5Al_{10}Cu_{20}Ni_8$	640 *	725 *	-	1140	85	20	-	0.561	0.407	1.450	104
$Zr_{41.2}Ti_{13.8}Cu_{12.5}Ni_{10}Be_{22.5}$	625	705 *	937	993	49	40	0.667	0.629	0.436	1.916	37, 71
PdNiP	576	678	-	991	102	25	-	0.581	0.433	1.634	105,106
$Pd_{40}Ni_{10}Cu_{30}P_{20}$ [b]	575	677	740 *	810 *	95	72	0.777	0.710	0.489	2.881	38,107

Table 2.5 (continued).

Alloy	T_g (K)	T_x (K)	T_m (K)	T_l (K)	ΔT_x	Z_c (mm)	T_{rg}^m	T_{rg}^l	γ	δ	Ref.s
$Ti_{50}Ni_{15}Cu_{32}Sn_3$ [c]	686	759	1205	1283	73	1	0.569	0.535	0.385	1.271	108
$Ti_{50}Ni_{15}Cu_{25}Sn_3Be_7$ [c]	688	733	1122	1207	45	2	0.613	0.570	0.387	1.412	108
$Ti_{45}Ni_{15}Cu_{25}Sn_3Be_7Zr_5$ [c]	680	741	1064	1142	61	5	0.639	0.595	0.407	1.604	108
$Ti_{40}Zr_{25}Ni_8Cu_9Be_{18}$ [c]	621	668	948	1009	47	8	0.655	0.615	0.410	1.722	108
$Au_{46}Ag_5Cu_{29}Si_{20}$	395	420	620 *	664	25	1	0.637	0.595	0.397	1.561	109
$Au_{52}Pd_{2.3}Cu_{29.2}Si_{16.5}$	393	427	630 *	651	34	2	0.624	0.604	0.409	1.655	109
$Au_{49}Ag_{5.5}Pd_{2.3}Cu_{26.9}Si_{16.3}$	401	459	615 *	644	58	5	0.652	0.623	0.439	1.889	109
$Ce_{60}Al_{10}Ni_{10}Cu_{20}$ [a]	374	441	645	672	67	1	0.580	0.557	0.422	1.480	110
$Ce_{57}Al_{10}Ni_{12.5}Cu_{15.5}Nb_5$ [a]	369	415	638	677	46	2	0.578	0.545	0.397	1.347	110
$Ce_{60}Al_{15}Ni_{15}Cu_{10}$ [a]	390	468	644	685	78	3	0.606	0.569	0.435	1.586	110
$Ce_{65}Al_{10}Ni_{10}Cu_{10}Nb_5$ [a]	359	384	637	702	25	5	0.564	0.511	0.362	1.120	110
$Fe_{58}Co_4Ni_6Zr_{10}Mo_5W_2B_{15}$	872	940	1427	1511	68	1	0.611	0.577	0.394	1.471	111
$Fe_{58}Co_6Ni_4Zr_{10}Mo_5W_2B_{15}$	887	957	1440	1503	70	3	0.616	0.590	0.400	1.554	111
$Fe_{72}Y_6B_{22}$	898	944	1391	1419	46	2	0.646	0.633	0.407	1.812	112
$Fe_{67}Ni_5Y_6B_{22}$	866	891	1345	1469	25	1	0.644	0.590	0.381	1.478	112
$Fe_{68}Ni_4Y_6B_{22}$	872	907	1365	1470	35	1.5	0.639	0.593	0.387	1.517	112
$Fe_{68}Co_4Y_6B_{22}$	896	941	1385	1414	45	2	0.647	0.633	0.407	1.723	112
$Fe_{58}C_{14}Y_6B_{22}$	880	925	1366	1485	45	2.5	0.644	0.593	0.391	1.529	112
$Fe_{71}Mo_1Y_6B_{22}$	902	960	1376	1517	58	2.5	0.656	0.595	0.396	1.561	112
$Fe_{70}Mo_2Y_6B_{22}$	907	969	1378	1508	62	3.5	0.658	0.601	0.401	1.612	112
$Fe_{69}Mo_3Y_6B_{22}$	908	958	1379	1488	59	6	0.658	0.610	0.400	1.652	112
$Fe_{68}Mo_4Y_6B_{22}$	915	944	1385	1488	29	6.5	0.661	0.615	0.393	1.647	112
$Fe_{43.7}Co_{7.3}Cr_{14.7}Mo_{12.6}C_{15.5}B_{4.3}Y_{1.9}$	821	868	1380	1440	47	10	0.595	0.570	0.384	1.402	113
$Fe_{41}Co_7Cr_{15}Mo_{14}C_{15}B_6Y_2$ [c]	838	876	1387	1437	38	16	0.604	0.583	0.385	1.462	36

2.5 Alloy Design

2.5.1 Early Design

The first metallic glasses were made by vapour deposition techniques. Even amorphous elemental metals could be fabricated. However, glasses made by this technique are not necessarily stable at elevated temperature. For example, Kramer [39] claims to have produced amorphous zinc which has a crystallization temperature of 133 K (-140°C).

Early research into metallic glass forming systems found that it is much easier to produce a stable metallic glass if a binary alloy is used and the composition is at a eutectic point in that binary system. Various measurements show that in a melt of a eutectic composition there is a high degree of short range ordering [115]. This means the liquid is more stable so the liquidus temperature is depressed from its ideal solution liquidus temperature (T_l^o). The interval between T_l and T_g is therefore smaller than in other parts of the system, meaning that it is easier to cool through that interval without inducing crystallization (i.e. R_c is low).

It has been shown the best glass forming range in a system does not necessarily include the eutectic composition [116]. The reason for this concerns the coupled zone – the region where composition and temperature allow a stable eutectic interface during growth [117], i.e. the growth velocity of the eutectic interface exceeds the growth velocity of both the primary phases. If a glass is produced on quenching into a coupled zone there will be two crystalline phases competing for nucleation and growth in a highly viscous environment on heating. This means that the glass is more stable against crystallization than one where only a single primary phase grows. In a normal (symmetric) eutectic the coupled zone sits centrally under the eutectic point. For an anomalous (asymmetric) eutectic, the coupled

zone is skewed due to differences in the growth velocities of the various phases. This allows a glass to form with an off-eutectic composition, as has been demonstrated in the Cu-Zr system [116]. However, the composition cannot be too far displaced from the eutectic as the difference between T_l and T_g becomes too large and an impractical R_c is required. Figure 2.18 shows typical normal and anomalous phase diagrams along with growth velocity curves.

2.5.2 Modern Design

The design of stable metallic glasses, whether based on eutectic compositions or more complex alloys, relies on finding systems whose compositions enable the avoidance of nucleation of the crystalline phase, or the suppression of crystal growth.

The atoms in a melt (at temperatures above T_l) have considerable energy and are in constant motion giving rise to local fluctuations in composition and density, meaning small clusters, or embryos, of solid material are continually being created and broken up. For a stable nucleus to form a critical energy barrier ΔG^* must be overcome. Assuming a spherical nucleus this value is expressed by the following equation:

$$\Delta G^* = \frac{16\pi\gamma^3}{3(\Delta G_{LS})^2} \qquad (2.3)$$

Where γ is the interfacial energy between particle and liquid, and ΔG_{LS} is the difference in Gibbs free energy between liquid and solid. An alloy which has crystalline phases requiring high values of ΔG^* is therefore more likely to be able to form a metallic glass.

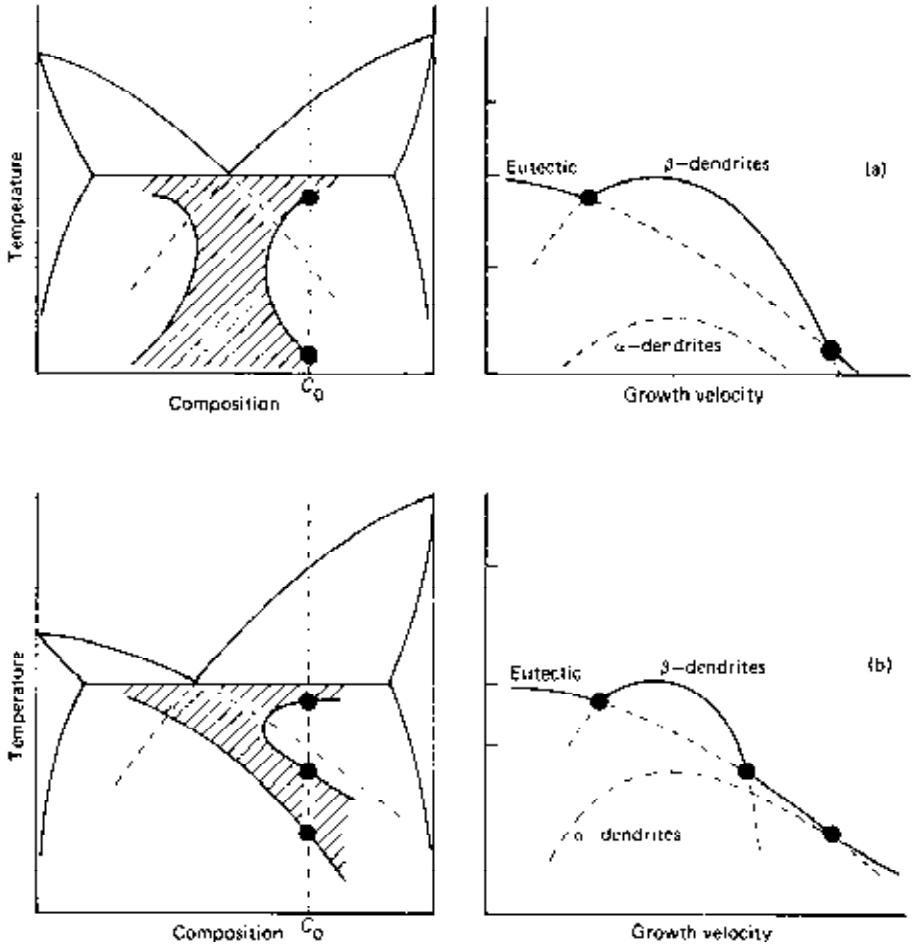

Figure 2.18 Coupled zone and temperature-growth velocity for: (a) normal eutectic, (b) anomalous eutectic systems [117]. A glass is more likely to be formed at composition C_o in (b) as there will be two phases competing for nucleation and growth, rather than where there is a single primary phase at C_o in (a).

If ΔG* is exceeded, the rate of nucleation (I) and crystal growth rate (U) are represented by the following two equations:

$$I = AD\exp\left(-\frac{\Delta G^*}{kT}\right) \qquad (2.4)$$

$$U = f\frac{D}{l}\left[1-\exp\left(-\frac{n\Delta G_{LS}}{kT}\right)\right] \qquad (2.5)$$

Where A is a constant, D effective diffusivity, k is Boltzmann's constant, T is absolute temperature, f is the fraction of sites at the crystal-liquid interface where atoms are preferentially added or removed, l is the average atomic diameter, and n is the atomic volume.

It can be seen both I and U are controlled by kinetic and thermal parameters, with D and Δg being common terms in both equations. Diffusivity is particularly important as it can be use to show why the plot on a TTT diagram is a c-shape. Within a liquid D is proportional to temperature and inversely proportional to viscosity as shown in the Stokes-Einstein relationship:

$$D = \frac{kT}{6\pi\eta r_a} \qquad (2.6)$$

In fact, a TTT diagram could also be presented as a time-diffusivity-transformation diagram. At elevated temperatures where diffusivity is high the chance of an embryonic nucleus forming is also high, but the chance of it being stable is low. This is because dissolution of the embryo is likely to occur before the embryo can reach the critical radius needed for it to be stable, as the difference in free energy of the embryo (proportional to $r^3\Delta T$) and the interfacial energy (proportional to r^2) between it and the liquid is low. At lower temperature diffusivity is decreased the chance of an embryo forming is reduced, but

conversely the chance of it remaining in place increases, so the chance of a stable nucleus forming is higher. As diffusivity decreases further, formation of nuclei becomes more difficult until transformation becomes dominated by growth of nuclei already formed. The nose of the c-curve is the point where there is an optimal balance between nucleation and growth processes.

2.5.2.1 Empirical Guidelines for Alloy Design

Over the years that metallic glasses have been studied many alloy systems have been developed. In addition to hindering mass diffusion by the extremely rapid cooling of a melt, or the use of a eutectic composition as the starting point for development of a glass forming alloy, it has been noticed that many systems exhibit common trends related to alloy composition. These have been collated by Inoue [107] and written in the form of a set of empirical guidelines for selection of alloy compositions which should, but not necessarily will, lead to the production of BMGs. They are:

I. The alloy should be a multi-component system consisting of more than three elements.
II. There should be significant difference in atomic size ratio (ASR) above 12% between the main three constituent elements.
III. There should be a negative heat of mixing among the elements.

Rule one is sometimes referred to as ‘the confusion principle’ [118]. With many different atoms present it is more difficult for a crystal structure to form. By increasing the number of elements present, the complexity and size of the crystal unit cell is increased. The

energetic advantage of forming an ordered periodic structure is therefore reduced [5] as it requires both time and energy for atomic rearrangement to occur.

Rule two is a reversal of the Hume-Rothery rules for solid solubility, meaning that insolubility in the solid is actually desirable. With a large difference in atomic size strain is introduced into the crystal lattice so the crystal structure becomes destabilised. This also leads to a high packing density and so to a small free volume in the liquid state [5]. This lowers the diffusion coefficient and raises viscosity of the supercooled liquid, thereby making it physically difficult for atomic rearrangement. Hence, rule two is a method for suppressing both nucleation and growth processes.

The third rule's requirement for negative heat of mixing (also referred to as enthalpy of mixing) means that is it is thermodynamically favourable to have dissimilar atoms as nearest neighbours [119]. This causes clustering of dissimilar of atoms within the melt and therefore, provided that chemical segregation doesn't occur, major atomic rearrangement is required to form a crystal nucleus. This means the liquid becomes more stable and leads to the reduction in the R_c needed to form a metallic glass. There is also an increase in the energy barrier at the liquid-solid interface [5] as any clusters that are present will not have a smooth interface with the embryonic crystal nuclei that form. This, in turn, will raise ΔG^* thus the third rule also leads to the suppression of nucleation.

Figure 2.19 shows a chart which summarizes the rules and shows how they lead to and increase in T_{rg} which is generally required for a system with good glass-forming ability.

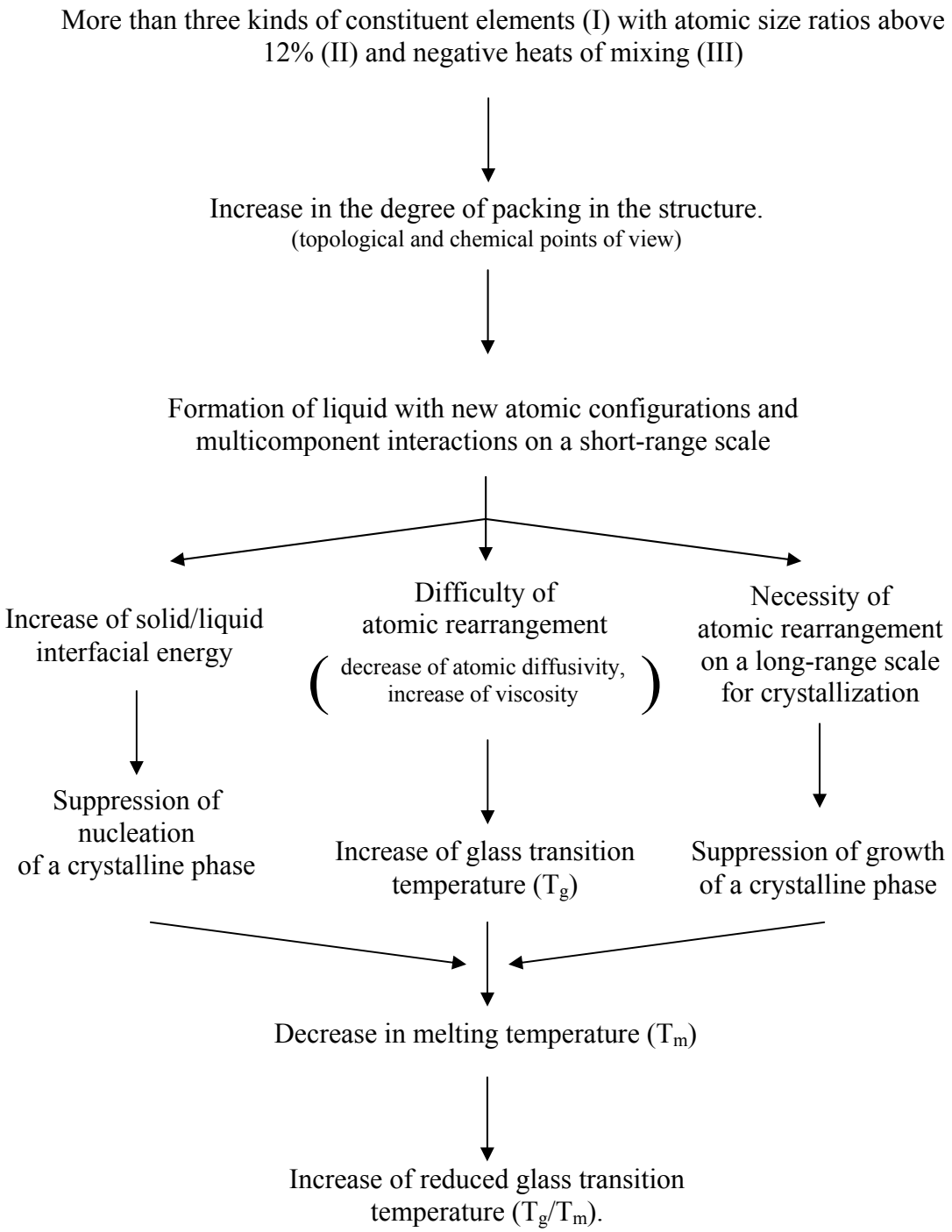

Figure 2.19 Chart showing mechanisms for the stabilization of supercooled liquid alloys with subsequent high glass-forming ability. After Inoue [31].

2.5.2.1.1 Guideline Refinements

Since the beginning of the twenty-first century there have been some new suggestions on how BMG compositions might be found. They are basically variations of the established guidelines.

Egami Modifications

An analysis by Egami [120] has suggested the following changes should help the formation of BMGs.

(1) *Increase the atomic size ratio of constituent elements.* This introduces even greater strains into a crystal lattice thereby further destabilising the crystalline phase.

(2) *Increase the number of elements.* This further increases the complexity of a crystal unit cell and correspondingly reduces the thermodynamic advantage of forming an ordered structure.

(3) *Increase the interaction between small and large atoms.* This stabilises the melt through increased clustering of dissimilar atoms.

(4) *Introduce repulsive interactions between small atoms.* This is a parameter not included in the empirical guidelines. The small atoms in an alloy diffuse relatively quickly, so by adding a repulsive force between them their rate of diffusion is retarded. This has the effect of raising T_g and also that crystal formation and growth is further suppressed.

Senkov & Scott Modifications

Senkov & Scott's suggestions [121] are all based on the guideline II. They are a means for enhancing the packing density through consideration of various geometric configurations of atoms thereby hindering the atomic rearrangements necessary for a crystal nucleus to form.

(1) Radius of the main element (solvent) should be equal to, or greater than, 0.15nm.

(2) Solute elements should be selected with radii ratios R (where $R=R_{solute}/R_{solvent}$) equal to one of the critical ratios R (where R* = 0.62, 0.71, 0.8, 0.88, or 0.9).*

(3) Elements with a R of 0.62, 0.71, or 0.8 should form binary eutectics with solvent.*

Fecht & Johnson Modifications

Fecht & Johnson have made a study of the thermodynamic properties of BMGs [122]. They have found some common conditions necessary for the formation of a BMG with a low R_c. They are:

(1) Deep eutectic temperatures and steeply plunging T_o-lines (equality of solid and liquid Gibbs free energy). If the T_o curves do not intersect then their boundaries can give an indication of the compositional range for good GFA. Outside these boundaries, or if the T_o curves intersect, the chance of partitionless (massive) transformation is increased.

(2) Difference in atomic size ratio of more than 15%.

(3) Reduced driving force for crystallisation ΔG. If ΔG is small then ΔG^* becomes larger so nucleation is therefore suppressed.

(4) *High reduced glass transition temperature.*

(5) *Avoid liquid-liquid phase separation.* In other words the liquid needs to remain complex. If phase separation occurs then the resulting liquids would be more simple so guideline I would no longer be fulfilled.

2.5.2.2 Composition Optimization

It has been reported that by adjusting the composition of an alloy so that its e/a ratio (conduction electrons to atom) is increased, the GFA of that system can be improved [123]. Although the work is based on ternary zirconium systems, where an increase in e/a from 1.37 to 1.53 has a corresponding increase in T_g from 673K to 721K, it may also be applicable to other BMG systems. It is not fully understood how increasing e/a improves GFA but it is thought that the contribution of electronic energy towards the energy of phase formation is partially responsible.

2.5.2.3 The Alpha Parameter

This is a new computational approach to finding glass forming compositions but it is based on the old empirical finding that GFA is enhanced around the eutectic point of an alloy. Rather than finding eutectic compositions from published phase diagrams Cheney and Vecchio [124] have defined the alpha (α) parameter as the ratio between an alloy's ideal solution liquidus temperature and its calculated liquidus temperature:

$$\alpha = \frac{\sum_{i=1}^{n} x_i T_i}{T_l} \qquad (2.6)$$

where n is the number of elements in the alloy, x_i is the atomic fraction of element i, T_i is the melting temperature of element i, and T_l is the calculated liquidus of the alloy. T_l can be

generated through one of several software packages, such as ThermoCalc TCC, which use experimentally derived thermodynamic databases to perform various operations on multi-component systems including the calculation of liquidus profiles.

The α parameter is a measure of deviation from the weighted liquidus (average of individual component liquiduses), so eutectic compositions will generate a value greater than one, with deeper eutectics giving larger α values. Any peak within the profile of a system will indicate the ideal composition for producing a metallic glass. An example of a ternary profile is shown in figure 2.20. As the α parameter is dimensionless, it can be used to compare alloys with different constituents and liquidus profiles. From their analysis of every possible ternary alloy composition Cheney and Vecchio concluded that any alloys with a maximum α value just above 1 are likely to have limited GFA while those with maximum values near or above 1.5 will likely have good GFA enabling them to be produced in bulk form.

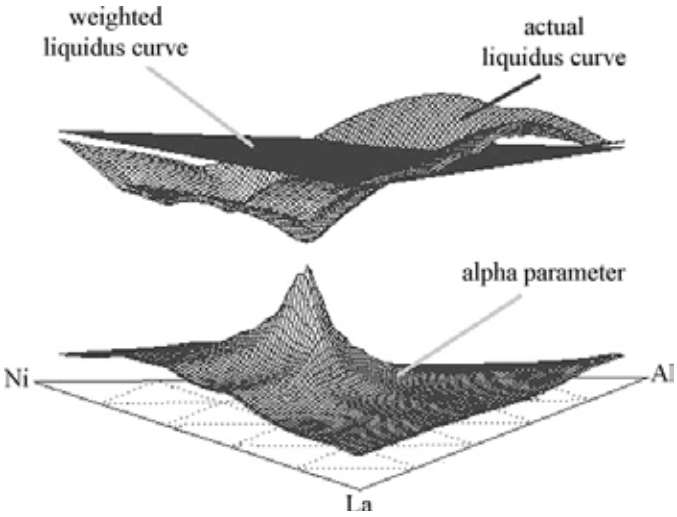

Figure 2.20 Example plot of alpha (α) parameter [124], which can be used to predict likely glass forming compositions in an alloy system. It is the ratio of ideal (weighted) liquidus to actual (calculated) liquidus. Alloys which have large critical casting dimensions have an α value in excess of 1.5.

2.5.2.4 Primary Compositions for Research Project

In this project, initial ternary Fe-C-B alloy compositions were selected from invariant points (e.g. ternary eutectic) of Fe-C-B phase diagrams and eutectic/eutectoid sections found in binary Fe-C and Fe-B systems, and are listed in table 2.6.

Table 2.6 Ternary alloy compositions.

	Elements in atomic% (weight%)		
Alloy	**Fe**	**C**	**B**
1	80 (95.02)	14.8 (3.78)	5.2 (1.2)
2	80.7 (95.49)	3.7 (0.94)	15.6 (3.57)
3	76.5 (94.2)	7.6 (2.01)	15.9 (3.79)
4	80.9 (95.51)	5 (1.27)	14.1 (3.22)
5	82.9 (95.92)	10 (2.49)	7.1 (1.59)
6	81.2 (95.97)	6 (1.52)	12.8 (2.92)
7*	79.54 (95.17)	3.46 (0.89)	17 (3.94)
8*	82.85 (95.94)	8.65 (2.15)	8.5 (1.91)
9	65.7 (90.36)	17.3 (5.12)	17 (4.53)

* These are nominal compositions and processing methods are not expected to fabricate them to this accuracy. For the sake of uniformity alloys 7 and 8 will hereafter be listed as $Fe_{79.5}C_{3.5}B_{17}$ and $Fe_{82.8}C_{8.7}B_{8.3}$ respectively.

Alloys 1-6 are from the invariant points of the B-C-Fe system, of which there are four different versions in the *Handbook of Ternary Phase Diagrams* [125] and are reproduced in figures 2.21-2.24. Alloy 7 contains the metastable eutectoid carbon content of the Fe-C system and the boron content of the eutectic in the Fe-B system. Alloy 8 is a fifty-percent mixture of the eutectic compositions in Fe-B and Fe-C. Alloy 9 contains the metastable eutectic carbon content of the Fe-C system and the eutectic boron content of the Fe-B system. These values were taken from their respective phase diagrams in *Binary Alloy Phase Diagrams* [130,131] which are reproduced in figures 2.25 and 2.26.

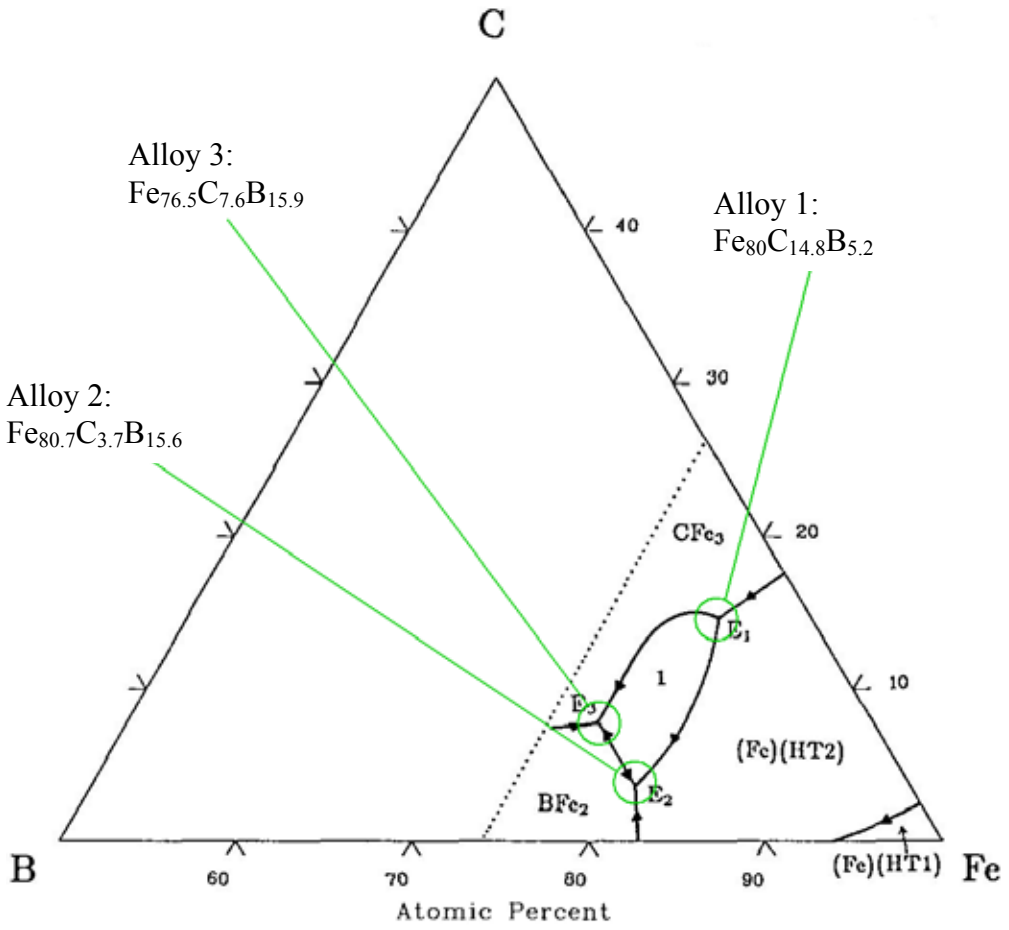

Figure 2.21 Metastable liquidus projection of the B-C-Fe system by Stadelmaier and Gregg [126], as referenced in [125], showing derivation of alloy compositions 1-3.

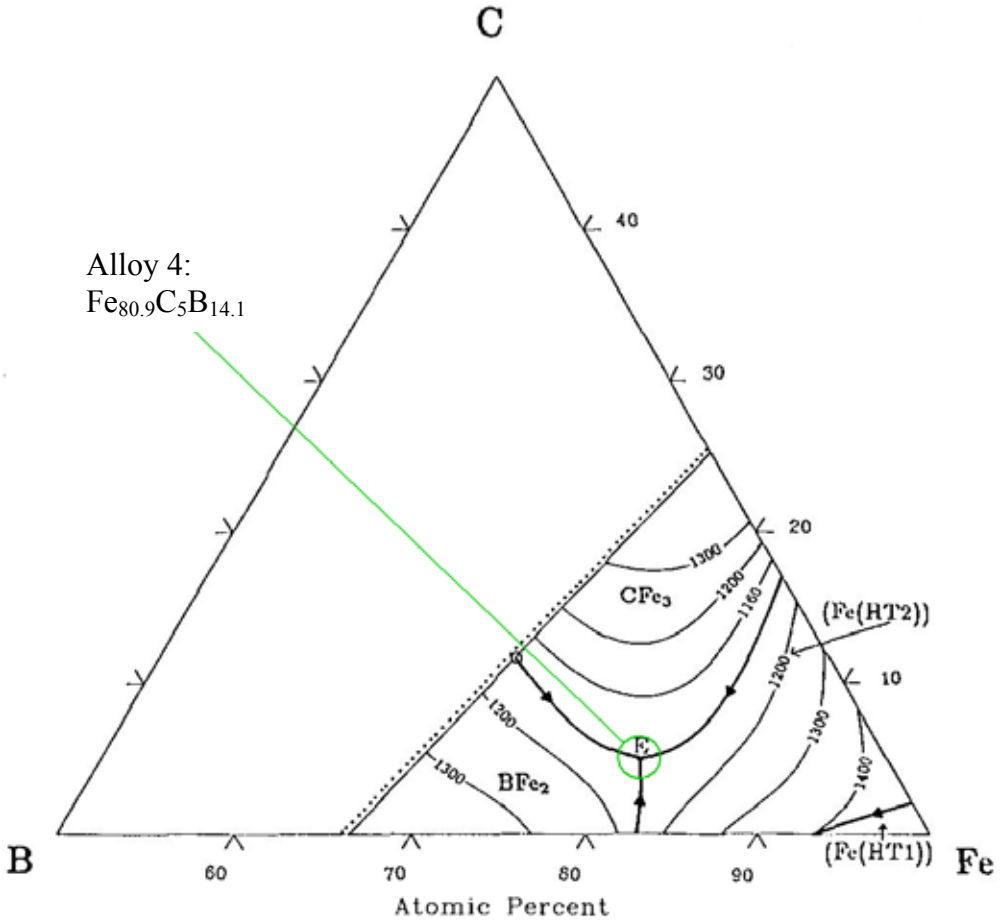

Figure 2.22 Metastable liquidus projection of the B-C-Fe system by Borlera and Pradelli [127], as referenced in [125], showing derivation of alloy composition 4, which has a liquidus stated as 1097°C.

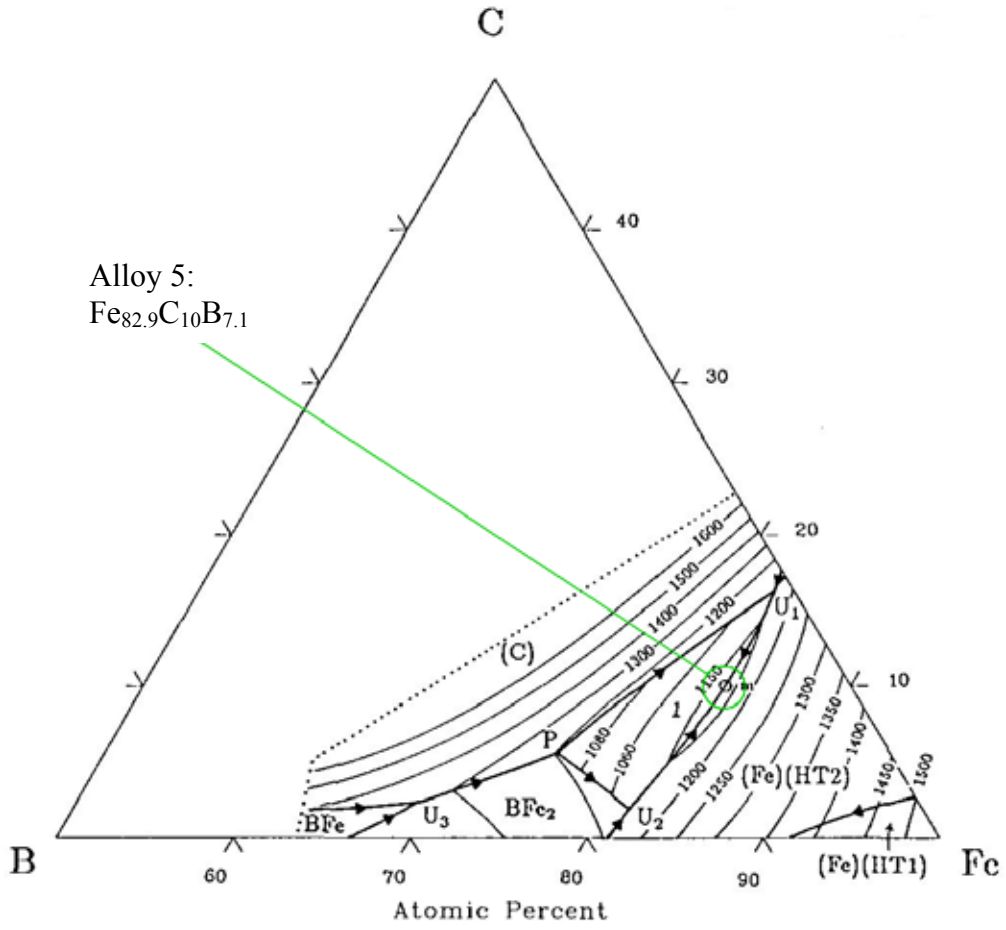

Figure 2.23 Liquidus projection of the B-C-Fe system by Schürmann and Li [128], as referenced in [125], showing derivation of alloy composition 5, which has a liquidus stated as 1129°C.

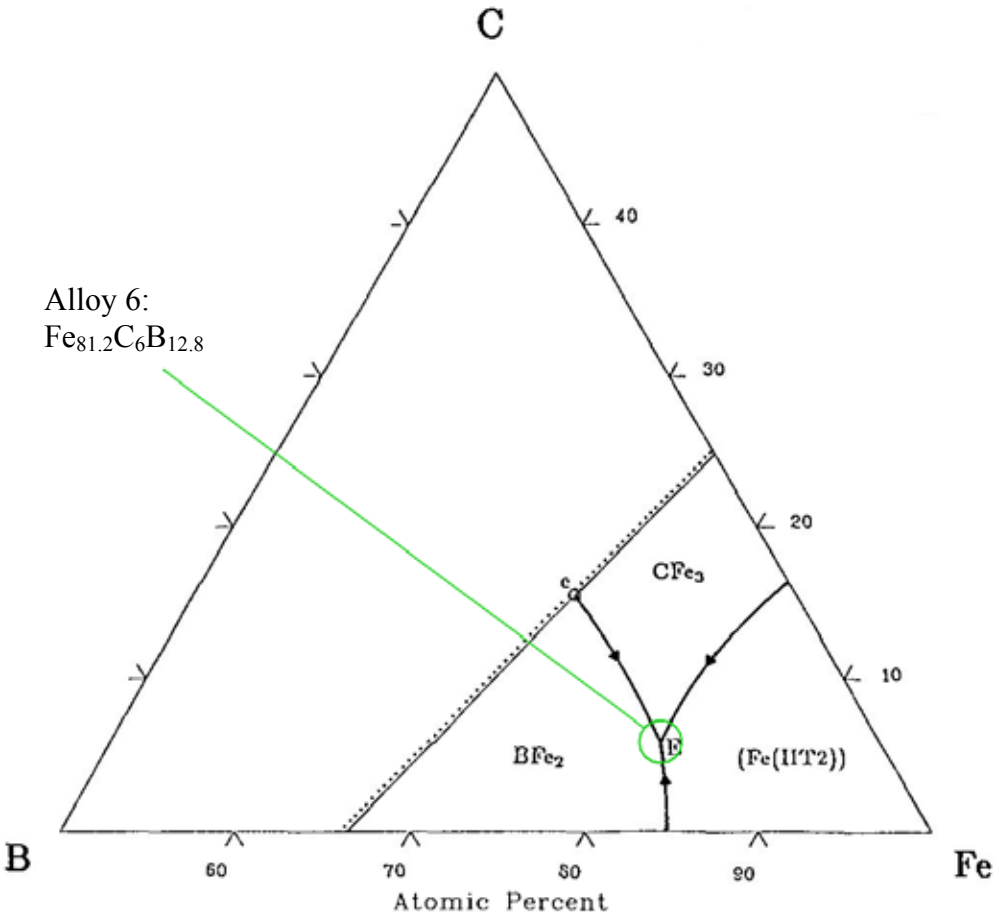

Figure 2.24 Metastable liquidus projection of the B-C-Fe system by Vogel and Tammann [129], as referenced in [125], showing derivation of alloy composition 6, which has a liquidus stated as 1100°C.

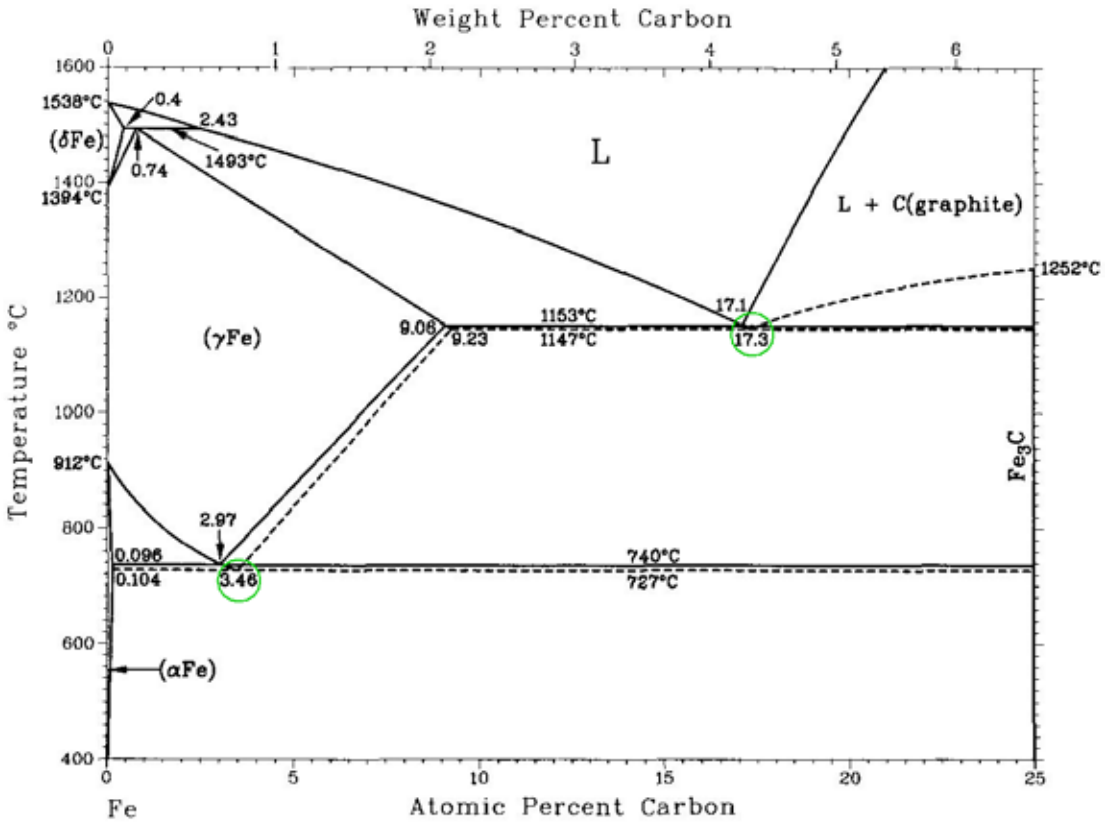

Figure 2.25 Iron-Carbon phase diagram by Okamoto [130] highlighting the metastable eutectoid and eutectic carbon content used for alloys 7-9.

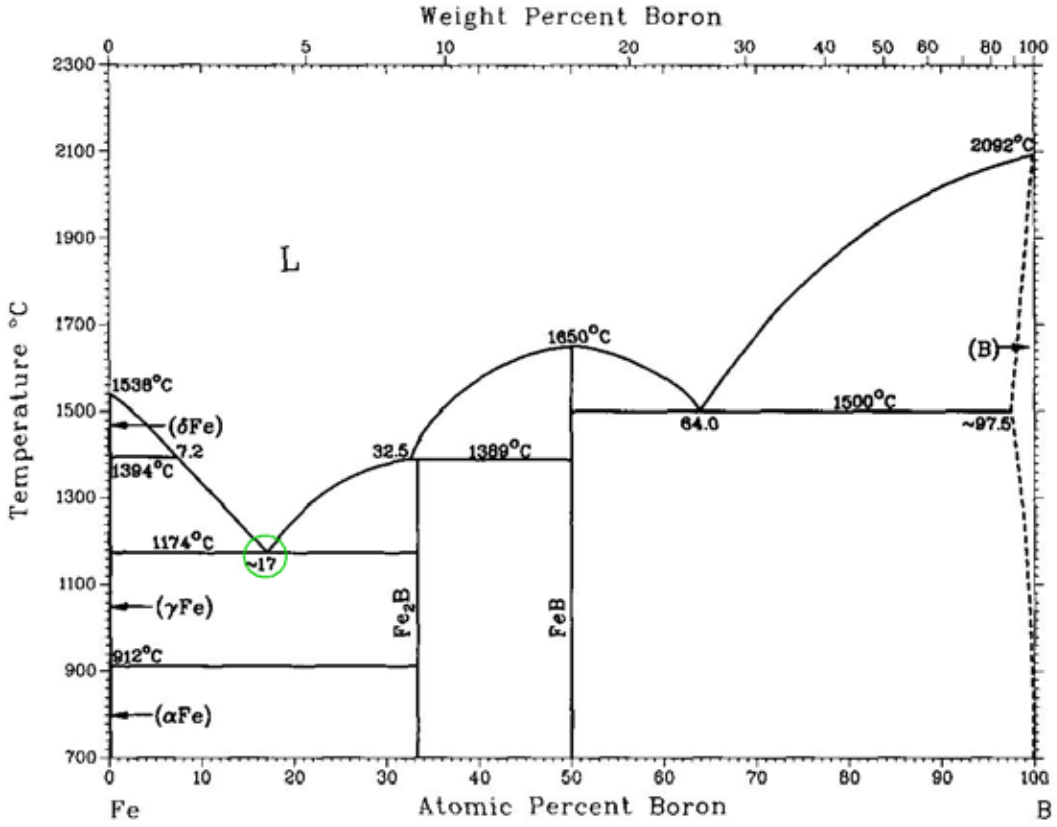

Figure 2.26 Iron-Boron phase diagram by Liao and Spear [131] highlighting the eutectic boron content used for alloys 7-9. The second eutectic at 64% boron was not used as this would make the alloys boron-based rather than iron-based.

CHAPTER 3

EXPERIMENTAL TECHNIQUES

3.1 Materials Processing

3.1.1 Starting Elements

The form, purity and suppliers of the elemental materials used in this project are listed in table 3.1. The manganese chips were heavily oxidised, so prior to alloy preparation the oxide layer was removed. This was achieved by placing the pieces in a 30% water / 70% orthophosphoric acid solution for 15 minutes. Once clean, each piece was washed in a water bath, then rinsed with industrial methylated spirits, before being dried by forced air convection.

Table 3.1 The form, %purity (by metals basis) and suppliers of the elements used in making the ternary and multi-component alloys.

Element	Form	%Purity	Suppliers
Iron	Chips	99.98	Sigma-Aldrich
	Pieces	99.97	Alfa Aesar
Carbon	Graphite rods Ø3mm	99.995	Sigma-Aldrich
	Graphite rods Ø6mm	99.995	Sigma-Aldrich
Boron	Pieces <60mm	99+	Sigma-Aldrich
Manganese	Slabs	99.9	Sigma-Aldrich
Molybdenum	Wire Ø0.5mm	99.95	Sigma-Aldrich
	Wire Ø1mm	99.95	Alfa Aesar

3.1.2 Alloy Compositions

The compositions of the alloys studied are stated in atomic percentages.

3.1.2.1 Ternary Alloys

(1) $Fe_{80}C_{14.8}B_{5.2}$, (2) $Fe_{80.7}C_{3.7}B_{15.6}$, (3) $Fe_{76.5}C_{7.6}B_{15.9}$, (4) $Fe_{80.9}C_5B_{14.1}$, (5) $Fe_{82.9}C_{10}B_{7.1}$,

(6) $Fe_{81.2}C_6B_{12.8}$, (7) $Fe_{79.5}C_{3.5}B_{17}$, (8) $Fe_{82.8}C_{8.7}B_{8.5}$, (9) $Fe_{65.7}C_{17.3}B_{17}$.

3.1.2.2 Multi-component Alloys

$Fe_{80.9-x}Mn_xC_5B_{14.1}$ (x = 2, 5, 10, 20), $Fe_{80.9-x}Mo_xC_5B_{14.1}$ (x = 2, 5, 10, 20),

$Fe_{80.9-x}(Mn_{50}Mo_{50})_xC_5B_{14.1}$ (x = 4, 10, 20), $Fe_{60.9}Mn_xMo_{20-x}C_5B_{14.1}$ (x = 4, 10, 16).

3.1.3 Alloy Production

Alloy mixtures were prepared by measuring elemental materials in the correct proportions to an accuracy of 0.001-0.004 grams using an AND GF-200-EC balance. The mixtures were arc-melted to produce ingots of approximately twelve grams. Ingots of the ternary alloy were prepared in a single stage process, while ingots of the multi-component alloys were prepared in a three stage process. In stage one the iron and carbon (and manganese when appropriate) components were arc-melted. In stage two boron and molybdenum were arc-melted. In stage three the two ingots were arc-melted to produce a single ingot of the desired composition.

Arc-melting was performed by loading the components into a hearth set in a water-cooled copper plate set inside the arc-melting chamber. The chamber was flushed with argon three times. Before melting was initiated the chamber evacuated to $8x10^{-2}$ Torr and then back-

filled with argon to a pressure of 500mB. A titanium getter was melted for two minutes to minimise the oxygen content remaining. The components were heated using an arc with a 330 amp current at 32 Volts The resulting ingot was turned and remelted three times allowing for a more homogeneous composition in the ingot. The turning of the ingot was carried out inside the arc-melting chamber, by use of the electrode tip (with the current turned off), when the resulting ingot had cooled to a 'red' heat.

A Struers Accutom-5 with a diamond cutting blade operating with a feed rate of 1.2mm/min and a blade rotation of 3000rpm was used to section the ingots for use in melt spinning and materials characterisation.

3.1.4 Melt Spinning

For each production run a piece of sectioned ingot weighing approximately five grams was placed inside a boron nitride coated silica crucible with an exit nozzle one millimetre in diameter. The casting chamber was flushed with argon gas twice. The chamber was evacuated $5x10^{-2}$ Torr and then backfilled with argon to 0.8 bar. The ingot was melted by induction heating at 140kV. The crucible was lowered to 3mm above a 150mm diameter copper wheel rotating at a speed of 3500 rpm (equivalent to 27.5 ms^{-1} circumferential speed) and the melt was ejected with an argon gas pressure of approximately 3 psi.

3.2 Materials Characterisation

3.2.1 Optical Microscopy

Specimens for optical and scanning electron microscopy analysis were set in conductive bakelite using a MetPrep PA 30 or ATM Opal 400 mounting press. Grinding and polishing were carried out on a Struers DAP-7 automated polisher. The polishing schedule is shown in table 3.2. Specimens were etched with Nital 2% solution.

A Leica DRMX microscope connected to KS300 software was used to obtain optical images. Image analysis of the ternary alloys was used to determine the area percentage of the dendritic and faceted phases.

3.2.2 X-Ray Diffraction (XRD)

A Philips X'Pert X-ray diffractometer using CuKα radiation, of wavelength 1.5418Å, was used to scan samples through angles 10° to 140° at a rate of 3° min^{-1}.

Sections of the as-cast ingots approximately 1.5mm thick were ground by hand, on 120 grit SiC paper, in order to remove uneven edges caused by the cutting process, thus allowing the sample to be mounted level with the surface of its holder. This is essential in XRD so that good signals can be acquired and also so that sample holders do not jam the automatic sample exchange system.

Small sections of ribbon produced by the melt spinning process were mounted on 10mm^2 glass slides using double-sided adhesive tape. A glass slide with just double sided adhesive tape was also scanned as a control measure.

Table 3.2 Polishing schedule for alloy samples. From step 5 onwards, at the end of each step the samples were cleaned with cotton wool and Teepol, and rinsed with water. The samples were then placed in a sonic bath, using industrial methylated spirit, for three minutes to remove any remaining debris. The samples were then dried by forced air convection.

Step	Disc	lubricant	speed	time
1	120 grit	water	250 rpm	15s
2	240 grit	water	250 rpm	60s
3	400 grit	water	250 rpm	60s
4	800 grit	water	250 rpm	90s
5	1200 grit	water	250 rpm	120s
6	Struers MD Mol	Kemet 6μm diamond suspension	125 rpm	4 min
7	Struers MD Nap	Kemet 1μm diamond suspension	125 rpm	4 min
8	Struers MD Chem	OP-A (acidic alumina suspension)	125 rpm	60s

3.2.3 Differential Scanning Calorimetry (DSC)

DSC was performed in a Netzsch 404C differential scanning calorimeter, under argon gas flowing at 100ml min^{-1}, following the simple heating regime is shown in figure 3.1. (It should be noted that 1250°C is the maximum temperature allowed to be used in the DSC.) Alumina reference and sample crucibles were used. The mass of each ribbon sample analysed was approximately 10mg.

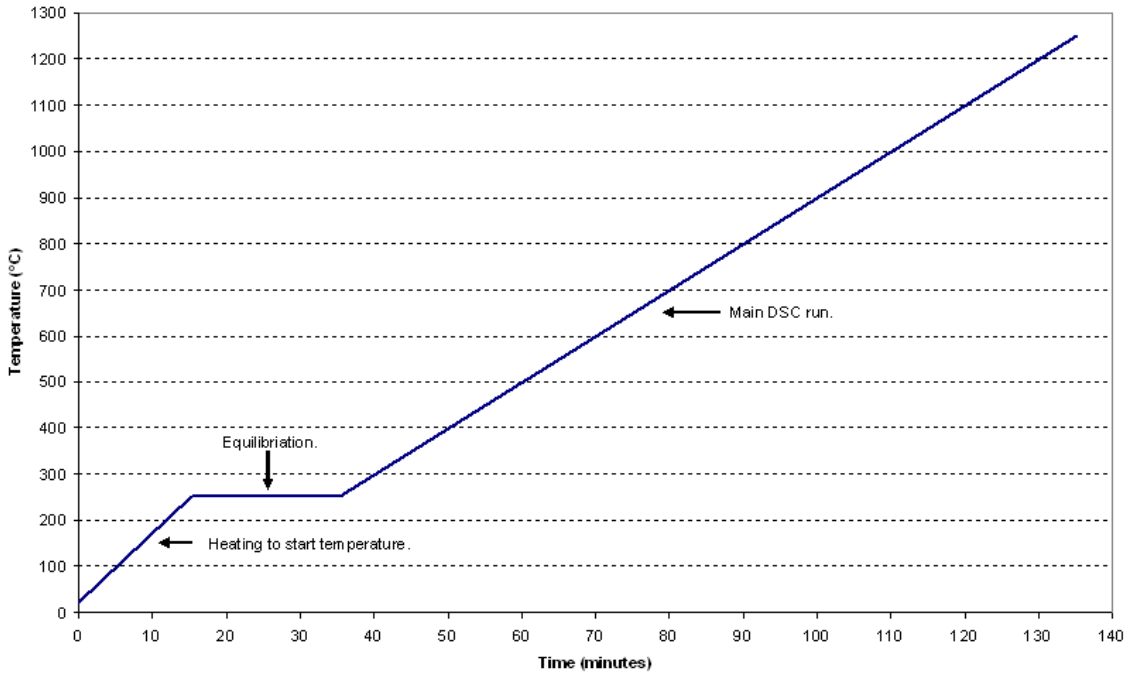

Figure 3.1 Heating schedule for DSC.

3.2.4 Scanning Electron Microscopy (SEM)

SEM was carried out using a Phililps XL-30 scanning electron microscope with a LaB_6 filament. Energy dispersive spectroscopy was unable to detect boron so quantitative analysis of phase compositions could not be performed.

3.2.5 Transmission Electron Microscopy (TEM)

In order to study the microstructure of the as-cast $Fe_{79.54}C_{3.46}B_{17}$ alloy a 1.5mm piece of previously sectioned sample was ground by hand to 200μm using 120 grit SiC paper with water as a lubricant. 3mm discs were trepanned from the sliver by electro-discharge machining. The discs were dimpled on a South Bay Technology Inc. Model 515 dimpler. For melt spun samples, small sections of ribbon were stuck onto 3mm copper discs with large centrally sited oval holes. Final ion beam thinning of all samples took place in a Gatan Model 691 Precision Ion Beam System with Ar+ ions accelerated through 5kV. As with SEM, boron could not be detected so quantitative analysis of phase compositions could not be performed. TEM was carried out, using a Philips CM20 operating at 200 kV.

3.2.6 Secondary Ion Mass Spectroscopy (SIMS)

The samples used for SIMS were taken from the optical microscopy samples. Measurements were carried out using a FEI FIB200-SIMS workstation equipped with a gallium focused ion beam (FIB) operating at 30keV. The FIB current was at 535pA with a beam spot size of 100nm. Various geometrical shapes were used for sputtering with an intended depth of at least one micron.

3.2.7 Micro-Hardness Testing

Ribbons were prepared for hardness testing in the same manner as the samples prepared for optical microscopy. The only difference being that in order to survive the grinding/polishing process the ribbons had to be mounted edge-on as the average thickness was less than 30μm. Steel clamps were used to maintain the orientation of the ribbons during the mounting process. A Mitutoyo MVK-H1 hardness testing machine with a Knoop indenter and a 200g load was used to test the hardness of the ribbons produced by melt spinning.

3.2.8 Computer Modelling

ThermoCalc software version Q, in conjunction with the TCFE2 database (both of which were developed by the Division of Computational Thermodynamics at the Royal Institute of Technology in Stockholm), was used to determine the theoretical liquidus temperature of the alloys in this study.

CHAPTER 4

DEVELOPMENT OF TERNARY IRON-CARBON-BORON ALLOYS

4.1 Introduction

In the year 2000 it was found that the addition of 0.4 weight percent of boron to the commercial cast iron FC20 (consisting mainly of iron, carbon, and silicon, with trace amounts of phosphorus and sulphur) enabled the formation of fully amorphous material up to 0.5mm in diameter [21]. Later, in 2005, an iron-based amorphous alloy was produced with a diameter of 16mm [36]. This was a multi-component alloy consisting of iron, cobalt, chromium, molybdenum, carbon, boron and yttrium. Many new bulk amorphous alloys are developed by adding new elements to, or varying the elemental ratios of known glass forming systems. It is apparent that both carbon and boron are important elements in

the formation of amorphous iron systems. It has long been known that the binary iron-boron system has a glass forming range 14-20 atomic% boron. The carbon to boron ratio has been optimised in at least one multi-component system [132] but less attention has been paid to the ternary Fe-C-B system.

In this chapter the development of an amorphous Fe-C-B alloy is described. Nine compositions are characterised, first in the as-cast state and secondly after rapid solidification processing. The glass forming ability of the compositions is discussed.

4.2 As-Cast Alloys

According to published data the phases expected to be seen in the as-cast are cementite (Fe_3C), iron boride (Fe_2B) and ferrite (α-iron)[125].

4.2.1 Optical Microscopy

4.2.1.1 Alloys with B/Fe Ratio ≥0.19 and Carbon Content >7 Atomic%

Figure 4.1 shows the microstructure of $Fe_{65.7}C_{17.3}B_{17}$ (alloy 9), with a B/Fe ratio of 0.26. It is almost fully dendritic with a residual 2-phase mixture being approximately 6% of the area. A faceted phase can also be seen. It was initially assumed that the dendrites were Fe_3C and the faceted phase was Fe_2B. According to results to be shown later, the faceted phase is indeed likely to be Fe_2B while the dendrites are $Fe_3(C,B)$ rather than Fe_3C. It is thought that some of the carbon atoms in the cementite have been substitutionally replaced by boron atoms, thereby forming an orthorhombic crystal system of iron boro-carbide – $Fe_3(C,B)$ – the only effect on the crystal structure being that the lattice parameters are slightly changed. It is assumed the residual 2-phase mixture consists of ferrite and

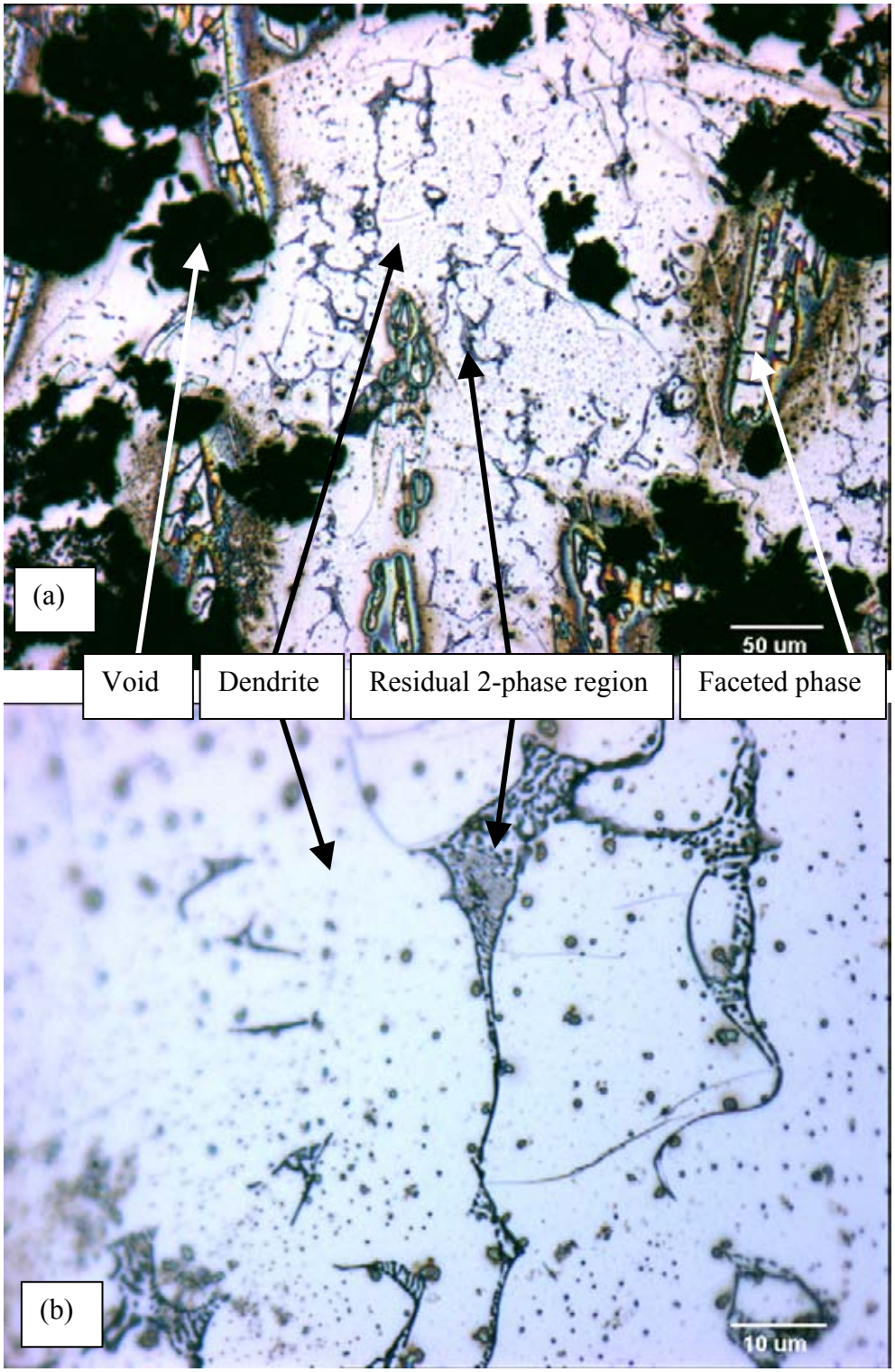

Figure 4.1 Microstructure of $Fe_{65.7}C_{17.3}B_{17}$ (alloy 9). (a) Low magnification view showing high concentration of dendrites, a faceted phase, voids, and a residual region. (b) High magnification view clearly showing residual region consists of two phases.

$Fe_3(C,B)$ lamellae. This alloy also contains large voids. It was initially thought that they were the product of extreme overetching, but this is disproved by regarding a polished but unetched sample of the same alloy, shown in figure 4.2, which also contains voids of the same size and distribution. Due to their shape, the voids are probably caused by interdendritic porosity which occurred during solidification of a particularly viscous melt, rather from where material has been pulled out of the sample during sectioning of the ingot.

Figure 4.3 shows the microstructure of $Fe_{76.5}C_{7.6}B_{15.9}$ (alloy 3), with a B/Fe ratio of 0.21. It is similar to the previous alloy as it contains $Fe_3(C,B)$ dendrites and a faceted Fe_2B phase. It differs in that it lacks the voids, and the residual 2-phase region is larger, being approximately 20% of the area. The Fe_2B phase takes up approximately 2% of the area of the overall structure.

4.2.1.2 Alloys with B/Fe Ratio ≥0.19 and Carbon Content <7 Atomic%

Figure 4.4 shows the microstructure of $Fe_{79.5}C_{3.5}B_{17}$ (alloy 7), with a B/Fe ratio of 0.21. It consists of a 68% area 2-phase matrix of finely spaced $Fe_3(C,B)$ and ferrite lamellae, with the remainder being $Fe_3(C,B)$ dendrites some of which contain a faceted Fe_2B phase. The Fe_2B phase is approximately 8% of the area of the overall structure.

Figure 4.5 shows the microstructure of $Fe_{80.7}C_{3.7}B_{15.6}$ (alloy 2), with a B/Fe ratio of 0.19. It is similar in appearance to the previous alloy. It consists of a 64% area 2-phase matrix of finely spaced $Fe_3(C,B)$ and ferrite lamellae, with the remainder being $Fe_3(C,B)$ dendrites some of which contain a Fe_2B phase. The matrix is assumed to consist of $Fe_3(C,B)$ and ferrite. The Fe_2B phase is approximately 2% of the area of the overall structure.

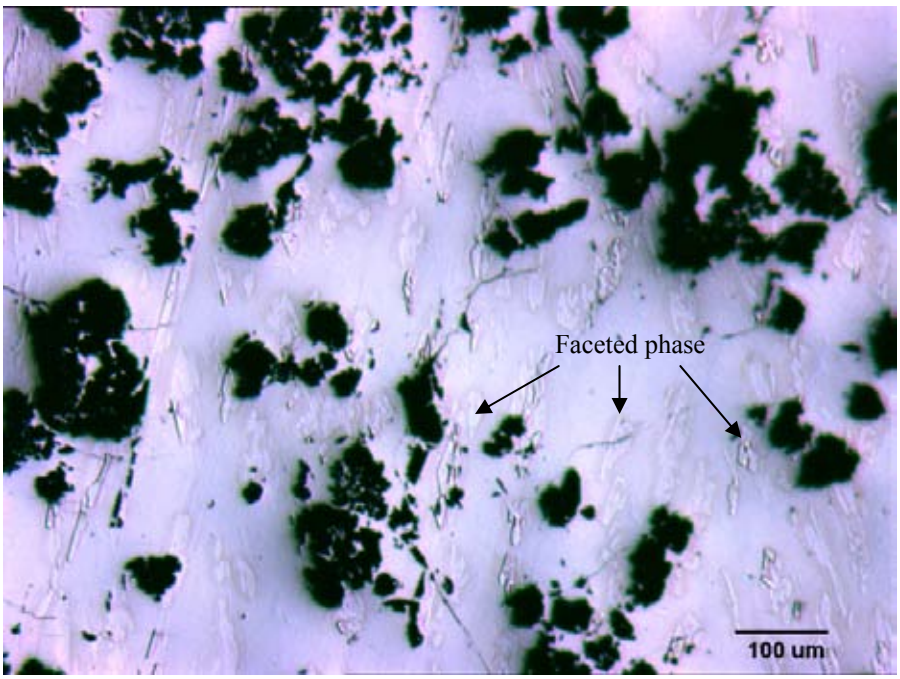

Figure 4.2 Polished but unetched view of $Fe_{65.7}C_{17.3}B_{17}$ (alloy 9) revealing voids which are most likely to be the result of interdendritic porosity. A faceted phase is also visible.

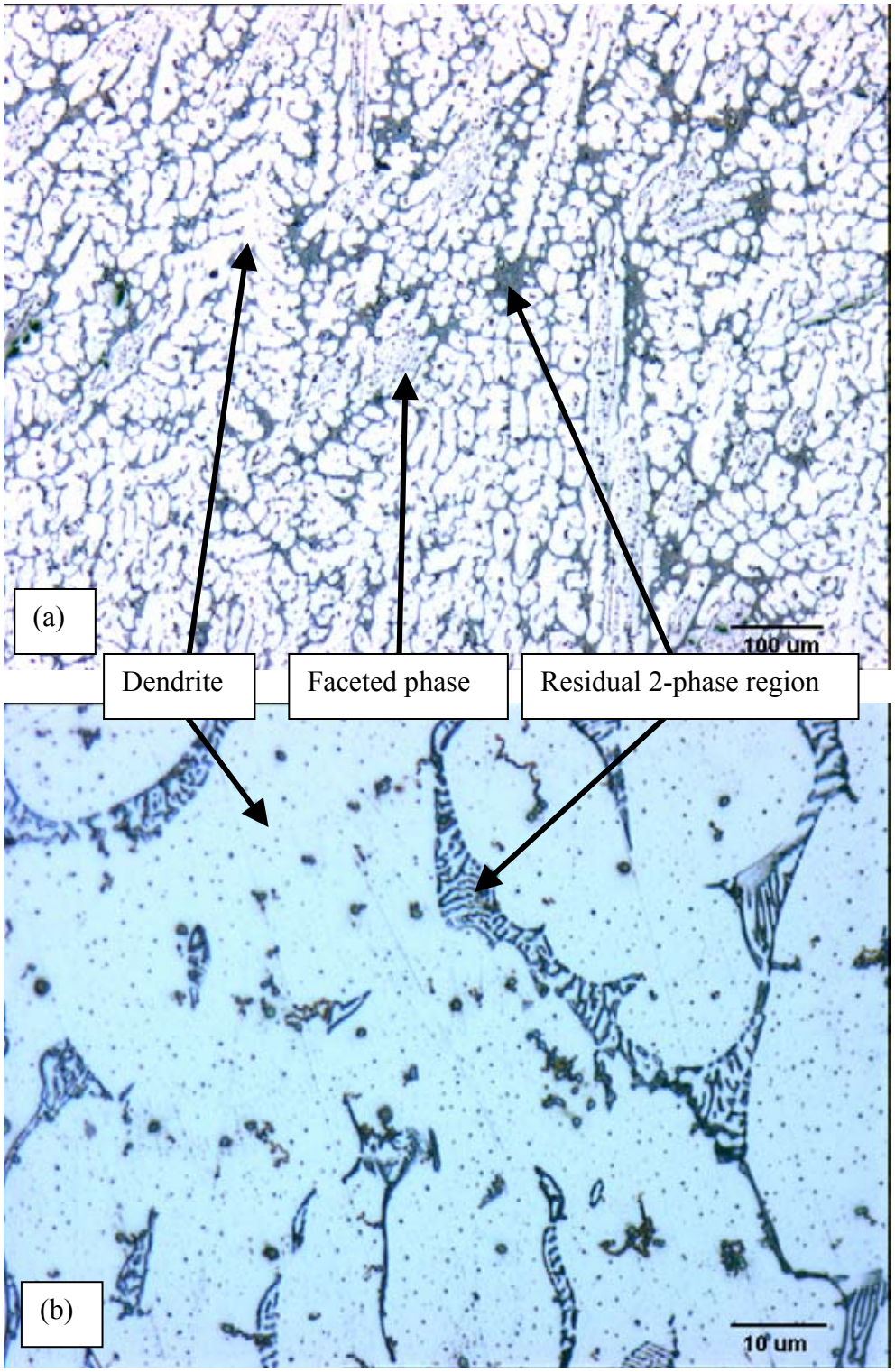

Figure 4.3 Microstructure of $Fe_{76.5}C_{7.6}B_{15.9}$ (alloy 3). (a) Low magnification view showing a high concentration of dendrites, some of which contain a faceted phase, and an unresolved residual 2-phase region. (b) High magnification view clearly showing lamellae in the 2-phase region.

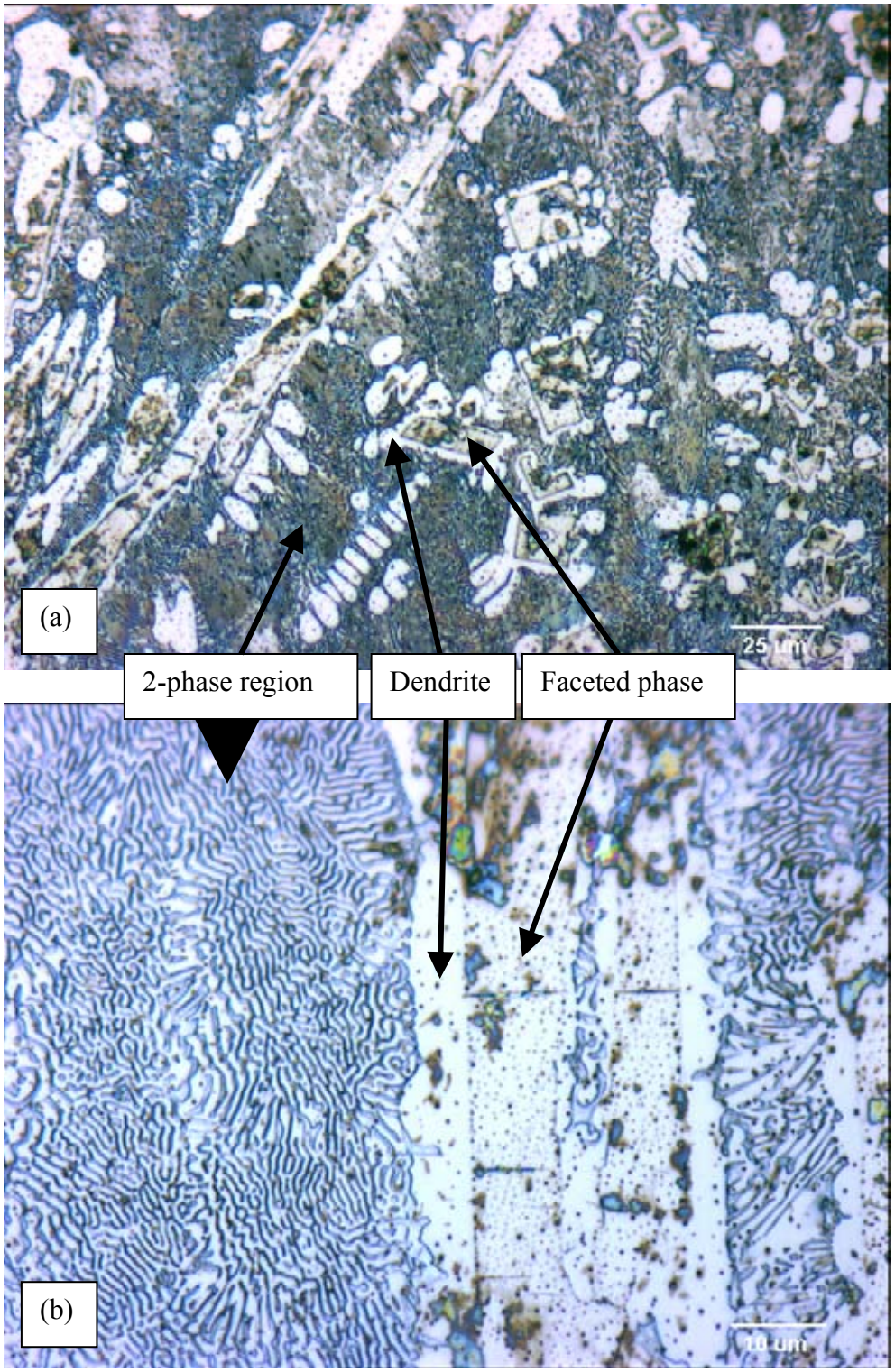

Figure 4.4 Microstructure of $Fe_{79.5}C_{3.5}B_{17}$ (alloy 7). (a) Low magnification view showing a 2-phase matrix and dendrites containing a faceted phase. (b) High magnification showing fine lamellae in the 2-phase region and part of a dendrite containing the faceted phase.

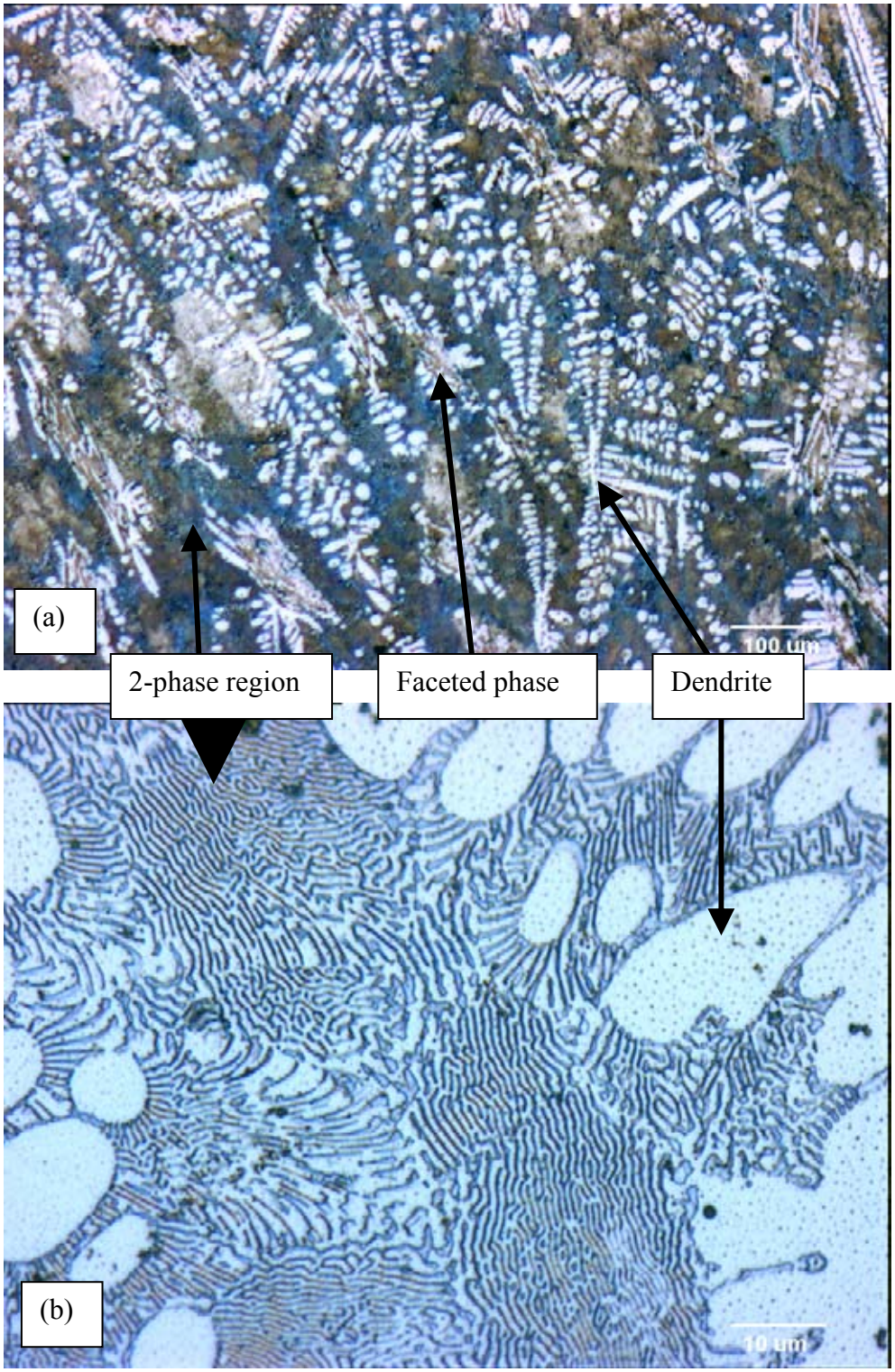

Figure 4.5 Microstructure of $Fe_{80.7}C_{3.7}B_{15.6}$ (alloy 2). (a) Low magnification view showing an unresolved matrix with dendrites containing a faceted phase. (b) High magnification view of matrix showing it to be a 2-phase region consisting of fine lammellae.

4.2.1.3 Alloys with B/Fe Ratio 0.16 to 0.17

Figure 4.6 shows the microstructure of $Fe_{80.9}C_5B_{14.1}$ (alloy 4) with a B/Fe ratio of 0.17. It consists of a 63% area 2-phase matrix of finely spaced $Fe_3(C,B)$ and ferrite lamellae, with the remainder being $Fe_3(C,B)$ dendrites. Unlike the previous alloys a faceted phase is not seen.

Figure 4.7 shows the microstructure of $Fe_{81.2}C_6B_{12.8}$ (alloy 6) with a B/Fe ratio of 0.16 and is similar in appearance to the previous alloy. It consists of a 78% area 2-phase matrix of finely spaced $Fe_3(C,B)$ and ferrite lamellae, with the remainder being $Fe_3(C,B)$ dendrites, and once again a faceted phase is not visible.

The small unresolved spots seen within the $Fe_3(C,B)$ phase in all the previous alloys are believed to be small Fe_2B particles (or sites from which they were removed during polishing) rather than pitting caused by the etchant used to reveal the microstructure. See section 4.2.2

4.2.1.4 Alloys with B/Fe Ratio 0.09 to 0.1

Figure 4.8 shows the microstructure of $Fe_{82.8}C_{8.7}B_{8.5}$ (alloy 8) with a B/Fe ratio of 0.1. It consists of a 91% area 2-phase matrix of finely spaced lamellae, with the remainder being dendrites. The matrix is believed to consist of $Fe_3(C,B)$ and ferrite. The dendrites in this alloy have a different appearance to those shown in previous figures, indicating that their composition may be different from those in previous figures. According to results shown later the dendrites are degenerate pearlite formed from a primary austenite phase.

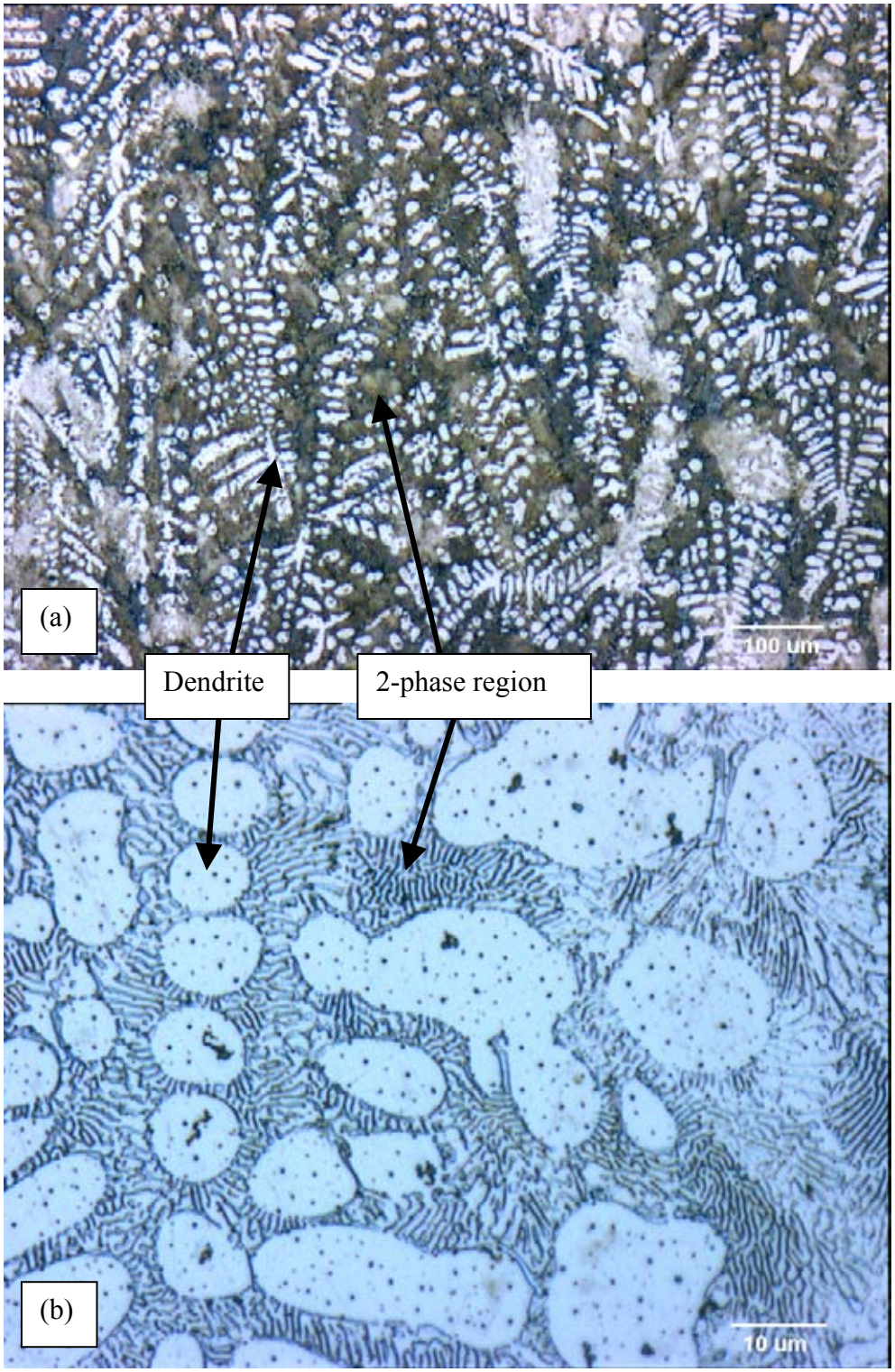

Figure 4.6 Microstructure of $Fe_{80.9}C_5B_{14.1}$ (alloy 4). (a) Low magnification view showing an unresolved matrix and dendrites. (b) High magnification of matrix showing it to be a 2-phase region consisting of fine lamellae.

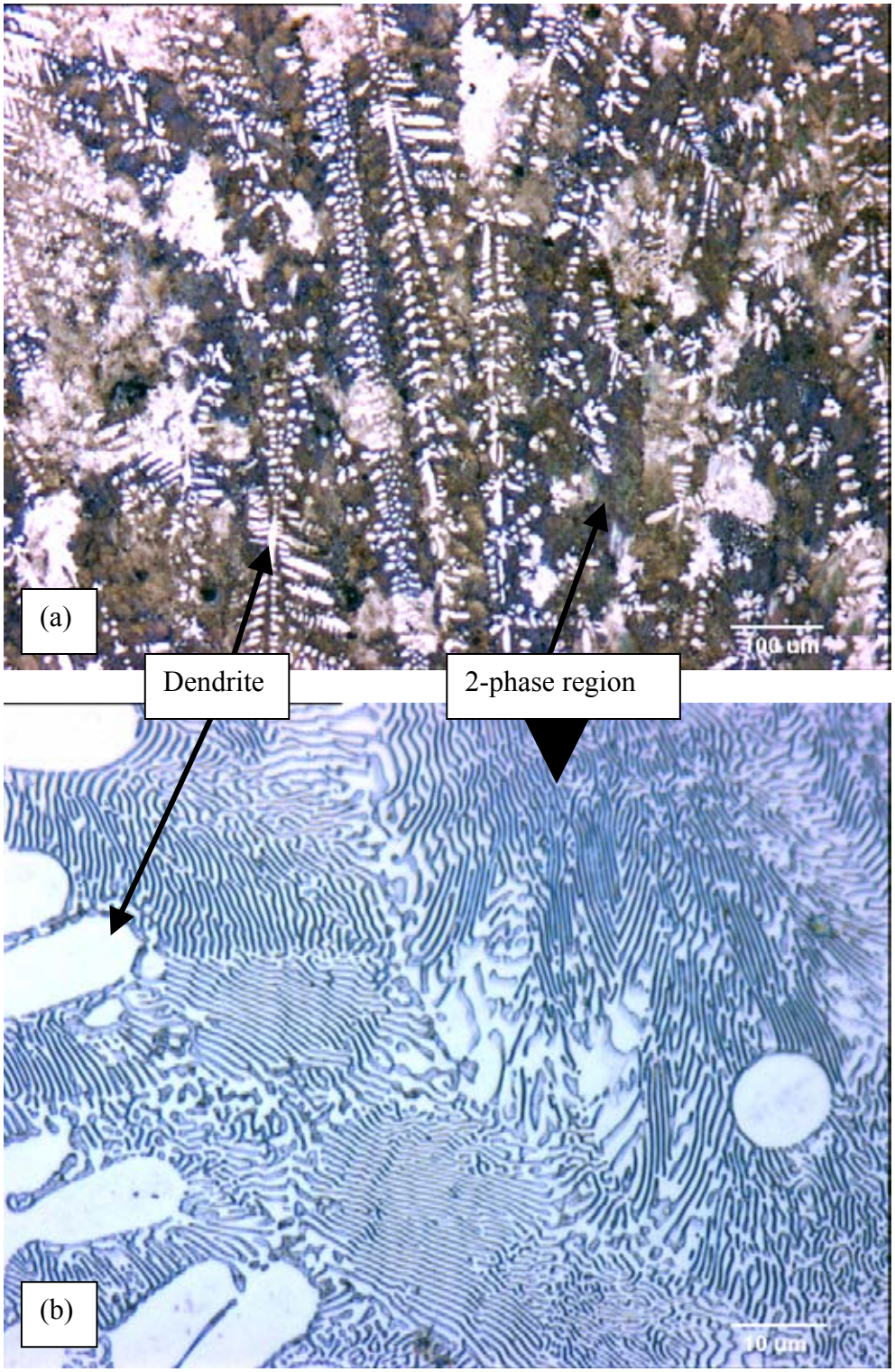

Figure 4.7 Microstructure of $Fe_{81.2}C_6B_{12.8}$ (alloy 6). (a) Low magnification view showing an unresolved matrix and dendrites. (b) High magnification of matrix showing it to be a 2-phase region consisting of fine lamellae.

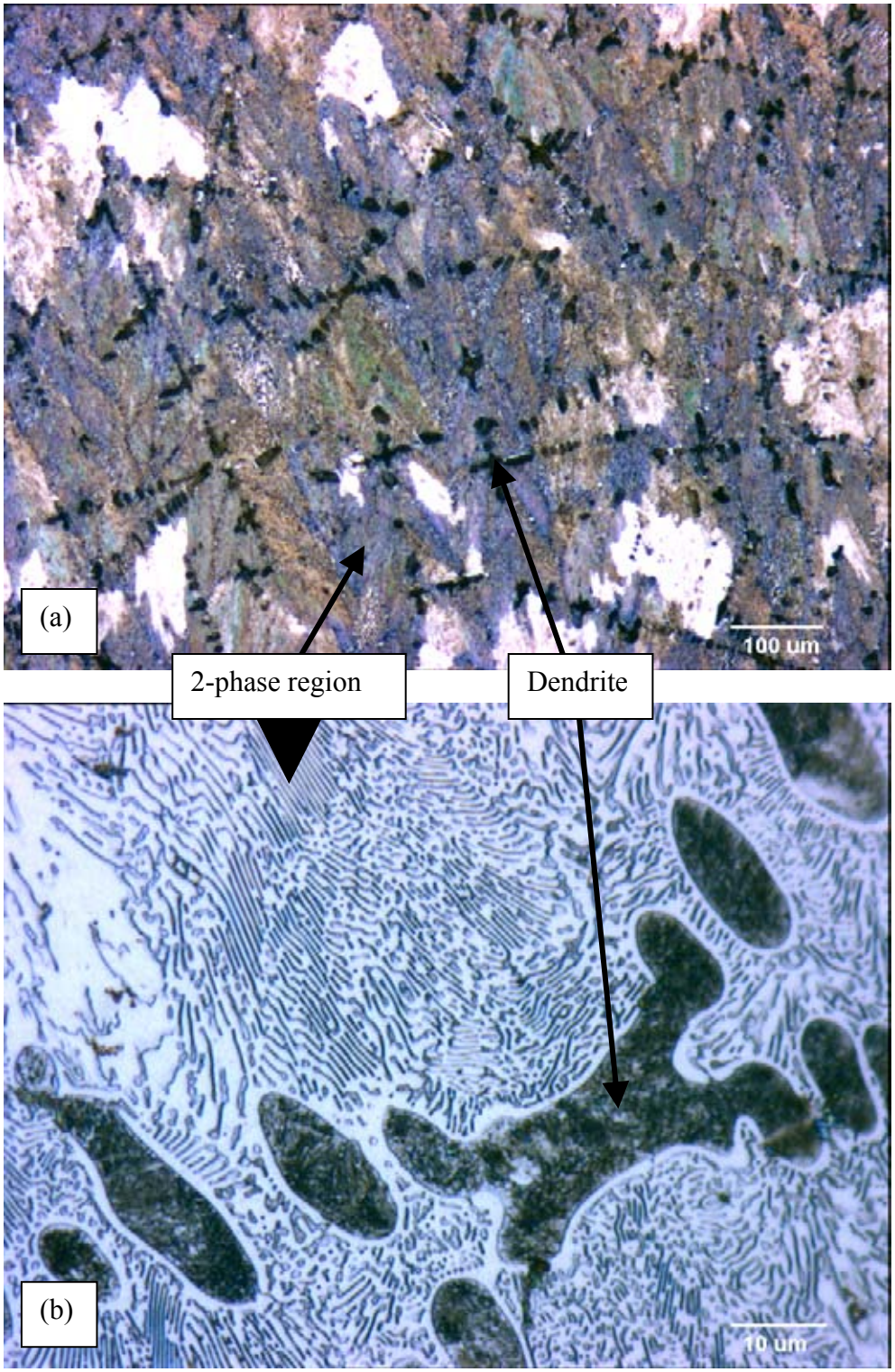

Figure 4.8 Microstructure of $Fe_{82.8}C_{8.7}B_{8.5}$ (alloy 8). (a) Low magnification view showing an unresolved matrix containing a low concentration of dendrites. (b) High magnification of matrix showing it to be a 2-phase region consisting of fine lamellae.

Figure 4.9 shows the microstructure of $Fe_{82.9}C_{10}B_{7.1}$ (alloy 5) with a B/Fe ratio of 0.16. It is similar in appearance to previous alloy. It consists of a 90% area 2-phase matrix of finely spaced $Fe_3(C,B)$ and ferrite lamellae, with the remainder being dendrites of degenerate pearlite.

4.2.1.5 Alloy with B/Fe Ratio 0.07

Figure 4.10 shows the microstructure of $Fe_{80}C_{14.8}B_{5.2}$ (alloy 1) with a B/Fe ratio of 0.07. It consists of a 66% area 2-phase matrix of irregular $Fe_3(C,B)$ and ferrite lamellae, with the remainder being angular $Fe_3(C,B)$ dendrites. The unresolved spots are shown to be polishing debris in the following section.

4.2.2 Scanning Electron Microscopy (SEM)

Quantitative analysis was not possible as energy dispersive spectroscopy (EDS) does not usually detect boron - the element with the lowest atomic weight in the alloy systems. However, it is possible to detect the presence of boron if the phase being analysed contains a high proportion of boron. This can be achieved if the accelerating voltage is lower than the 20kV used in imaging and the spot size is large enough to compensate for the reduction in return signal caused by the drop in kV. This decreases the interaction volume of the electron beam in the sample and correspondingly reduces interference from the surrounding material thereby slightly increasing sensitivity.

4.2.2.1 Alloys with B/Fe Ratio ≥0.19

Figure 4.11 shows a typical BSE image of a faceted phase seen in $Fe_{65.7}C_{17.3}B_{17}$ (alloy 9), $Fe_{76.5}C_{7.6}B_{15.9}$ (alloy 3), $Fe_{79.5}C_{3.5}B_{17}$ (alloy 7) and $Fe_{80.7}C_{3.7}B_{15.6}$ (alloy 2). It appears much darker than the surrounding dendrite. As this image was taken in BSE mode this indicates

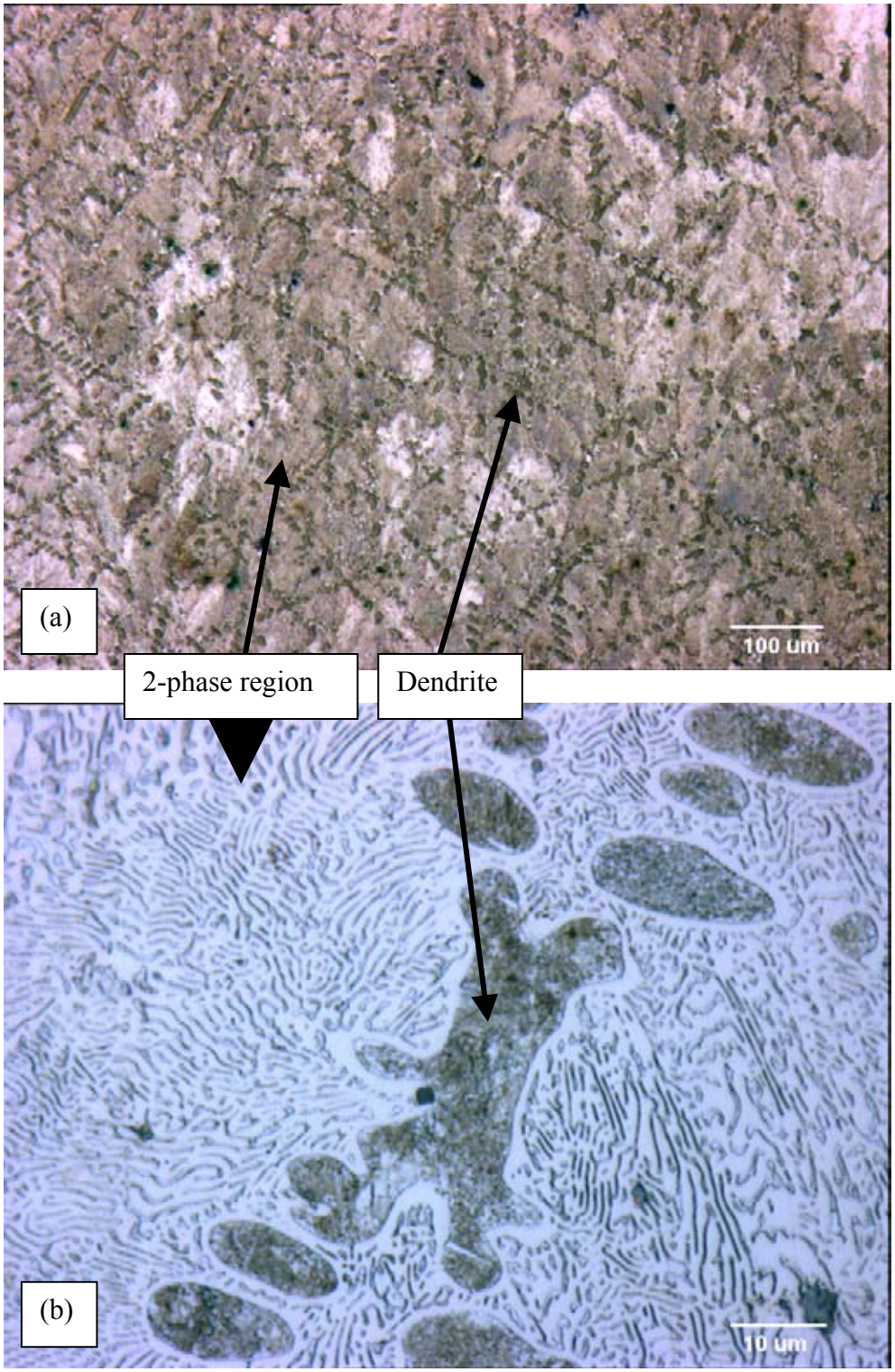

Figure 4.9 Microstructure of $Fe_{82.9}C_{10}B_{7.1}$ (alloy 5). (a) Low magnification view showing an unresolved matrix containing a low concentration of dendrites. (b) High magnification of matrix showing it to be a 2-phase region consisting of fine lamellae.

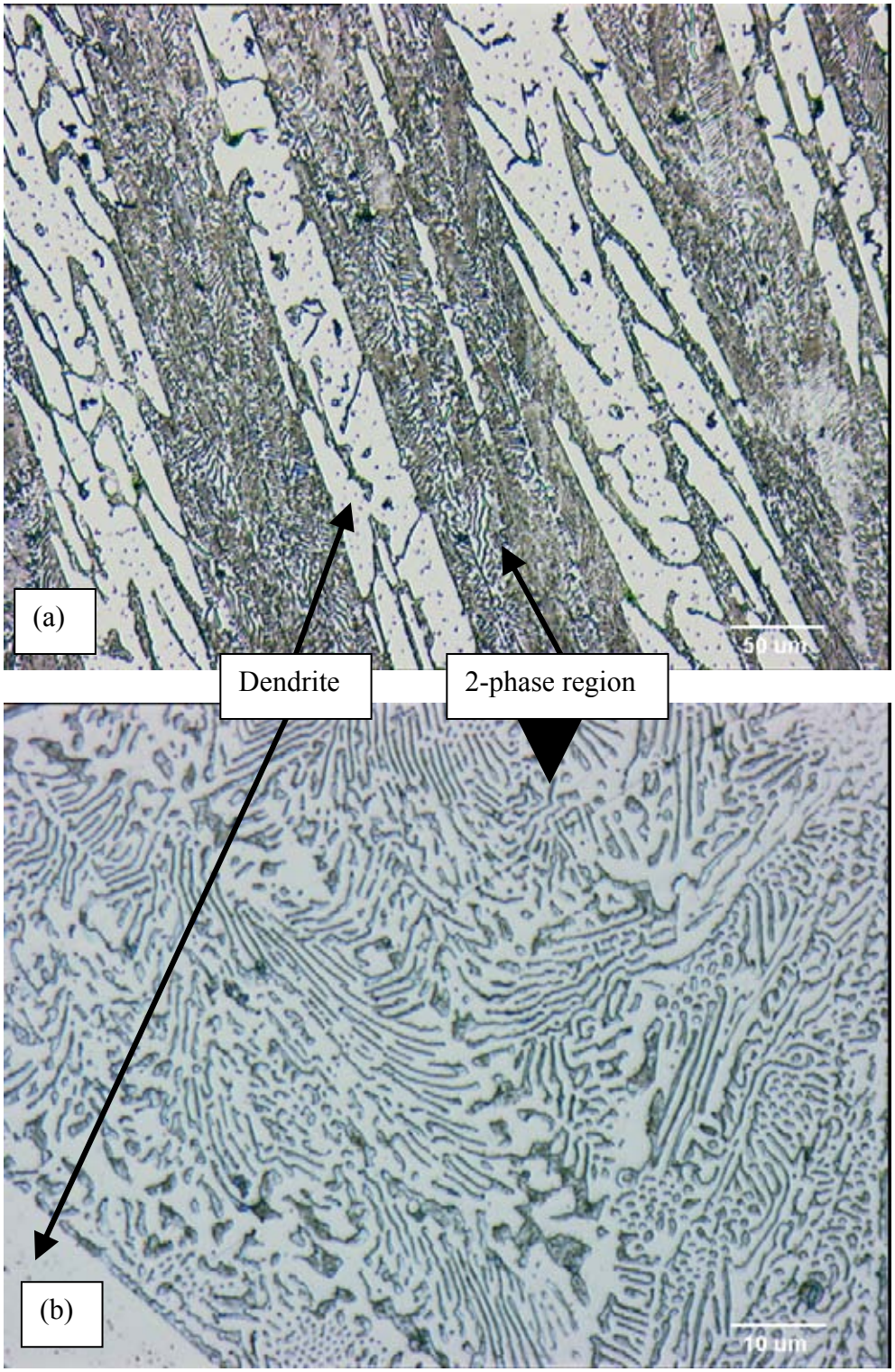

Figure 4.10 Microstructure of $Fe_{80}C_{14.8}B_{5.2}$ (alloy 1). (a) Low magnification view showing a 2-phase matrix containing angular dendrites. (b) High magnification view of 2-phase region showing irregular lamellae.

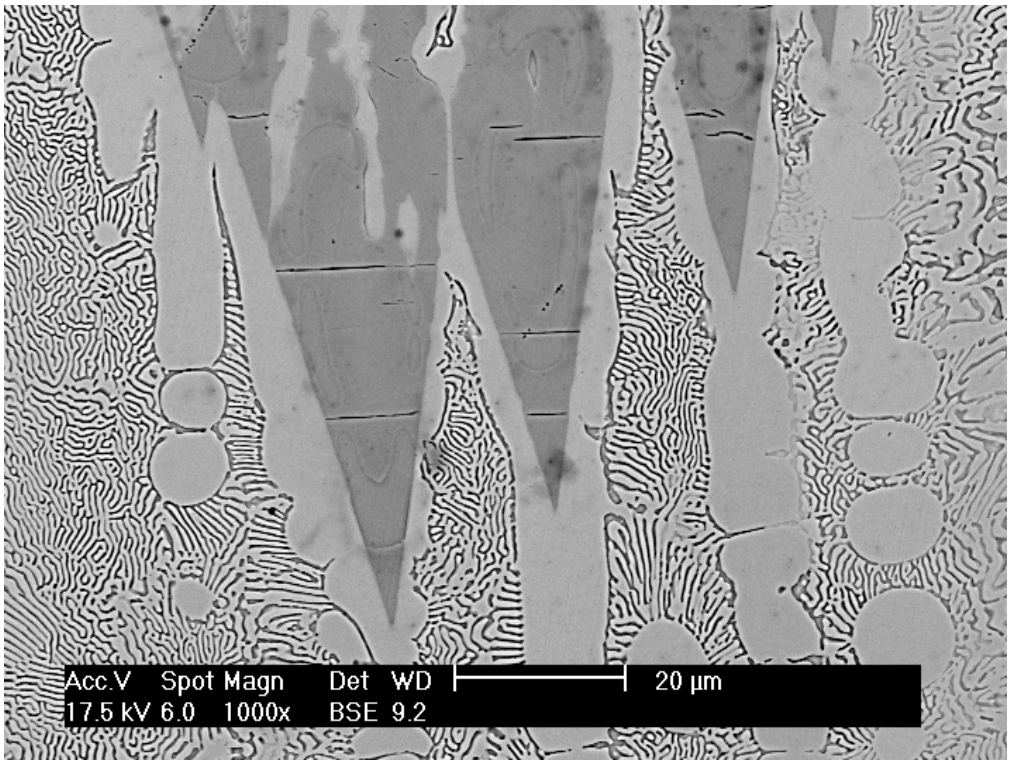

Figure 4.11 Representative BSE image (taken from alloy 7) of the faceted phase seen in $Fe_{65.7}C_{17.3}B_{17}$ (alloy 9), $Fe_{76.5}C_{7.6}B_{15.9}$ (alloy 3), $Fe_{79.5}C_{3.5}B_{17}$ (alloy 7) and $Fe_{80.7}C_{3.7}B_{15.6}$ (alloy 2). The surrounding dendrites are much lighter in contrast indicating they have a lower concentration of metalloid elements. The faceted phase is therefore Fe_2B while the dendrites are $Fe_3(C,B)$.

that the composition of the faceted phase contains a higher concentration of elements with a low atomic mass compared to the composition of the dendrite. It has been mentioned that the main phases that can be found at room temperature in the Fe-C-B system are cementite, iron II boride, and ferrite. This leads to the conclusion that the faceted phase is Fe_2B (B/Fe ratio 0.5) and the dendrites are cementite (C/Fe ratio 0.33), while the lamellae region is cementite and ferrite. This is supported by the fact that boron can be detected by EDS only in the faceted phase. However, according to the SIMS analysis shown in section 4.23, boron is found to be present not only in the faceted phase but also in the dendrites. The dendrites (and their corresponding lamellae) are therefore not cementite but are instead iron boro-carbides - $Fe_3(C,B)$.

4.2.2.2 Alloys with B/Fe Ratio ≥0.16

Figure 4.12 shows images of the unresolved spots seen within the dendrites shown in figure 4.1 and figures 4.3 to 4.6. Figure 4.12a is a view of $Fe_{81.2}C_6B_{12.8}$ (alloy 6). The spots are revealed to be small voids rather than pitting as the sample is unetched. Figure 4.12b is another view of the same alloy but this time it has been etched. Small voids are present and dome-like features can also be seen. In figure 4.12c (taken from $Fe_{76.5}C_{7.6}B_{15.9}$, alloy3) the dome-like features are degraded to various degrees and are revealed to be coverings for small crystals. The pits are therefore former sites of crystals which have been removed during the polishing process. As these alloys all have a boron content of 12.8 atomic percent or greater, it is believed the crystals are the Fe_2B precipitates which have formed on cooling of the $Fe_3(C,B)$ phase.

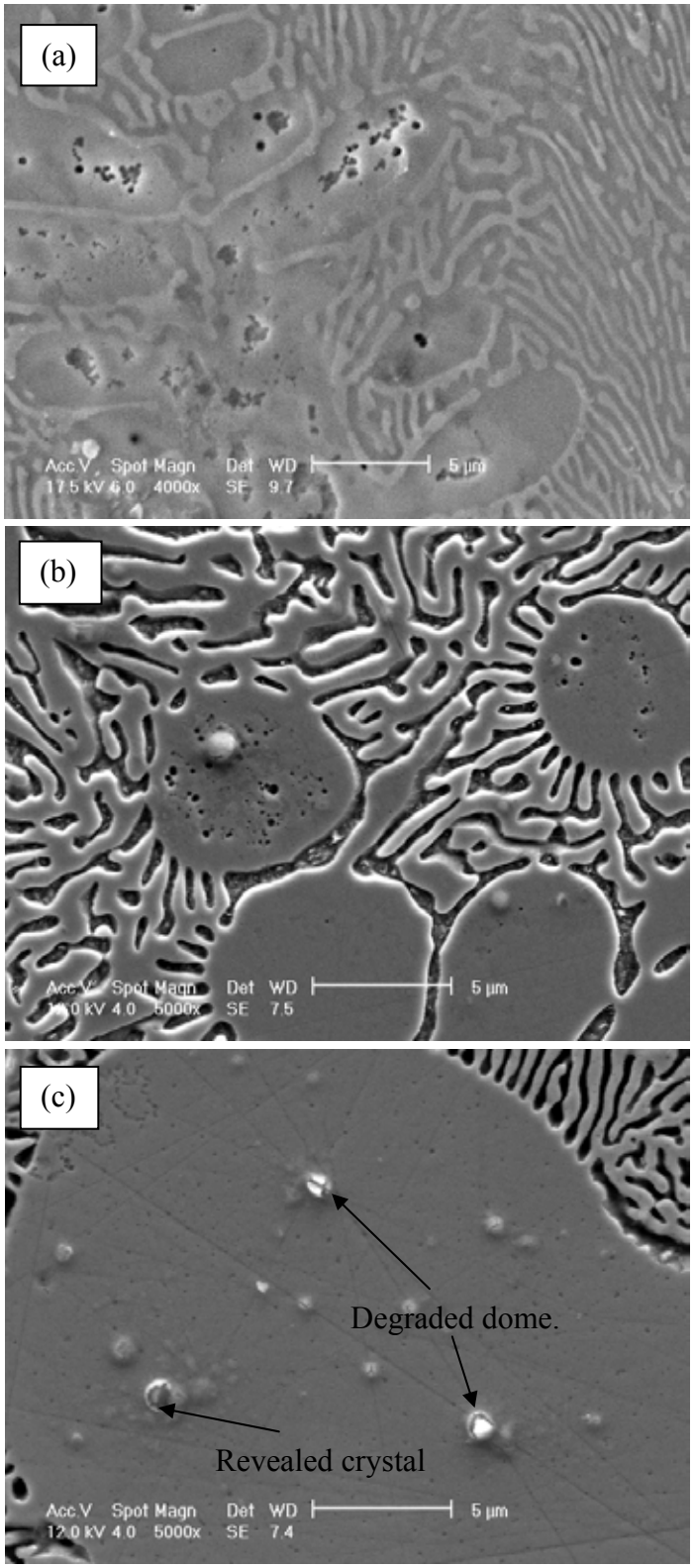

Figure 4.12 Representative SEM images of unresolved spots within the dendrites seen in figure 4.1 and figures 4.3 to 4.6. (a) Unetched $Fe_{81.2}C_6B_{12.8}$ (alloy 6), showing pitting. (b) Etched $Fe_{81.2}C_6B_{12.8}$ where pitting and dome-like features can be seen. (c) $Fe_{76.5}C_{7.6}B_{15.9}$ (alloy 3) showing degraded domes revealing previously covered crystals. Spots in optical images are crystals, or former sites of crystals which were removed during specimen preparation.

4.2.2.3 Alloys with B/Fe Ratio 0.09 to 0.1

Figure 4.13 shows images of the dendrites found only in $Fe_{82.8}C_{8.7}B_{8.5}$ (alloy 8) and $Fe_{82.9}C_{10}B_{7.1}$ (alloy 5). Figure 4.13a is a general view revealing there are structures within the dendrites with a dark appearance seen in figures 4.8 and 4.9. The structure is shown in greater detail in figure 4.13b. It is a two-phase mixture of very fine plates. The primary solidification product of these compositions is austenite [125], so it appears that the dendrites undergo a solid sate transformation after solidification – i.e. eutectoid decomposition – and form what is know as degenerate pearlite [133].

4.2.2.4 Alloys with Additional Features

Figure 4.14 displays a view of the spots which appear in the optical micrograph (figure 4.10a) for $Fe_{80}C_{14.8}B_{5.2}$ (alloy 1). Unlike other alloys the spots are not small Fe_2B crystals (or former sites of crystals) but are a polishing defect: they appear to be an agglomeration of matter, most likely the softer ferrite phase, which has been ripped from the sample and smeared into the surrounding area during polishing.

Figure 4.15 shows the voids seen in $Fe_{65.7}C_{17.3}B_{17}$ (alloy 9). Some annealed irons have similar sized voids where temper graphite has been pulled out during polishing, but as this composition is not expected to produce graphite and has not undergone any heat treatment, this is not the cause of the voids. It can be seen that in most cases the voids have been back-filled with bakelite during specimen preparation, which was subsequently not fully removed during the grinding and polishing process. In the centre of the image, however, there is clearly a deep hole which cannot be the result of pull-out of either graphite or a faceted phase. This confirms the suggestion in section 4.2.1.1 that the voids are the result of interdendritic porosity.

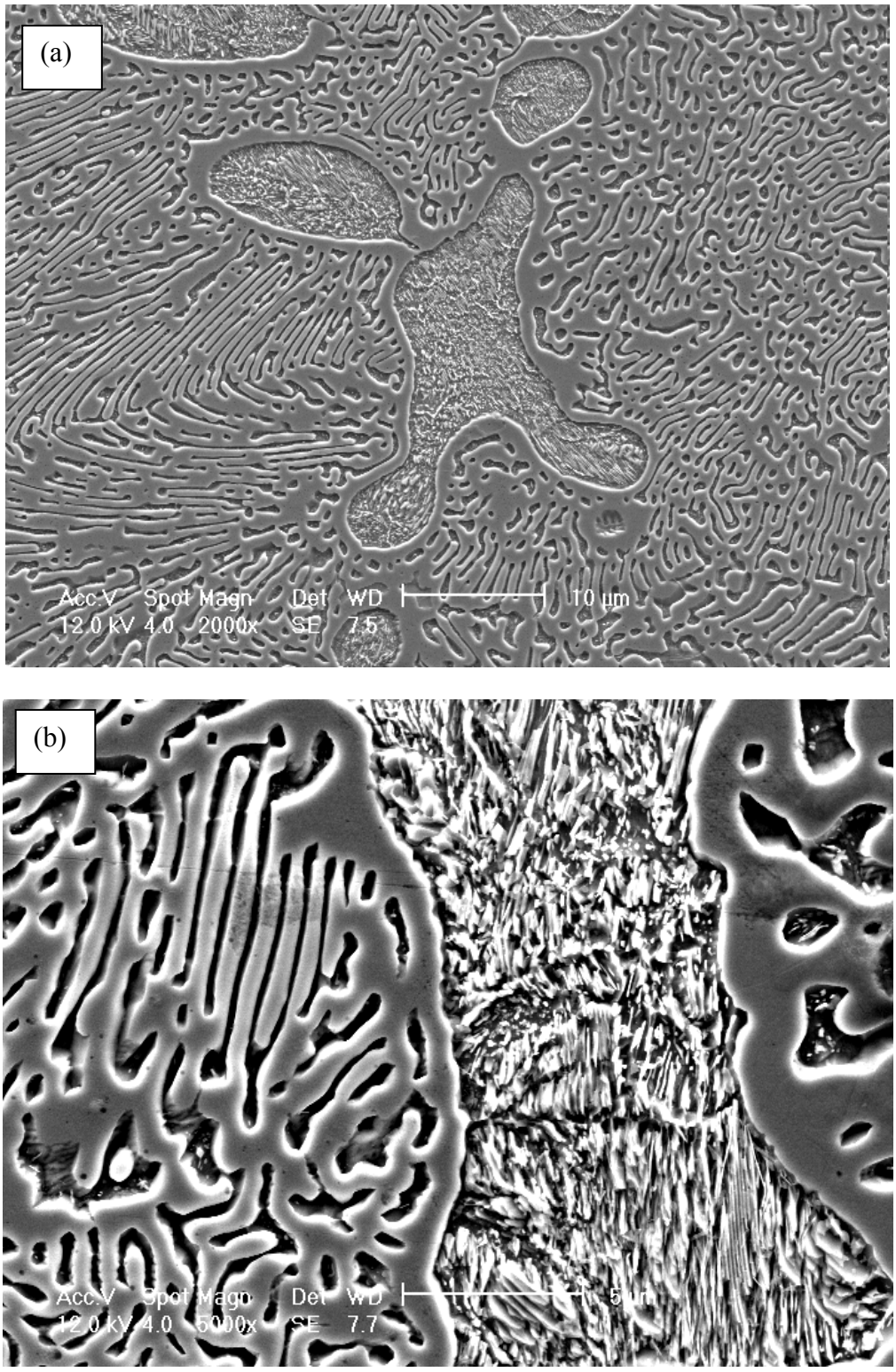

Figure 4.13 Secondary electron images of the dendrites seen in figures 4.8 and 4.9. (a) General view of dendrite in $Fe_{82.8}C_{8.7}B_{8.5}$ (alloy 8) showing a textured surface. (b) Closer view of a dendrite in $Fe_{82.9}C_{10}B_{7.1}$ (alloy 5) clearly showing a two-phase structure consisting of very fine plates.

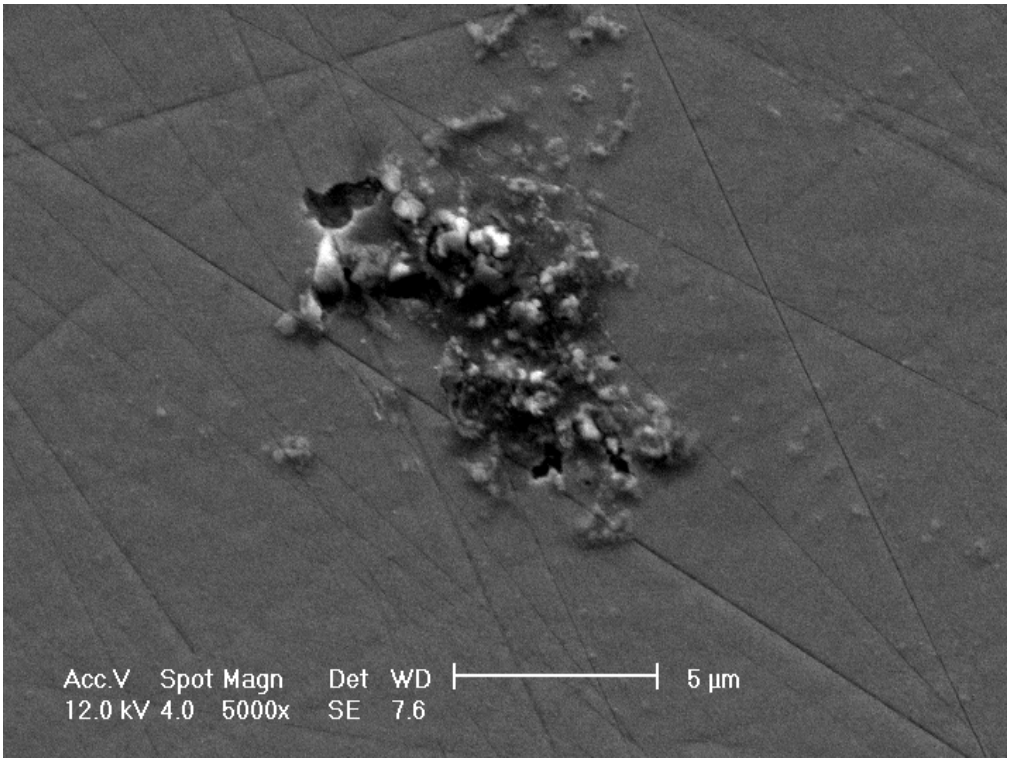

Figure 4.14 Secondary electron image of a polishing defect in $Fe_{80}C_{14.8}B_{5.2}$ (alloy 1). A large agglomeration of material, probably ripped from sample surface, has been smeared into surrounding area.

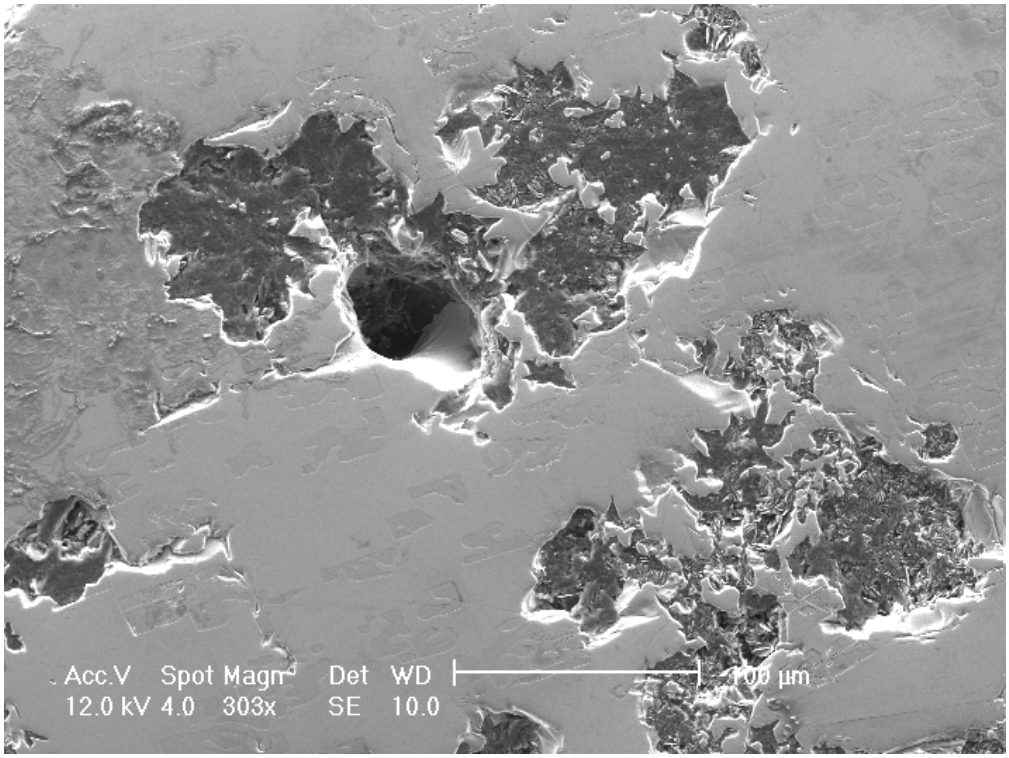

Figure 4.15 Secondary electron image of voids, which are the result of interdendritic porosity, seen in $Fe_{65.7}C_{17.3}B_{17}$ (alloy 9). The voids have been back-filled with bakelite during specimen preparation, apart from near the centre of the image, where a deep hole can bee seen.

4.2.3 Secondary Ion Mass Spectroscopy (SIMS)

A limited analysis measuring the boron to carbon ratio in features of interest was performed on four of the alloys. The results are shown in table 4.1. It can be seen that boron is present in all the features. It is assumed that this is also the case for the remaining alloys. This confirms the XRD result that one of the phases present is orthorhombic iron borocarbide – $Fe_3(C,B)$ – rather than cementite (Fe_3C). The B/C ratio is particularly high in the faceted regions, which supports the SEM conclusion that the faceted phase is Fe_2B.

Table 4.1 Boron/carbon ratio in selected compositions.

Alloy	Faceted Core	Dendrite	Lamellae Area
(7) $Fe_{79.5}C_{3.5}B_{17}$	15.63±0.06	10.36±0.06	5.94±0.06
(3) $Fe_{76.5}C_{7.6}B_{15.9}$	15.97±0.19	5.25±0.2	4.28±0.14
(8) $Fe_{82.8}C_{8.7}B_{8.5}$	n/a	0.59±0.06	3.37±0.04
(1) $Fe_{80}C_{14.8}B_{5.2}$	n/a	1.91±0.04	2.02±0.05

4.2.4 X-Ray Diffraction (XRD)

Figure 4.16 shows the XRD traces for each of the as-cast alloys. In all alloys there are XRD peaks corresponding to a crystalline phase similar to cementite (orthorhombic Fe_3C) and the orthorhombic version of Fe_3B (which can also have a tetragonal crystal structure), implying that they represent $Fe_3(C,B)$ - an orthorhombic iron boro-carbide phase. This is supported by the SIMS analysis which detected the presence of boron in the dendrites of the samples sent for analysis. The peak positions for the orthorhombic phase vary between

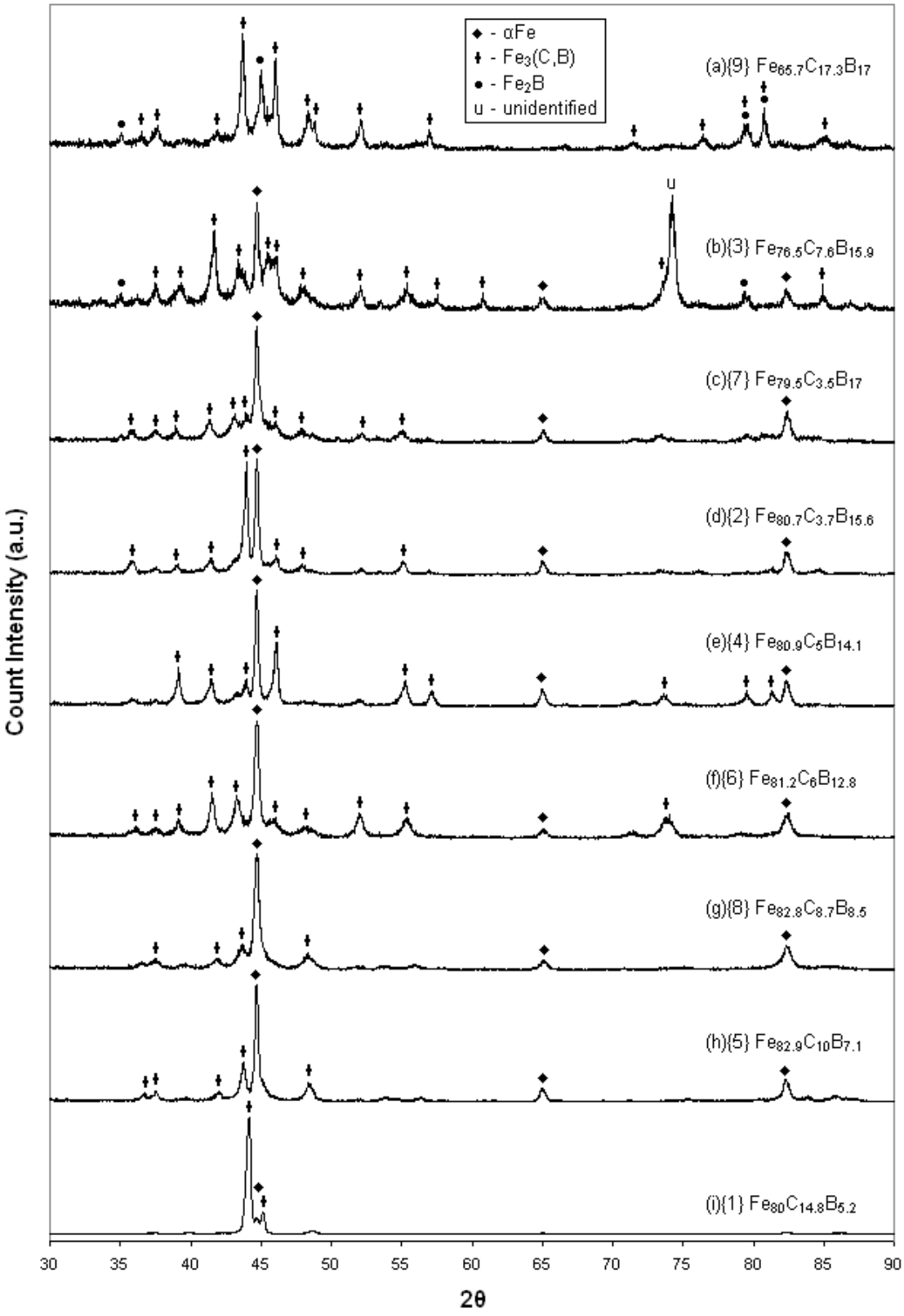

Figure 4.16 XRD trace for as-cast alloys ({x} = alloy number). $Fe_3(C,B)$ peaks are visible for each composition. Ferrite peaks are visible in each trace apart from (a). Peaks corresponding to Fe_2B are only visible in (a) and (b).

alloys indicating a change in lattice parameters of the unit cell which is most likely due to a change in composition. This is not surprising as the boron to carbon ratio varies from alloy to alloy.

In all alloys there are XRD peaks corresponding to α-iron (ferrite). The only exception is figure 4.16a which is the trace for $Fe_{65.7}C_{17.3}B_{17}$ (alloy 9) - the alloy with a residual 2-phase mixture (see figure 4.1). From this, it can be deduced that one set of lamellae in the 2-phase mixture are composed of ferrite, which is what one would expect to see in an iron-based alloy. As ferrite and $Fe_3(C,B)$ are the only phases identified in figures 4.16c to 4.16i, it is reasonable to infer that the second set of lamellae found in the 2-phase mixture are $Fe_3(C,B)$. It is no surprise that ferrite is not detected in $Fe_{65.7}C_{17.3}B_{17}$ as the relative count intensities for ferrite XRD peaks compared to those for other crystalline phases are so low as to make them indistinguishable from background noise.

In the traces for $Fe_{65.7}C_{17.3}B_{17}$ (alloy 9) and $Fe_{76.5}C_{7.6}B_{15.9}$ (alloy 3) – figures 4.16a and 4.16b – XRD peaks corresponding to Fe_2B can be seen. These are two of the alloys which showed a faceted phase (concluded to be Fe_2B in section 4.2.2) in their corresponding micrographs (figures 4.1 and 4.3). From this it would be expected that figures 4.16c and 4.16d should also have XRD peaks for Fe_2B as they also show a faceted phase in their corresponding micrographs (figures 4.4 and 4.5). However, this is not the case. It is believed that Fe_2B peaks are not seen for these two alloys because the peak counts for this phase are too low relative to the peak counts for ferrite and become lost in the background noise. (Ferrite is found in the 2-phase mixture of which there is only a residual amount in $Fe_{65.7}C_{17.3}B_{17}$, a minor amount of 20% in $Fe_{76.5}C_{7.6}B_{15.9}$, and is the major structure in excess of 60% in $Fe_{79.5}C_{3.5}B_{17}$ (alloy 7) and $Fe_{80.7}C_{3.7}B_{15.6}$ (alloy2)).

4.2.5 Transmission Electron Microscopy (TEM)

CaRine Crystallography v3 software was used to generate the crystallographic data used for this analysis. The ferrite data was created from the BCC crystal system (space group/number: Im3m/229) with the lattice parameters a=b=c=2.8664Å. The $Fe_3(C,B)$ data was created from the orthorhombic crystal system (space group/number: Pnma/62) using the following lattice parameters: a=5.411Å, b=6.629Å and c=4.45Å. With these parameters the calculated XRD peaks have a better match with the XRD trace (figure 4.16) than those from the cementite (Fe_3C) or orthorhombic Fe_3B standards in the Philips XRD database.

Figure 4.17 shows a bright field image of $Fe_{79.5}C_{3.5}B_{17}$ (alloy 7). Thick light-coloured lamellae can be seen extending from a large region of material with the same contrast which is assumed to be the tip/edge of a dendrite. Thin dark-coloured lamellae make-up the remainder of the 2-phase mixture. From the previous results it is expected that the lamellae consist of αFe and $Fe_3(C,B)$. Quantitative analysis of the specimen by EDS could not be performed so an attempt was made to determine the composition of the phases by comparing the selected area diffraction patterns (SADPs) with calculated SADPs.

Figures 4.18 and 4.19 show selected SADPs (experimental and calculated) for the dark and light lamellae respectively.

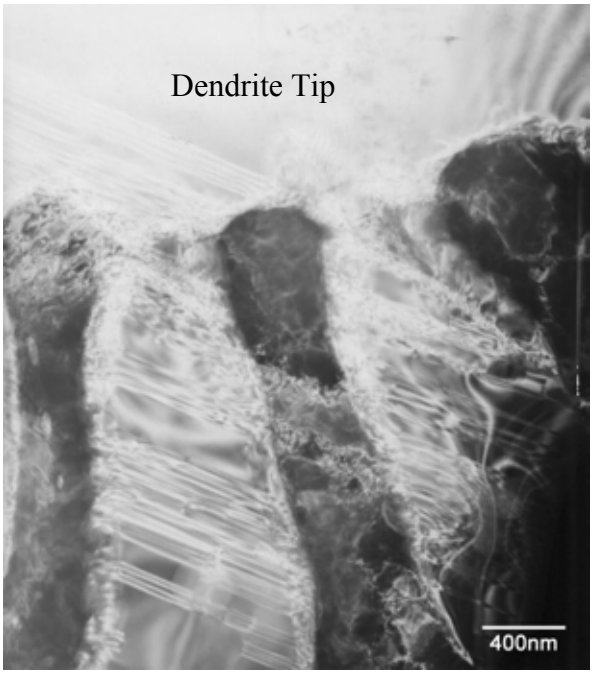

Figure 4.17 Bright field image of $Fe_{79.5}C_{3.5}B_{17}$ (alloy 7). Thick bright lamellae can be seen extending from the edge of a dendrite in the top part of the image. The thin dark lamellae are the second component of the eutectic phase.

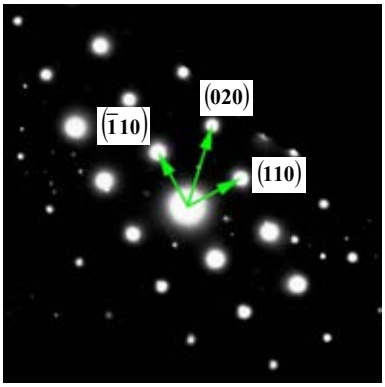

[001]

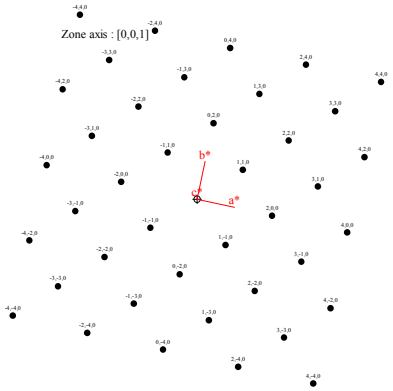

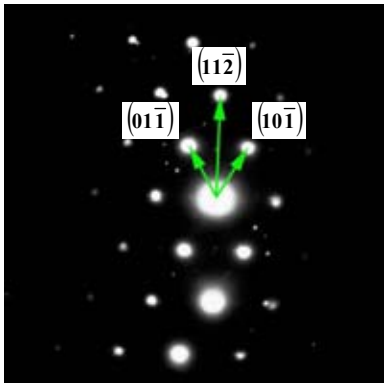

[111]

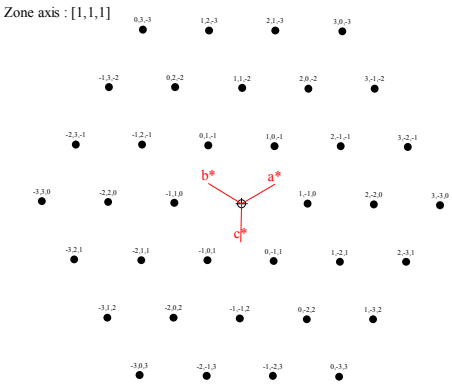

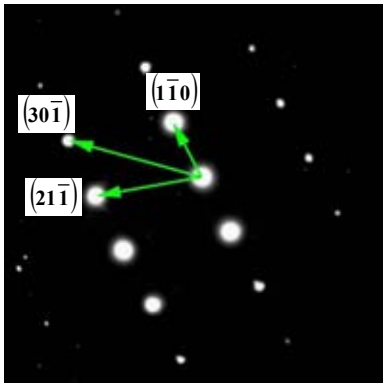

[113]

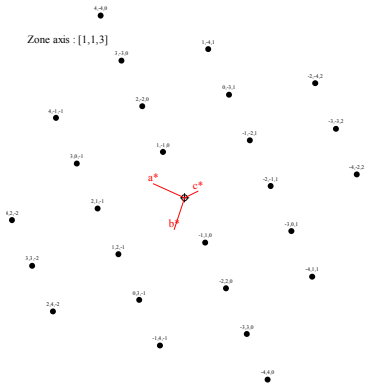

Figure 4.18 Selected area diffraction patterns of the thin dark lamellae – for $Fe_{79.5}C_{3.5}B_{17}$ (alloy 7) – shown in figure 4.17, with corresponding patterns generated by CaRIne Crystallography software. They correspond to a body centred cubic crystal system. The dark lamellae are therefore ferrite-based.

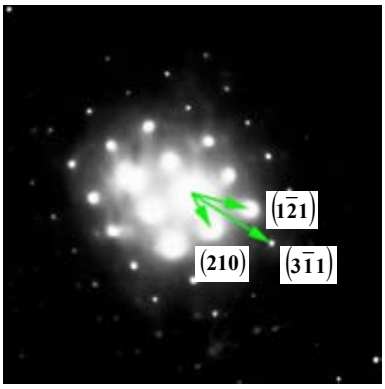

$[\bar{1}25]$

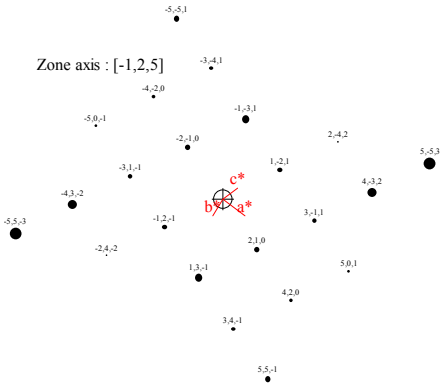

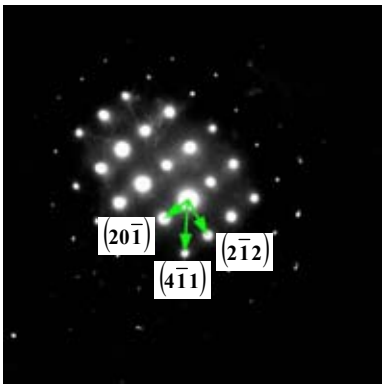

$[162]$

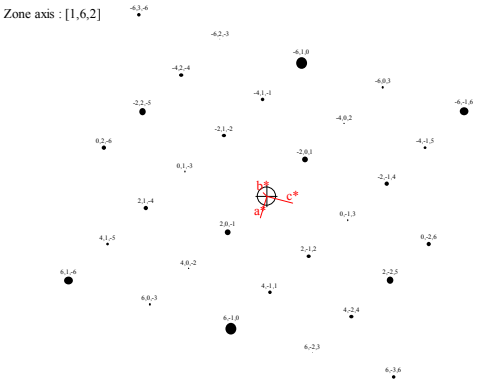

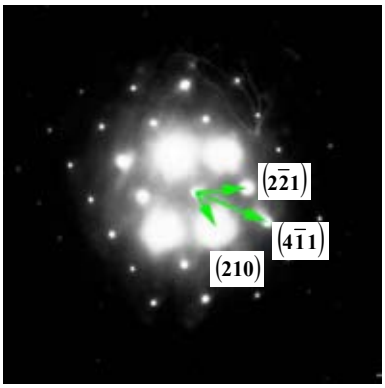

$[\bar{1}26]$

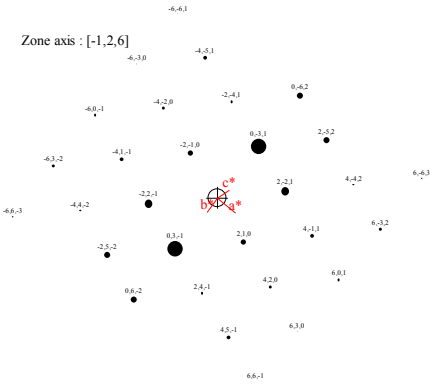

Figure 4.19 Selected area diffraction patterns of the bright lamellae – for $Fe_{79.5}C_{3.5}B_{17}$ (alloy 7) – shown in figure 4.17, with corresponding patterns generated by CaRIne Crystallography software. They correspond to an orthorhombic crystal system. The bright lamellae therefore represent a cementite-like phase, i.e. $Fe_3(C,B)$.

The R ratios of the SADPs in figure 4.18 have good correlation with d ratios taken from the XRD ferrite standard. The measured angles between the spots have good correlation with calculated angle between planes. The calculated SADPs (included in figure 4.18) closely match the experimental ones. It is concluded that the thin dark lamellae in figure 4.17 are ferrite.

The R ratios of the SADPs in figure 4.19 have good correlation with d ratios taken from the calculated $Fe_3(C,B)$ data. The measured angles between the spots have good correlation with calculated angle between planes. The calculated SADPs (included in figure 4.19) closely match the experimental ones. It is concluded that the thick light lamellae in figure 4.16 are orthorhombic $Fe_3(C,B)$.

4.2.6 Differential Scanning Calorimetry (DSC)

4.2.6.1 Alloys with B/Fe Ratio ≥0.19 and Carbon Content >7 Atomic%

For $Fe_{65.7}C_{17.3}B_{17}$ (alloy 9) there is a shallow hump centred at 1135°C and a distinct peak centred at 1200°C (figure 4.20a).

For $Fe_{76.5}C_{7.6}B_{15.9}$ (alloy 3) there are two distinct peaks. The first is centred on 1140°C while the second is centred on 1185°C (figure 4.20b).

4.2.6.2 Alloys B/Fe Ratio ≥0.19 and Carbon Content <7 Atomic%

For $Fe_{79.5}C_{3.5}B_{17}$ (alloy 5) there is a single peak, centred on 1150°C, with a shoulder on its right-hand side (figure 4.20c).

For $Fe_{80.7}C_{3.7}B_{15.6}$ (alloy 2) there appear to be two peaks very close to one another, and centred at 1150°C (figure 4.20d).

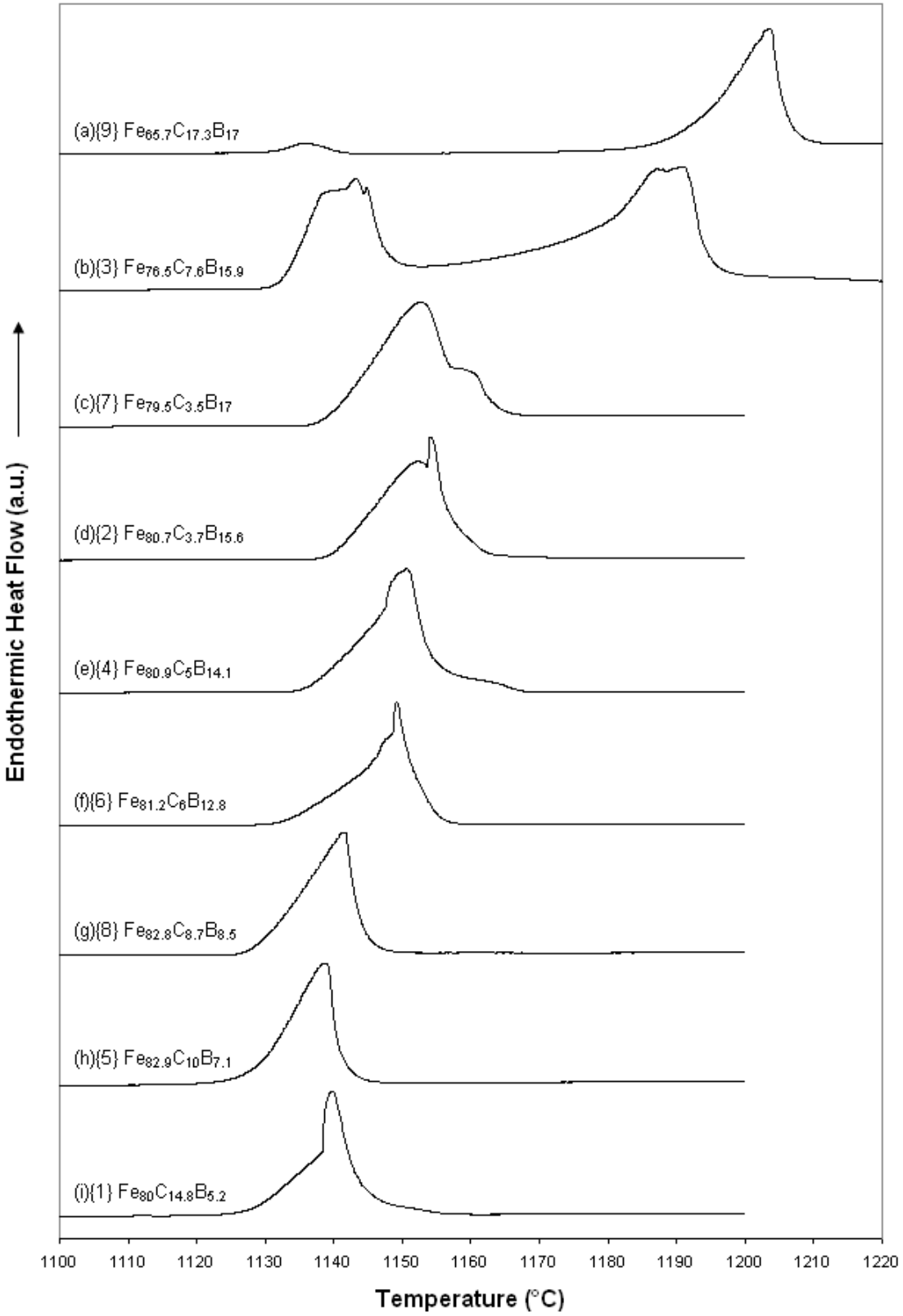

Figure 4.20 DSC traces of as-cast material ({x} = alloy number). In most traces the melting of different phases occur almost simultaneously indicating alloys with compositions close to eutectic. In (a) and (b) there are clearly two separate endothermic events which indicate the alloys are far from a eutectic composition.

4.2.6.3 Alloys B/Fe Ratio <0.19

For $Fe_{80.9}C_5B_{14.1}$ (alloy 4) and $Fe_{81.2}C_6B_{12.8}$ (alloy 6) there is only a single peak in each case, which is centred at 1150°C (figures 4.20e and 4.20f respectively).

For $Fe_{82.8}C_{8.7}B_{8.5}$ (alloy 8), $Fe_{82.9}C_{10}B_{7.1}$ (alloy 5) and $Fe_{80}C_{14.8}B_{5.2}$ (alloy 1) there is again a single in each case, which this time is centred on 1140°C (figures 4.20g – 4.20i respectively).

From the DSC traces in figure 4.20 it can be seen that for each alloy there is a peak at about 1140°C, which corresponds to the melting of austenite.

For $Fe_{65.7}C_{17.3}B_{17}$ (alloy 9) and $Fe_{76.5}C_{7.6}B_{15.9}$ (alloy 3) the first peak represents the melting of austenite only, as for these two alloys there is a second distinct peak at about 1200°C (figures 4.120a and 4.20b). Both alloys melted fully, so the second peak represents the melting of the Fe_2B and $Fe_3(C,B)$ phases where the melting temperatures are so close that they can not be distinguished. On heating $Fe_{65.7}C_{17.3}B_{17}$, austenite forms by dissolution of the lamellae. This alloy is the composition where a residual 2-phase mixture is seen in the cast material (figure 4.1). Consequently only a small amount of austenite is formed during heating of this alloy. For $Fe_{65.7}C_{17.3}B_{17}$ (figure 4.20a) the first peak is very weak, which is the justification for saying the first peak in $Fe_{65.7}C_{17.3}B_{17}$ and $Fe_{76.5}C_{7.6}B_{15.9}$ corresponds to the melting of austenite only.

For the remaining alloys (figures 4.20c to 4.20i), which also melted fully, the single peak at 1140°C corresponds to the simultaneous melting of all phases and therefore indicates that the alloys are much closer to having a ternary eutectic composition. This is supported

by their corresponding optical micrographs (figures 4.4 to 4.10) which show the 2-phase mixture being the majority phase with an area (and presumably volume too) of not less than 66%. The traces for $Fe_{82.8}C_{8.7}B_{8.5}$ (alloy 8) and $Fe_{82.9}C_{10}B_{7.1}$ (alloy 5), shown in figures 4.20g and 4.20h, are particularly smooth indicating the alloy compositions are closest to being ternary eutectic, and this is backed up by their corresponding micrographs (figures 4.8 and 4.9) which show the 2-phase mixture in excess of 90% of the overall area.

4.3 Melt-Spinning

For the ternary alloys in this investigation only short strips or 'flakes' (strips less than one centimetre long) with a thickness of less than 40 microns were produced rather than the long continuous strips of ribbon-like material normally associated with the melt-spinning process. Examples are shown in figure 4.21. The equipment used in this project has previously produced long continuous strips of rapidly solidified material [62,63], so the form of these rapidly solidified alloys is thought to be due to alloy composition and not the production process.

Figure 4.21 Examples of different forms of material both produced using the same melt-spinning equipment. (a) $Fe_{80.9}C_5B_{14.1}$ (alloy 4) and (b) $Zr_{65}Al_{7.5}Cu_{17.5}Ni_{10}$.

4.3.1 X-Ray Analysis

Figure 4.22 shows the XRD traces for the melt-spun alloys. Each trace has some sharp peaks indicating that there is a degree of crystallinity in all alloys. In a repeat of the as-cast XRD results, many of the peaks have similarity with cementite and orthorhombic Fe_3B, so one of the phases is believed to be $Fe_3(C,B)$. There are good matches of some peaks with α-iron, so ferrite is present in most of the ribbons. The remaining peaks have strong correlation with $Fe_{23}(C,B)_6$ which is a metastable phase that can be formed directly from the melt during rapid cooling, or from annealing of amorphous iron-based alloys [134,135,136,137]. It is thought that the B/C ratio within the $Fe_3(C,B)$ and $Fe_{23}(C,B)_6$ phases is different between each alloy composition, and therefore creates small changes in the lattice parameters of the crystals, which is the reason why the peak positions for these phases vary slightly from one trace to another. $Fe_{23}(C,B)_6$ can be seen in all traces apart from figure 4.20i which is for $Fe_{80}C_{14.8}B_{5.2}$ (alloy 1) - the one with the lowest boron content. Only the traces for $Fe_{79.5}C_{3.5}B_{17}$ (alloy 7), $Fe_{80.7}C_{3.7}B_{15.6}$ (alloy 2), $Fe_{80.9}C_5B_{14.1}$ (alloy 4) and $Fe_{81.2}C_6B_{12.8}$ (alloy 6), figures 4.22c to 4.22f respectively, show a broad peak which is representative of an amorphous phase.

$Fe_{79.5}C_{3.5}B_{17}$ (alloy 7), $Fe_{80.9}C_5B_{14.1}$ (alloy 4) and $Fe_{81.2}C_6B_{12.8}$ (alloy 6) – figures 4.22c, 4.22e and 4.22f – are almost fully amorphous as their peaks are pointed rather than rounded. $Fe_{80.7}C_{3.7}B_{17}$ (figure 4.22d) has strong sharp peaks superimposed over the broad peak indicating that the ribbon material is highly crystalline with an amorphous matrix. The trace for $Fe_{81.2}C_6B_{12.8}$ (figure 4.22f) shows an unidentified sharp peak at $2\theta \approx 36°$. It is possible that the peak represents iron oxide, as the strongest diffraction peak for Fe_2O_3 matches this position. However, there are no peaks corresponding to the remaining Fe_2O_3

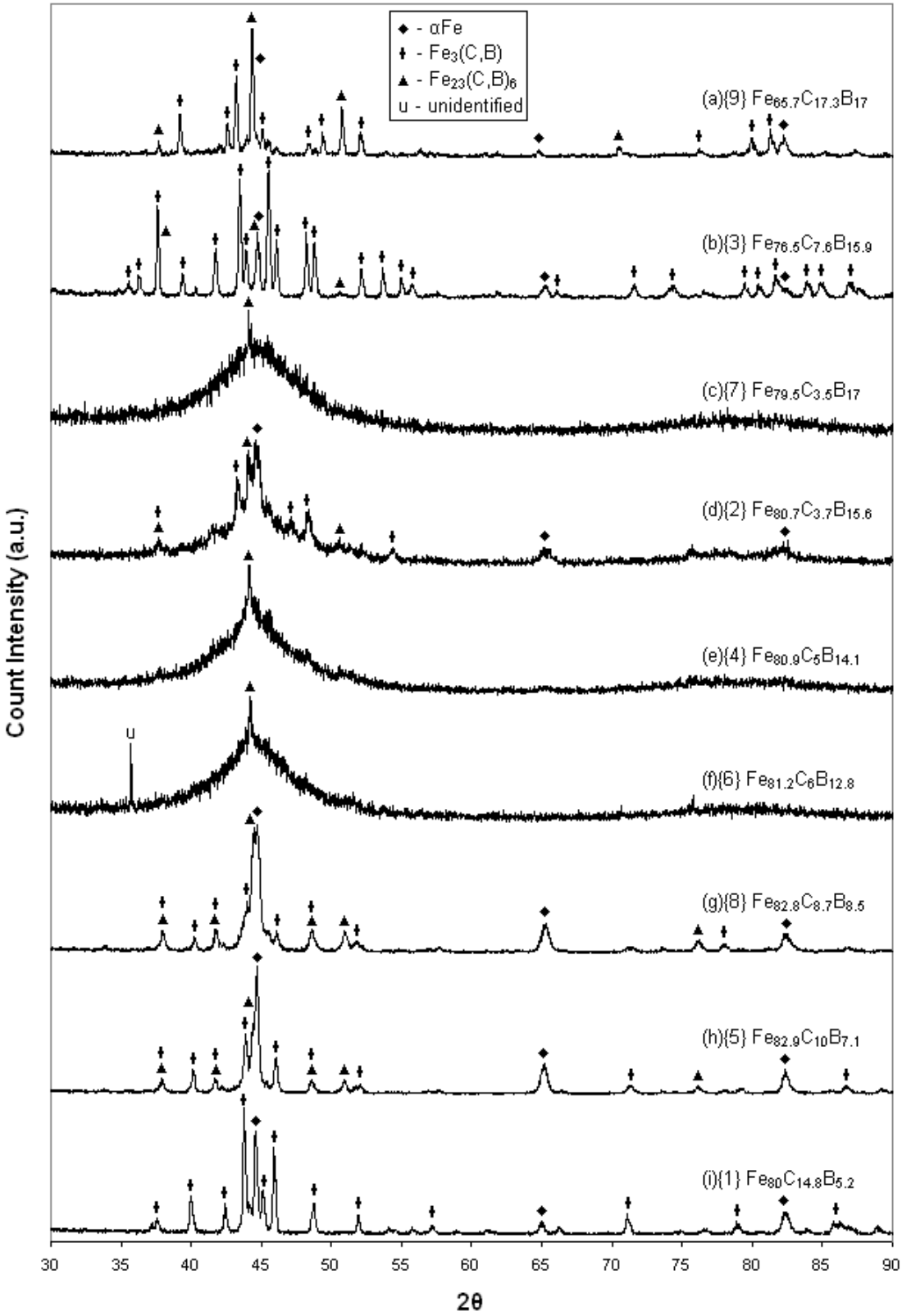

Figure 4.22 XRD traces of melt-spun alloys ({x}= alloy number). (a), (b), (g), (h) and (i) show only sharp narrow peaks, indicating they are fully crystalline. (c), (e) and (f) show a pointed broad peak indicative of an amorphous phase containing some small crystals. (d) shows sharp peaks superimposed on a broad peak. This indicates the material is heavily crystalline with a residual amorphous matrix.

positions, so positive identification of this peak is uncertain. The peaks seen in these four traces are unlikely to be caused by partial recrystallisation from a fully amorphous matrix. Given that the ribbons for the other alloys appear fully crystalline, it is much more likely that the peaks are due to crystals which have nucleated from the melt. It is therefore probably true to say that for all alloys the cooling rate was insufficient to prevent crystal nucleation, but for $Fe_{79.5}C_{3.5}B_{17}$, $Fe_{80.7}C_{3.7}B_{15.6}$, $Fe_{80.9}C_5B_{14.1}$ and $Fe_{81.2}C_6B_{12.8}$ it was good enough to suppress crystal growth to varying degrees of success.

4.3.2 Differential Scanning Calorimetry (DSC)

4.3.2.1 Devitrification

Figure 4.23 shows the low temperature DSC traces for $Fe_{79.5}C_{3.5}B_{17}$ (alloy 7), $Fe_{80.7}C_{3.7}B_{15.6}$ (alloy 2), $Fe_{80.9}C_5B_{14.1}$ (alloy 4) and $Fe_{81.2}C_6B_{12.8}$ (alloy 6) - the alloys where exothermic events (i.e. crystallisation) occurred. The peaks confirm the XRD results (figure 4.23c 4.23f) that an amorphous phase was present. The onset of crystallisation is around 415°C for each alloy. The glass transition is not apparent in any of the traces. This is not a complete surprise as the absence of T_g has been noted in Al-, Mg- and Fe- based systems [138,139,140]. An explanation of why this happens concerns the methods by which a metallic glass can be formed:

Under nucleation control, a fully amorphous alloy is formed if the cooling rate is rapid enough to completely bypass the onset of crystallisation of all possible stable and metastable phases. Upon reheating the formation of critical nuclei is suppressed while viscosity remains high (and diffusivity is limited), so T_g is detectable.

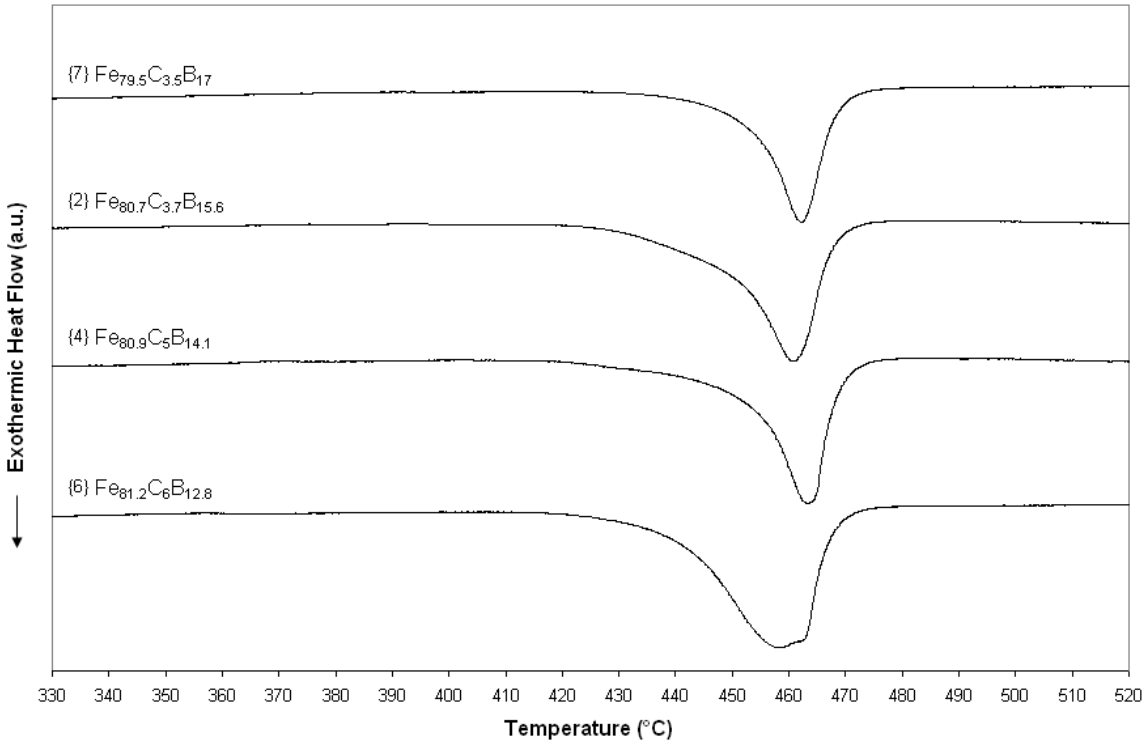

Figure 4.23 DSC traces for the melt-spun alloys which exhibit exothermic events ({x} = alloy number). A single crystallisation peak in each of the alloys shows an amorphous phase was produced. There is no apparent glass transition. The traces for the remaining alloys are not shown as they do not exhibit any exothermic events, indicating they are fully crystalline.

Under growth control the cooling rate is not sufficient to bypass nucleation, resulting in the formation of crystallites which are constrained from growing due to increasing viscosity caused by the rapid cooling. Upon reheating the quenched-in nuclei are able to grow rapidly at T_g, so T_x and T_g effectively coincide [114].

$Fe_{65.7}C_{17.3}B_{17}$ (alloy 9), $Fe_{76.5}C_{7.6}B_{15.9}$ (alloy3), $Fe_{82.8}C_{8.7}B_{8.5}$ (alloy 8), $Fe_{82.9}C_{10}B_{7.1}$ (alloy 5) and $Fe_{80}C_{14.8}B_{5.2}$ (alloy 1) did not exhibit any exothermic events, which means they do not contain an amorphous phase, and confirms the XRD results that the ribbons are fully crystalline.

From these and the XRD results it can be concluded that for all the alloys the cooling rate provided by the melt-spinning process was insufficient to bypass nucleation of crystalline phases.

4.3.2.2 Melting

4.3.2.2.1 Alloys with B/Fe Ratio ≥0.19 and Carbon Content >7 Atomic%

For $Fe_{65.7}C_{17.3}B_{17}$ (alloy 9) there is a small disturbance in the trace at 1145°C and a distinct peak centred at 1190°C (figure 4.24a).

For $Fe_{76.5}C_{7.6}B_{15.9}$ (alloy 3) there are two distinct peaks. The first is centred on 1145°C while the second smaller peak is centred on 1170°C (figure 4.24b).

4.3.2.2.2 Alloys with B/Fe Ratio ≥0.19 and Carbon Content <7 Atomic%

For $Fe_{79.5}C_{3.5}B_{17}$ (alloy 7) there are two peaks close to one another. The first is centred on 1150°C while the second is centred at 1160°C (figure 4.24c).

For $Fe_{80.7}C_{3.7}B_{15.6}$ (alloy 2) there are again two peaks very close to one another. The first is centred on 1150°C while the second is centred at 1155°C (figure 4.24d).

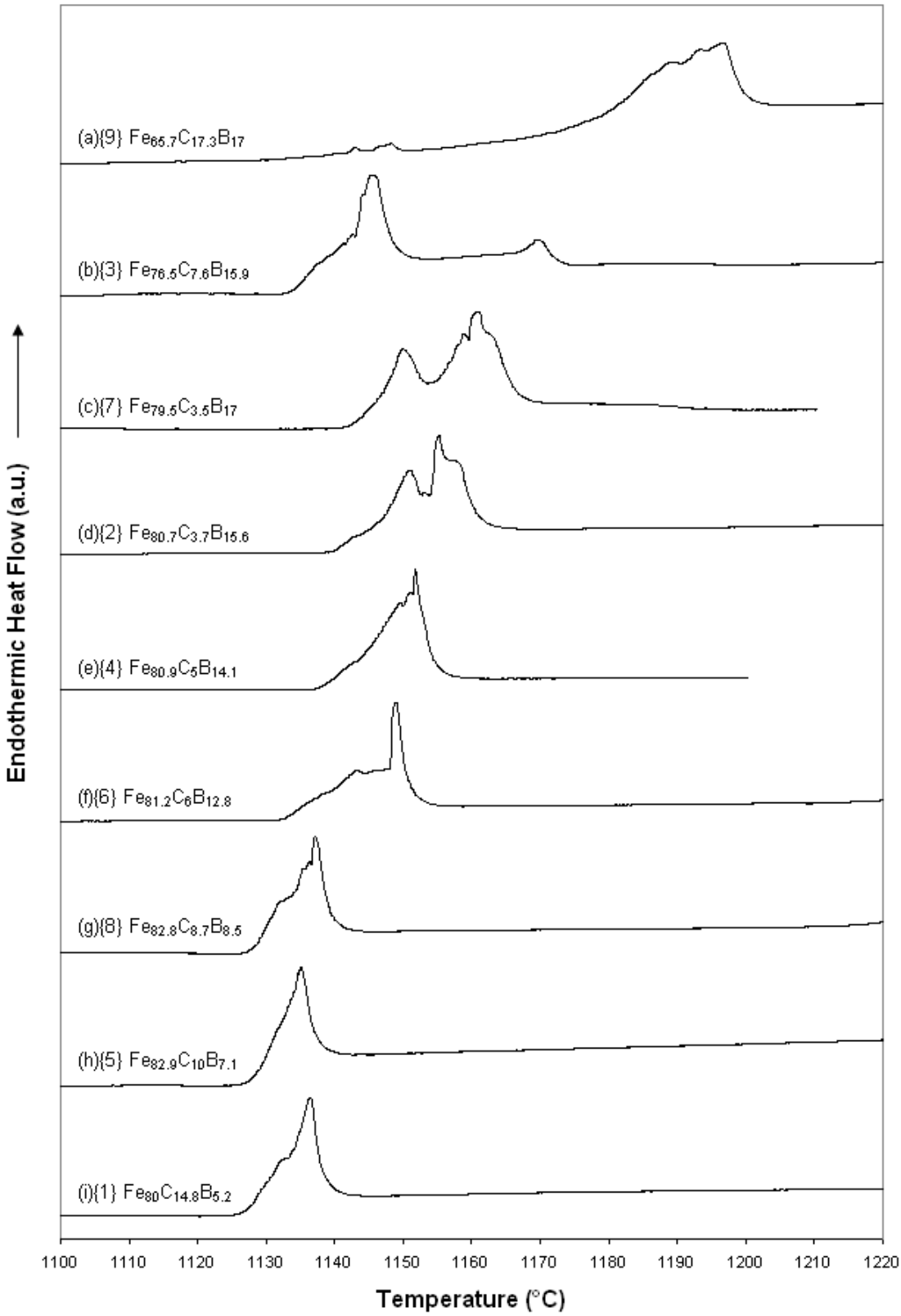

Figure 4.24 DSC traces of melt-spun material ({x} = alloy number). Compared to the as-cast material (figure 4.20) the melting behaviour is the almost the same. The only differences are in (b) where the melting range is narrower and in (c) and (d) where there is clearer separation of the higher temperature peaks.

4.3.2.2.3 Alloys with B/Fe Ratio <0.19

For $Fe_{80.9}C_5B_{14.1}$ (alloy 4) there is a single peak centred on 1150°C (figure 4.24e).

For $Fe_{81.2}C_6B_{12.8}$ (alloy 6) there is a single peak, with a rather broad shoulder situated on its left-hand side, centred at 1145°C (figure 4.24f).

For $Fe_{82.8}C_{8.7}B_{8.5}$ (alloy 8), $Fe_{82.9}C_{10}B_{7.1}$ (alloy 5) and $Fe_{80}C_{14.8}B_{5.2}$ (alloy 1) – figures 4.24g to 4.24i respectively – there is again a single peak in each case, which is centred on 1135°C.

It can be seen that each peak has an irregular profile and it is thought that this is due to the use of multiple ribbon pieces in the DSC studies. It is believed that there is poor thermal contact between the pieces of ribbon, and between the ribbon and crucibles, which leads to uneven heat flow and consequently to perturbations in the heat flow signal. Also as each ribbon piece enters the semi-molten state it is able to move to a certain degree and therefore causes further disruptions.

In figures 4.24c and 4.24d – for $Fe_{79.5}C_{3.5}B_{17}$ (alloy 7) and $Fe_{80.7}C_{3.7}B_{15.6}$ (alloy 2) respectively – there are two peaks merging in each trace. This is a clearer separation of the peaks seen in figures 4.20c and 4.20d and is thought to be due to a reduction in thermal lag (response time of DSC sensor) caused be reduction in the mass used for DSC analysis (≈9mg for ribbons and 30mg for as-cast material).

When the melt-spun and as-cast DSC traces are compared it can be seen that, within the limits of acceptable experimental error, the onset of melting and the liquidus temperatures are in close agreement with one another. This indicates that the final crystallisation

products of the melt-spun ribbons are the same as those in the as-cast ingots. There is one exception (figure 4.24b) to the agreement between melt-spun and as-cast results and this is found in $Fe_{76.5}C_{7.6}B_{15.9}$ (alloy 3). For this alloy there is difference in T_l of over 20°C. The reason for this is currently not known. A possible explanation is that the ribbon composition was not homogeneous. Therefore the final crystallisation products may have had small changes in composition, particularly with respect to B/C ratio in the $Fe_3(C,B)$ phase, consequently leading to changes in the melting temperature of those phases.

4.4 Discussion

In principle any alloy can be vitrified if the rate of cooling is rapid enough to suppress the nucleation and/or growth of crystals or quasi-crystals. In practice the glass-forming ranges of alloys are limited due to the extremely high cooling rates needed to hinder the long range diffusion that is required for crystal formation. The development of amorphous alloys therefore depends on the selection of compositions which inhibit diffusion and thus enable vitrification at practically obtainable cooling rates.

In the following paragraphs the results presented in this chapter will be used to describe the solidification behaviour of the iron-rich portion of the Fe-B-C system. The alpha-parameter predictive model for glass forming systems will be discussed with respect to the Fe-C-B system. Finally, the glass forming ability of the Fe-B-C system will be discussed.

4.4.1 Solidification Sequences

4.4.1.1 Transformation During Slow Cooling of the Melt

The master ingots used for experiments were fabricated by arc-melting. The basic process uses a plasma arc to melt the alloy components together in a water-cooled copper hearth. This means that solidification of ingots takes place under non-equilibrium conditions, so it should be noted that the microstructures and the relative proportions of the phases are not necessarily the same as those obtained by equilibrium cooling. The optical images were taken from the centre of the cross-section of each ingot where cooling rate would have been slower than where the melt was in contact with the hearth, or exposed to the argon atmosphere, so the features should be closer to the equilibrium microstructures.

The nine alloys can be grouped into four basic sets of microstructure. Set 1: alloys with a faceted phase plus bright dendrites containing precipitates ($Fe_{65.7}C_{17.3}B_{17}$, $Fe_{76.5}C_{7.6}B_{15.9}$ and $Fe_{79.5}C_{3.5}B_{17}$). Set 2: alloys with bright dendrites containing precipitates, but no faceted phase ($Fe_{80.7}C_{3.7}B_{15.6}$, $Fe_{80.9}C_5B_{14.1}$and $Fe_{81.2}C_6B_{12.8}$). Set 3: the alloy with angular dendrites ($Fe_{76.5}C_{7.6}B_{15.9}$). Set 4: alloys with dendrites consisting of a two-phase fine plate-like structure ($Fe_{82.2}C_{8.7}B_{8.5}$ and $Fe_{82.9}C_{10}B_{7.1}$).

Figure 4.25 shows each of the compositions plotted on the Fe-B-C liquidus projection by Vogel and Tammann [125,129]. In most cases it can be seen that the observed microstructure is in agreement with one of the ranges defined by the initial solidification product. Set 1 falls into the Fe_2B range, set 3 into the Fe_3C range, and set 4 into the austenite range. Set 2 is the exception. The primary solidification product is believed to be $Fe_3(C,B)$ but the alloys fall within the iron boride range rather than the cementite range.

This discrepancy could be rectified if the liquidus projection is amended (as indicated by the orange lines) to take into account the fact that the iron-boron eutectic is at 83% iron [131] rather than the 85% as shown.

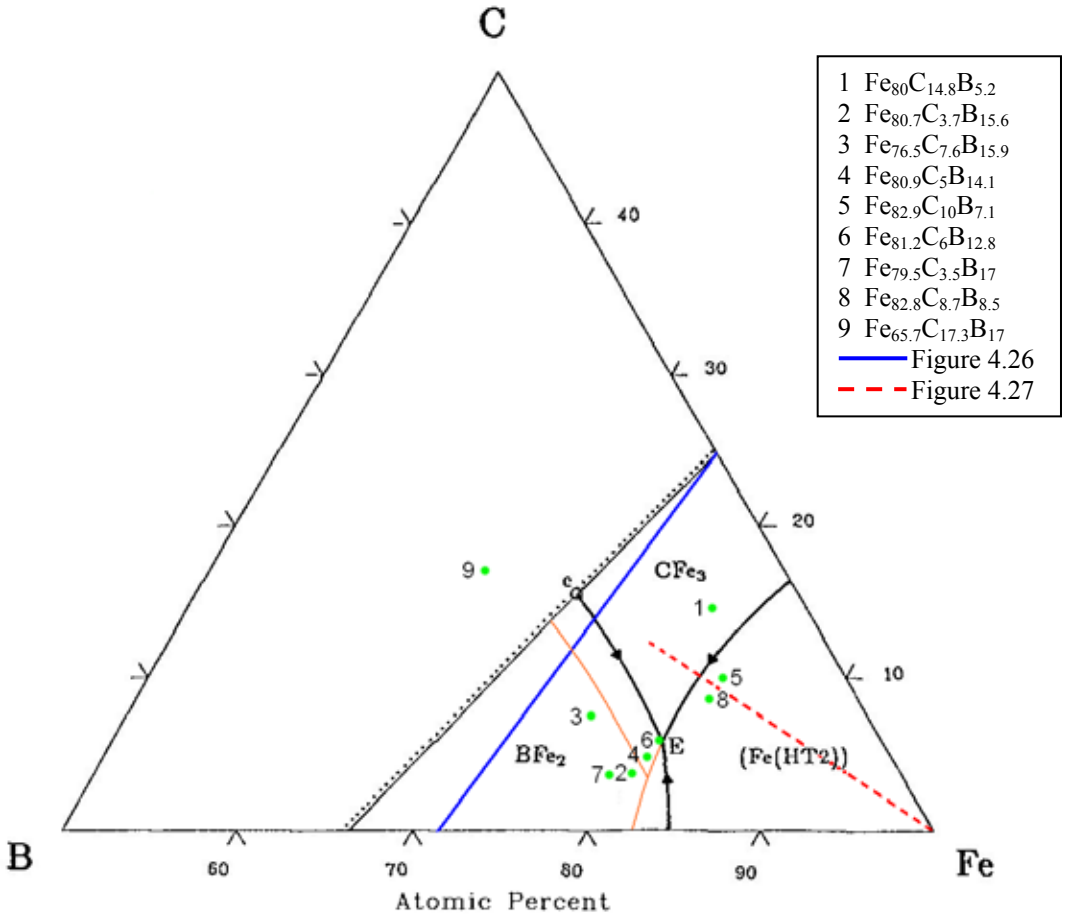

Figure 4.25 Liquidus projection showing position of the alloy compositions. The orange lines represent an amendment to the eutectic valleys which could be used to explain the apparent solidification sequences of the as-cast alloys.

A blue line is drawn on figure 4.25 and this marks the range of the isopleth shown in figure 4.26. The isopleth does not contain any of the alloy compositions but it can be used as a guide to the solidification sequence of sets 1, 2 and 3. It is also assumed that wherever Fe_3C is marked it is actually $Fe_3(B,C)$ rather than pure cementite, which is certainly the case for the alloys as the SIMS results show there is some boron present in the dendrites of all the alloys in this study.

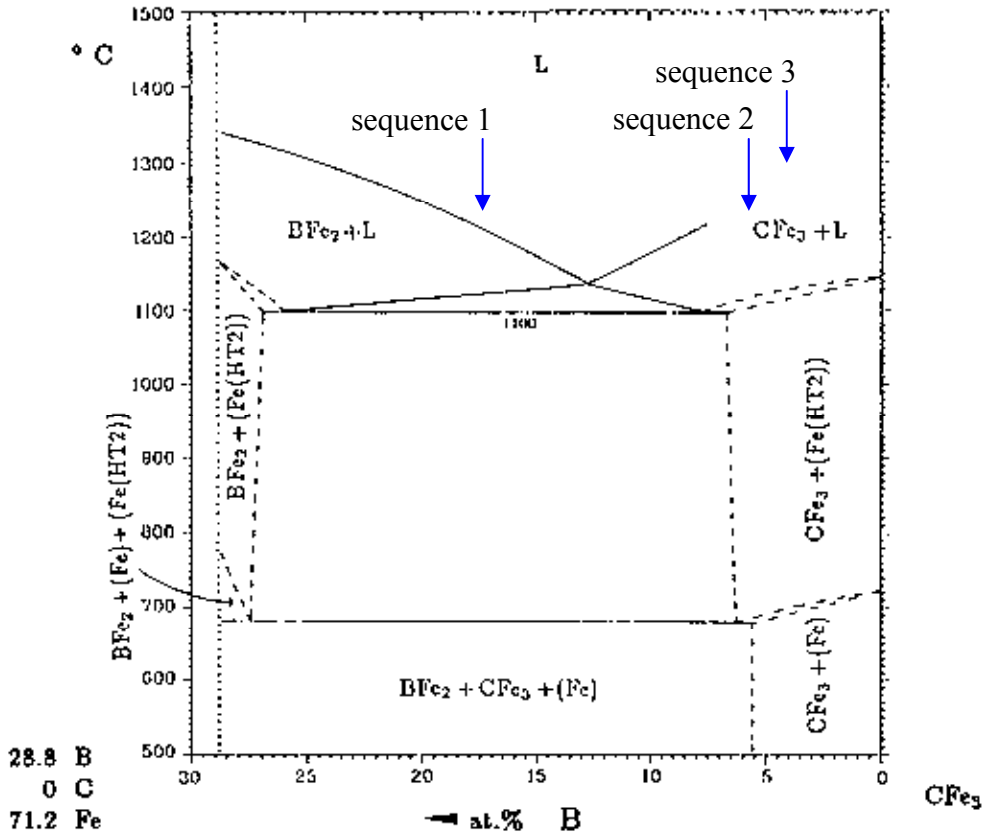

Figure 4.26 Isopleth (a section represented by the blue line in figure 4.25) of the B-C-Fe system [125]. It does not contain the compositions in this study but can be used as a guide to the solidification sequences for compositions other than $Fe_{82.9}C_{10}B_{7.1}$ and $Fe_{82.8}C_{8.7}B_{8.5}$ (alloys 5 and 8 respectively) where austenite is the primary solidification product.

Sequence 1 (for alloys with a faceted phase):

The first phase to form is the faceted iron boride. This provides nucleation sites for the next phase: primary $Fe_3(C,B)'$. The remaining liquid transforms to austenite, which then undergoes the eutectoid decomposition to ferrite and secondary $Fe_3(C,B)''$. At this temperature it is believed that the primary $Fe(C,B)'$ is no longer able to accommodate as much boron, so secondary Fe_2B'' forms as precipitates within the $Fe_3(C,B)'$ dendrites.

$$L \rightarrow Fe_2B + L \rightarrow$$

$$Fe_2B + Fe_3(B,C)' + L \rightarrow$$

$$Fe_2B + Fe_3(B,C)' + \gamma Fe \rightarrow$$

$$Fe_2B + Fe_3(B,C)' + Fe_2B'' + \alpha Fe + Fe_3(B,C)''$$

Sequence 2 (for alloys with dendrites containing precipitates):

The first phase to form is primary $Fe_3(C,B)'$. The remaining liquid transforms to austenite, which later undergoes eutectoid decomposition to ferrite plus secondary $Fe_3(C,B)''$. At this temperature it is believed that the primary $Fe(C,B)'$ is no longer able to accommodate as much boron, so Fe_2B forms as precipitates within the $Fe_3(C,B)'$ dendrites.

$$L \rightarrow Fe_3(B,C)' + L \rightarrow$$

$$Fe_3(B,C)' + \gamma Fe \rightarrow$$

$$Fe_3(B,C)' + Fe_2B + \alpha Fe + Fe_3(B,C)''$$

Sequence 3 (for alloys with angular dendrites):

The first phase to form is primary $Fe_3(C,B)'$. The remaining liquid transforms to austenite, which later undergoes eutectoid decomposition to ferrite plus secondary $Fe_3(C,B)''$.

$$L \rightarrow Fe_3(B,C)' + L \rightarrow$$

$$Fe_3(B,C)' + \gamma Fe \rightarrow$$

$$Fe_3(B,C)' + \alpha Fe + Fe_3(B,C)''$$

Sequence 4 (for alloys with dendrites containing plate-like features):

The first phase to form is austenite (γFe'). The remaining liquid then transforms to secondary austenite (γFe'') which has a different composition to the primary austenite. Both the austenite phases undergo eutectoid decomposition to ferrite and $Fe_3(C,B)$.

$$L \rightarrow \gamma Fe' + L \rightarrow$$

$$\gamma Fe' + \gamma Fe'' \rightarrow$$

$$\alpha Fe + Fe_3(B,C) + \alpha Fe'' + Fe_3(B,C)''$$

This sequence is the same as for steels with a eutectoid composition. However, the compositions of the alloys which follow this sequence have carbon content 8.7-10 atomic% which are far in excess of the binary eutectoid carbon content. Boron can be considered an austenite stabiliser, as austenite is one of the phases seen between 912°C and 1394°C in the iron rich portion of the binary Fe-B system. It is proposed that a speculative isopleth (figure 4.27) which could explain this solidification sequence would be based on the Fe-Fe_3C phase diagram in which boron has caused a large expansion of the austenite phase field.

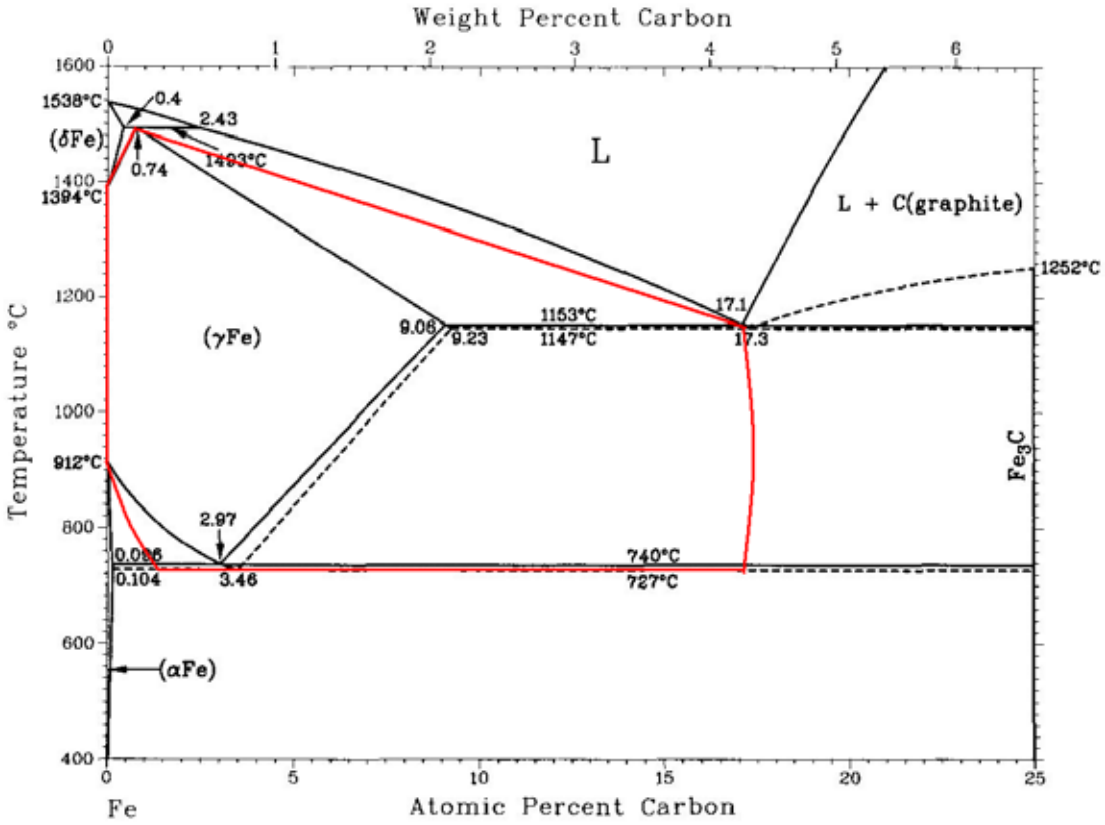

Figure 4.27 This is a speculative section of the B-C-Fe system represented by the dashed red line in figure 4.25 based on the iron-cementite phase diagram [130]. It is suggested that the austenite phase field is vastly expanded (depicted by solid red line) for metalloid content up to 17-19 atomic percent where the carbon to boron ratio is approximately 1:1. This could be an explanation for solidification sequence 4.

4.4.1.2 Transformation During Rapid Cooling of the Melt

From the XRD results it can be seen that $Fe_{23}(C,B)_6$ is present in all alloys except $Fe_{80}C_{14.8}B_{5.2}$. This shows that during rapid cooling the alloys follow different solidification paths to those from when they are cooled slowly. It is proposed that there are four sequences which are as follows:

Sequence 5:

This applies to $Fe_{65.7}C_{17.3}B_{17}$, $Fe_{76.5}C_{7.6}B_{15.9}$, $Fe_{82.8}C_{8.7}B_{8.5}$ and $Fe_{82.9}C_{10}B_{7.1}$. The first phase to nucleate is $Fe_{23}(C,B)_6$ followed by austenite. The austenite then undergoes eutectoidal decomposition to $Fe_3(C,B)$ and ferrite.

$$L \rightarrow Fe_{23}(C,B)_6 + L \rightarrow$$

$$Fe_{23}(C,B)_6 + \gamma Fe \rightarrow$$

$$Fe_{23}(C,B)_6 + \alpha Fe + Fe_3(C,B)$$

Sequence 6:

This applies to $Fe_{79.5}C_{3.5}B_{17}$, $Fe_{80.9}C_5B_{14.1}$ and $Fe_{81.2}C_6B_{12.8}$. $Fe_{23}(C,B)_6$ nucleates then the remaining liquid becomes locked into the amorphous state.

$$L \rightarrow Fe_{23}(C,B)_6 + L \rightarrow$$

$$Fe_{23}(C,B)_6 + amorphous$$

Sequence 7:

This applies to $Fe_{80.7}C_{3.7}B_{15.6}$. The first phase to nucleate is $Fe_{23}(C,B)_6$. The second phase to nucleate is austenite, but the cooling rate is sufficient to prevent crystallisation going to completion so the remaining liquid becomes locked in the amorphous state. Finally the austenite undergoes eutectoidal decomposition to $Fe_3(C,B)$ and ferrite

$$L \rightarrow Fe_{23}(C,B)_6 + L \rightarrow$$

$$Fe_{23}(C,B)_6 + \gamma Fe + amorphous \rightarrow$$

$$Fe_{23}(C,B)_6 + \alpha Fe + Fe_3(C,B) + amorphous$$

Sequence 8:

This applies to $Fe_{80}C_{14.8}B_{5.2}$. This is the alloy with the lowest boron content and it is believed the melt-spun solidification sequence is the same as the as-cast solidification sequence, so the first phase to form is primary $Fe_3(C,B)$. The remaining liquid transforms to austenite, which later undergoes eutectoid decomposition to ferrite plus secondary $Fe_3(C,B)$.

$$L \rightarrow Fe_3(B,C)' + L \rightarrow$$

$$Fe_3(B,C)' + \gamma Fe \rightarrow$$

$$Fe_3(B,C)' + \alpha Fe + Fe_3(B,C)''$$

Table 4.2 shows a summary of which solidification sequence each alloy follows under slow and rapid cooling.

Table 4.2 A summary of the solidification sequences for slow and rapidly solidified alloys.

	Arc-Melted				**Melt-Spun**			
Alloy	**1**	**2**	**3**	**4**	**5**	**6**	**7**	**8**
(1) $Fe_{80}C_{14.8}B_{5.2}$			X					X
(2) $Fe_{80.7}C_{3.7}B_{15.6}$	X						X	
(3) $Fe_{76.5}C_{7.6}B_{15.9}$	X				X			
(4) $Fe_{80.9}C_{5}B_{14.1}$		X				X		
(5) $Fe_{82.9}C_{10}B_{7.1}$				X	X			
(6) $Fe_{81.2}C_{6}B_{12.8}$		X				X		
(7) $Fe_{79.5}C_{3.5}B_{17}$	X					X		
(8) $Fe_{82.8}C_{8.7}B_{8.5}$				X	X			
(9) $Fe_{65.7}C_{17.3}B_{17}$	X				X			

4.4.2 Predicting GFA

4.4.2.1 Observation of As-Cast Microstructure

One of the earliest discoveries in the search for glass forming alloys was the result that vitrification of the melt is more easily obtainable if the alloy is of the eutectic composition of that system. It was later shown that the glass forming range of a system does not necessarily have to include the actual eutectic composition. In this study it would appear that none of the alloys are of eutectic composition, even though some of them were taken from the invariant points of published metastable liquidus projections.

As a means for estimating whether or not a particular alloy is able to form a glass phase, the quantity of 2-phase mixture observed in the as-cast starting material is only partially helpful. It might be expected that the greater the amount of 2-phase mixture, then the more likely it is that the alloy can be more easily vitrified. This is not the case for this study. As might be expected, the alloys with the largest quantity of dendrites in their microstructures did not form a glassy phase. However, the alloys which were closest to consisting mainly of an apparent eutectic microstructure (i.e. those where the 2-phase mixture was approximately 90%) did not form a glassy phase. The alloys which did form a glassy phase had a 2-phase matrix between 60-80 area%. This result supports the findings that the best glass forming compositions can be off-eutectic. However, even this range for the amount of 2-phase mixture visible in the as-cast material cannot be used to predict which alloy compositions will form a glass on quenching from the melt, as $Fe_{80}C_{14.8}B_{5.2}$ (alloy 1) had an apparent eutectic matrix of 68% and was fully crystalline after melt-spinning.

4.4.2.2 The Alpha (α) Parameter

One of the problems in designing amorphous systems is that an alloy's GFA is characterised by various combinations of its thermodynamic or physical properties. This requires the alloy be made first and so can not be used as a predictive tool. The term *glass forming ability* is slightly misleading and perhaps would be better referred to as glass performance ability. Even by studying the microstructure of alloys before they undergo a rapid solidification procedure requires that the alloys be made first. In each case this may be acceptable if only a few compositions are to be made, but when a wide range of compositions are used the cost can become prohibitive in both time and materials. Cheney and Vecchio developed the alpha parameter [124] as a true GFA indicator – a method to predict the likelihood of a particular alloy to form a glass without having to actually make the alloy. The alpha values for the ternary alloys in this study range from 1.36 to 1.578 and are listed in table 4.3. The predicted liquidus temperatures used in determining α were calculated with ThermoCalc version Q software using the TCFE2 database. This is a steels database and as such the values obtained should be regarded with a degree of uncertainty given that the boron should only be used in trace amounts while carbon should be no more than 2 weight% (8.7 atomic% for binary Fe-C).

For an alloy to have good GFA the value of α should be greater than 1.5. From table 4.3 it can be seen that the highest α value of 1.578 is for $Fe_{80}C_{14.8}B_{5.2}$ which would indicate this composition should be the one most easily vitrified. From the XRD trace in figure 4.22 it is clear that an amorphous phase was not produced by the melt-spinning process. Considering all the other alloys have an α value of approximately 1.4 one could conclude that the ThermoCalc software has given an erroneous result for this particular alloy. However,

Table 4.3 The alpha values for the alloys in this study. The calculated liquidus was determined using ThermoCalc version Q with the TCFE2 database.

Alloy	Weighted Liquidus (K)	Calculated Liquidus (K)	α
(9) $Fe_{65.7}C_{17.3}B_{17}$	2266	1592	1.423
(3) $Fe_{76.5}C_{7.6}B_{15.9}$	2064	1419	1.455
(7) $Fe_{79.5}C_{3.5}B_{17}$	1987	1461	1.360
(2) $Fe_{80.7}C_{3.7}B_{15.6}$	1983	1426	1.391
(4) $Fe_{80.9}C_{5}B_{14.1}$	2000	1388	1.441
(6) $Fe_{81.2}C_{6}B_{12.8}$	2011	1403	1.433
(8) $Fe_{82.85}C_{8.65}B_{8.5}$	2037	1458	1.397
(5) $Fe_{82.9}C_{10}B_{7.1}$	2055	1457	1.410
(1) $Fe_{80}C_{14.8}B_{5.2}$	2140	1356	1.578

$Fe_{80}C_{14.8}B_{5.2}$ (alloy 1) is close to being the base composition of the DARVA type 1 iron-based bulk metallic glasses. In these alloys carbon content is 15 or 16 atomic% and boron content is 6 or 7 atomic%. The experimentally determined liquidus temperatures for these compositions do not vary greatly and are approximately 1350 K (1080 ± 10°C) [141] while the predicted liquidus for $Fe_{80}C_{14.8}B_{5.2}$ is 1356 K. It is likely then that the high α value for $Fe_{80}C_{14.8}B_{5.2}$ is correct. This leads to the assumption that liquidus temperatures predicted by ThermoCalc for the iron rich portion of the Fe-C-B system are realistic values, even though the solute atoms are greatly in excess of the recommended maximum amounts.

It should be noted that α only indicates how likely it is that an alloy can form a glass, not that it will, as factors other than the relative depth of the eutectic also affect GFA. In support of this it should also be noted that $Fe_{79.5}C_{3.5}B_{17}$ (alloy 7) had the lowest value for α (1.36) yet still produced an amorphous phase after melt-spinning. In the Nd-Fe-Al-(Y) system the composition with the highest casting diameter has an alpha value of 1.34 [124]. It has also been shown that in the $Fe_{67-x}C_{10}B_9Mo_{7+x}Cr_4W_3$ system the glass forming range is from x=8-14, with α increasing from 1.55 to 1.65, but when x=0-8, α ranges from 1.55 to 1.67 the system is unable to form a glass [137]. It is clear that although the α parameter can be used for some systems, it is unable to predict the glass forming compositions in the Fe-C-B system.

4.4.3 Glass Formation in the Fe-C-B System

The melt spinning process is thought to give a cooling rate of approximately 10^5 °Cs^{-1}. This depends not only on the angular velocity of the wheel but also on the gas pressure used to eject the melt from the crucible onto the wheel. A higher wheel speed and optimisation of the gas ejection pressure used in this study would have produced a higher cooling rate. However, further experiments with different processing parameters were not carried out, as one of the aims in developing amorphous alloys by cooling the melt is the reduction of the cooling rate in order to allow production in bulk form.

None of the ternary alloys formed fully amorphous ribbons after melt-spinning. The XRD results show that there were varying degrees of crystallinity between each alloy, ranging from fully crystalline (multiple sharp diffraction peaks) to highly amorphous (broad peaks with small spikes). It is clear that, due to the processing parameters used, the cooling rate was insufficient to prevent nucleation of crystals from the melt. During the production runs the temperature of the melt could not be measured and could only be gauged to be in the same range by visual inspection. If, in each case, the melt has been heated too far above the liquidus temperature of a composition then this could be an additional factor in the inability to form an amorphous phase.

Regardless of the processing conditions, an amorphous phase was produced in $Fe_{79.5}C_{3.5}B_{17}$ (alloy 7), $Fe_{80.7}C_{3.7}B_{15.6}$ (alloy 2), $Fe_{80.9}C_5B_{14.1}$ (alloy 4) and $Fe_{81.2}C_6B_{12.8}$ (alloy 6). A possible reason for this success could be an extension of the idea of competitive formation [142]. This theory is really a restatement of the commonly accepted idea of glass formation through growth control and is usually described with reference to binary systems. It allows

for nucleation of a primary phase provided that cooling rate is sufficient to bypass the formation of the eutectic phase, and results in a composite material of crystallites in an amorphous matrix.

Applied to ternary or larger systems this means that multiple phases are possible provided the cooling rate is sufficient to bypass nucleation of the eutectic phase and prevent growth of any crystals. This is represented in the stylised TTT diagram shown in figure 4.28. In the diagram the blue line represents the cooling curve for nucleation control as it misses all the possible phases. The red line represents the cooling curve for growth control. It completely bypasses the onset curves for α and β phases and if these were the only phases a glass would be formed through nucleation control. However, the cooling curve just passes through the onset curves for a metastable (m) and γ phase but remains far from the corresponding completion curves. So, although nucleation of two phases occurs, growth is suppressed, as both phases are competing for resources in an environment where viscosity is increasing and diffusivity is decreasing.

The four alloys which formed an amorphous phase are close to a eutectic composition. Rapid solidification of these alloys provides a cooling rate sufficient to bypass the nucleation of either of the primary phases – Fe_2B and $Fe_3(C,B)$ – and allows formation of other phases such as $Fe_{23}(C,B)_6$ and austenite (which would later decompose to ferrite and $Fe_3(C,B)$). It is proposed that the competition between a metastable phase and austenite, rather than iron boride and cementite, helps stabilise the melt thus allowing formation of a glassy phase on continued cooling.

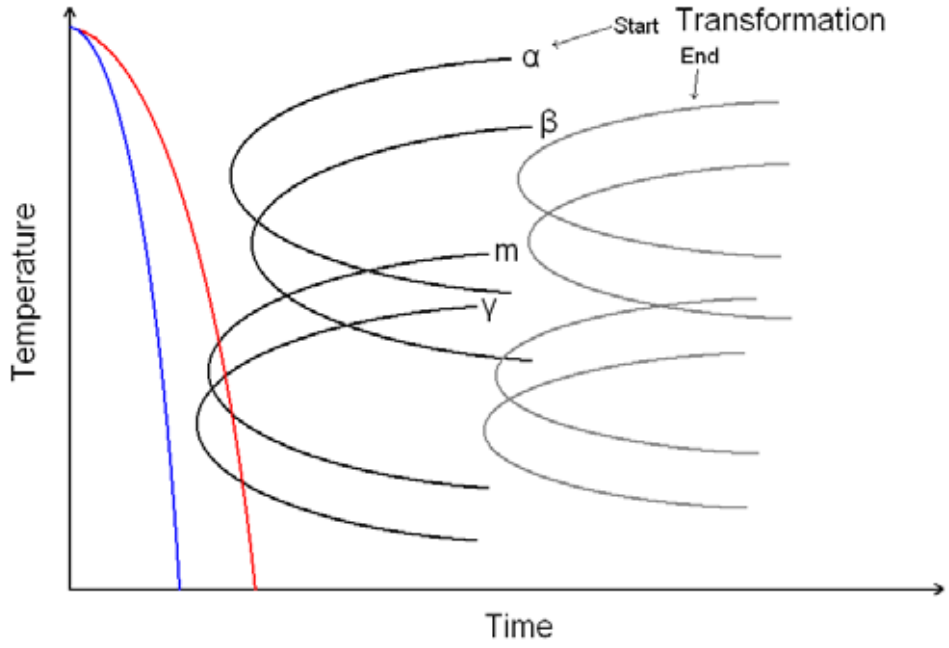

Figure 4.28 A stylised TTT diagram. α, β, γ and *m* are possible phases in a system. The blue line represents the cooling rate necessary for nucleation control while the red line represents growth control. In this diagram the red line indicates that the *m* and γ phases would be competing for resources in an environment where viscosity is increasing and diffusivity is decreasing, thus keeping the remaining liquid stable until it becomes locked in the amorphous state.

CHAPTER 5

DEVELOPMENT

OF MULTI-COMPONENT

IRON-BASED AMORPHOUS ALLOY

5.1 Introduction

In the previous chapter the glass forming ability of the Fe-C-B system was investigated. Of the ternary compositions only $Fe_{79.5}C_{3.5}B_{17}$ (alloy 7), $Fe_{80.7}C_{3.7}B_{15.6}$ (alloy 2), $Fe_{80.9}C_5B_{14.1}$ (alloy 4) and $Fe_{81.2}C_6B_{12.8}$ (alloy 6) produced an amorphous phase after melt-spinning. From the XRD results (figure 4.22c - 4.22f) it can be seen that $Fe_{79.5}C_{3.5}B_{17}$ and $Fe_{80.9}C_5B_{14.1}$ have the smoothest traces. There is only a single broad peak in each case. Both peaks are pointed rather than rounded which shows that there are crystallites present in both materials. To select the composition to be used as the base alloy for developing a multi-component system, various thermal parameters of the two compositions were

compared. These are shown in table 5.1. For all parameters the higher the value the better is the GFA, the exception being the liquidus temperature, where a lower value would imply better GFA through more efficient heat extraction. In all cases the parameters show that $Fe_{80.9}C_5B_{14.1}$ has the best GFA and is therefore the composition most suitable for use as a base alloy.

Table 5.1 Thermal parameters for $Fe_{79.5}C_{3.5}B_{17}$ and $Fe_{80.9}C_5B_{14.1}$. T_{rg}, γ and δ were calculated using T_x as a substitute for T_g (which was not seen in the ternary alloys).

	α	T_l (K) exp.	T_x (K)	T_{rg}	γ	δ
$Fe_{79.5}C_{3.5}B_{17}$	1.360	1434	723	0.504	0.335	1.017
$Fe_{80.9}C_5B_{14.1}$	1.441	1428	727	0.509	0.337	1.037

Manganese and molybdenum were selected as alloying additions not only to increase the complexity of $Fe_{80.9}C_5B_{14.1}$, but also to determine if their effect on crystal structure would have an affect on its GFA: Mn is an austenite (γFe) stabiliser while Mo is a ferrite (αFe) stabiliser, as can be seen in the respective binary phase diagrams shown in figure 5.1.

In this chapter the microstructures of the as-cast alloys are compared to the microstructure of the base alloy $Fe_{80.9}C_5B_{14.1}$. The effect of adding varying proportions of manganese and/or molybdenum to the base alloy are described, and the GFA of the melt-spun alloys is characterised.

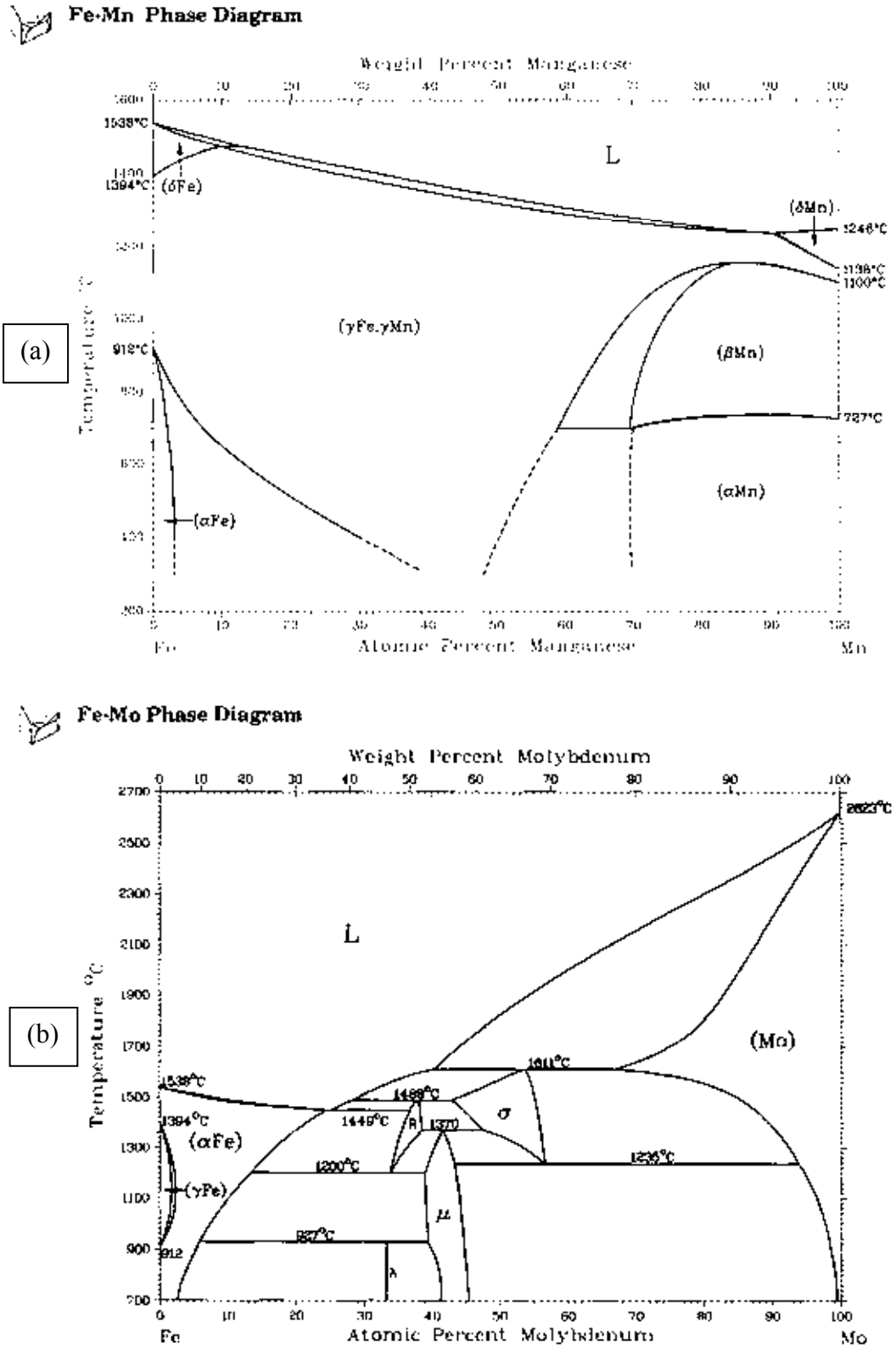

Figure 5.1 Phase diagrams of iron-manganese and iron-molybdenum [143]. In (a) it can be seen that Mn is an austenite stabiliser as there is an expanded gamma field. In (b) it can be seen that Mo is a ferrite stabiliser as there is a small closed gamma loop and a large region of solid solution of αFe and Mo.

5.2 As-Cast Alloys

5.2.1 Optical Microscopy

Figure 5.2 shows the microstructure of the base alloy $Fe_{80.9}C_5B_{14.1}$. It consists of a 2-phase matrix of finely spaced laths of $Fe_3(C,B)$ and ferrite, with $Fe_3(C,B)$ dendrites containing Fe_2B crystals.

5.2.1.1 Alloys with Manganese Additions

Figures 5.3 to5.6 show the microstructures of the $Fe_{80.9-x}Mn_xC_5B_{14.1}$ group (where x = 2, 5, 10, 20). At low magnification each appears similar to the base composition, $Fe_{80.9}C_5B_{14.1}$, with the only difference being that the proportion of dendrites in each micrograph is greater. At higher magnification the microstructures remain similar, with each showing fine lamellae and dendrites containing small crystals. The exception is $Fe_{60.9}Mn_{20}C_5B_{14.1}$ (figure 5.6), where there are almost no crystals within the dendrites.

5.2.1.2 Alloys with Molybdenum Additions

Figures 5.7 to 5.10 show the microstructures of the $Fe_{80.9-x}Mo_xC_5B_{14.1}$ group (where x = 2, 5, 10, 20). At low magnification $Fe_{78.9}Mo_2C_5B_{14.1}$ and $Fe_{75.9}Mo_5C_5B_{14.1}$ (figures 5.7 and 5.8) appear similar to the base alloy with both having dendrites in what appears to be an unresolved matrix of fine lamellae. However, at higher magnification the matrix is revealed to be a non-lamellae structure, consisting of interpenetrating dendrite arms and interdendritic pockets of an unresolved phase, which are later revealed to be small pearlite colonies (see figure 5.17). $Fe_{70.9}Mo_{10}C_5B_{14.1}$ (figure 5.9) has a completely different and complex microstructure. At low magnification little detail can be seen although a faceted phase is visible. At higher magnification some dendrites are also visible. It is assumed that for this composition the alloy follows a different solidification path and in this case the

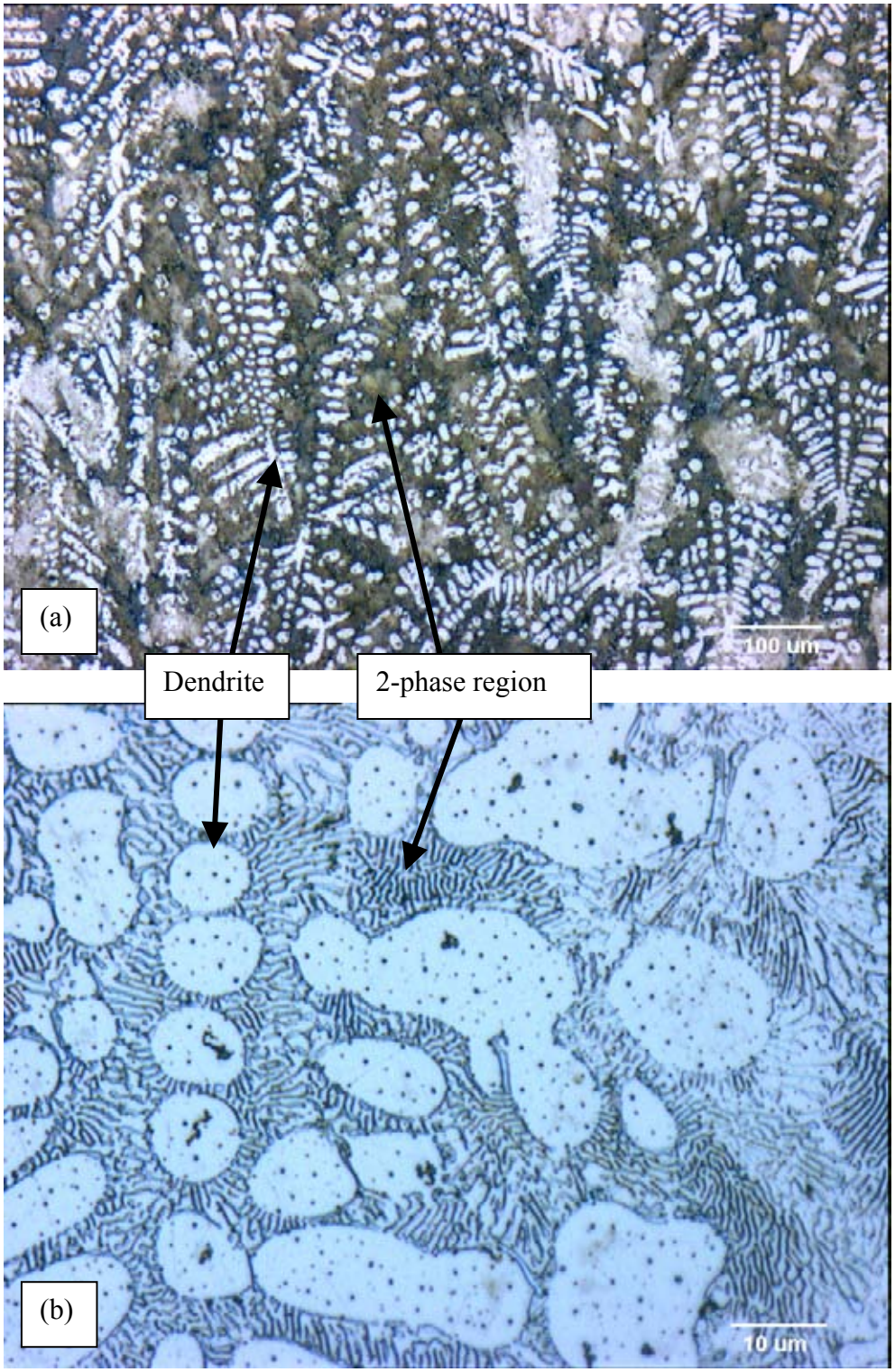

Figure 5.2 Microstructure of the base alloy - $Fe_{80.9}C_5B_{14.1}$. (a) Low magnification view showing an unresolved matrix and dendrites. (b) High magnification view showing matrix to be a 2-phase region consisting of fine lamellae. The spots within the dendrites are small crystals.

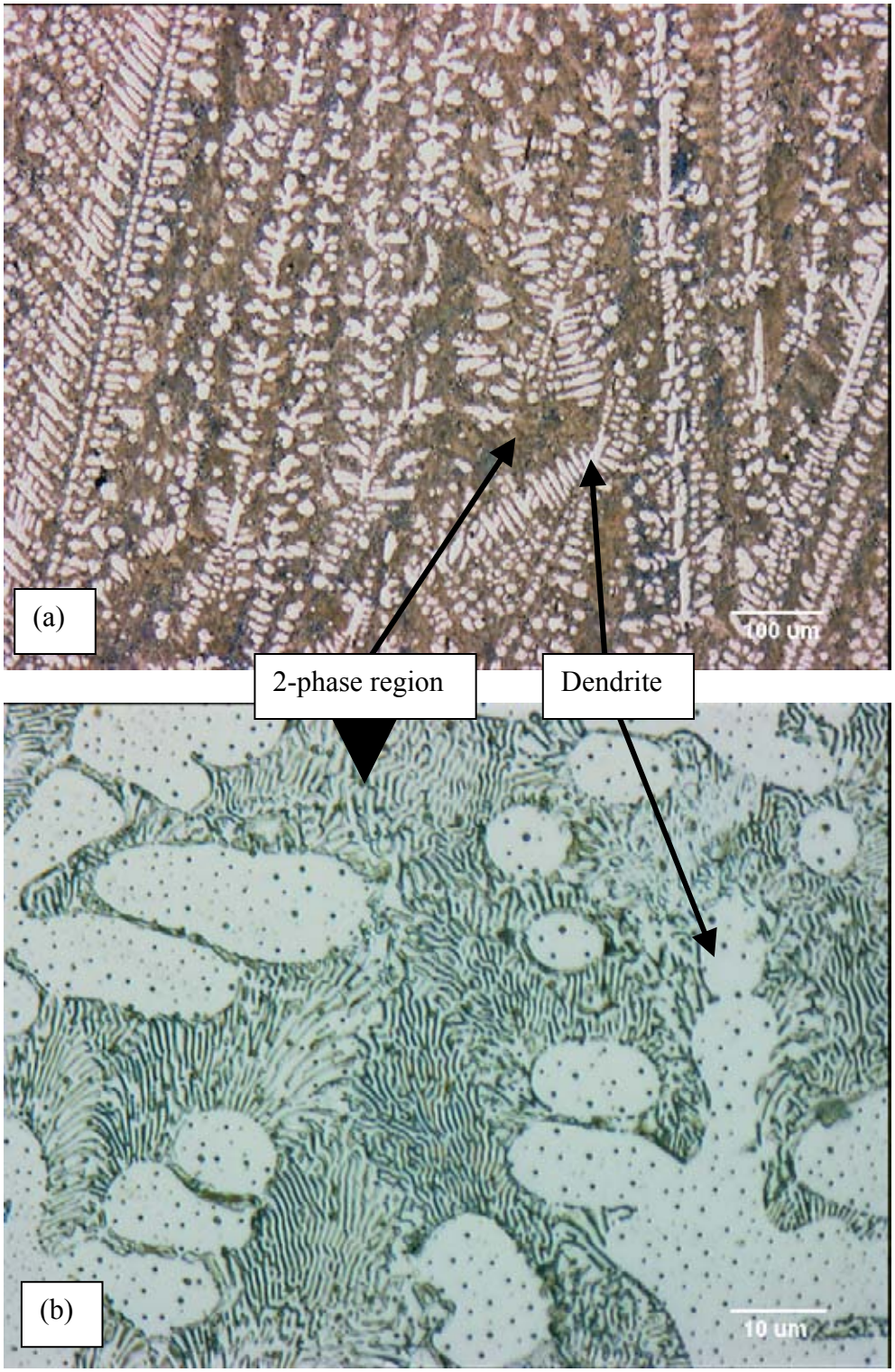

Figure 5.3 Microstructure of $Fe_{78.9}Mn_2C_5B_{14.1}$. (a) Low magnification view showing an unresolved matrix and dendrites. (b) High magnification view showing matrix to be a 2-phase region consisting of fine lamellae. The spots within the dendrites are small crystals.

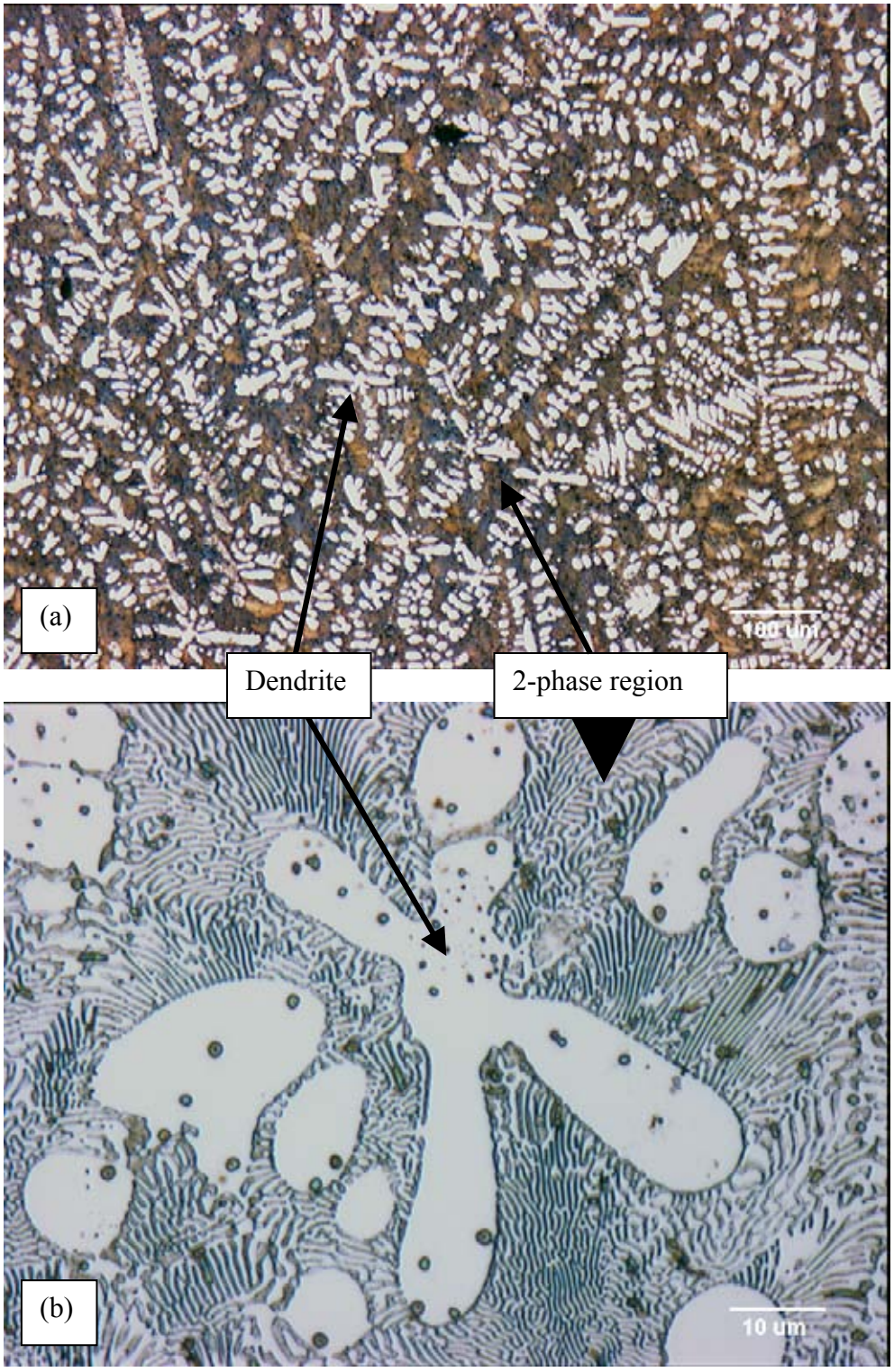

Figure 5.4 Microstructure of $Fe_{75.9}Mn_5C_5B_{14.1}$. (a) Low magnification view showing an unresolved matrix and dendrites. (b) High magnification view showing matrix to be a 2-phase region consisting of fine lamellae. The spots within the dendrites are small crystals.

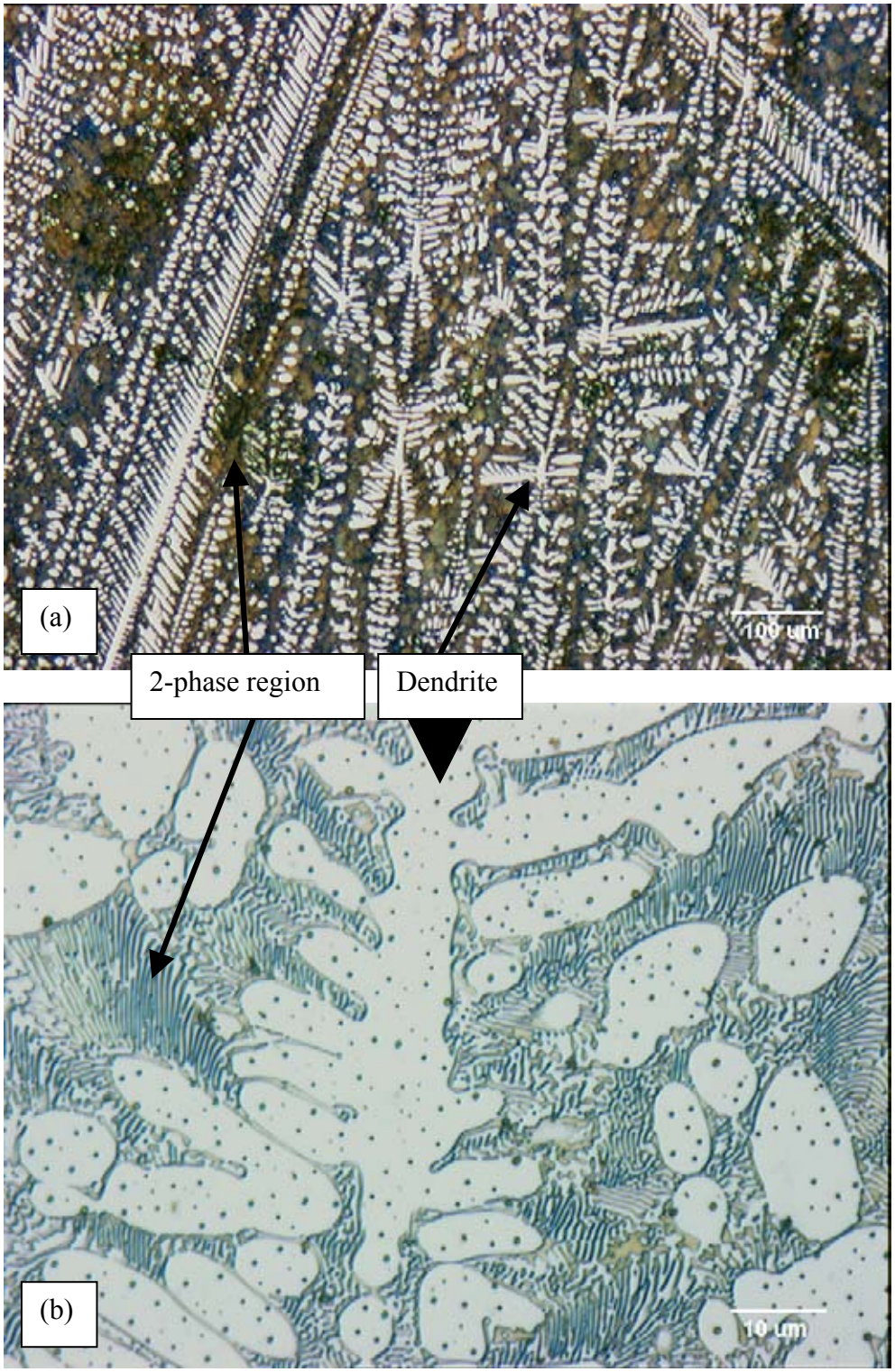

Figure 5.5 Microstructure of $Fe_{70.9}Mn_{10}C_5B_{14.1}$. (a) Low magnification view showing an unresolved matrix and dendrites. (b) High magnification view showing matrix to be a 2-phase region consisting of fine lamellae. The spots within the dendrites are small crystals.

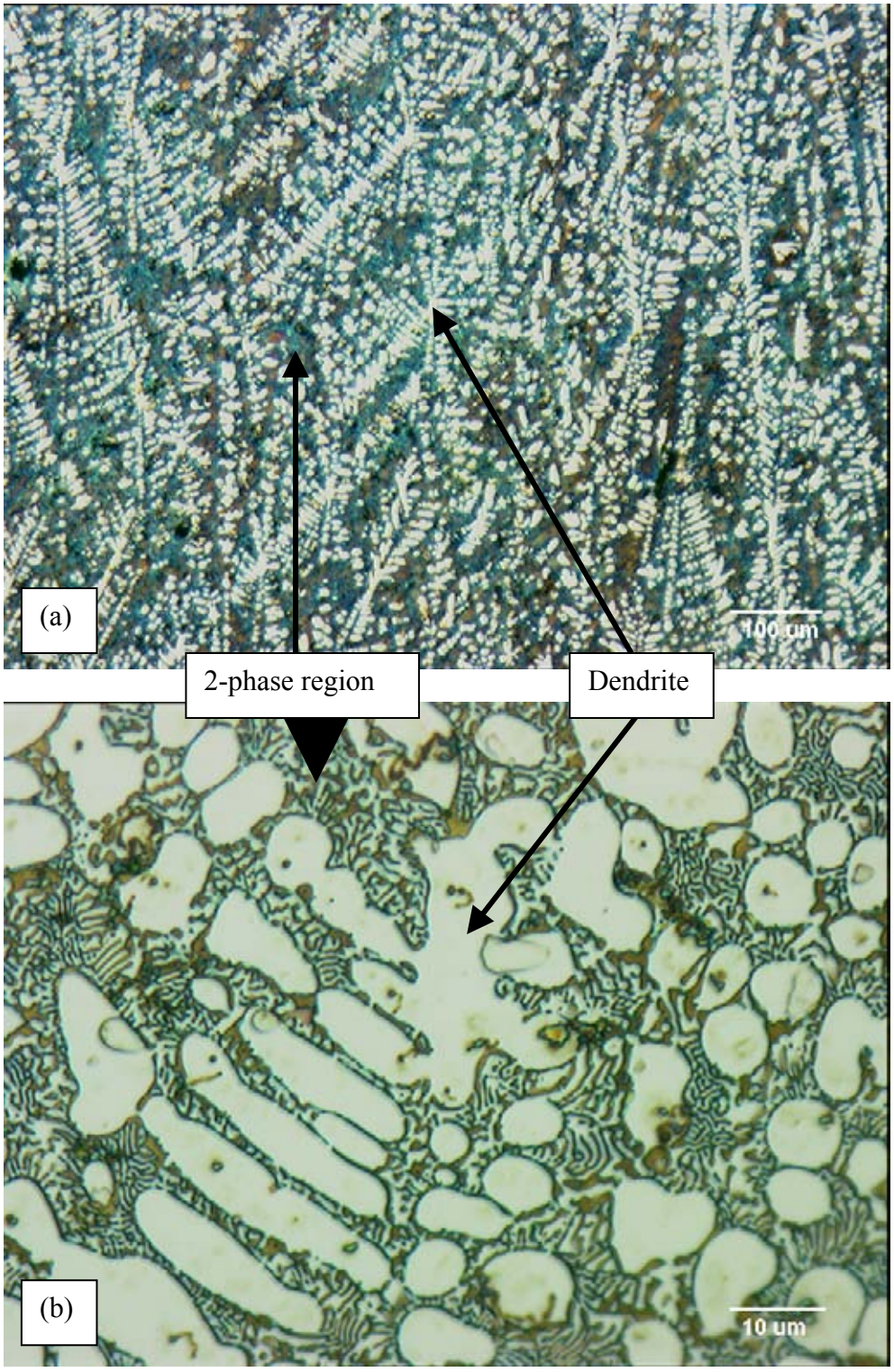

Figure 5.6 Microstructure of $Fe_{60.9}Mn_{20}C_5B_{14.1}$. (a) Low magnification view showing an unresolved matrix and dendrites. (b) High magnification view showing almost no crystals within the dendrites and revealing the lamellae to be less regular than those for the alloys where the manganese content is lower.

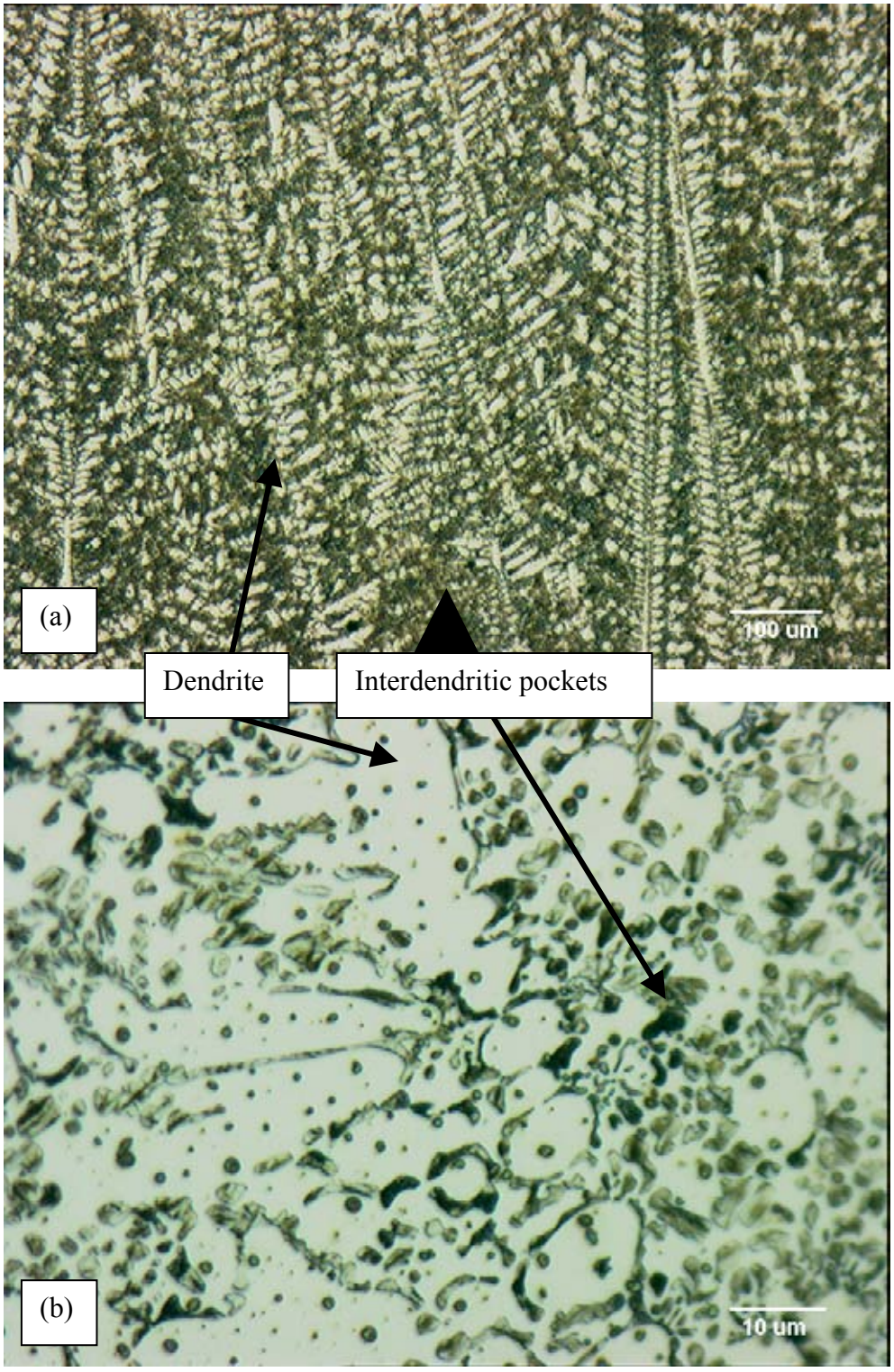

Figure 5.7 Microstructure of $Fe_{78.9}Mo_2C_5B_{14.1}$. (a) Low magnification showing dendrites and unresolved matrix. (b) High magnification view showing matrix to consist of interdendritic pockets of eutectic composition.

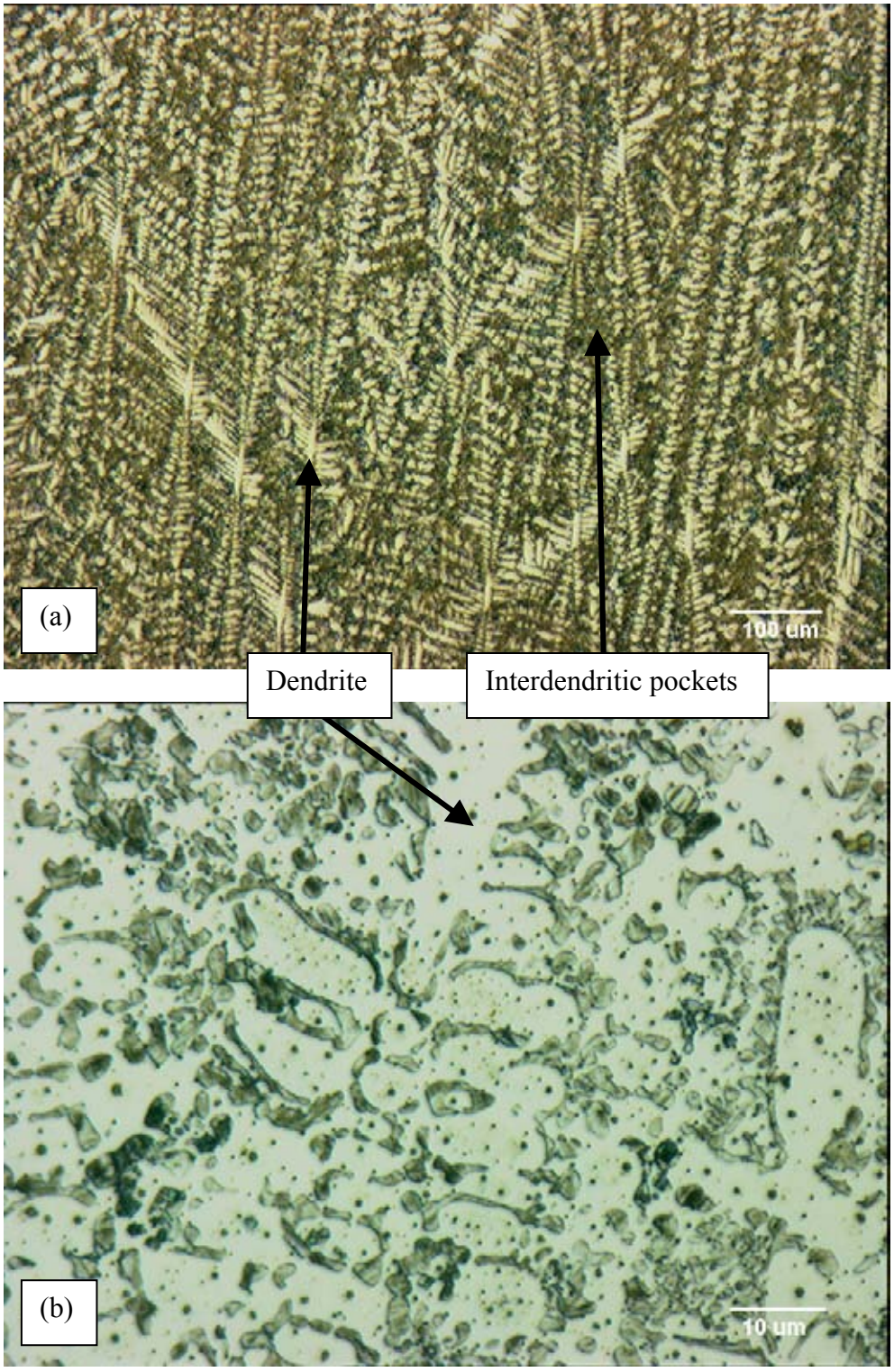

Figure 5.8 Microstructure of $Fe_{75.9}Mo_5C_5B_{14.1}$. (a) Low magnification showing dendrites and unresolved matrix. (b) High magnification view showing matrix to consist of interdendritic pockets of eutectic composition.

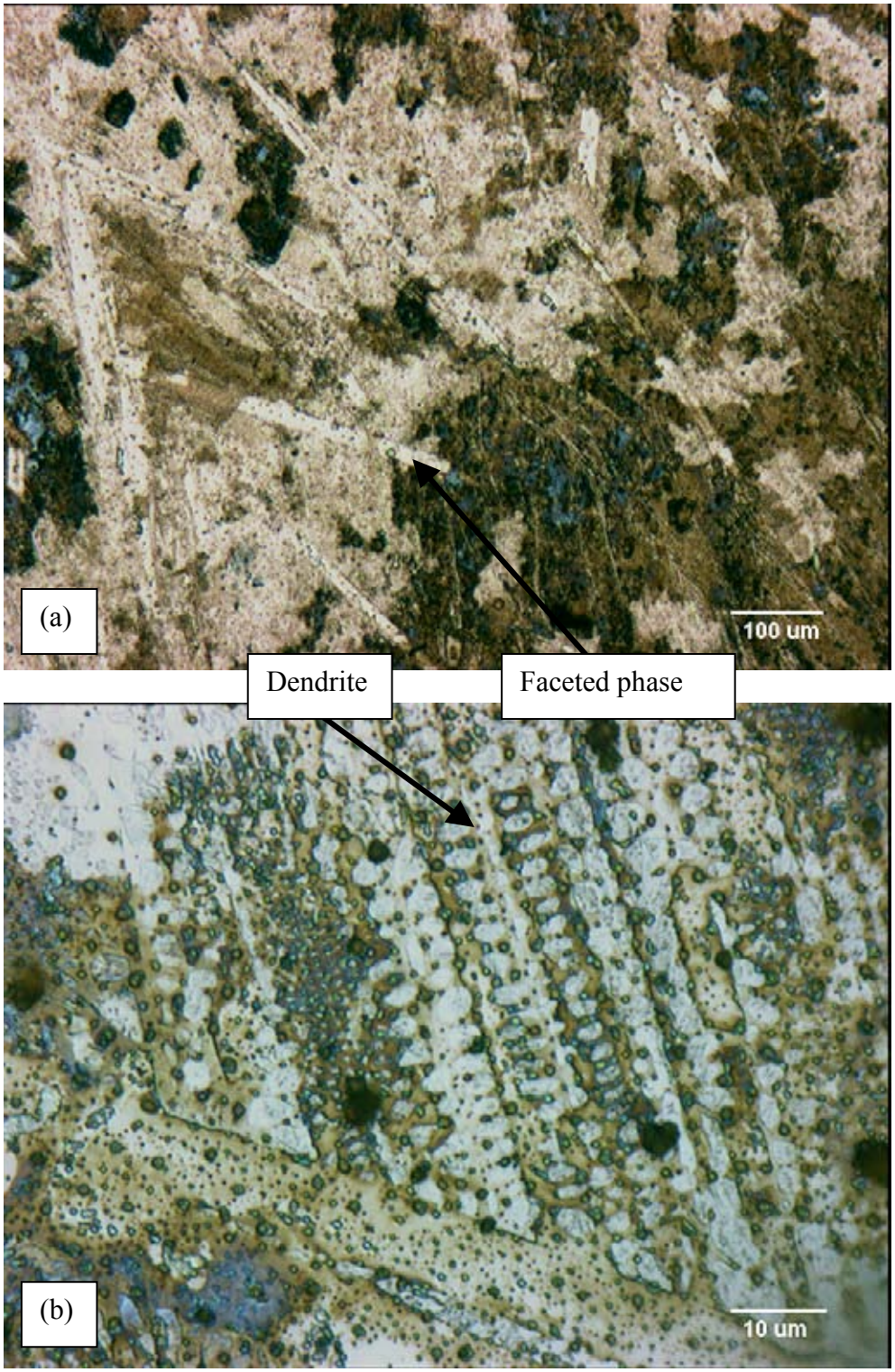

Figure 5.9 Microstructure of $Fe_{70.9}Mo_{10}C_5B_{14.1}$. (a) Low magnification view showing faceted phase. (b) High magnification view showing fine dendrite arms.

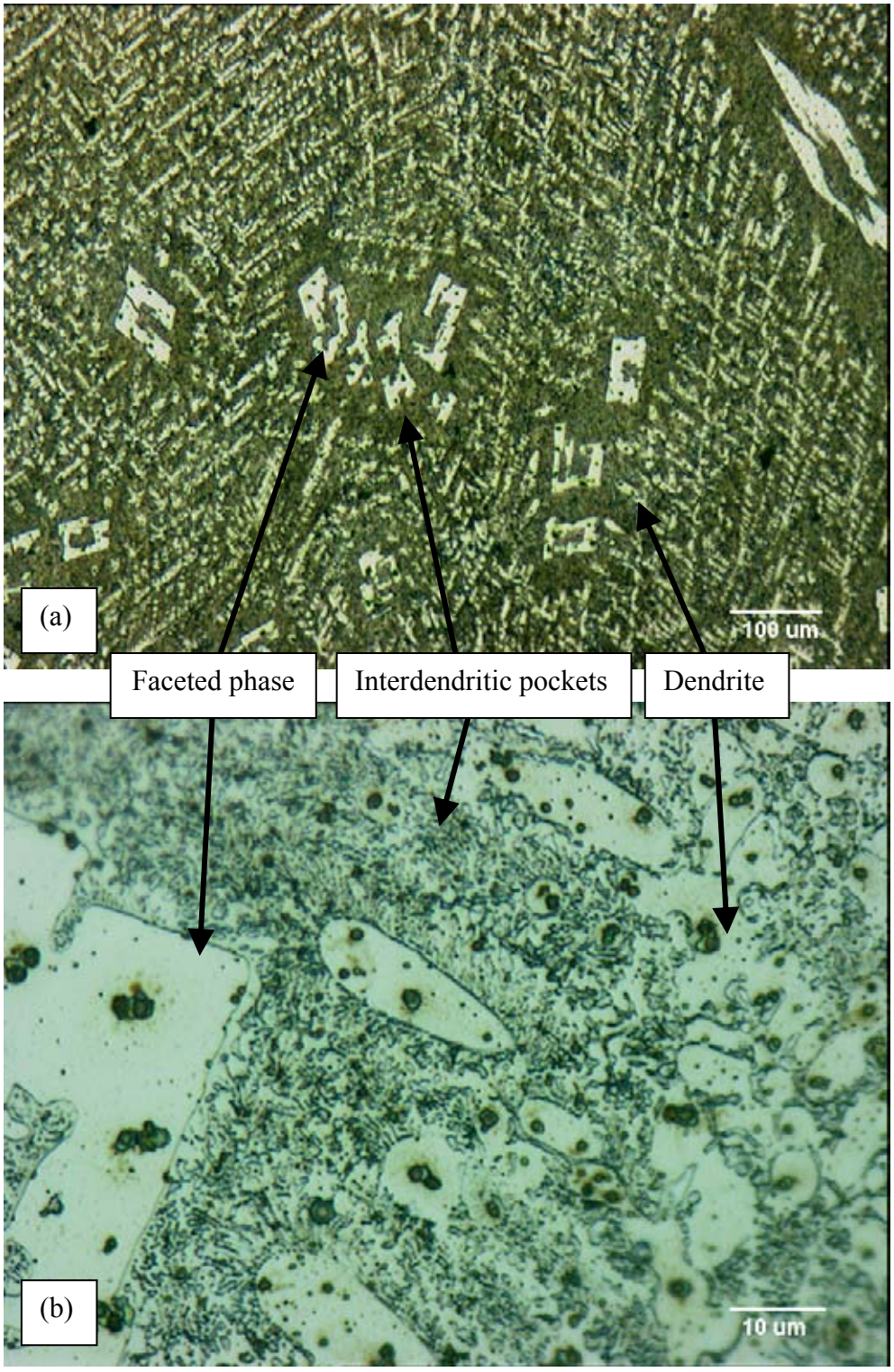

Figure 5.10 Microstructure of $Fe_{60.9}Mo_{20}C_5B_{14.1}$. (a) Low magnification view showing separate dendritic and faceted phases in an unresolved matrix. (b) High magnification view showing fine interdendritic pockets of eutectic composition.

etchant was not suitable for revealing the microstructure. $Fe_{60.9}Mo_{20}C_5B_{14.1}$ (figure 5.10) has the same features as $Fe_{78.9}Mo_2C_5B_{14.1}$ and $Fe_{75.9}Mo_5C_5B_{14.1}$ but with the addition of a faceted phase which is separate from the dendrites, unlike in the ternary alloys where faceted phase is seen inside the dendrites (figures 4.3 to 4.5).

5.2.1.3 Alloys with Manganese and Molybdenum Additions

Figures 5.11 to 5.13 show the microstructures of the $Fe_{80.9-x}(Mn_{50}Mo_{50})_xC_5B_{14.1}$ group (where x = 4, 10 and 20). $Fe_{76.9}Mn_2Mo_2C_5B_{14.1}$ (figure 5.11) has the same structure as the alloys with molybdenum at 2% and 5%, so at low magnification it appears similar to the base alloy with the appearance of having dendrites in a 2-phase matrix. However, at higher magnification the matrix is again revealed to be a non-lamellae structure, consisting of interpenetrating dendrite arms and interdendritic pockets of fine pearlite. $Fe_{70.9}Mn_5Mo_5C_5B_{14.1}$ and $Fe_{60.9}Mn_{10}Mo_{10}C_5B_{14.1}$ (figures 5.12 and 5.13 respectively) have a different microstructure. As with all the microstructures seen thus far primary dendrite arms can be seen. The matrix, though, is very different from either of the matrices for the alloys containing only manganese or molybdenum additions. At low magnification the matrix appears to consist of large angular grains. However, at higher magnification the microstructure is revealed to be a 2-phase mixture consisting of very fine rods (diameters of approximately 300nm) embedded in another phase. This structure is called ledeburite and is sometimes seen in cast iron alloys (as opposed to steels) that are close to the eutectic composition. The 'grains' seen at low magnification are therefore the boundaries of different colonies of ledeburite. The phases are not the same as those found in steel because instead of alternating plates of cementite and ferrite, ledeburite consists of cementite rods in an austenite matrix. This fine structure is not always retained as the austenite can decompose to ferrite and cementite [144].

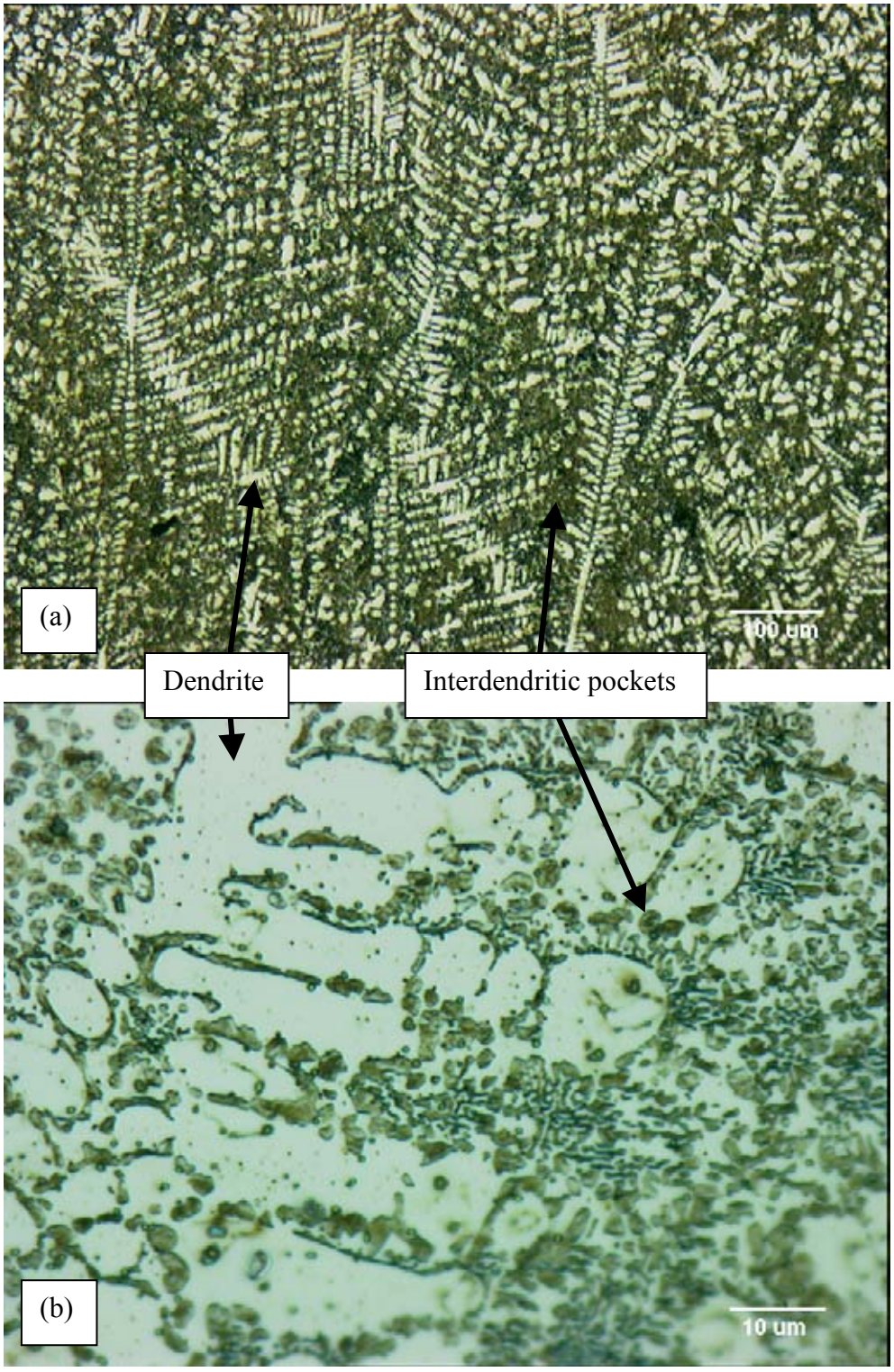

Figure 5.11 Microstructure of $Fe_{76.9}Mn_2Mo_2C_5B_{14.1}$. (a) Low magnification showing dendrites and unresolved matrix. (b) High magnification view showing matrix to consist of interdendritic pockets of eutectic composition.

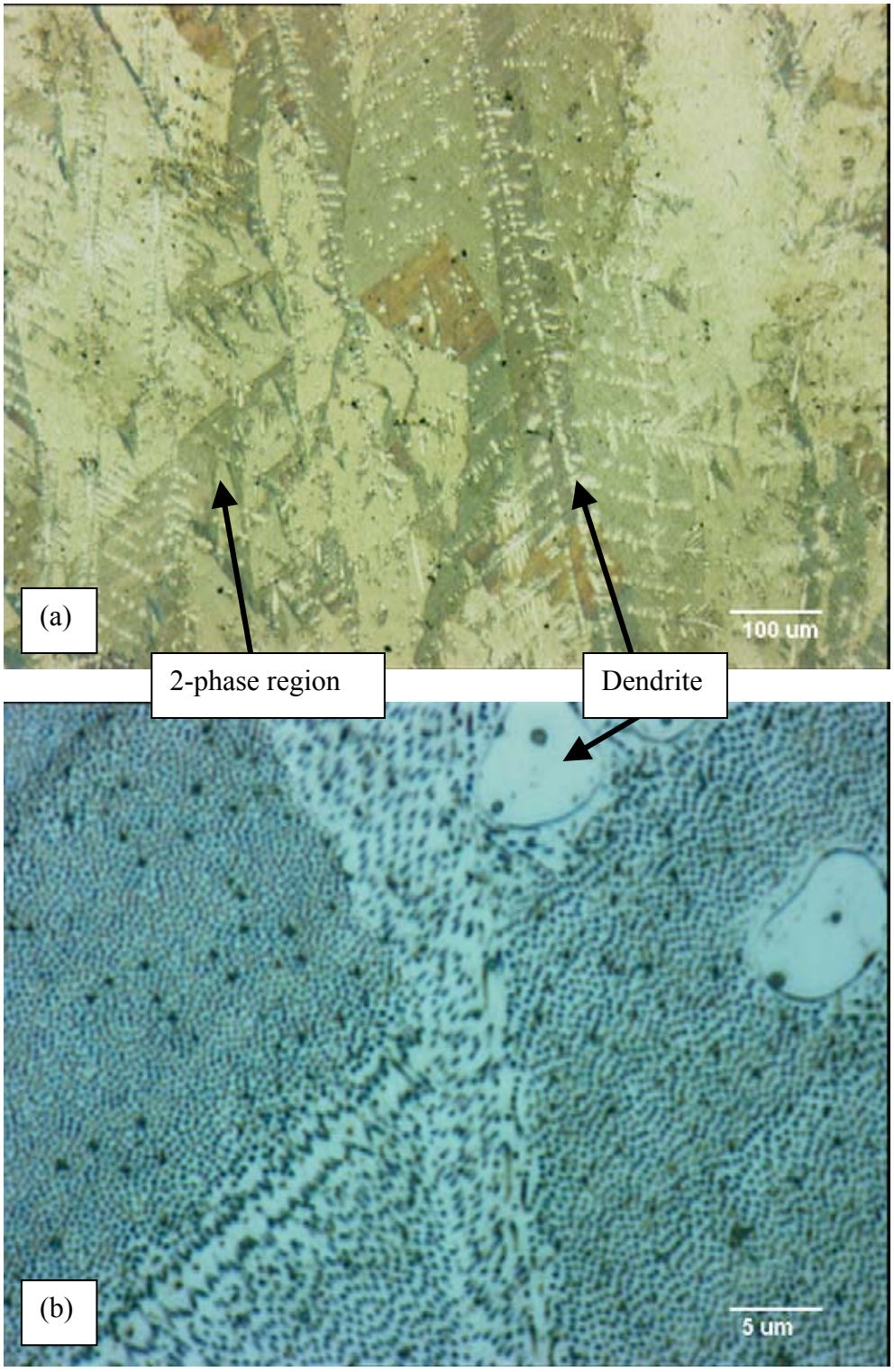

Figure 5.12 Microstructure of $Fe_{70.9}Mn_5Mo_5C_5B_{14.1}$. (a) Low magnification view showing dendrites in a matrix that appears to consist of large angular grains. (b) High magnification view revealing the matrix to be colonies of ledeburite.

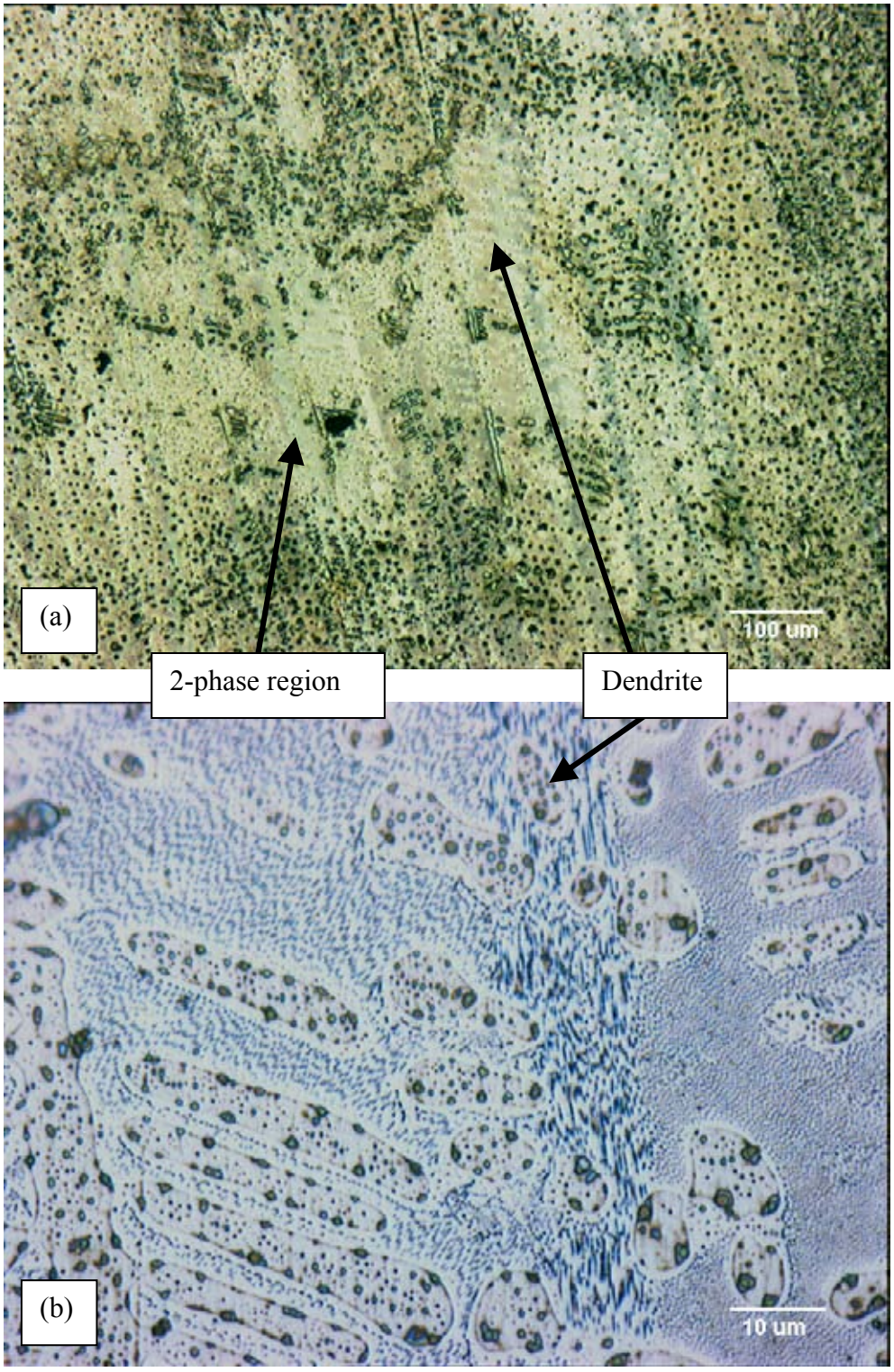

Figure 5.13 Microstructure of $Fe_{60.9}Mn_{10}Mo_{10}C_5B_{14.1}$. (a) Low magnification view showing dendrites in an unresolved matrix. (b) High magnification view revealing the matrix to be colonies of ledeburite.

Figures 5.14 and 5.15 show the microstructures of the $Fe_{60.9}Mn_xMo_{20-x}C_5B_{14.1}$ group (where x = 4 and 16). Where x=10 the composition is the same as when x=10 for the $Fe_{80.9-x}(Mn_{50}Mo_{50})_xC_5B_{14.1}$ group so figure 5.13 serves for both groups.

$Fe_{60.9}Mn_4Mo_{16}C_5B_{14.1}$ (figure 5.14) is another alloy which follows a different solidification path. It has an unusual leaf-like morphology with a residual matrix. At high magnification each 'leaf' is revealed to be a two-phase structure with a crystal at the centre on many occasions. $Fe_{60.9}Mn_{16}Mo_4C_5B_{14.1}$ (figure 5.15) has the same microstructure as $Fe_{70.9}Mn_5Mo_5C_5B_{14.1}$ and $Fe_{60.9}Mn_{10}Mo_{10}C_5B_{14.1}$ – that is $Fe_3(C,B)$ dendrites and retained (rather than transformed) ledeburite.

5.2.2 Scanning Electron Microscopy (SEM)

It has been mentioned that with EDS it is not possible to detect the presence of boron unless it is concentrated in certain areas. There is also a problem with carbon in that, although it can be detected, it is sometimes reported in alloys that do not contain carbon. Because of this no major compositional analysis of the alloys was undertaken. As an example of the unreliability of EDS analysis: boron was not detected in any of the $Fe_{80.9-x}Mn_xC_5B_{14.1}$ compositions while carbon was reported as anywhere between 10 to 20 atomic% in any place an area or spot measurement was taken, which is far more than is in the alloy as a whole. The problem with carbon readings in many analysis techniques is not uncommon and is usually due to contamination from the oil in the pumps used to control the vacuum system.

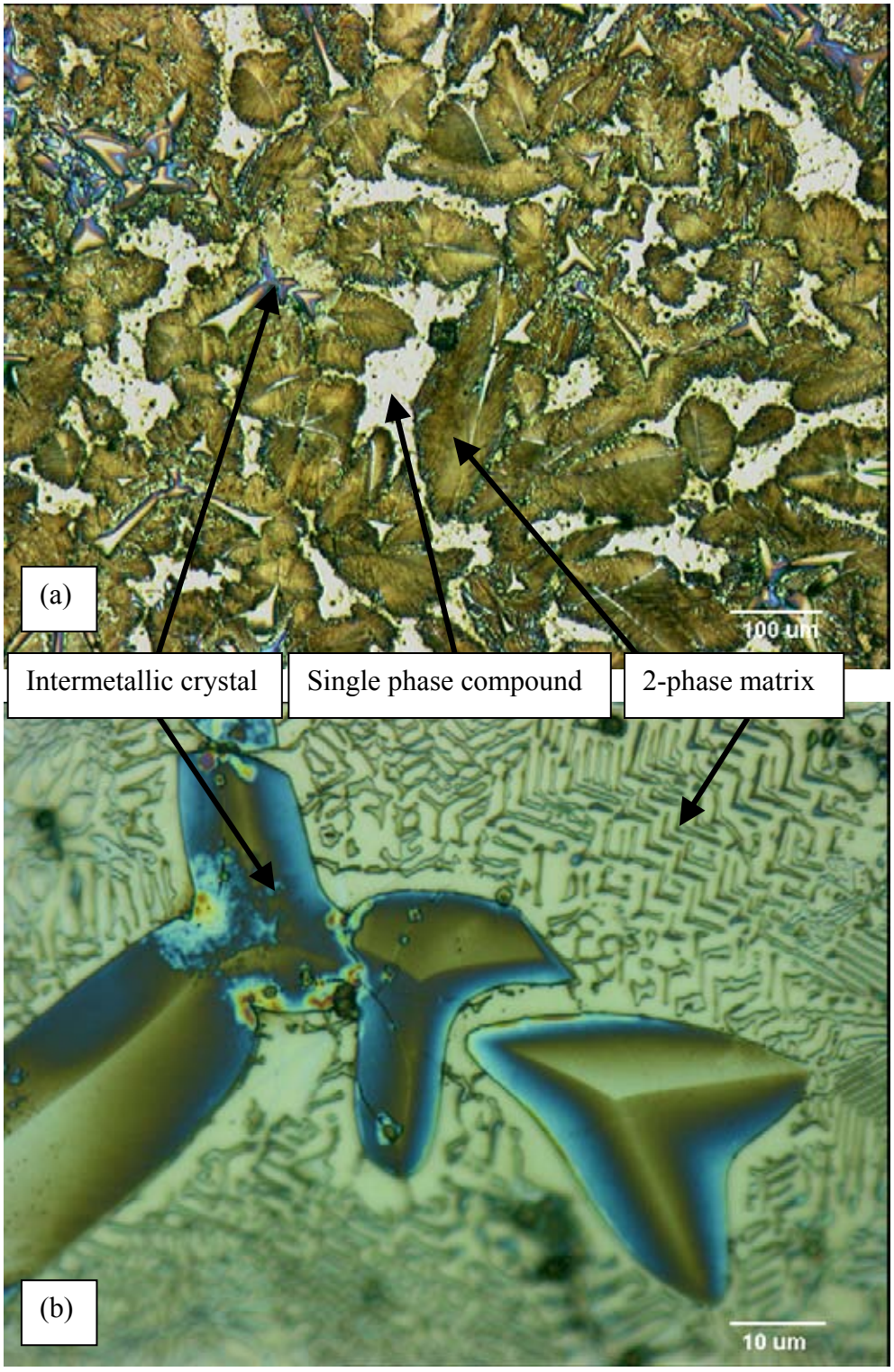

Figure 5.14 Microstructure of $Fe_{60.9}Mn_4Mo_{16}C_5B_{14.1}$. (a) Low magnification view of general structure (b) High magnification view showing B_2FeMo_2 intermetallic crystals embedded in a two-phase matrix.

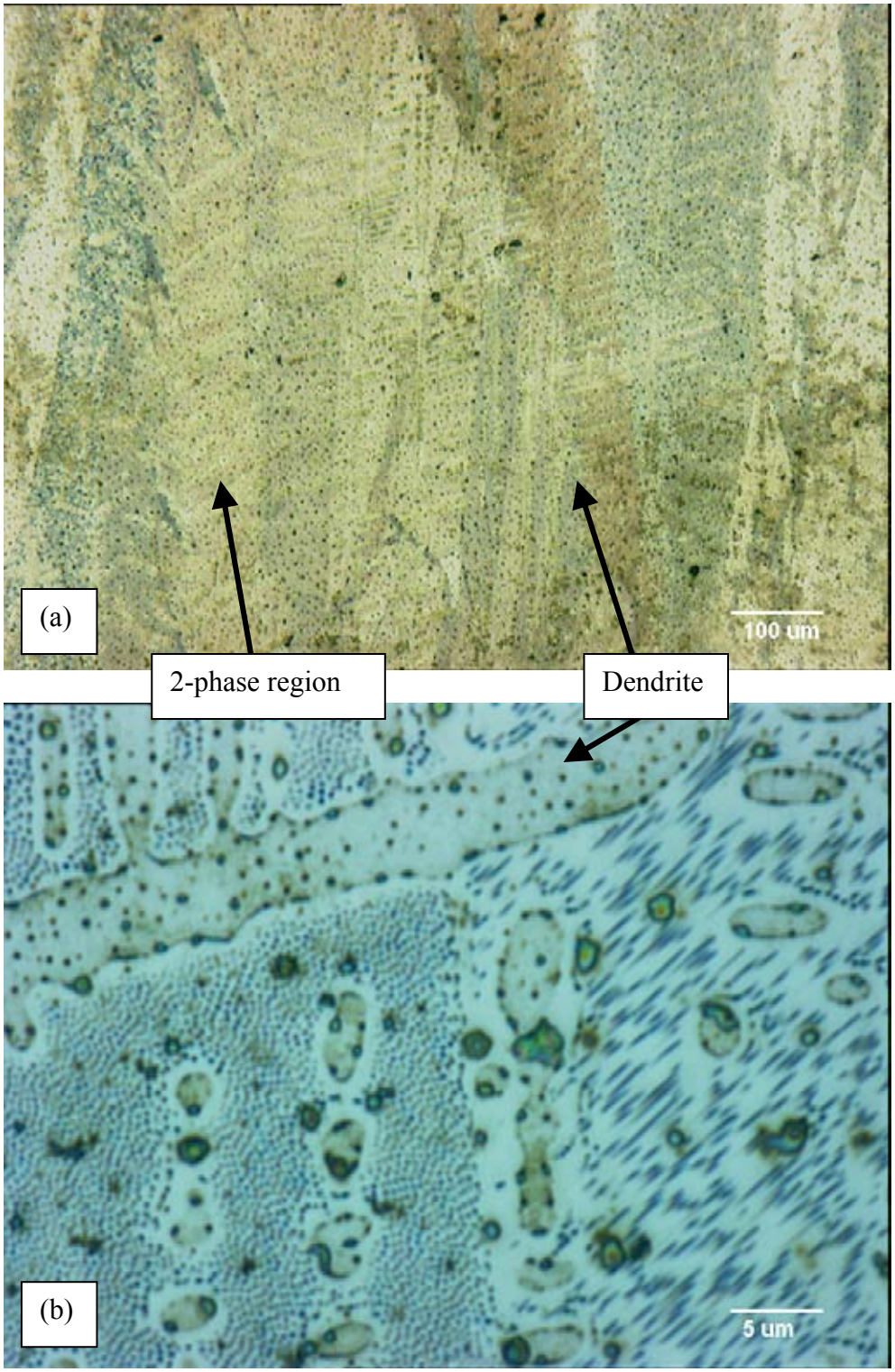

Figure 5.15 Microstructure of $Fe_{60.9}Mn_{16}Mo_4C_5B_{14.1}$. (a) Low magnification view showing dendrites in a matrix that appears to consist of large angular grains. (b) High magnification view revealing the matrix to be colonies of ledeburite.

Figure 5.16 shows secondary and backscattered electron images which are representative of the $Fe_{80.9-x}Mn_xC_5B_{14.1}$ group. It is believed that the spots in the dendrites are precipitates, as the image is scratch free. In backscattered mode the spots appear darker than the dendrites so it is assumed they are precipitates of Fe_2B.

Figure 5.17 shows a secondary electron image representative of the main features seen in the $Fe_{80.9-x}Mo_xC_5B_{14.1}$ (where x = 2, 5 or 20). The matrix consists of two components. The majority consists of interpenetrating dendrite arms while the interdendritic pockets, which were unresolved in optical microscopy, show small plate-like features. The interdendritic pockets are therefore assumed to be fine pearlite colonies.

Figure 5.18 shows a backscattered image of the faceted phase which appears in $Fe_{60.9}Mo_{20}C_5B_{14.1}$. This phase is separate from the dendrites and doesn't have a markedly different contrast, unlike the faceted phase seen in some of the ternary alloys (e.g. figure 4.11), so in this case it is not Fe_2B.

Figure 5.19 shows a backscattered image which is representative of the ledeburite phase seen in $Fe_{70.9}Mn_5Mo_5C_5B_{14.1}$, $Fe_{60.9}Mn_{10}Mo_{10}C_5B_{14.1}$ and $Fe_{60.9}Mn_{16}Mo_4C_5B_{14.1}$. Ledeburite consists of cementite rods in an austenite matrix. In figure 5.19 the rods are darkly contrasted with the matrix which confirms they have a high percentage of lightweight elements compared to the surrounding material. In the previous chapter it was shown that the cementite phase in the alloys was actually $Fe_3(C,B)$, and it is assumed that this is the same for the multi-component alloys too.

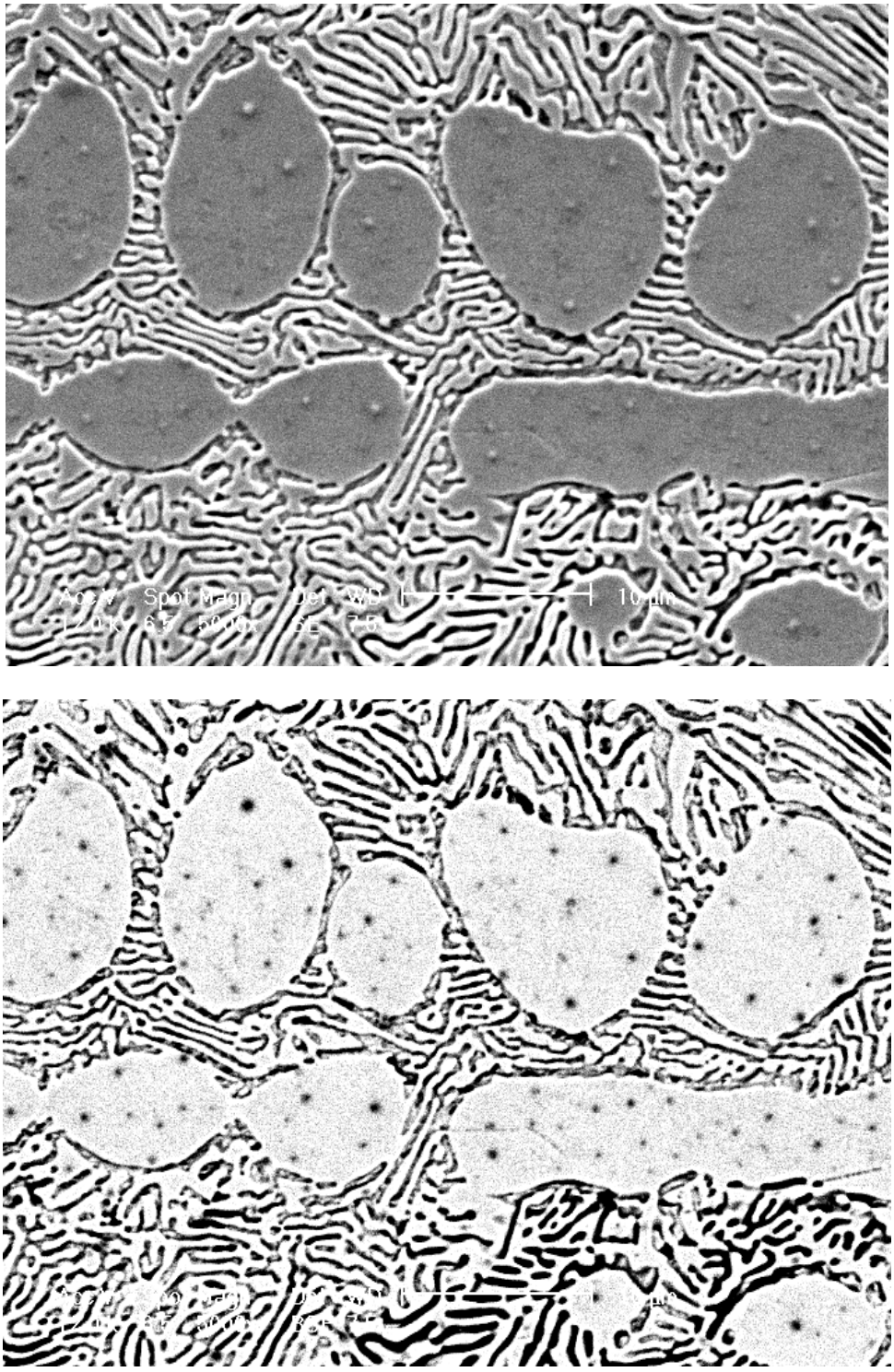

Figure 5.16 SE and BSE images representative of the features seen in the $Fe_{80.9-x}Mn_xC_5B_{14.1}$ group (where x=2, 5, 10 or 20). The spots within the dendrites are most likely to be Fe_2B crystals.

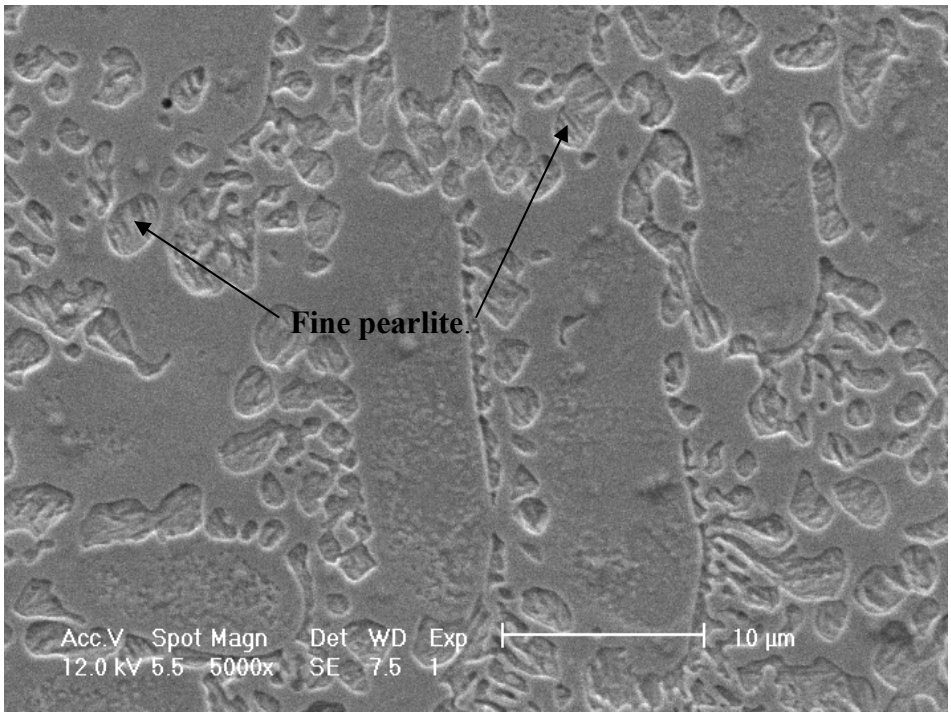

Figure 5.17 Secondary electron image representative of the features seen in the $Fe_{80.9-x}Mo_xC_5B_{14.1}$ group (where x=2, 5 or 20). The matrix consists interpenetrating fine dendrite arms with interdendritic pockets of fine pearlite.

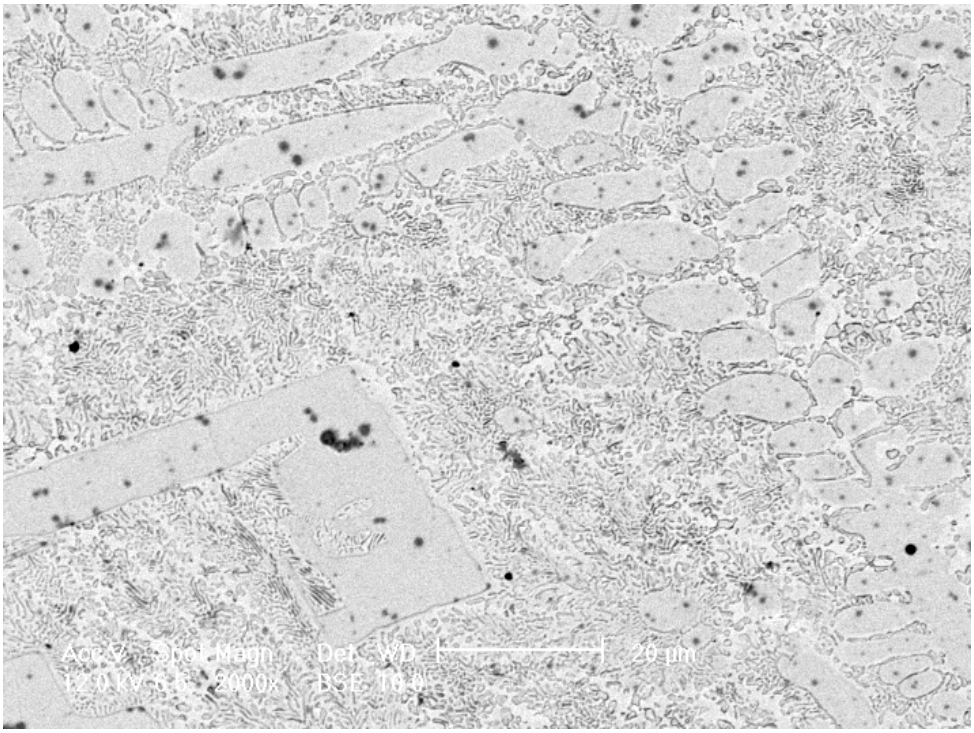

Figure 5.18 Backscattered image of $Fe_{60.9}Mo_{20}C_5B_{14.1}$ showing the faceted phase is separate from dendrites, unlike in the ternary alloys. The faceted phase has the same contrast as the dendrites, so it is not Fe_2B.

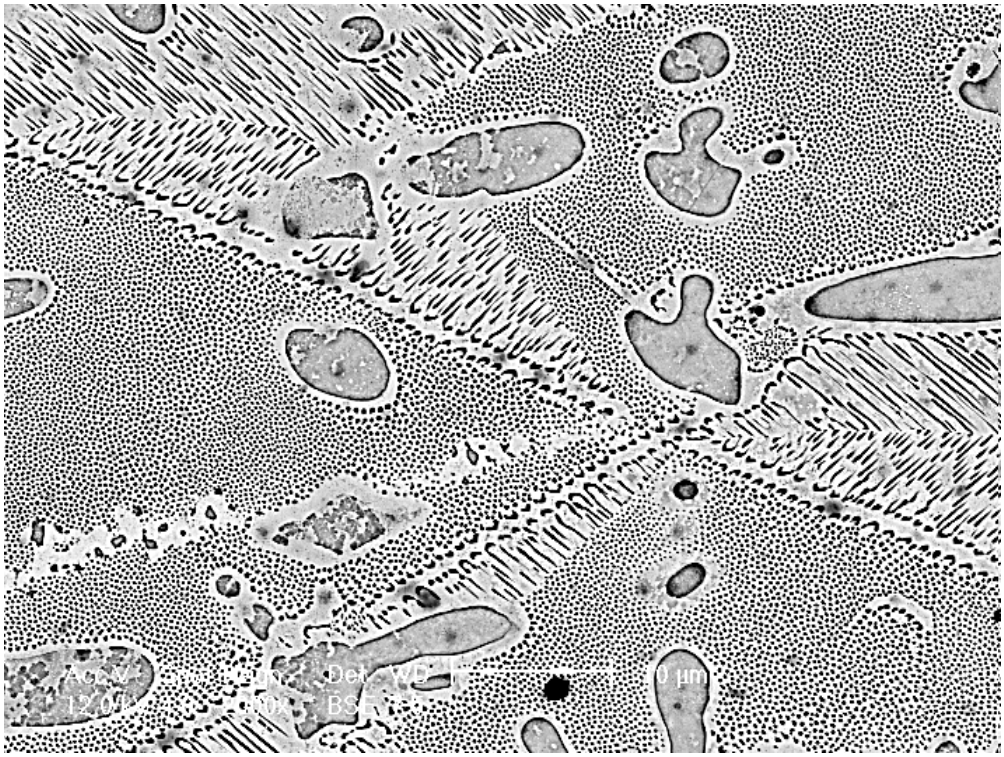

Figure 5.19 Backscattered image of ledeburite (cementite rods in an austenite matrix) with some primary $Fe_3(C,B)$ dendrites. These features are seen in $Fe_{70.9}Mn_5Mo_5C_5B_{14.1}$, $Fe_{60.9}Mn_{10}Mo_{10}C_5B_{14.1}$ and $Fe_{60.9}Mn_{16}Mo_4C_5B_{14.1}$.

Figure 5.20 shows a backscattered image of a typical crystal seen in the unusual microstructure of $Fe_{60.9}Mn_4Mo_{16}C_5B_{14.1}$. It has a high proportion of boron and molybdenum and is low in iron, and has no manganese or carbon. In the ternary Fe-Mo-B system [145] there is an intermetallic phase with similar proportions of boron, iron and molybdenum, leading to the conclusion that the crystal is B_2FeMo_2.

5.3 Melt-Spinning

The melt-spinning process for the multi-component alloys followed the same procedures as for the ternary alloys. Unlike the ternary alloys which were in the form of short strips or flakes, the multi-component alloys produced long continuous strips of ribbon. This shows that the material is more stable and less brittle, so is an indication of improvement in the GFA of the base material.

5.3.1 X-Ray Diffraction (XRD)

Figure 5.21 shows the XRD traces for the $Fe_{80.9-x}Mn_xC_5B_{14.1}$ group (where x = 2, 5, 10 or 20). All four traces show a broad peak which is representative of an amorphous phase. Only the trace for $Fe_{75.9}Mn_5C_5B_{14.1}$ shows a single broad peak with no additional sharp peaks, indicating this composition is either fully amorphous or contains crystallites/nuclei where the quantities are below the detection limit of the equipment (i.e. below 10% by volume). The trace for $Fe_{78.9}Mn_2C_5B_{14.1}$ shows sharpness to the broad peak - the same as happened for the base alloy - which indicates a limited amount of crystallisation has occurred. The broad peak for $Fe_{70.9}Mn_{10}C_5B_{14.1}$ is smooth rather than pointed but there is a small peak at $2\theta \approx 74°$ which again indicates a small amount of crystallisation has occurred.

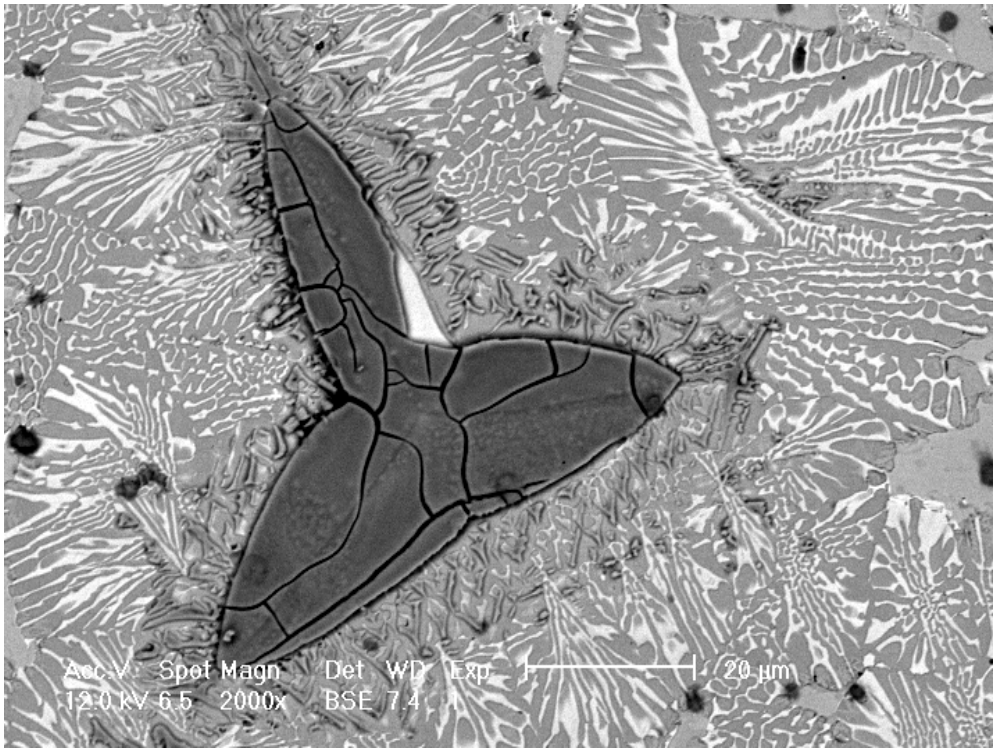

Figure 5.20 Backscattered image of a typical crystal seen in $Fe_{60.9}Mn_4Mo_{16}C_5B_{14.1}$. EDS analysis detects iron, molybdenum and boron in proportions which indicate the crystal is B_2FeMo_2.

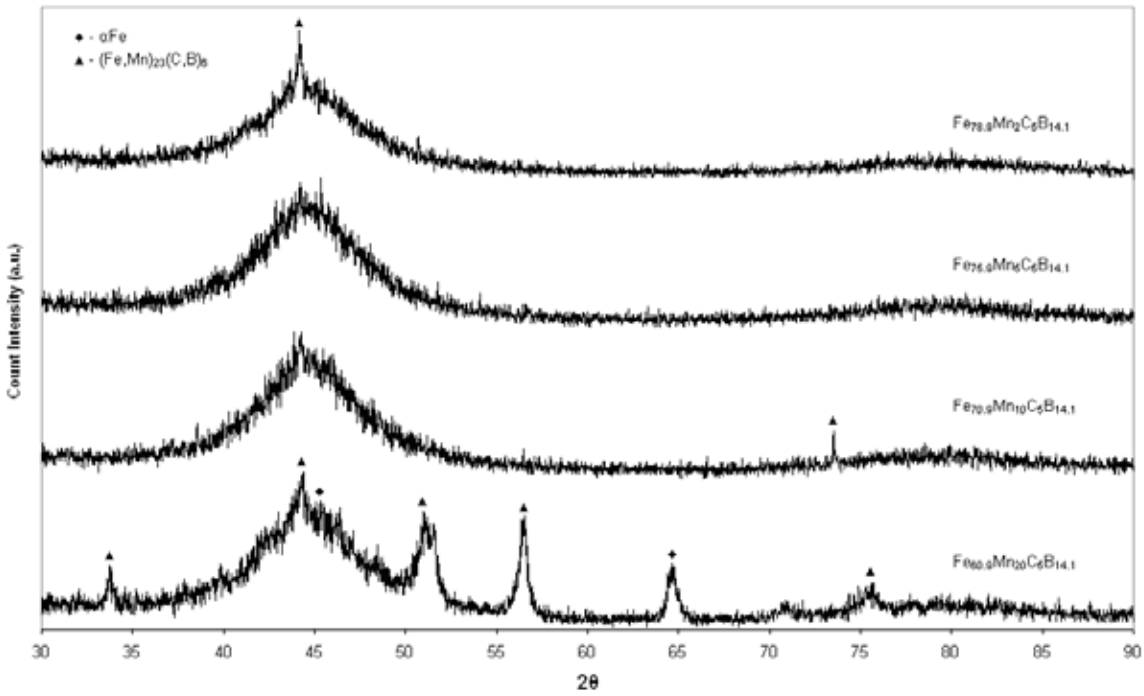

Figure 5.21 XRD traces showing broad peaks for all the $Fe_{80.9-x}Mn_xC_5B_{14.1}$ group, indicating the presence of an amorphous phase. Only $Fe_{75.9}Mn_5C_5B_{14.1}$ appears to be fully amorphous as the other traces show varying degrees of crystallinity.

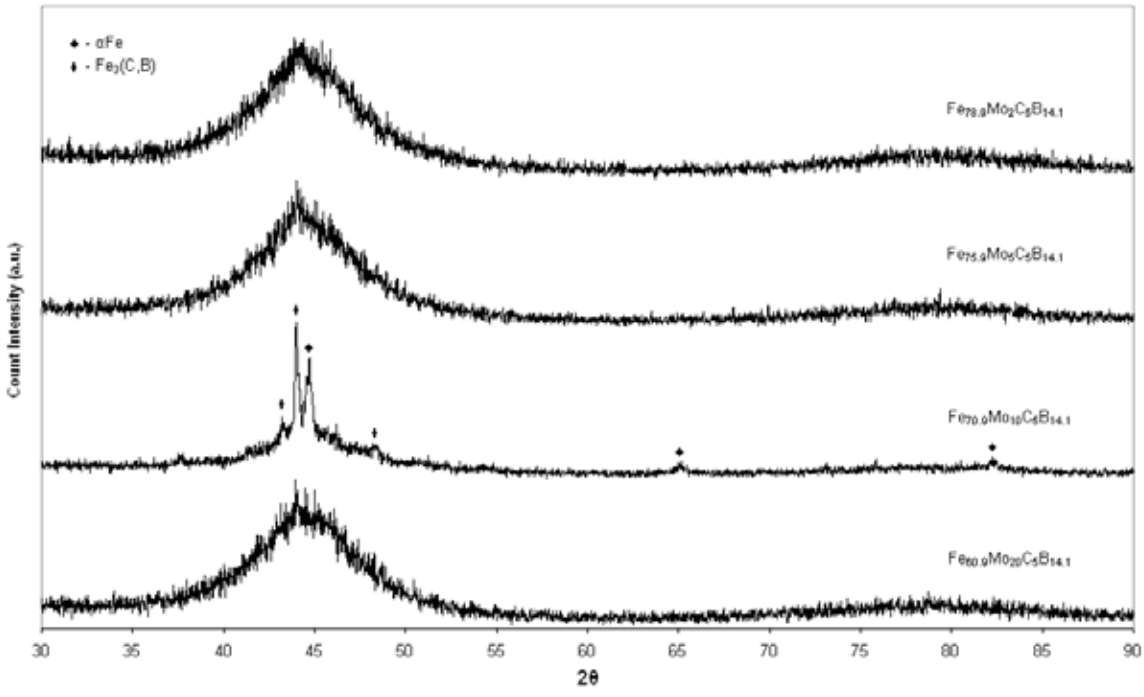

Figure 5.22 XRD traces showing broad peaks for all the $Fe_{80.9-x}Mo_xC_5B_{14.1}$ group, indicating the presence of an amorphous phase. Three of the compositions appear to be fully amorphous. $Fe_{70.9}Mo_{10}C_5B_{14.1}$ is highly crystalline as two strong peaks for αFe and $Fe_3(C,B)$ are superimposed on the broad peak.

$Fe_{60.9}Mn_{20}C_5B_{14.1}$ is obviously partially crystalline as there are several sharp peaks in addition to the broad peak. Where crystallisation has occurred the primary product is the metastable $M_{23}(C,B)_6$ phase and for $Fe_{60.9}Mn_{10}C_5B_{14.1}$ α-iron is also present.

Figure 5.22 shows the XRD traces for the $Fe_{80.9-x}Mo_xC_5B_{14.1}$ group (where x = 2, 5, 10 or 20). All four traces show a broad peak representative of an amorphous phase. For $Fe_{78.9}Mo_2C_5B_{14.1}$, $Fe_{75.9}Mo_5C_5B_{14.1}$ and $Fe_{60.9}Mo_{20}C_5B_{14.1}$ the broad peak is smooth indicating that each alloy is fully amorphous according to x-ray detection. $Fe_{70.9}Mo_{10}C_5B_{14.1}$ is highly crystalline as there a couple of sharp peaks superimposed on the broad peak. The peaks correspond to $Fe_3(C,B)$ and α-iron.

Figure 5.23 shows the XRD traces for the $Fe_{80.9-x}(Mn_{50}Mo_{50})_xC_5B_{14.1}$ group (where x = 4, 10 or 20). All three have a single smooth broad peak which indicates each is amorphous, but again does not preclude any of them from having crystals too small for the x-rays to interact with.

Figure 5.24 shows the XRD traces for the $Fe_{60.9}Mn_xMo_{20-x}C_5B_{14.1}$ group (where x = 4, 10 or 16). $Fe_{60.9}Mn_4Mo_{16}C_5B_{14.1}$ and $Fe_{60.9}Mn_{10}Mo_{10}C_5B_{14.1}$ appear fully amorphous while $Fe_{60.9}Mn_{16}Mo_4C_5B_{14.1}$ has no apparent amorphous phase. The main crystallisation product is the $M_{23}(C,B)_6$ phase while a small amount of α-iron is also present.

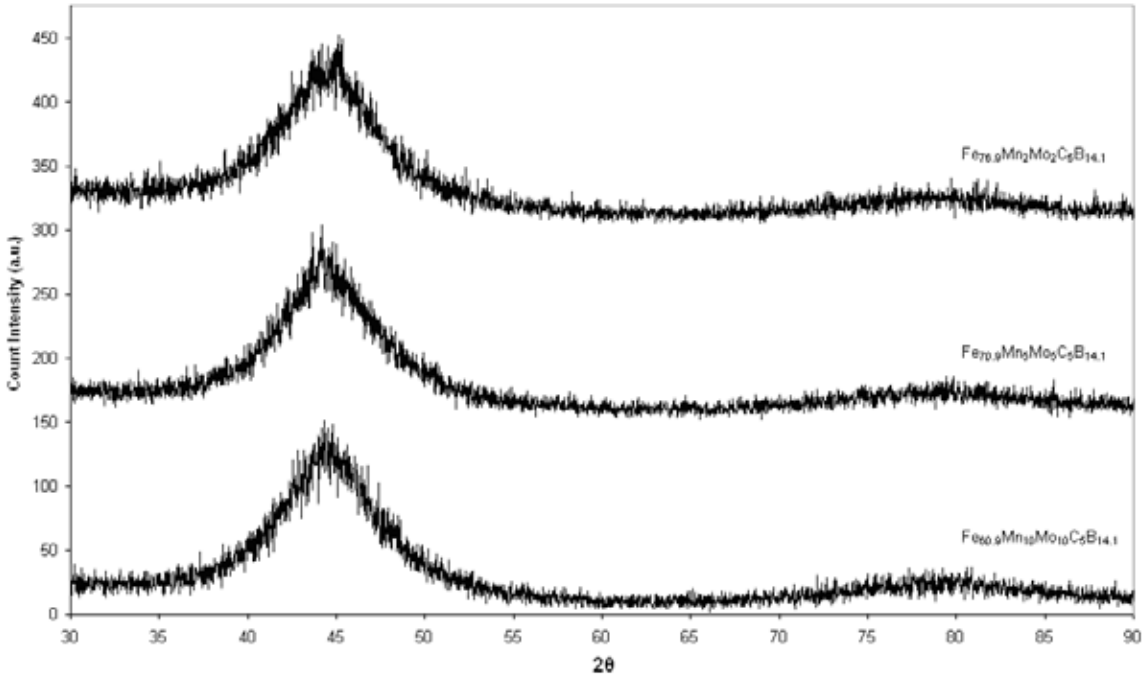

Figure 5.23 XRD traces showing smooth broad peaks for all the $Fe_{80.9-x}(Mn_{50}Mo_{50})_xC_5B_{14.1}$ group. This indicates the three compositions may be fully amorphous.

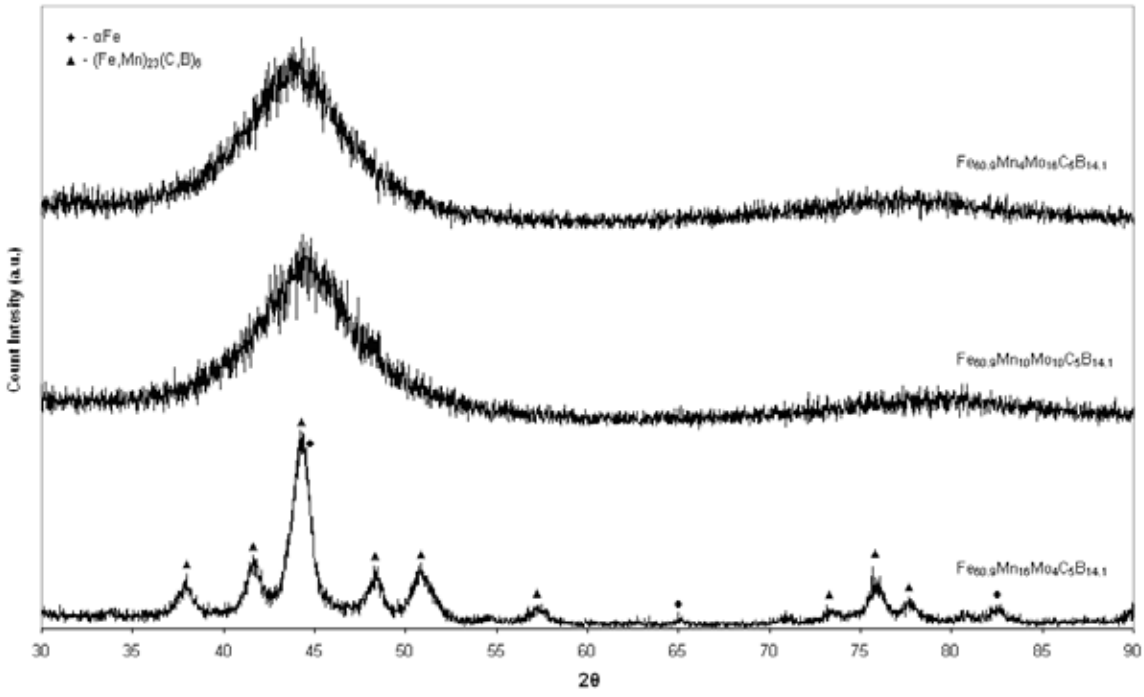

Figure 5.24 XRD traces for the $Fe_{60.9}Mn_xMo_{20-x}C_5B_{14.1}$ group. The smooth broad peaks for $Fe_{60.9}Mn_4Mo_{16}C_5B_{14.1}$ and $Fe_{60.9}Mn_{10}Mo_{10}C_5B_{14.1}$ indicate these compositions may be fully amorphous. The trace for $Fe_{60.9}Mn_{16}Mo_4C_5B_{14.1}$ has several strong narrow peaks which indicate the composition may be fully crystalline.

5.3.2 Differential Scanning Calorimetry (DSC)

5.3.2.1 Devitrification of the Amorphous Phase

Figures 5.25 to 5.28 show the DSC traces of all compositions for the temperature range around where crystallisation occurred in the base alloy. The glass transition temperature is not apparent in any of the traces. Lack of T_g is sometimes attributed to vitrification occurring through growth control rather than nucleation control, meaning that even in alloys which appear fully amorphous by XRD there are a number of quenched in nuclei which can grow rapidly as T_g of the matrix is approached, thereby masking the T_g signal. Alternatively the amorphous alloy can be thought of as a 'fragile glass' (one that is not particularly resistant to re-ordering) where glass transition and crystallisation temperatures coincide.

Figure 5.25 shows the traces for the $Fe_{80.9-x}Mn_xC_5B_{14.1}$ group (where x = 2, 5, 10 or 20). There is a single peak for each composition. It can be seen that the peak crystallisation temperature (T_{xp}) rises with increasing manganese content. The peak for $Fe_{60.9}Mn_{20}C_5B_{14.1}$ is the most shallow and is likely to be due to crystallisation of the residual amorphous phase, rather than coarsening of the crystals already present. (From XRD trace in figure 5.21 it is obvious that the melt-spun ribbon is partially crystalline).

Figure 5.26 shows the traces for the $Fe_{80.9-x}Mo_xC_5B_{14.1}$ group (where x = 2, 5, 10 or 20). For $Fe_{78.9}Mo_2C_5B_{14.1,}$ $Fe_{75.9}Mo_5C_5B_{14.1}$ and $Fe_{60.9}Mo_{20}C_5B_{14.1}$ there is a single sharp peak and T_{xp} rises with increasing molybdenum content. $Fe_{70.9}Mo_{10}C_5B_{14.1}$ has an exothermic event occurring over a broad range and starting at a lower temperature than the other compositions. The XRD trace for this composition (seen in figure 5.22) show that it is

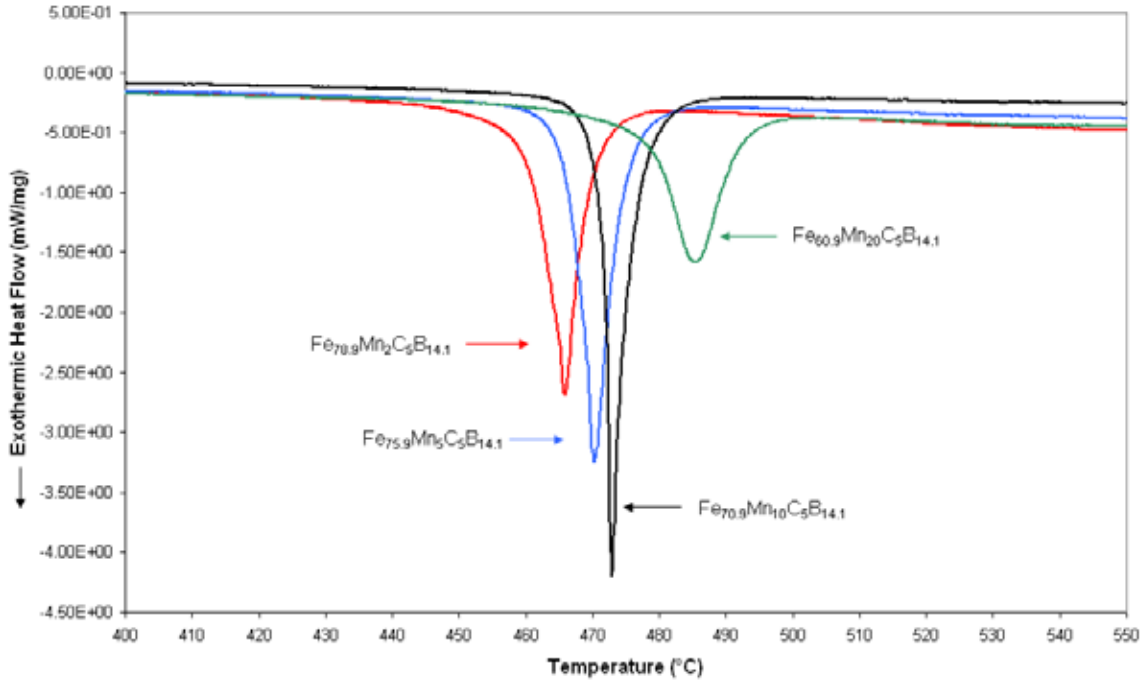

Figure 5.25 DSC traces showing crystallisation occurring in the $Fe_{80.9-x}Mn_xC_5B_{14.1}$ group.

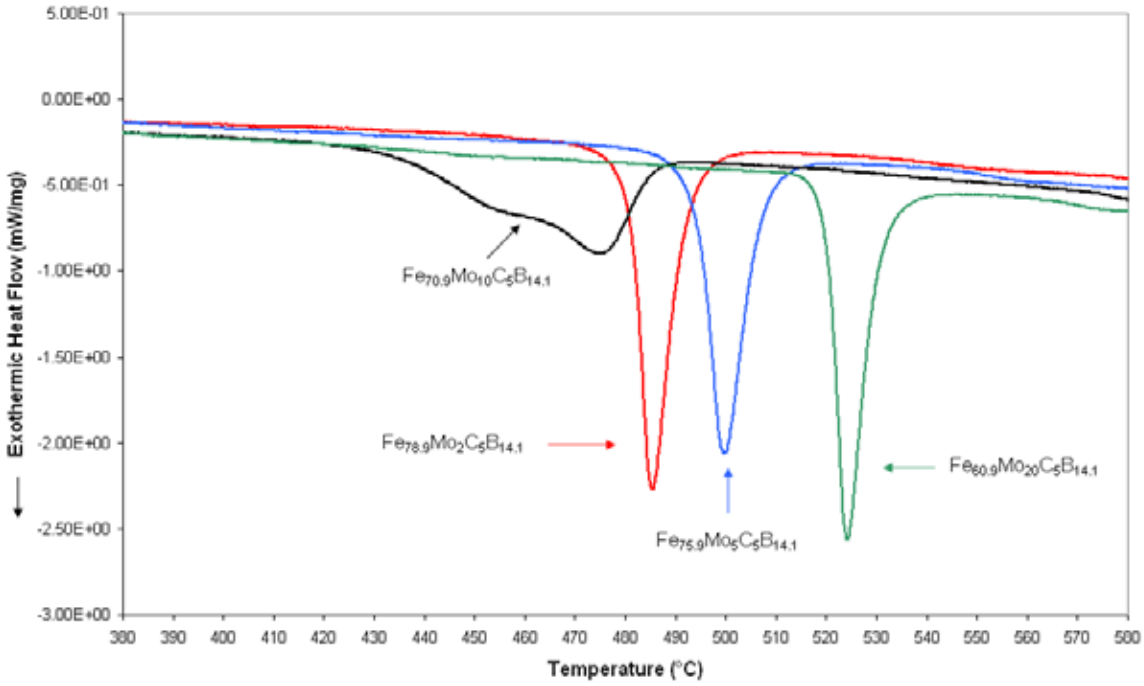

Figure 5.26 DSC traces showing crystallisation occurring in the $Fe_{80.9-x}Mo_xC_5B_{14.1}$ group.

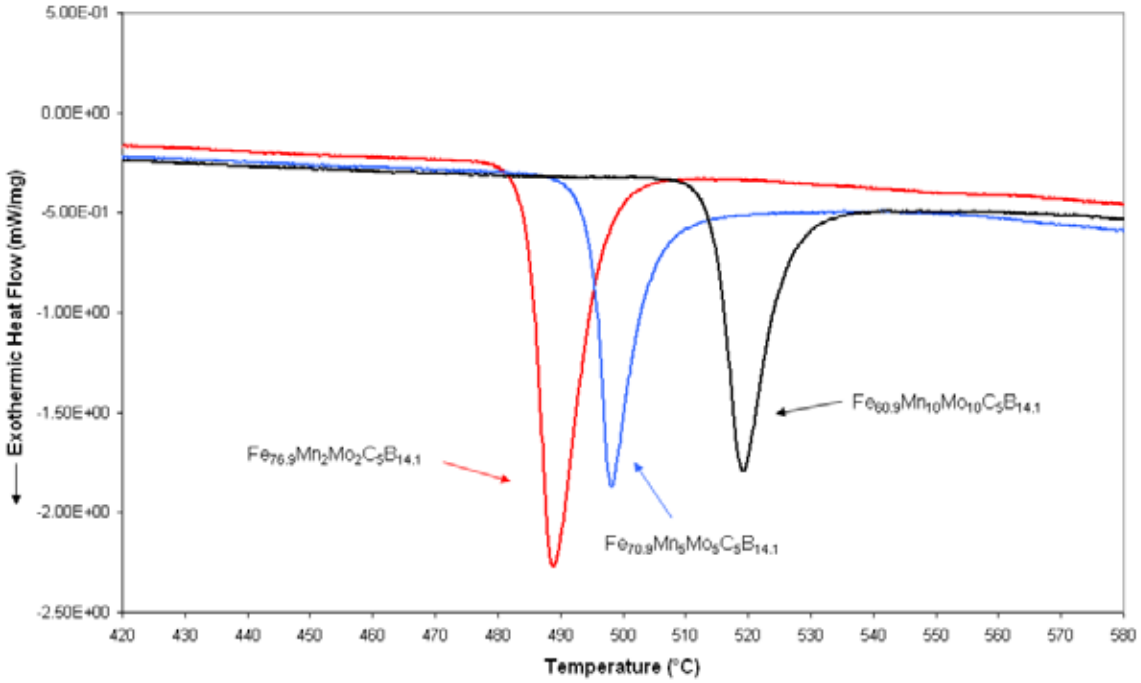

Figure 5.27 DSC traces showing crystallisation occurring in the $Fe_{80.9-x}(Mn_{50}Mo_{50})_xC_5B_{14.1}$ group.

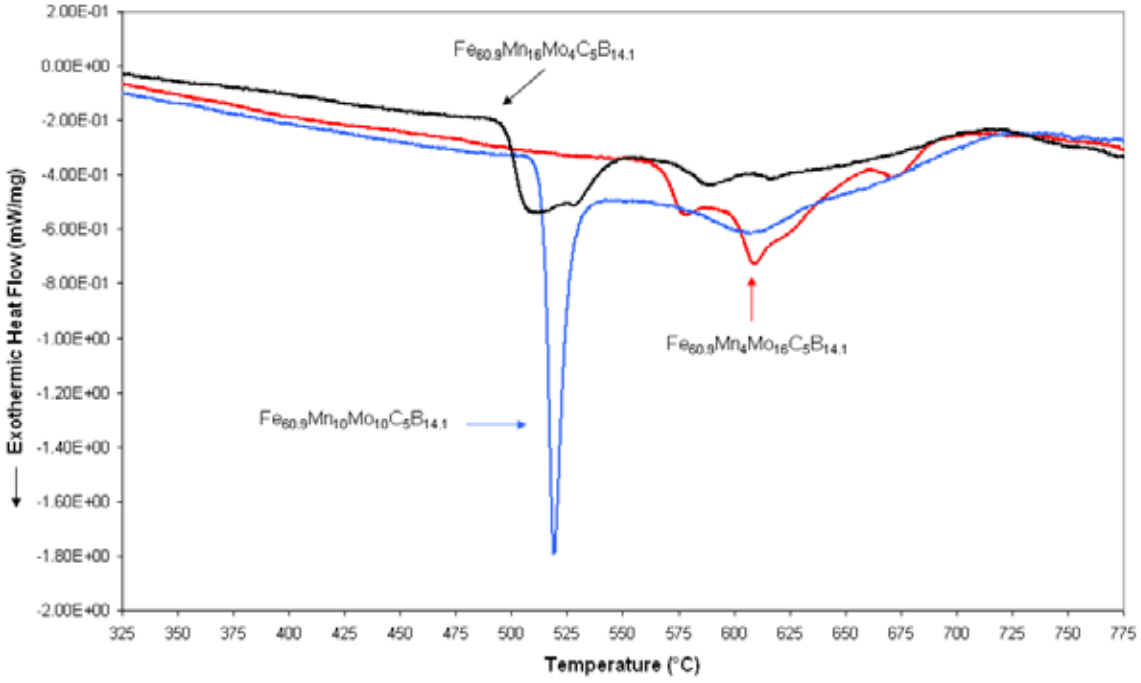

Figure 5.28 DSC traces showing crystallisation occurring in the $Fe_{60.9}Mn_xMo_{20-x}C_5B_{14.1}$ group.

highly crystalline as there are sharp diffraction peaks for $Fe_3(C,B)$ and αFe, while the broad amorphous peak is barely visible. This indicates the exothermic event is showing crystallisation of the residual amorphous phase along with coarsening of the crystals that are already present.

Figure 5.27 shows the traces for the $Fe_{80.9-x}(Mn_{50}Mo_{50})_xC_5B_{14.1}$ group (where x = 4, 10 or 20) There is a single sharp peak for each composition and T_{xp} rises with increasing manganese and molybdenum content.

Figure 5.28 shows the traces for the $Fe_{60.9}Mn_xMo_{20-x}C_5B_{14.1}$ group (where x = 4, 10 or 20). The onset of the exothermic events rises with each increase in the Mo/Mn ratio. For $Fe_{60.9}Mn_{16}Mo_4C_5B_{14.1}$ the exothermic events are probably not due to crystallisation and are more likely to be the result of coarsening of crystals, as there is no evidence of a broad peak in its XRD trace (figure 5.24). The XRD diffraction peaks are well defined but are relatively broad compared to the XRD traces of the fully crystalline ternary alloys (figures 4.16 and 4.22) so the crystals are smaller. For $Fe_{60.9}Mn_{10}Mo_{10}C_5B_{14.1}$ there is a single sharp peak followed by a broad shallow hump. This is assumed to represent full crystallisation of the amorphous material followed by coarsening of the grains. For $Fe_{60.9}Mn_4Mo_{16}C_5B_{14.1}$ there are multiple peaks which most likely represent crystallisation and coarsening of the three phases seen in the optical image of the as-cast material (figure 5.14).

5.3.2.2 Melting

Figure 5.29 shows the traces for the $Fe_{80.9-x}Mn_xC_5B_{14.1}$ group (where x = 2, 5, 10 or 20). This is a move towards an invariant (or even eutectic) composition which can be seen by the gradual merging of the melting peaks of the different phases: for $Fe_{78.9}Mn_2C_5B_{14.1}$ there are two distinct peak tips close to one another while for $Fe_{60.9}Mn_{20}C_5B_{14.1}$ the melting temperatures of the phases are so close that they are indistinguishable.

Figure 5.30 shows the traces for the $Fe_{80.9-x}Mo_xC_5B_{14.1}$ group (where x = 2, 5, 10 or 20). $Fe_{75.9}Mo_5C_5B_{14.1}$ and $Fe_{78.9}Mo_2C_5B_{14.1}$ are similar in that their melting ranges are both centred around 1130°C, but the range for $Fe_{75.9}Mo_5C_5B_{14.1}$ is narrower which indicates that of the two alloys this one is closer to an invariant composition. $Fe_{70.9}Mo_{10}C_5B_{14.1}$ has the highest liquidus temperature and only one distinct peak. This is the alloy which had a much different microstructure from the other alloys in the group and was also the only one to be highly crystalline after melt-spinning.

Figure 5.31 shows the traces for the $Fe_{80.9-x}(Mn_{50}Mo_{50})_xC_5B_{14.1}$ group (where x = 4, 10 or 20). All the alloys have a melting range centred around 1125°C. $Fe_{60.9}Mn_{10}Mo_{10}C_5B_{14.1}$ has two distinct peaks close to one another while $Fe_{70.9}Mn_5Mo_5C_5B_{14.1}$ and $Fe_{76.9}Mn_2Mo_2C_5B_{14.1}$ appear to have two peaks almost fully merged. The melting range for $Fe_{70.9}Mn_5Mo_5C_5B_{14.1}$ is slightly narrower than for $Fe_{76.9}Mn_2Mo_2C_5B_{14.1}$, so this alloy is nearest to an invariant composition.

Figure 5.32 shows the traces for the $Fe_{60.9}Mn_xMo_{20-x}C_5B_{14.1}$ group (where x = 4,10 or 20). $Fe_{60.9}Mn_{10}Mo_{10}C_5B_{14.1}$ and $Fe_{60.9}Mn_{16}Mo_{20-x}C_5B_{14.1}$ have a similar profile but the melting range is larger for $Fe_{60.9}Mn_{10}Mo_{10}C_5B_{14.1}$ and it has two distinct peaks. Although

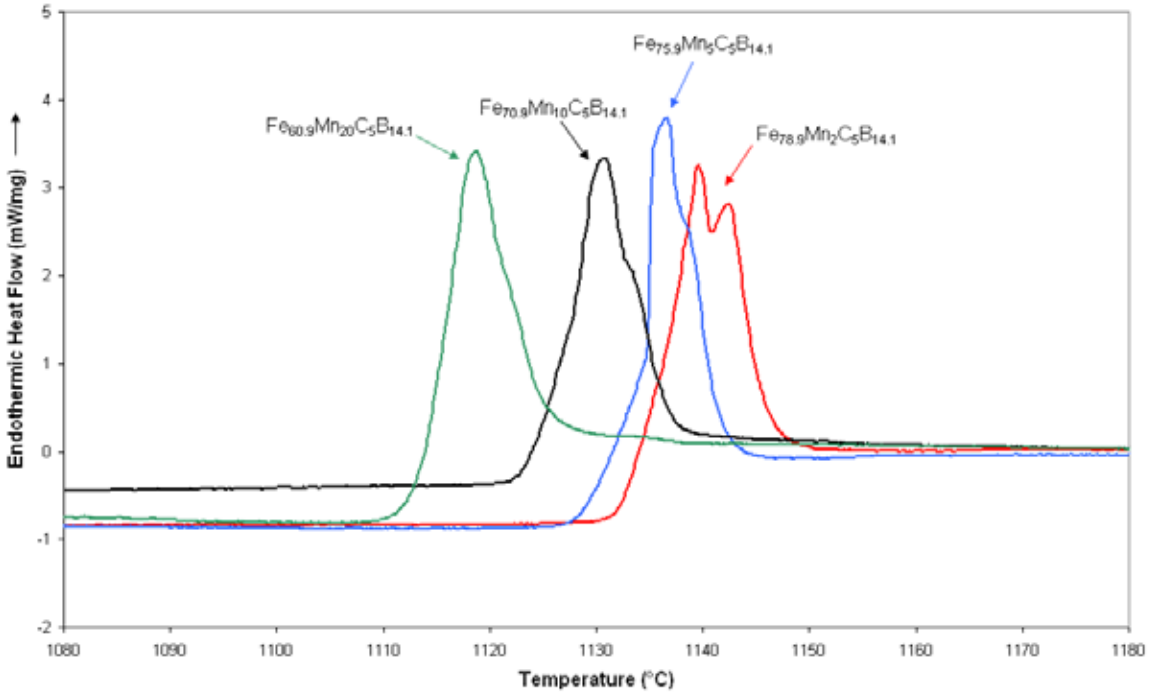

Figure 5.29 DSC traces showing melting behaviour in the $Fe_{80.9-x}Mn_xC_5B_{14.1}$ group.

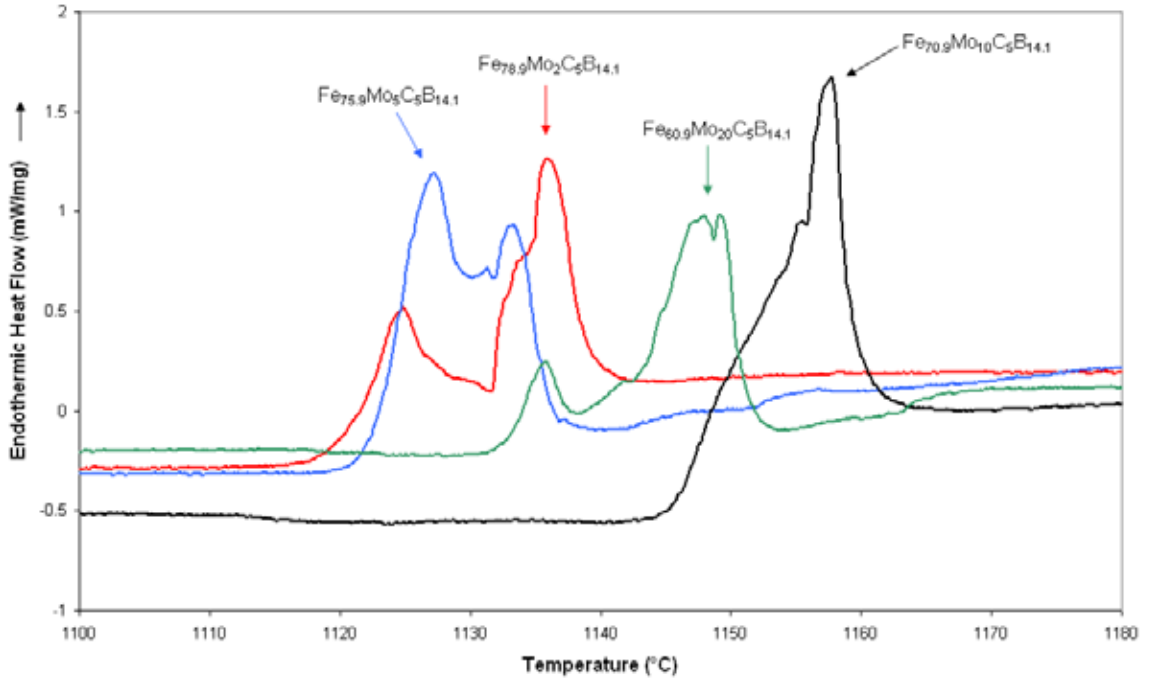

Figure 5.30 DSC traces showing melting behaviour in the $Fe_{80.9-x}Mo_xC_5B_{14.1}$ group.

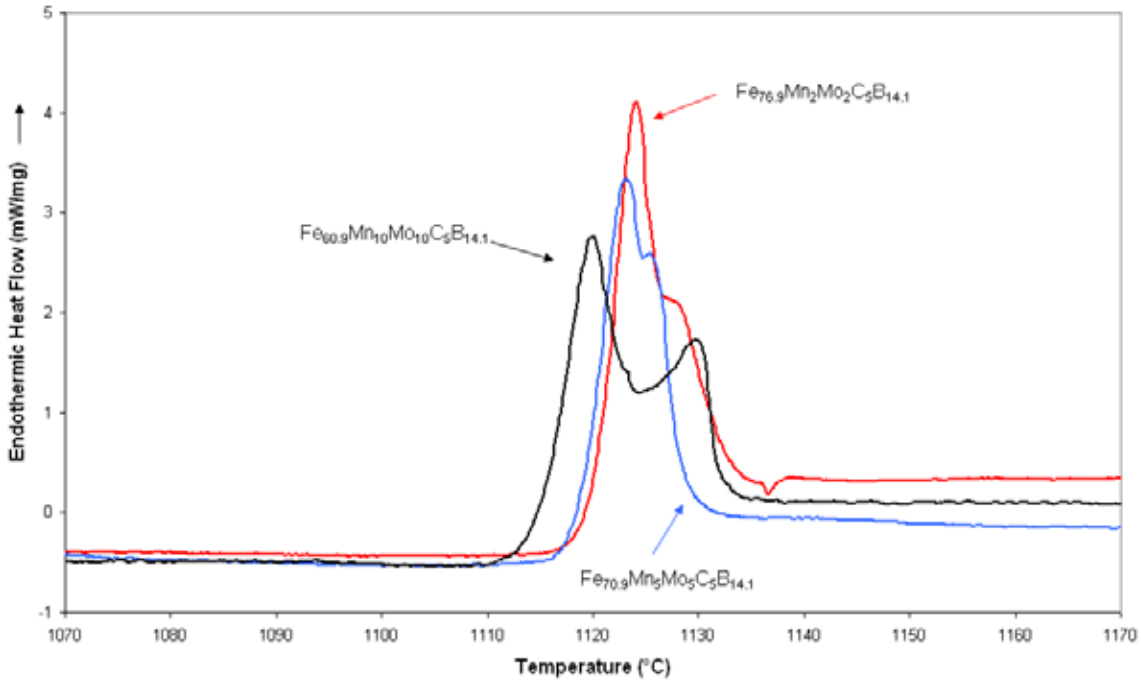

Figure 5.31 DSC traces showing the melting behaviour of the $Fe_{80.9-x}(Mn_{50}Mo_{50})_xC_5B_{14.1}$ group.

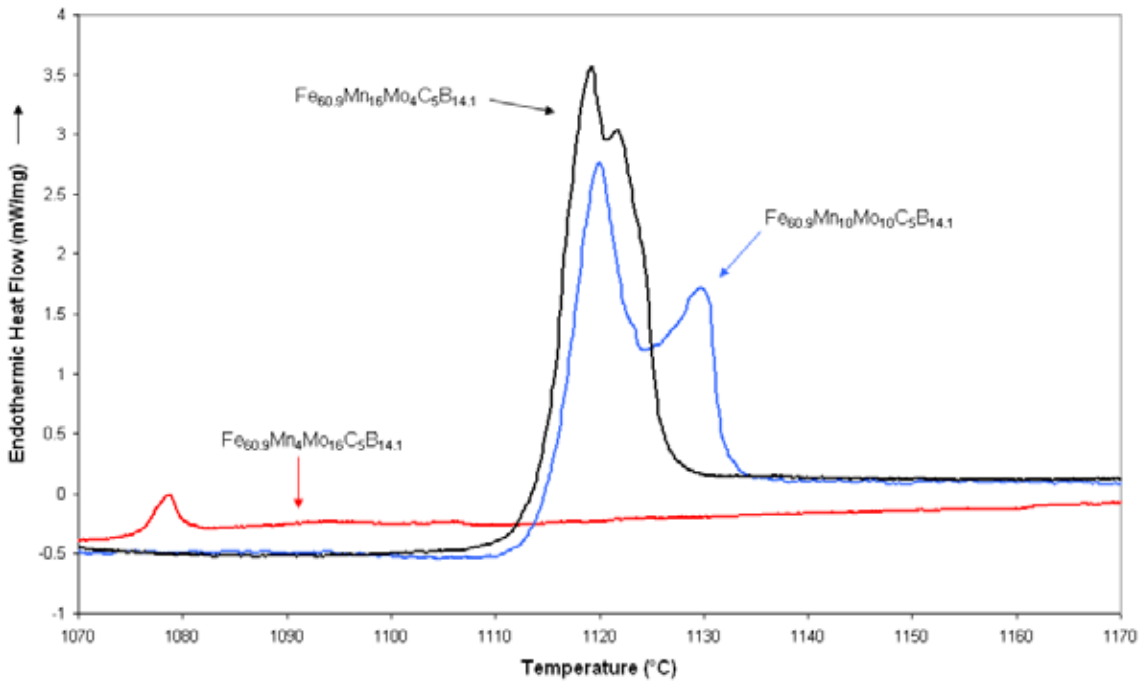

Figure 5.32 DSC traces showing melting behaviour of the $Fe_{60.9}Mn_xMo_{20-x}C_5B_{14.1}$ group.

$Fe_{60.9}Mn_{16}Mo_4C_5B_{14.1}$ is closer to an invariant composition this alloy did not show an amorphous phase in its XRD trace (figure 5.24). The melting behaviour for $Fe_{60.9}Mn_4Mo_{16}C_5B_{14.1}$ was not fully revealed due to the limits of the calorimeter. If the melting behaviour can be inferred from the microstructure of the as-cast alloy (figure 5.14) then small peak at 1075°C most likely represents the melting of the residual single phase compound. Therefore, this indicates a solidification sequence quite different from the other alloys as the invariant temperature is much lower.

5.3.3 Hardness Testing

Figure 5.33 is a bar chart showing the Vickers hardness of the melt-spun ribbons of the base alloy ($Fe_{80.9}C_5B_{14.1}$) and all the multi-component alloys. The first thing that can be seen is that in general the additions to the base alloy have softened the melt-spun material, with exceptions being the quinary alloys containing 60.9 atomic% of iron, where there is only a marginal increase in hardness.

In the $Fe_{80.9-x}Mn_xC_5B_{14.1}$ group there is a trend for hardness to increase as the Mn/Fe ratio increases.

In the $Fe_{80.9-x}Mo_xC_5B_{14.1}$ group there is a trend for the hardness to increase as the Mo/Fe ratio increases. An obvious exception is $Fe_{70.9}Mo_{10}C_5B_{14.1}$ which has the lowest HV of all the alloys. This alloy is highly crystalline and has an obscured amorphous peak in its XRD trace (figure 5.22).

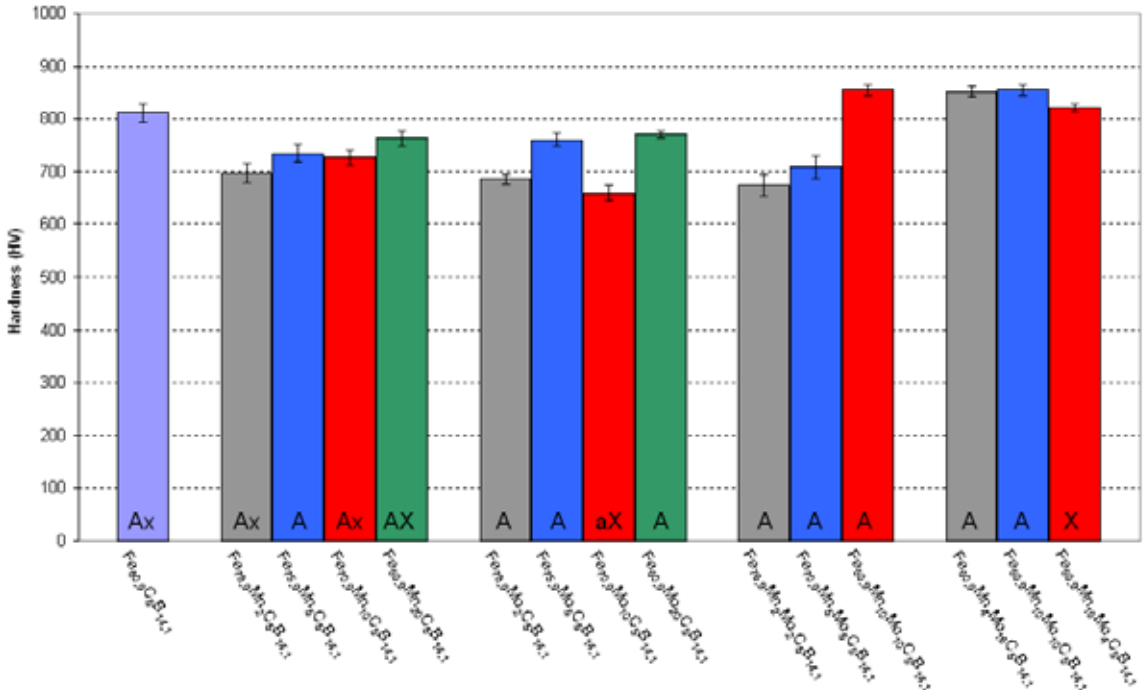

Figure 5.33 Hardness values of the multi-component alloys and the ternary base-alloy, with error bars showing standard deviation. A = broad amorphous peak, a = weak amorphous peak, X = strong sharp peaks, x = weak spikes in XRD traces.

In the $Fe_{80.9-x}(Mn_{50}Mo_{50})_xC_5B_{14.1}$ group there is a trend is for hardness to increase as the (MnMo)/Fe ratio increases.

In the $Fe_{60.9}Mn_xMo_{20-x}C_5B_{14.1}$ group the hardness values are similar to one another and all slightly higher than for the base alloy. The HV of $Fe_{60.9}Mn_{16}Mo_4C_5B_{14.1}$ is marginally lower than the other two compositions but it should be noted that this is the alloy which appears fully crystalline in its XRD trace (figure 5.24).

5.4 Discussion

5.4.1 Observation of As-Cast Microstructure

In Chapter 4 it was shown that as-cast microstructure alone could not be used to predict whether or not a particular alloy would form an amorphous phase on rapid solidification of the melt. This finding is corroborated by the results for the multi-component alloys in this chapter: there was more than one type of microstructure yet an amorphous phase was produced by each composition (apart from $Fe_{60.9}Mn_{16}Mo_4C_5B_{14.1}$).

5.4.2 Glass Forming Ability of Multi-Component Fe-Based Systems

In literature some of the terms used in describing GFA are: the liquidus temperature (T_l); the crystallisation temperature (T_x); the reduced glass transition temperature (T_{rg}); the gamma-parameter (γ); the delta-parameter (δ); and the alpha-parameter (α). These are listed for the multi-component alloys in table 5.2 and will be referred to in the subsequent discussions. T_{rg}, γ and δ all show the same trends so for sake of clarity only δ will be used as it is the most recently developed indicator of GFA and also shows a more pronounced difference within a system.

Table 5.2 Some thermal parameters of the multi-component alloys. T_{rg}, γ and δ were calculated using the crystallisation temperature (T_x) as a substitute for the glass transition temperature which was not apparent in the traces from differential scanning calorimetry.

Alloy	α	T_x (K)	T_l(K)	T_{rg}	γ	δ
$Fe_{80.9}C_5B_{14.1}$	1.441	727	1428	0.509	0.337	1.037
$Fe_{78.9}Mn_2C_5B_{14.1}$ *	1.428	733	1420	0.516	0.340	1.067
$Fe_{75.9}Mn_5C_5B_{14.1}$	1.407	738	1415	0.522	0.343	1.090
$Fe_{70.9}Mn_{10}C_5B_{14.1}$ *	1.382	744	1410	0.527	0.345	1.117
$Fe_{60.9}Mn_{20}C_5B_{14.1}$ *	1.349	750	1399	0.536	0.349	1.156
$Fe_{78.9}Mo_2C_5B_{14.1}$	1.401	753	1412	0.533	0.348	1.143
$Fe_{75.9}Mo_5C_5B_{14.1}$	1.349	766	1409	0.544	0.352	1.191
$Fe_{70.9}Mo_{10}C_5B_{14.1}$ *	1.290	706	1433	0.493	0.330	0.971
$Fe_{60.9}Mo_{20}C_5B_{14.1}$	1.226	792	1425	0.556	0.357	1.251
$Fe_{76.9}Mn_2Mo_2C_5B_{14.1}$	1.384	757	1406	0.538	0.350	1.166
$Fe_{70.9}Mn_5Mo_5C_5B_{14.1}$	1.311	767	1402	0.547	0.354	1.208
$Fe_{60.9}Mn_{10}Mo_{10}C_5B_{14.1}$	1.222	787	1405	0.560	0.359	1.273
$Fe_{60.9}Mn_4Mo_{16}C_5B_{14.1}$	1.220	839	1573[e]	0.533	0.347	1.143
$Fe_{60.9}Mn_{16}Mo_4C_5B_{14.1}$ *	1.260	770	1399	0.550	0.355	1.224

* Obvious crystallinity in the XRD traces of the melt-spun ribbons.
[e] Estimated temperature.

5.4.2.1 The Alpha Parameter

In Chapter 4 it was shown liquidus temperatures predicted by ThermoCalc were reasonable values although they were slightly lower than for the experimentally determined ones. The α-parameter for each of the alloys was determined using calculated values. Marginal glass forming tendency was predicted for all the ternary alloys except $Fe_{80}C_{14.8}B_{5.2}$ (alloy 1) where the possibility of bulk metallic glass formation was indicated. This alloy was fully crystalline after melt-spinning, as were four others, so it was concluded that the α-parameter was not suitable for predicting GFA in the ternary compositions.

The α-parameter was calculated for the multi-component alloys in order to see if moving to systems larger than ternary would improve its suitability for GFA prediction. From table 5.2 it can be seen that α values are all lower than for the base alloy $Fe_{80.9}C_5B_{14.1}$, implying that increasing the complexity of the system would be detrimental to GFA, even though the results show that an amorphous phase was formed in most of the alloys. The unsuitability of this predictive tool for iron-based systems is not fully confirmed though. It is probable that the α values are erroneous because it appears that the ThermoCalc is unable to calculate accurate liquidus temperatures for complex systems due to the database used containing insufficient information. For example: $Fe_{60.9}Mo_{20}C_5B_{14.1}$, which appeared fully amorphous in its XRD trace (figure 5.22), has a measured T_l of 1425 K while the calculated value is 1808 K.

5.4.2.2 The Effect of Manganese Addition to $Fe_{80.9}C_5B_{14.1}$

The addition of manganese to the base alloy improves the stability of the amorphous phase – i.e. increases the onset of crystallisation temperature (T_x) – and depresses the liquidus temperature (see figures 5.25 and 5.29 respectively). With each increase in manganese content T_x is increased and T_l is lowered. It might be expected that the composition with the lowest T_l ($Fe_{60.9}Mn_{20}C_5B_{14.1}$) would be the easiest to vitrify, but strong diffraction peaks can be seen in its XRD trace (figure 5.21) meaning it was the most difficult composition to vitrify. $Fe_{78.9}Mn_2C_5B_{14.1}$ and $Fe_{70.9}Mn_{10}C_5B_{14.1}$ have some diffraction peaks in their XRD traces so $Fe_{75.9}Mn_5C_5B_{14.1}$, having no obvious crystallinity, is considered to have the best GFA in the $Fe_{80.9-x}Mn_xC_5B_{14.1}$ group. δ should not really be used to compare within the group as it would actually be comparing the GFA of the residual amorphous matrix which would not have the composition of the liquid.

5.4.2.3 The Effect of Molybdenum Addition to $Fe_{80.9}C_5B_{14.1}$

The addition of molybdenum to the base alloy improves the stability of the amorphous phase and depresses the liquidus temperature (see figures 5.26 and 5.30 respectively) in most cases. Unlike the Mn additions, the change in thermodynamic properties does not show a correlation with the quantity of Mo in the alloys. However, there is correlation with the as-cast microstructures. $Fe_{78.9}Mo_2C_5B_{14.1}$ and $Fe_{75.9}Mo_5C_5B_{14.1}$ have the same features (figures 5.7 and 5.8): dendrites containing small crystals, in a matrix consisting of interpenetrating fine dendrite arms and a eutectic phase in the residual interdendritic regions. These two have similar melting behaviours both centred around 1130°C. $Fe_{70.9}Mo_{10}C_5B_{14.1}$ and $Fe_{60.9}Mo_{20}C_5B_{14.1}$ follow a different solidification path as they both show a faceted phase as well as a dendritic phase. $Fe_{60.9}Mo_{20}C_5B_{14.1}$ has a matrix similar to

$Fe_{78.9}Mo_2C_5B_{14.1}$ and $Fe_{75.9}Mo_5C_5B_{14.1}$ (figures 5.7 and 5.8), whereas two primary phases of $Fe_{70.9}Mo_{10}C_5B_{14.1}$ appear to make up most, if not all, of the microstructure (figure 5.9) meaning this alloy is the furthest from a eutectic composition. This is also the composition which had a weak amorphous peak obscured by sharp diffraction peaks in its XRD trace (figure 5.22). This is backed up by the DSC traces of their melting behaviour (figure 5.26). For $Fe_{70.9}Mo_{10}C_5B_{14.1}$ the peaks are centred at 1155°C and are almost fully merged, but for $Fe_{60.9}Mo_{20}C_5B_{14.1}$ the peaks of the primary phases are almost fully merged and are centred at 1145°C while there is a clearly separate peak for the residual eutectic phases at 1135°C. $Fe_{78.9}Mo_2C_5B_{14.1}$, $Fe_{75.9}Mo_5C_5B_{14.1}$ and $Fe_{60.9}Mo_{20}C_5B_{14.1}$ all appear to be amorphous according to their XRD traces (figure 5.22). $Fe_{60.9}Mo_{20}C_5B_{14.1}$ is considered to have the best GFA of the three compositions because it has the highest δ value.

5.4.2.4 The Effect of Manganese and Molybdenum Addition to $Fe_{80.9}C_5B_{14.1}$

As with individual additions of manganese and molybdenum, the addition of both elements to the base alloy once again stabilises the amorphous phase (figures 5.27 and 5.28) and depresses the liquidus temperature in most cases (figures 5.31 and 5.32). The melting peaks for alloys where the Mn/Mo ratio is 1:1 are all centred around 1125°C, while the DSC traces show T_x is improved with each increase in the quantity of Mn and Mo. The melting peaks for alloys where the Mn/Mo ratio varies are also all centred around 1125°C, except for $Fe_{60.9}Mn_4Mo_{16}C_5B_{14.1}$ – which has the unique microstructure containing B_2FeMo_2 crystals (figure 5.14) – where full melting behaviour is not revealed. T_x is improved with each decrease in the Mn/Mo ratio. This is due to the increasing proportion of molybdenum, which has a greater effect on thermal stability than does manganese. This can be seen in table 5.2 which shows that the quaternary alloys containing Mo have higher

T_x values (apart from the value for $Fe_{70.9}Mo_{10}C_5B_{14.1}$, which represents crystallisation from a residual amorphous phase) than any of those containing Mn. Of the quinary compositions, $Fe_{60.9}Mn_{10}Mo_{10}C_5B_{14.1}$ is considered to have the best GFA because it shows no obvious crystallinity in its XRD trace (figure 5.24) and has the highest δ value.

5.4.2.5 Glass Forming Ability of Multi-Component Alloys

As mentioned in the literature review, three empirical guidelines were derived in order to facilitate the development of new amorphous systems, particularly with melt-processing techniques in mind.

The first guideline is "the alloy should be a multi-component system containing more than three elements". The reasoning behind this is that the size and complexity of a crystal unit cell would be increased thus making it harder to form an ordered structure, and less thermodynamically favourable than a simpler crystal system.

The second is "that there should be significant atomic size ratio above 12% for the three main elements". This requirement means that crystal structures become destabilised due to strain in the crystal lattice. It also leads to a higher packing density in the liquid state, thus raising diffusion coefficients, and increasing viscosity, thereby creating kinetic hindrance to the atomic arrangement necessary for nucleation and growth of crystals.

The third is "there should be negative heat of mixing between the elements". This leads to clustering of atoms in the melt thus reducing the chances of critical sized embryos forming.

Iron was selected as the solvent element for this study on the basis of cost and the fact that the only database available for thermodynamic modelling in ThermoCalc was a steels one. This made design of the multi-component alloy with regard to the empirical guidelines and the subsequent refinements problematical. The refinements' main thrust is for an increase in the atomic size ratio but the database is limited to which alloying additions could be selected. Manganese and molybdenum were chosen solely on the basis that they are almost the same size (radii of 136.7pm and 136.3pm respectively [146]) but have different effects on the crystal structure of iron.

Mn and Mo might not be expected to enhance the GFA of $Fe_{80.9}C_5B_{14.1}$ as they do not completely satisfy the three guidelines. The first requirement is satisfied as the system is moving from ternary to quaternary or quinary. The second guideline is partially satisfied as Mn and Mo are approximately only 10% larger than iron (which has a radius of 124.1pm [146]). This means they are substitutional atoms with regard to iron and would not be expected to introduce enough strain into the crystal lattice to cause destabilisation. However, the 10% difference is probably sufficient to improve packing density in the melt and therefore improve viscosity and decrease diffusivity. The third guideline is also only partially satisfied. The heat of mixing for Fe-Mo is negative (-9kJ) while for Fe-Mn it is positive (+1kJ) [147]. The heat of mixing value for Fe-Mn is so small, and as Mn is substitutional with Fe, it is thought that in terms of causing clustering it will not have a significant effect as the majority of clustering is likely to be between iron and boron where the heat of mixing is (-26kJ) [147].

It evident that the addition of Mn and Mo did, in general, improve the GFA of the base alloy even though there was only partial satisfaction of the empirical guidelines. In terms of Poon's classification of bulk metallic glasses all compositions in this project almost fall under the LS category [27] and would be written (Fe,Mn,Mo)-C-B. Given that Mo is only 10% larger than Fe it should be noted that in table 2.1 Fe-Cr-C-B-P-(Mo) is wrongly classified as MSL if the medium (M), small (S) and large (L) atomic size ratios are supposed to follow the guideline requirement of a differences of 12% or greater. The qualifier of 'almost' means that although the sizes are correct the proportions are wrong as the quantity of small atoms should be between 25-60 at% and in the alloys with the best GFA they only total 19.1 at%.

Of the alloys where there is no obvious crystallinity in the XRD traces, the two alloys with the best GFA are $Fe_{60.9}Mo_{20}C_5B_{14.1}$ and $Fe_{60.9}Mn_{10}Mo_{10}C_5B_{14.1}$ with δ values of 1.251 and 1.273 respectively. The improvement of the quinary over the quaternary alloy may not be due to the increased satisfaction of the empirical guidelines for selecting glass forming compositions. Manganese and molybdenum are almost the same size and could be considered substitutional atoms so there is not much increase in the complexity of the system when changing from one alloying element to two. Also, there is no change in satisfaction of the second guideline because the packing density between the compositions will not vary as the additions total 20 atomic% in both cases. The improvement of the quinary over the quaternary alloy must therefore be due to another explanation. Mn and Mo were selected because of their effects on the crystal structure of iron. It is proposed that competition for nucleation between the austenite and alpha stabilisers (Mn and Mo respectively) causes further stabilisation of the supercooled liquid and is the reason for the enhancement in GFA of the quinary alloy.

CHAPTER 6

CONCLUSIONS AND FUTURE WORK

6.1 Conclusions

The findings of this project can be summarised as follows:

1. Glass forming compositions in iron-based systems cannot be predicted by the study of as-cast microstructure. The assumption being that good glass forming ability (GFA) in multi-component alloys follows the well known finding for binary alloys where good GFA is found at, or close to eutectic compositions. It was shown that even for alloys whose microstructures were clearly not eutectic (i.e. consisting of a matrix of interpenetrating dendrites with small residual interdendritic pockets of eutectic material) it was possible for an amorphous phase to be present after rapid solidification of the melt.

2. The alpha-parameter, which is an indicator of the relative depth of a eutectic composition (or at least the relative deviation of a calculated liquidus temperature from the temperature of an ideal solution), cannot be used to predict compositions with good GFA in iron-based systems. Marginal glass forming ability was suggested for all ternary alloys apart from $Fe_{80}C_{14.8}B_{5.2,}$ where possible bulk glass formation was indicated. However, after rapid solidification, $Fe_{80}C_{14.8}B_{5.2}$ did not form an amorphous phase and was fully crystalline. The alpha-parameter of the multi-component alloys could not be used as an indicator of GFA due to the unreliability of the values which are thought to have been calculated using a database with insufficient information.

3. The cooling rate provided by the melt-spinning equipment was insufficient to allow full vitrification of any composition. This is shown by the absence of the glass transition temperature in the traces from differential scanning calorimetry (DSC). This is believed to be caused by the rapid growth of quenched in nuclei at, or close to, the glass transition temperature. For many compositions this is certainly the case while for some others the lack of a glass transition could indicate the alloy is simply a fragile glass.

4. In the ternary Fe-C-B system vitrification was only possible for alloys where the compositions were close to the eutectic point of the liquidus projection by Vogel and Tammann [127]. It is believed that rapid cooling allows nucleation of primary equilibrium phases to be bypassed and that stabilisation of the supercooled liquid is due to competition between austenite and a metastable phase.

5. $Fe_{79.5}C_{3.5}B_{17}$ and $Fe_{80.9}C_5B_{14.1}$ were the only ternary alloys to show no obvious crystallinity in their X-ray diffraction (XRD) patterns. $Fe_{80.9}C_5B_{14.1}$ was selected as the base for the multi-component alloys as all glass forming parameters inidicated it had the best GFA of the two alloys.

6. The GFA of iron-based alloys is generally improved by moving from ternary to quaternary or larger systems. This is due to better, but not complete, satisfaction of the empirical rules for selecting glass forming compositions which in simple terms means that suppression of nucleation and growth of crystals is enhanced.

7. Of the multi-component alloys $Fe_{60.9}Mn_{10}Mo_{10}C_5B_{14.1}$ is considered to have the best GFA as it had the highest values among the various GFA parameters used. It is believed that this is due to competition between the austenite stabiliser (manganese) and the alpha stabiliser (molybdenum) causing enhanced stability of the supercooled liquid.

6.2 Future Work

1. This project has shown that the addition of elements to a ternary iron-based composition known to produce an amorphous phase (by the melt-spinning process) can result in improved GFA. It would be interesting to see if increasing the complexity of one of the ternary iron-based compositions which did not produce an amorphous phase would enable vitrification on rapid solidification.

2. The crystallisation behaviour of amorphous multi-component alloys in this project has not been studied. Further work would involve annealing, DSC and TEM, which could shed additional light on the GFA of the different systems. (i.e. Fe-Mn-C-B, Fe-Mo-C-B and Fe-Mn-Mo-C-B).

3. The cause of the highest GFA in the multi-component alloys is believed to be due to competition between an austenite stabiliser (Mn) and an alpha former (Mo). Neither of these elements satisfy the empirical guideline which requires that atoms should have a significant size difference (>12 atomic percent) with the solvent metal as they are only ten-percent larger than iron. The size difference will have some effect on the packing density and therefore the viscosity of the liquid. To determine how strong the effect of competition between austenite stabilisers and alpha formers is, the addition to the base alloy of elements with an even closer ratio to iron should be investigated. It is suggested that chromium (as the alpha former) and nickel (as the austenite stabiliser) would be ideal elements.

4. In terms of the empirical guideline requirement for large size differences, the multi-component systems studied only contained large atoms (Fe, Mn and Mo) and small atoms (C and B). The introduction of elements significantly larger than iron should enhance GFA of the alloys through strain induced destabilisation of the crystal lattice and improved packing density in the supercooled liquid. To this end there are many different options worth investigating. Aluminium, titanium and niobium are all significantly larger than iron and also have a strong negative heat of mixing with iron. Other suitable additions, at least in terms of size, would be yttrium, lanthanum, hafnium, or even the rare-earth mixtures known as mischmetal.

5. If thermodynamic modelling is not required an alternative low cost system that would be worth studying could be based on aluminium. In a similar manner to this study, compositions close to the eutectic point in the aluminium-silicon-calcium system (approximately $Al_{86}Si_{12}Ca_2$) might be expected to be easily vitrified. The alloying elements also have the benefit of fully satisfying the empirical guidelines, as Si is significantly smaller than Al and Ca is significantly larger, and they both have negative heat of mixing with Al.

REFERENCES

1. Janot, C., *Quasicrystals: A Primer*. Second Edition. Oxford University Press (1994). p1.
2. Nissen, H-U., and Beeli, C., *Electron Microscopy and Surface Investigations of Quasicrystals*, in *Quasicrystals: An Introduction to Structure, Physical Properties, and Applications*. Suck, J-B., Schreiber, M., Hussler, P., Editors. Springer-Verlag Berlin Heidelberg (2002).p115-116.
3. Suck, J.B., *Prehistory of Quasicrystals*, in *Quasicrystals: An Introduction to Structure, Physical Properties, and Applications*. Suck, J-B., Schreiber, M., Hussler, P., Editors. Springer-Verlag Berlin Heidelberg (2002).p3
4. Hashimoto, K., *Chemical Properties*, in *Amorphous Metallic Alloys*, Luborsky, F.E., Editor. Butterworth & Co. (Publishers) Ltd. (1983) p471-486.
5. Telford, M. *The Case for Bulk Metallic Glass.* Materials Today 7 (March 2004). 36-43.
6. Lemely, B. *Glassy Metal: Harder, Stronger, and Better – The Material of the Future.* Discover Magazine. April 2004.
7. Liu, Y.J., Chang, I.T.H., Lees, M.R. *Thermodynamic and Magnetic Properties of Multicomponent* $(Fe,Ni)_{70}Zr_{10}B_{20}$ *Amorphous Alloy Powders Made by Mechanical Alloying.* Materials Science and Engineering A304-306 (2001) 992-996.
8. Luborsky, F.E., *Amorphous Metallic Alloys*, in *Amorphous Metallic Alloys*, Luborsky, F.E., Editor. Butterworth & Co. (Publishers) Ltd. (1983) p1-7.
9. Warlimont, H. *Amorphous Metals Driving Materials and Process Innovations.* Materials Science and Engineering A304-306 (2001) 61-67.
10. Rao, K.V., *Electrical Transport Properties*, in *Amorphous Metallic Alloys*, Luborsky, F.E., Editor. Butterworth & Co. (Publishers) Ltd. (1983) p401-431.
11. Kim, Y-H., Inoue, A., Masumoto, T. *Ultrahigh Tensile Strengths of* $Al_{88}Y_2Ni_9M_1$ *(M=Mn or Fe) Amorphous Alloys Containing Finely Dispersed fcc-Al Particles.* Materials Transactions, JIM, Vol. 31, No.8 (1990), pp 747-749.
12. Inoue, A., Ohtera, K., Tsai, A-P., Masumoto, T. *Aluminium-Based Amorphous Alloys with Tensile Strength Above 980 MPa (100 kg/mm*^{2}*).* Japanese Journal Of Applied Physics, Volume 27, No. 4 (April 1988) pp. L479-L482.
13. http://www.liquidmetal.com, accessed: 3rd June 2008.
14. http://www.metglas.com, accessed: 3rd June 2008.
15. http://www.alfa-chemcat.com/onlinecatalogue/suche.asp, Alfa Aesar Online Catalogue, accessed: 12th February 2009.
16. Yu, P., Bai, H.Y., *Poisson's Ratio and Plasticity in CuZrAl Bulk Metallic Glasses*. Materials Science & Engineering A 485 (2008) 1-4.
17. Jia, P., Guo, H., Li, Y., Xu, J., Ma, E., *A New Cu-Hf-Al Ternary Bulk Metallic Glass With High Glass Forming Ability and Ductility*. Scripta Materialia 54 (2006) 2165-2168.
18. http://www.webelements.com, accessed: 3rd June 2008.
19. Zheng, Q., Cheng, S., Strader, J.H., Ma, E., Xu, J., *Critical Size and Strength of the Best Bulk Glass Former in the Mg-Cu-Gd Ternary System*. Scipta Materialia 56 (2007) 161-164.

20. Gittins, A., *Processing of Mg-Based Bulk Metallic Glass for Potential Sports Applications*. Final Year Project (2008) University of Birmingham.
21. Inoue, A., Wang, X.M., *Bulk Amorphous FC20 (Fe-C-Si) Alloys With Small Amounts of B and Their Crystallized Structure and Mechanical Properties*. Acta Materialia 48 (2000) 1383-1395.
22. Marcus, M., Turnbull, D., *On the Correlation Between Glass-Forming Tendency and Liquidus Temperature in Metallic Alloys*. Materials Science and Engineering 23 (1976) 211-214.
23. Bernal, J.D., *A Geometrical Approach to the Structure of Liquids*. Nature 183 (1959) 141-147.
24. http://en.wikipedia.org/wiki/Image:Coloured_Voronoi_2D.png, accessed: 23rd June 2008.
25. Scott,G.D., *Packing of Spheres*. Nature 188 (1960) 908-909.
26. Clarke, A.S., Wiley, J.D., *Numerical Simulation of the Dense Random Packing of a Binary Mixture of Hard Spheres: Amorphous Metals*. Physical Review B 35 (1987) 7350-7356.
27. Poon, S.J., Shiflet, G.J., Guo, F.Q., Ponnambalam, V., *Glass Formability of Ferrous- and Aluminium-Based Structural Metallic Alloys*. Journal of Non-Crystalline Solids 317 (2003) 1-9.
28. Miracle. D.B., Senkov, O.N., *A Geometric Model for Atomic Configurations in Amorphous Al Alloys*. Journal of Non-Crystalline Solids 319 (2003) 174-191.
29. Zachariasen, W.H., *The Atomic Arrangement in Glass*. Journal of the American Chemical Society 54 (1932) 3841-3851.
30. Imafuku, M., Sato, S., Matsubara, E., Inoue, A., *Structural Study of $Fe_{90-x}Nb_{10}B_x$ (x=10, 20 and 30) Glassy Alloys*. Journal of Non-Crystalline Solids 312-314 (2002) 589-593.
31. Inoue, A., *Stabilization of Metallic Supercooled Liquid and Bulk Amorphous Alloys*. Acta Materialia 48 (2000) 279-306.
32. Matsubara, E., Sato, S., Imafuku, M., Nakamura, T., Koshiba, H., Inoue, A., Waseda, Y., *Structural Study of Amorphous $Fe_{70}M_{10}B_{20}$ (M=Zr, Nb and Cr) Alloys by X-Ray Diffraction*. Materials Science and Engineering A 312 (2001) 136-144.
33. Senkov, O.N., Miracle, D.B., *Effect of the Atomic Size Distribution on Glass Forming Ability of Amorphous Metallic Alloys*. Materials Research Bulletin 36 (2001) 2183-2198.
34. Miracle, D.B. *On the Universal Model for Medium-Range Order in Amorphous Metal Structures*. Journal of Non-Crystalline Solids 317 (2003) 40-44.
35. Wang, W.H., Dong, C., Shek, C.H., *Bulk Metallic Glasses*. Materials Science and Engineering R 44 (2004) 45-89.
36. Shen J., Chen, Q., Sun, J., Fan, H., Wang, G., *Exceptionally High Glass-Forming Ability of an FeCoCrMoCBY Alloy*. Applied Physics Letters 86 (2005) 151907.
37. Lu, J., Ravichandran, G., Johnson, W.L., *Deformation Behaviour of the $Zr_{41.2}Ti_{13.8}Cu_{12.5}Ni_{10}Be_{22.5}$ Bulk Metallic Glass Over a Wide Range of Strain-Rates and Temperatures*. Acta Materialia 51 (2003) 3429-3443.
38. Inoue, A., Nishiyama, N., Kimura, H., *Preparation and Thermal Stability of Bulk Amorphous $Pd_{40}Cu_{30}Ni_{10}P_{20}$ Alloy Cylinder of 72mm in Diameter*. Materials Transactions, JIM 38 (1997) 179-183.
39. Kramer, J., *Über Nichtleitende Metallmodifikationen*, Annalen der Physik 411 (1934) 37-64.

40. Duwez, P., *Metallic Glasses*. American Society For Metals (1978) Forward.
41. Senkov, O.N., Uchic, M.D., Menon, S., Miracle, D.B., *Crystallization Kinetics of an Amorphous TiAl Sheet Produced by PVD*. Scripta Materialia 46 (2002)187-192.
42. Shin, J., Kim, H-W., Hwang, G.S., Ekerdt, J.G., *Chemical Routes to Ultra Thin Films for Copper Barriers and Liners*. Surface & Coatings Technology 201 (2007) 9526-9259.
43. Li, G., Gao, Y.P., Liu, R.P., *Binary Ni-P Bulk Amorphous Glass Prepared by Electrodepostion Method*. Journal of Non-Crystalline Solids 353 (2007) 4199-4202.
44. Wang, S-l., *Electroless Deposition of Ni-Co-B Alloy Films and Influence of Heat Treatment on the Structure and the Magnetic Performances of the Film*. Thin Solid Films 515 (2007) 8419-8423.
45. Berkowitz, A.E., Hansen, M.F., Parker, F.T., Vecchio, K.S., Spada, F.E., Lavernia, E.J., Rodriguez, R., *Amorphous Soft Magnetic Particles Produced by Spark Erosion*. Journal of Magnetism and Magnetic Materials 254-255 (2003) 1-6.
46. Nagase, T., Nino, A., Umakoshi, Y., *In Situ Observation of Solid-State Amorphization in $Nd_2Fe_{14}B$ Alloy by Electron Irradiation*. Materials Science and Engineering A 449-451 (2007) 1111-1114.
47. Wang, T.L., Li, J.H., Tai, K.P., Liu, B.X., *Formation of Amorphous Phases in an Immiscible Cu-Nb System Studied by Molecular Dynamics Simulation and Ion Beam Mixing*. Scripta Materialia 57 (2007) 157-160.
48. Ponyatovsky, E.G., Barakov, O.I., *Pressure-Induced Amorphous Phases*. Materials Science Reports 8 (1992) 147-191.
49. Komatsu, M., Kiritani, M., *Amorphization of Eutectic Alloys by Shock Compression*. Materials Science and Engineering A 350 (2003) 150-154.
50. Schwarz, R.B., Johnson, W.L., *Formation of an Amorphous Alloy by Solid-State Reaction of the Pure Polycrystalline Metals*. Physical Review Letters 51 (1983) 415-418.
51. Suzuki, K., Ishikawa, K., Aoki, K, Cadogan, J.M., Ishamaru, M., Hirotsu, Y., *Exchange Interactions in Hydrogen-Induced Amorphous YFe_2*. Journal of Non-Crystalline Solids 353 (2007) 748-752.
52. Cho, Y.S., Koch, C.C., *Mechanical Milling of Ordered Intermetallic Compounds: The Role of Defects in Amorphization*. Journal of Alloys and Compounds 194 (1993) 287-294
53. Liu, Y.J., Chang, I.T.H., *Compositional Dependence of Crystallization Behaviour of Mechanically Alloyed Amorphous Fe-Ni-Zr-B Alloys*. Materials Science and Engineering A 325 (2002) 25-30.
54. Dong, P., Hou, W.L., Chang, X.C., Quan, M.X., Wang, J.Q., *Amorphous and Nanostructured $Al_{85}Ni_5Y_6Co_2Fe_2$ Powder Prepared by Nitrogen Gas-Atomization*. Journal of Alloys and Compounds 436 (2007) 118-123.
55. Godec, M., Nolan, D., Jenko, M., *Characterisation of Crystallization in Amorphous Soft Magnetic $Fe_{74}Si_{11}B_{14}Ni_1$ Powders by EBSD Method*. Materials Science and Engineering B 129 (2006) 31-38.
56. Miller, S.A., Murphy, R.J., *A Gas-Water Atomization Process for Producing Amorphous Powders*. Scripta Metallurgica 13 (1979) 673-676.
57. Oguchi, M., Inoue, A., Masumoto, T., *Flaky Amorphous Powders in Fe-, Co- and Al-Based Systems Prepared by a two-stage quenching technique*. Materials Science and Engineering A 133 (1991) 688-691.

58. Perel, J., Mahoney, J.F., Taylor, S., Shanfield, Z., Levi, C., *An Automated Laboratory Apparatus for the Production of Rapidly Solidified Submicron Powders*, in *Rapidly Solidified Amorphous and Crystalline Alloys*. Kear, B.H., Giessen, B.C., Cohen, M., Editors. Elsevier Science Publishing Co., Inc. (1982) 131-135.
59. Duwez, P., Willens, R.H., Klement, W., *Non-Crystalline Structure in Solidified Gold-Silicon Alloys*. Nature 187 (1960) 869-870.
60. Fontana, M., Bormioli, M., Arcondo, B., *Quenched GaTeFe Alloys Near the $Ga_{20}Te_{80}$ Composition.* Journal of Non-Crystalline Solids 231 (1998) 234-239.
61. Barault, G., Rohr, L., Greneche, J.M., *Magnetic Texture in Splat-Cooled Metglasses Investigated by Mössbauer Spectroscopy*. Journal of Magnetism and Magnetic Materials 128 (1993) 258-266.
62. Squire, P.J., *Alloy Development of Al-Based Metallic Glasses*. Final Year Project (2004). University of Birmingham.
63. Squire, P.J., Chang, I.T.H., *Development of Rapidly Solidified Al-Y-Ni-Based Alloys*. Materials Science and Engineering A 449-451 (2007) 1009-1012.
64. Yavari, A.R., Joud, J.C., Bellissent-Funel, M.C., *SANS Evidence for Density Fluctuations in $Pd_{80}(Si_xGe_{1-x})_{20}$ Glassy Ribbons Prepared by Panar-Flow-Casting and Melt-Spinning*. Physics Letters 105A (1984) 88-92.
65. Inomata, K., Murata, S., *U.S. Patent* 4 517 017.
66. Masumoto, T., Ohnaka, I., Inoue, A., Hagiwara, M., *Production of Pd-Cu-Si Amorphous Wires by Melt Spinning Method Using Rotating Water*. Scripta Metallurgica 15 (1981) 293-296.
67. Ames, S.L., Gray, T.H., Kish, L.L., *U.S. Patent* 4 501 316.
68. Inoue, A., Katsuya, A., Amiya, K., Masumoto, T., *Preparation of Amorphous Fe-Si-B and Co-Si-B Alloy Wires by a Melt Extraction Method and Their Mechanical and Magnetic Properties*. Materials Transactions JIM 36 (1995) 802-809.
69. Chiriac, H., *Preparation and Characterization of Glass Covered Magnetic Wires*. Materials Science and Engineering A 304-306 (2001) 166-171.
70. Wang, Q., Qiang, J., Wang, Y., Xia, J., Huang, H., Wang, D., Dong, C., *The Thermal Stability and Activation Energy of Crystallization of $(Cu_{61.8}Zr_{38.2})_{1-x}Al_x$ Bulk Metallic Glasses*. Journal of Non-Crystalline Solids 353 (2007) 3421-3424.
71. Peker, A., Johnson, W.L., *A Highly Processable Metallic Glass: $Zr_{41.2}Ti_{13.8}Cu_{12.5}Ni_{10}Be_{22.5}$*. Applied Physics Letters 63 (1993) 2342-2344.
72. Fetzer, C., Gránásy, L., Kemény, T., Kótai, E., Tegze, M., Vincze, I., Hoving, W., van der Woude, F., *Laser-Melted Amorphous and Crystalline Fe-B Alloys*. Physical Review B 42 (1990) 548-554.
73. Klaumünzer, S., Hou, M-d., Schumacher, G., *Coulomb Explosions in a Metallic Glass Due to the Passage of Fast Heavy Ions?* Physical Review Letters 57 (1986) 850-853.
74. Johnson, W.L., *Thermodynamic and Kinetic Aspects of the Crystal to Glass Treansformation in Metallic Materials*. Progress in Materials Science 30 (1986) 81-134.
75. Greer, A.L., Karpe, N., Bøttiger, J., *Diffusional Aspects of the Solid State Amorphization Reaction*. Journal of Alloys and Compounds 194 (1993) 199-211.
76. Katagiri, M., Onodera, H., *Hydrogen-Induced Phase Transformation*. Journal of Phase Equilibria 22 (2001) 418-423.

77. Jayalakshmi, J., Ahn., J.P., Kim, K.B., Fleury, E., *Hydrogen-Induced Amorphization and Embrittlement Resistance in Ti-based in situ Composite with BCC-phase in an Amorphous Matrix.* Journal of Materials Research 22 (2007) 428-436.
78. Cottrell, Sir A, *An Introduction to Metallurgy*. Second Edition. The Institute of Materials (1995). p168.
79. Chen, H.S., *Glassy Metals*. Reports on Progress in Physics 43 (1980) 353-432.
80. Davies, H.A., *Metallic Glass Formation*, in *Amorphous Metallic Alloys*, Luborsky, F.E., Editor. Butterworth & Co. (Publishers) Ltd. (1983) 8-25.
81. Elliot, S.R., *Physics of Amorphous Materials*. Longman Group Limited (1984). Chp2.
82. Gloriant, T., *Microhardness and Abrasive Wear Resistance of Metallic Glasses and Nanostructured Composite Materials*. Journal of Non-Crystalline Solids 316 (2003) 96-103.
83. Chen, H.S., Jackson, K.A., *The Influence of Alloy Composition on Glass Formation and Properties*, in *Metallic Glasses*. American Society For Metals (1978) 74-96.
84. Johnson, W.L., *Bulk Metallic Glasses – A New Engineering Material*. Current Opinion in Solid State & Materials Science 1 (1996) 383-386.
85. Fuquian, Z., Ming, X., Jiangliang, L, Xianyong, L., Weiming, G, An, S., Zhongmin, D., *Study of Rapidly Solidified Atomization Technique and Production of Metal Alloy Powders*. Materials Science and Engineering A 304-306 (2001) 579-592.
86. Callister Jr., W.D., *Materials Science and Engineering: An Introduction*. Sixth Edition. John Wiley & Sons, Inc. (2003) 660,756,757
87. Liebermann, H.H., *Sample Preparation: Methods and Process Characterization*, in *Amorphous Metallic Alloys*, Luborsky, F.E., Editor. Butterworth & Co. (Publishers) Ltd. (1983) 26-41.
88. Inoue, A., *Flux Treated Pd-Cu-Ni-P Amorphous Alloy Having Low Critical Cooling Rate*. Materials Transactions, JIM 38 (1997) 464-472.
89. Chang, Dr. I.T.H. *Private Discussion.*
90. Aindow, M., Unpublished data.
91 Polk, D.E., Giessen, B.C., *Overview of Principle and Applications*, in *Metallic Glasses*. American Society for Metals (1978) 1-35.
92. Zhang, Z., Xie, J., *A Numerical Simulation of Super-Plastic Die Forging Process for Zr-based Bulk Metallic Glass Spur Gear*. Materials Science and Engineering A 433 (2006) 323-328.
93. Schroers, J., Pham, Q., Peker, A., Paton, N., Curtis, R.V., *Blow Molding of Bulk Metallic Glass*. Scripta Materialia 57 (2007) 341-344.
94. Lu, Z.P., Liu, C.T. *A New Glass-Forming Ability Criterion for Bulk Metallic Glasses.* Acta Materialia (2002) 3501-3512.
95. Chen, Q., Shen, J., Zhang, D., Fan, H., Sun, J., McCartney, D.G., *A New Criterion for Evaluating the Glass-Forming Ability of Bulk Metallic Glasses*. Materials Science and Engineering A 433 (2006) 155-160.
96. Xu, D., Duan, G., Johnson, W.L., *Unusual Glass-Forming Ability of Bulk Amorphous Alloys Based on Ordinary Metal Copper*. Physical Review Letters 92 (2004) 245504.
97. Guo, F., Poon, S.J., Shiflet, G.J., *Metallic Glass Ingots Based on Yttrium*. Applied Physics Letters 83 (2003) 2575-2577.

98. Li, Y., Liu, H.Y., Jones, H., *Easy Glass Formation in Magnesium-based Mg-N-Nd Alloys*. Journal of Materials Science 31 (1996) 1857-1863.
99. Liu, W.Y., Zhang, H.F., Hu, Z.Q., Wang, H., *Formation and Mechanical Properties of $Mg_{65}Cu_{25}Er_{10}$ and $Mg_{65}Cu_{15}Ag_{10}Er_{10}$ Bulk Amorphous Alloys*. Journal of Alloys and Compounds 397 (2005) 202-206.
100. Ma, H., Ma, E., Xu, J., *A New $Mg_{65}Cu_{7.5}Ni_{7.5}Zn_5Ag_5Y_{10}$ Bulk Metallic Glass with Strong Glass-forming Ability*. Journal of Materials Research 18 (2003) 2288-2291.
101. Inoue, A., Zhang, T., Nishiyama, N., Ohba, K., Masumoto, T., *Preparation of 16mm Diameter Rod of Amorphous $Zr_{65}Al_{7.5}Ni_{10}Cu_{17.5}$ Alloy*. Materials Transactions JIM 34 (1993) 1234-1237.
102. Wiest, A., Duan, G., Demetriou, M.D., Wiest, L.A., Peck, A., Kaltenboeck, G., Wiest, B., Johnson, W.L., *Z-Ti-Based Be-Bearing Glasses Optimized for High Thermal Stability and Thermoplastic Formability*. Acta Materialia 56 (2008) 2625-2630.
103. Duan, G., Lind, M.L., De Blauwe, K., Wiest, A., Johnson, W.L., *Thermal and Elastic Properties of Cu-Zr-Be Bulk Metallic Glass Forming Alloys*. Applied Physics Letters 90 (2007) 211901.
104. Xing, L.Q., Ochin, P., *Bulk Glass Formation in the Zr-Ti-Al-Cu-Ni System*. Journal of Materials Science Letters 16 (1997) 1277-1280.
105. He, Y., Schwarz, R.B., Archuleta, J.I., *Bulk Glass Formation in the Pd-Ni-P System*. Applied Physics Letters 69 (1996)1861-1863.
106. He, Y., Shen, T., Schwarz, R.B., *Bulk Amorphous Metallic Alloys: Synthesis by Fluxing Techniques and Properties*. Metallurgical and Materials Transactions A 29A (1998) 1795-1803.
107. Nishiyama, N., Inoue, A., *Glass-Forming Ability of Bulk $Pd_{40}Ni_{10}Cu_{30}P_{20}$ Alloy*. Materials Transactions JIM 37 (1996) 1531-1539.
108. Kim, Y.C., Kim, W.T., Kim, D.H., *A Development of Ti-based Bulk Metallic Glass*. Materials Science and Engineering A 375-377 (2004) 127-135.
109. Schroers, J., Lohwaongwatana, B., Johnson, W.L., Peker, A., *Gold Based Bulk Metallic Glass*. Applied Physics Letters 87 (2005) 061912.
110. Zhang, B., Pan, M.X., Zhao, D.Q., Wang, W.H., *"Soft" Bulk Metallic Glasses Based on Cerium*. Applied Physics Letters 85 (2004) 61-63.
111. Chen, Q.J., Fan, H.B., Ye, L., Ringer, S., Sun, J.F., Shen, J., McCartney, D.G., *Enhanced Glass Forming Ability of Fe-Co-Zr-Mo-W-B Alloys With Ni Addition*. Materials Science and Engineering A 402 (2005) 188-192.
112. Huang, X.M., Chang, C.T., Chang, Z.Y., Wang, X.D., Cao, Q.P., Shen, B.L., Inoue, A., Jiang, J.Z., *Formation of Bulk Metallic Glasses in the Fe-M-Y-B (M=Transition Metal) System*. Journal of Alloys and Compounds 460 (2008) 708-713.
113. Pan, J., Chen, Q., Li, N., Liu, L., *Formation of Centimeter Fe-based Bulk Metallic Glasses in Low Vacuum Environment*. Journal of Alloys and Compounds 463 (2008) 246-249.
114. Perepezko, J.H., Wilde, G., *Amorphization and Alloy Metastability in Undercooled Systems*. Journal of Non-Crystalline Solids 274 (2000) 271-281.
115. Allen, J.W., Wright, A.C., Connell, G.A.N., *Hybridization, Short Range Order, and Entropy in Metallic Glass Formation*. Journal of Non-Crystalline Solids 42 (1980) 509-524.

116. Wang, D., Li, Y., Sun, B.B., Sui, M.L., Lu, K., Ma, E., *Bulk Metallic Glass Formation in the Binary Cu-Zr System*. Applied Physics Letters 84 (2004) 4029-4031.
117. Elliot, R., *Eutectic Solidification Processing*. Butterworths & Co. (Publishers) Ltd. (1983) 284-286.
118. Greer, L., *Confusion by Design*. Nature 366 (1993) 303-304.
119. http://www.doitpoms.ac.uk/tlplib/phase-diagrams/printall.php, accessed: 13th June 2008.
120. Egami, T., *Atomistic Mechanism of Bulk Metallic Glass Formation*. Journal of Non-Crystalline Solids 317 (2003) 30-33.
121. Senkov, O.N., Scott, J.M., *Specific Criteria for Selection of Alloy Compositions for Bulk Metallic Glasses*. Scripta Materialia 50 (2004) 449-452.
122. Fecht, H.-J., Johnson, W.L., *Thermodynamic Properties and Metastability of Bulk Metallic Glasses*. Materials Science and Engineering A 375-377 (2004) 2-8.
123. Wang, Y.M., Shek, C.H., Qiang, J.B., Wong, C.H., Chen, W.R., Dong, C. *The e/a Factor Governing the Formation and Stability of $(Zr_{76}Ni_{24})_{1-x}Al_x$ Bulk Metallic Glasses.* Scripta Materialia 48 (2003) 1525-1529.
124. Cheney, J., Vecchio, K., *Prediction of Glass-Forming Compositions Using Liquidus Temperature Calculations*. Materials Science and Engineering A 471 (2007) 135-143.
125. *Handbook of Ternary Alloy Phase Diagrams. Volume 5*. Villars, P., Prince, A., Okamoto, H., Editors. ASM International (1995). p5330-5333.
126. Stadelmaier, H.H. and Gregg, R.A., *Die Ternäre Phase $Fe_{23}C_3B_3$ im Dreistoffsystem Eisen-Kohlenstoff-Bor*. Metall (Berlin) 17 (1963) 412-414.
127. Borlera, M.L. and Pradelli, G., *Sul Sistema Ferro-Boro-Carbonio*. Metallurgica Italiana 60 (1968) 140-146.
128. Schürmann, E. and Li, S-X., *Untersuchung der Schmelzgleichgewichte im der Ternären System Eisen-Kohlenstoff-Bor*. Giessereiforschung 37 (1985) 121-129.
129. Vogel, R. and Tammann, G., *Über das Ternäre System Eisen-Bor-Kohlenstoff*. Zeitschrift fuer Anorganische und Allgemeine Chemie 123 (1922) 225-275.
130. *Binary Alloy Phase Diagrams. Volume 1*. Massalski, T.B., Editor-In-Chief. ASM International (1990). p843.
131. *Binary Alloy Phase Diagrams. Volume 1*. Massalski, T.B., Editor-In-Chief. ASM International (1990). p482.
132. Pang, S.J., Zhang, T., Asami, K., Inoue, A., *Synthesis of Fe-Cr-Mo-C-B-P Bulk Metallic Glasses With High Corrosion Resistance*. Acta Materialia 50 (2002) 489-487.
133. Strangwood, Dr. M., *Private discussion*.
134. Yoshizawa, Y., Fujii, S., *Microstructure and Magnetic Properties of FeCoMoBC Alloys*. Journal of Magnetism and Magnetic Materials 290-291 (2005) 1543-1546.
135. Berns, H., Fischer, A., *Microstructure of Fe-Cr-C Hardfacing Alloys with Additions of Nb, Ti and B*. Metallography 20 (1987) 401-429.
136. Inal, O.T., Scherer, A., Reineke, E.G., Borden. M.J., *Characterization of Crystallization in Amorphous 2605 SC Alloy*. Thin Solid Films 119 (1984) 395-412.
137. Khalifa, H.E., Cheney, J.L. and Vecchio, K.S., *Effect of Mo-Fe Substitution on Glass Forming Ability, Thermal Stability, and Hardness of Fe-C-B-Mo-Cr-W Bulk Amorphous Alloys*. Materials Science and Engineering A 490 (2008) 221-228.

138. Perepezko, J.H., Hildal, K., *Metallic Glass Formation Reactions and Interfaces*. Materials Science & Engineering B 148 (2008) 171-178.
139. Calka, A., Madhava, M., Polk, D.E., Giessen, B.C., *A Transition-Metal-Free Amorphous Alloy: $Mg_{70}Zn_{30}$.* Scripta Metallurgica 11 (1977) 65-70.
140. Han, Z., Zhang, J., Li, Y., *Quaternary Fe-Based Bulk Metallic Glasses with a Diameter of 5mm.* Intermetallics 15 (2007) 1447-1452.
141. Ponnambalamb, V., Poon, S.J., Shiflet, G.J., Keppens, V.M., Taylor, R., Petculescu, G., *Synthesis of Iron-Based Bulk Metallic Glasses as Nonferromagnetic Amorphous Steel Alloys*. Applied Physics Letters 83 (2003) 1131-1133.
142. Lu, Z.P., Ma, D., Liu, C.T., Chang, Y.A., *Competitive Formation of Glasses and Glass-Matrix Composites*. Intermetallics 15 (2007) 253-259.
143. *Binary Alloy Phase Diagrams. Volume 2*. Massalski, T.B., Editor-In-Chief. ASM International (1990). p1724-1728.
144. *ASM Handbook. Volume 9*. Vander Voort, G.F., Editor. ASM International (2004). p105.
145. *Handbook of Ternary Alloy Phase Diagrams. Volume 5*. Villars, P., Prince, A., Okamoto, H., Editors. ASM International (1995). p5592.
146. *Periodic Table of the Elements*. WILEY-VCH (1999) 2nd Edition.
147. Chenney, J., Vecchio, K., *Evaluation of Glass-Forming Ability in Metals Using Multi-Model Techniques*. Journal of Alloys and Compounds 471 (2009) 222-240.